Book of Abstracts

20th International Workshop on Computational Nanotechnology

- IWCN 2019 -

May 20-24, 2019

Hilton Orrington Hotel
Evanston, Illinois, USA

www.iue.tuwien.ac.at/iwcn2019/

Edited by

David K. Ferry
Stephen M. Goodnick
Wolfgang Porod
Dragica Vasileska
Josef Weinbub

ISBN 978-3-9504738-0-3

© 2019 Institute for Microelectronics, TU Wien
Gußhausstraße 27-29/E360, 1040 Wien, Austria

Welcome to IWCN 2019!

The International Workshop on Computational Nanotechnology (IWCN) is a forum for research on the development and application of advanced simulations of nanostructures, nanomaterials, and nanodevices.

Topics include electronic structure calculations; simulations of electronic, optical and mechanical properties of nanostructures; simulations of electronic, thermal, spin and molecular transport processes; multiscale and multiphysics simulations; computational design and evaluation of engineered nanomaterials and nanostructures; simulation of nanodevice processing and performance.

This IWCN is the 20th in the series of International Workshops, until 2015 titled "Computational Electronics" and changed to "Computational Nanotechnology" in 2017. The new name, IWCN, reflects the longstanding aim of the Workshop to generate interdisciplinary research and collaboration in solid-state materials and device simulation, and the increasingly dominant presence of nanoscale structures and devices in high performance electronics and photonics. The full history of workshops is provided at the IWCN portal website.

This year, the IWCN will host two satellite workshops: The two-day International Wigner Workshop will be held before the main conference, and the one-day (split up in two half-days) Workshop on High Performance TCAD will be held after.

The Organizing Committee

General Chair
Wolfgang Porod, University of Notre Dame, USA

Program Committee Co-Chairs
David K. Ferry, Arizona State University, USA
Dragica Vasileska, Arizona State University, USA

Local Arrangements Chair
Stephen M. Goodnick, Arizona State University, USA

Communications Chair
Josef Weinbub, TU Wien, Austria

ISBN 978-3-9504738-0-3

International Advisory and Program Committee

Marc Bescond, CNRS/The University of Tokyo, Japan
György Csaba, Pázmány Péter Catholic University, Hungary
Aldo Di Carlo, University of Rome “Tor Vergata”, Italy
Philippe Dollfus, University of Paris-Sud/CNRS, France
David K. Ferry, Arizona State University, USA
Massimo Fischetti, University of Texas, Dallas, USA
Stephen Goodnick, Arizona State University, USA
Karol Kalna, Swansea University, UK
Robert Kelsall, University of Leeds, UK
Gerhard Klimeck, Purdue University, USA
Irena Knezevic, University of Wisconsin, Madison, USA
Hans Kosina, TU Wien, Austria
Tillman Kubis, Purdue University, USA
Paolo Lugli, Free University of Bozen-Bolzano, Italy
Massimo Macucci, University of Pisa, Italy
Nobuya Mori, Osaka University, Japan
Xavier Oriols, Universidad Autonoma de Barcelona, Spain
Wolfgang Porod, University of Notre Dame, USA
Nobuyuki Sano, Tsukuba University, Japan
Siegfried Selberherr, TU Wien, Austria
Mincheol Shin, Korea Advanced Institute of Science and Technology, Korea
Dragica Vasileska, Arizona State University, USA

20th International Workshop on Computational Nanotechnology

May 20-24, 2019

Monday, May 20

3:00 pm **Registration (Grand Ballroom Foyer 2nd floor)**

6:00 pm **Welcoming Reception (Grand Ballroom 2nd floor)**

Please note that authors had the option to have (or to have not) their abstracts published in this *Book of Abstracts*. The contributions of those authors opting not to have their abstracts included are greyed out.

ISBN 978-3-9504738-0-3

Tuesday, May 21

8:45 am **General Welcome (Grand Ballroom)**, Wolfgang Porod, *Conference Chair*

Session Tu1: Future Computing
Chair: Paolo Lugli

9:00 am B. Venitucci, L. Bourdet, Y.-M. Niquet, *University Grenoble Alpes, CEA, France*, "Electrical Manipulation of Electron and Hole Spins in Si Qubits," (*Invited*) 1

9:30 D. Querlioz, CNRS, France, "Neuromorphic Computing" (*Invited*)

10:00 M. Gal[1], L. Seitner[1], B. Radeleczki[1], W. Porod[2], G. Csaba[1], *[1]Pazmany Peter Catholic University, Hungary, [2]Notre Dame University, USA*, "Sub-Harmonic Locked Oscillators for Neuromorphic Computing" 3

10:15 *Coffee Break*

10:45 M. Di Ventra, *University of California, San Diego, USA*, "Memcomputing: Leveraging Memory and Physics to Compute Efficiently" (*invited*) 5

11:15 S. S. Pidaparthi, C. S. Lent, *Notre Dame University, USA*, "Exponentially Adiabatic Switching in Quantum-Dot Bits" 7

11:30 D. Pandey[1], L. Bellentani[2], M. Villani[1], G. Albareda[3], P. Bordone[2,4], A. Bertoni[4], X. Oriols[1], *[1]Universitat Autonoma de Barcelona, Spain, [2]Universita degli Studi di Modena e Reggio Emilia, Italy, [3]Max Planck Institute for Structure and Dynamics of Matter, Germany, [4]S3, Instituto nanoscienze-CNR, Italy,* "Eliminating Quantum Uncertainty in Quantum Electron Devices: Leveraging Classical and Quantum Computing" 9

ISBN 978-3-9504738-0-3

Session Tu2: Solar Cells
Chair: Massimo Macucci

11:45 D. K. Ferry[1], I. R. Sellers[2], V. R. Whiteside[2], H. Esmaeilpour[2], M. B. Santos[2], [1]*Arizona State University, USA,* University of Oklahoma, USA "Hot Carrier Solar Cells: A New Approach" 11

12:00 A. Di Vito[1], A. Pecchia[2], D. Rossi[1], M. Auf der Maur[1], A. Agresti[1], S. Pescetelli[1], A. Pazniak[3], A. Di Carlo[1,3], [1]*University of Rome Tor Vergata, Italy*, [2]*CNRS-ISMN, Italy,* [3]*National University of Science and Technology, Russia* "DFT Simulations and Device Modeling of MXene/Perovskite Solar Cells" 13

12:15 *Lunch (Grand Ballroom)*

Session Tu3: Modeling Thermal Effects in Devices
Chair: Tilman Kubis

2:00 Z. Aksamija, *University of Massachusetts, Amherst, USA*, "Thermal Effects in Semiconductors and Nano-Devices" (*Invited)* 15

2:30 L. Lindsay, *Oak Ridge National Laboratories, USA*, "Thermal Effects in Semiconductors and Nano-Devices," (*Invited*) 16

3:00 B. Davier[1], J. Larroque[1], P. Dollfus[1], L. Chaput[2], S. Volz[3], D. Lacroix[2], J. Saint-Martin[1], *Universite Paris-Sud, France*, [2]*LEMTA, CNRS, France,* [3]*LIMMS, University of Tokyo, Japan,* "Nanoscale Heat Transfer via Ab-Initio Monte Carlo Simulation" 17

3:15 R. Daugherty, D. Vasileska, *Arizona State University, USA*, "Multi-Scale Thermal and Electrical Modeling of CMOS Devices and Circuits" 19

3:30 *Coffee Break*

4:00 Y. Chu, J. Shi, K. Miao, Y. Zhong, P. Sarangapani, X. Ruan, T. Kubis, *Purdue University, USA*, "Thermal Boundary Resistance Predictions with Non-Equilibrium Green's Function and Molecular Dynamics Simulations" 21

4:15 K. Vuttivorakulchai, M. Luisier, A. Schenk, *ETH Zurich, Switzerland*, "Effect of Stacking Faults and Surface Roughness on the Thermal Conductivity of Si Nanowires" 23

ISBN 978-3-9504738-0-3

4:30 P. La Torraca[1], Y. Ricci[1], A. Falco[2], P. Lugli[2], L. Larcher[1], [1]*Universita degli Modena e Reggio Emilia,* [2]*Free University of Bozen-Bolzano, Italy*, “Multiphysics Simulation of Nanostructured Thermoacoustic Loudspeakers” 25

4:45 M. Jo[1,2], E. Kirkor[2,4], S. Sinha[3,4], A. Scheeline[1,4], P. Martin[1], U. Ravaioli[1], [1]*University of Illinois,* [2]*Rose-Hulman Institute of Technology,* [3]*University of New Haven,* [4]*Anchor Science, USA*, “Dynamic Thermal Interface Material (D-TIM) Simulation and Parameter Optimization Using Genetic Algorithm” 27

Wednesday: May 22

Session We1: Nanowires
Chair: Steve Goodnick

8:50 A. Antipov, *Microsoft Station Q, San Diego, USA*, "Modeling of Nanowires with Superconducting Cladding," (*Invited*) 30

9:20 A. Asenov, *University of Glasgow, UK*, "Simulation of Nanowire Transistors," (*Invited*) 31

9:50 K. Kalna[1], D. Nagy[2], A. J. Garcia-Loureiro[2], N. Seoane[2], [1]*Swansea University, UK,* [2]*Universidade de Santiago de Compostela, Spa*in, "3D Schrödinger Equation Quantum Corrected Monte Carlo and Drift Diffusion Simulations of Stacked Nanosheet Gate-All-Around Transistors" 33

10:05 H. Lee, M. Shin, *Korea Advanced Institute of Science and Technology, Korea*, "Quantum Transport Simulations of Gate-All-Around Nanowire pFETs with Arbitrary Shaped Cross-Section in the Presence of Hole-Phonon Interaction" 37

10:20 *Coffee Break*

Session We2: Heterostructures and Semiconductors
Chair: Philippe Dollfus

10:50 M. Bescond[1,2], A. Yangui[1,2], T. Yan[1], N. Nagai[1], K. Hirakawa[1,2], [1]*University of Tokyo, Japan*, [2]*LIMMS/CNRS-IIS, Tokyo, Japan*, "Evaporative Electron Cooling in Asymmetric Double Barrier Semiconductor Heterostructrues" (*Invited*)

11:20 N. C. Miller[1], M. Grupen[1], J. D. Albrecht[2], [1]*Air Force Research Laboratory, WPAFB,* [2]*Michigan State University, USA,* "Investigation of the Kink Effect in GaN HEMT Technology Using Fermi Kinetics Transport" 39

11:35 P. Sarangapani, Y. Chu, J. Charles, T. Kubis, *Purdue University, USA*, "Prediction of Urbach Tails and Band Gap Narrowing in Bulk and Confined III-V Devices with Atomistic Non-Equilibrium Green's Function" 41

ISBN 978-3-9504738-0-3

11:50 B. Thorpe[1], F. Langbein[2], S. Schirmer[1], K. Kalna[1], [1]*Swansea University, UK,* [2]*Cardiff University, UK*, "Temperature Affected Non-Equilibrium Spin Transport in Nanoscale $In_{0.3}Ga_{0.7}As$ Transistors" 43

12:05 *Lunch Buffet (Grand Ballroom)*

Session We3: Quantum Transport in Semiconductors
Chair: Karol Kalna

2:00 M. Van de Put, W. G. Vandenberghe, A. A. Laturia, S. Chen, M. V. Fischetti, *University of Texas at Dallas, USA*, "Atomistic Quantum Transport using Empirical Pseudopotentials," (*Invited*) 47

2:30 D. Stradi, P. Khomyakov, U. Vej-Hansen, M. Lee, J. Wellendorff, S. Smidstrup, K. Stokbro, A. Blom, S. Aboud *Synopsis, Denmark and USA*, "Work-Function Engineering in Ultra-Scaled 2D-TFET Devices: an Atomistic DFT-NEGF Study" 49

2:45 K.-C. Wang, S. H. Sureshbabu, X. Guo, Y. Chu, T. Kubis, *Purdue University, USA*, "From Semiclassical to Quantum Transport Modeling Including Carrier Recombination and Generation" 51

3:00 Y. Lee[1], M. Liusier[1], D. Logoteta[2], N. Cavassilas[2], M. Lanoo[2], M. Bescond[3], [1]*ETH Zurich, Switzerland,* [2]*IM2NP, UMR CNRS, France,* [3]*University of Tokyo, Japan*, "Anharmonic Phonon-Phonon Scattering Modeling of Three-Dimensional Atomistic Transport: An Efficient Quantum Treatment"

3:15 M. King, F. Karimi, S. Schmidt, I. Knezevic, *University of Wisconsin, USA*, "Simulation Tool for Coupled Quantum Transport and Electrodynamics" 53

3:30 *Coffee Break*

4:00 Y. Ahn, B. Kim, M. Shin, *Korea Advanced Institute of Science and Technology, Korea*, "An Efficient Method for Atomistic-Level Non-Equilibrium Green's Function Simulations of Field-Effect Transistors Involving Heterostructures" 55

4:15 L. Schulz, D. Schulz, *Technische Hochschule Dortmund, Germany*, "Subdomain Algorithm for the Numerical Solution of the Liouville-von Neumann Equation" 57

4:30 M. Ballicchia[1,2], D. K. Ferry[3], M. Nedjalkov[2], J. Weinbub[2], [1]*Universita Politechnica delle Marche, Italy, [2]TU Wien, Austria, [3]Arizona State University, USA*, "Linking Wigner Function Negativity in Quantum Coherence in a Nanowire" 59

Thursday, May 23

Session Th1: Study of Materials
Chair: Max Fischetti

8:50 G. Galli, *University of Chicago, USA*, "First Principles Modeling of Material Properties," (*Invited*)

9:20 A. A. Laturia, M. L. Van de Put, M. V. Fischetti, W. G. Vandenberghe, *University of Texas at Dallas, USA*, "Empirical Pseudopotentials for 3D and 2D Materials: A Unified Approach" 61

9:35 P. Graziosi, C. Kumarasinghe, N. Neophytou, *University of Warwick, UK*, "Thermoelectric Properties of Complex Bandstructure Materials by Coupling DFT to Boltzmann Transport Equation Including all Energy Dependences" 63

9:50 B. Galvani[1], A. Delamarre[2], D. Suchet[2], M. Bescond[3], F. Michelini[1], M. Lannoo[1], J.-F. Guillemoles[2], N. Cavassilas[1,4], [1]*Universities of Toulon and* [4]*Bordeaux,* [2]*CNRS Palaiseau, France,* [3]*University of Tokyo, Japan*, "Impact of Electron-Phonon Scattering on Optical and Electrical Properties of Perovskite Material" 65

10:05 M. Nedjalkov[1,2], J. Weinbub[1], M. Ballicchia[1], S. Selberherr[1], I. Dimov[2], D. K. Ferry[3], K. Rupp[1], [1]*TU Wien, Austria,* [2]*Bulgarian Academy of Sciences, Bulgaria,* [3]*Arizona State University, USA*, "A Gauge-Invariant Wigner Function for General Electromagnetic Fields" 67

10:20 *Coffee Break*

Session Th2: Magnetics and Resistive RAM
Chair: Gyorgy Csaba

10:50 R. Orio[1], A. Makarov[1], S. Selberherr[1], W. Goes[2], J. Ender[1], S. Fiorentini[1], V. Sverdlov[1], [1]*TU Wien, Austria,* [2]*Silvaco Europe, UK*, "Robust Magnetic Field Free Switching Scheme for Perpendicular Free Layer in Advanced Spin Orbit Torque Magnetoresistive Random Access Memory" 69

11:05 J. Cottom[1], M. Munde[1,2], A. Shluger[1], [1]*University College London, UK,* [2]*Phillips University Marburg, Germany*, "A Mechanism of Electroforming in SiO_2-Based ReRAM Devices Facilitated Electron Injection" 73

11:20 V. Sverdlov, S. Selberherr, *TU Wien, Austria*, "Hopping in a Multiple Ferromagnetic Terminal Configuration" 75

11:35 M. Chshiev, *University Grenoble Alpes, France*, "First Principles Insights into Spintronic and Spin-Orbitronic Phenomena in Magnetic Nanostructures" 79

Session Th3: Special Talks of General Interest
Chair: Xavier Oriols

11:50 B. Eisenberg, *Illinois Institute of Technology and Rush University, USA*, "Voltage Sensor of Sodium Channels: Natural Nanotechnology" 81

12:10 G. Klimeck, A. Strachan, T. Faltens, B. Hallberg, L. K. Zentner, M. G. Zentner, M. Hunt, *Purdue University, USA*, "Using nanoHUB.org in Research and Education—A Hands-on Tutorial" 83

12:30 *Lunch (on your own)*

Session Th3: Numerical Techniques
Chair: Marc Bescond

2:00 D. Connelly[1], G. Csaba[2], G. H. Bernstein[1], A. Orlov[1], J. Chisum[1], W. Porod[1], [1]*Notre Dame University, USA,* [2]*Pazmany Peter Catholic University, Hungary*, "Towards a Simulation Framework for Coupled Microwave and Micromagnetic Structures" 85

2:15 P. Muralidharan, S. M. Goodnick, D. Vasileska, *Arizona State University, USA*, "A Multi-Physics Model to Study Defect Assisted Transport in Amorphous Barrier Layers" 87

2:30 G. P. Szakmany, G. H. Bernstein, A. O. Orlov, W. Porod, *Notre Dame University, USA*, "Multi-Physics Simulations for the Design of IR and THz Nano-Antennas" 89

2:45 *L. Avazpour, S. Soleimanikahnoj, S. Suri, I. Knezevic,* University of Wisconsin, USA, "Finite-Difference Time-Domain Study of Phonon Dynamics and Rough-Interface Scattering in Nanostructures" 91

3:00 H. Kosina[1], G. Indalecio[2], [1]*TU Wien, Austria*, [2]*CITUS, University of Santiago de Compotela, Spain*, "A Two-Particle Monte Carlo Method for Carrier Transport in the Presence of Electron-Electron Scattering" 93

3:15 I. Welland, D. K. Ferry, *Arizona State University, USA*, "Electron Transport in Strained $In_{0.64}Al_{0.36}As$" 95

3:30 *Coffee Break and Posters*
Posters are listed at the end (so that they can be nicely detached from the program and used as a guide)

6:00 **Reception and Banquet (Heritage Ballroom, 2nd floor)**

ISBN 978-3-9504738-0-3

Friday, May 24

Session Fr1: Two-Dimensional Materials
Chair: Minsheol Shin

8:50 M. Luisier, C. Klinkert, C. Stieger, A. Szabo, Y. Lee, D. Campi, N. Marzari, *ETH Zurich, Switzerland*, "In Pursuit of the Next Wonder 2-D Materials: An *ab initio* Study" (*Invited*) 97

9:20 G. Gaddemane[1], M. L. Van de Put[1], W. G. Vandenberghe[1], S. Gopalan[1], E. Chen[2], M. V. Fischetti[1], [1]*University of Texas at Dallas, USA*, [2]*Taiwan Semiconductor Manufacturing, Taiwan*, "Intricacies and Limitations of the Ab-Initio Determination of Electronic Transport Properties in Two-Dimensional Materials" 99

9:35 M. Brahma[1], A. Kabiraj[1], M. Bescond[2], S. Mahapatra[1], [1]*Indian Institute of Technology, Bangalore, India*, [2]*University of Tokyo, Japan*, "Dissipative Quantum Transport in 20 nm Phosphorene FET"

9:50 G. Karimi, I. Knezevic, *University of Wisconsin, USA*, "Second-Order Optical Nonlinearity in MoS_2 Nano-Islands from Density-Matrix Calculations" 101

10:05 J. Choukroun[1], D. Logoteta[1,2], M. Pala[1], P. Dollfus[1], [1]*University Paris-Sud, France*, [2]*Universita di Pisa, Italy*, "Drain-Backgate-Enhanced TFET Bases on In-Plane $MoTe_2$/MoS_2 Heterojunction" 103

10:20 *Coffee Break*

10:50 P. B. Vyas, M. L. Van de Put, M. V. Fischetti, *University of Texas at Dallas, USA*, "Fano Resonance in Ultra-Thin-Body Double-Gate MOSFETs" 105

11:05 Z. Zhan[1,2], X. Kuang[1], E. Colomes[2], D. Pandey[2], S. Yuan[1], X. Oriols[2], [1]*Wuhan University, China*, [2]*Universitat Autonoma de Barcelona, Spain*, "Full Quantum Time-Dependent Simulation of Electron Devices with Linear 2D Band Structures: Holes or Electrons with Negative Kinetic Energy" 107

11:20 **Closing Remarks**, Wolfgang Porod

Poster Papers

Numerical Techniques

P1 L. F. Aguinsky[1], P. Manstetten[1], A. Hössinger[2], S. Selberherr[1], J. Weinbub[1], [1]*TU Wien, Austria*, [2]*Silvaco Europe, UK*, "A Mathematical Extension to Knudsen Diffusion Including Direct Flux and Accurate Geometric Description" 109

P2 P. Aguirre, S. Sant, A. Schenk, *ETH Zurich, Switzerland*, "TCAD Analysis of Leakage Currents in the Ballistic Regime" 111

P3 X. Klemenschits, S. Selberherr, L. Filipovic, *TU Wien, Austria*, "Fast Volume Evaluation on Sparse Level Sets" 113

Nanowires

P4 M. Ballicchia[1,2], M. Nedjalkov[2], J. Weinbub[2], [1]*Universita delle Marche, Italy*, [2]*TU Wien, Austria*, "Effects of Repulsive Dopants on Quantum Transport in a Nanowire" 115

P5 V. N. Kumar, D. Vasileska, *Arizona State University, USA*, "Mobility Modeling of Split-Gate Nanowires" 117

P6 S. R. Kola, Y. Li, *National Chiao Tung University, Taiwan*, "Random Telegraph Noise of Gate-All-Around Silicon Nanowire MOSFETs Induced by Single Charge Trap" 119

Two-Dimensional Materials

P7 C.-Y. Chen, Y. Li, *National Chiao Tung University, Taiwan*, "Monolayer Tungsten Disulfide with Transition Metal Doping" 121

P8 F. Hashimoto, N. Mori, *Osaka University, Japan*, "Effect of Stacking Order on Band-to-Band Tunneling in Van der Waals TMDC Heterojunctions" 123

P9 S.-C. Lu[1,2], Y. Chu[2], M. Mohamed[3], Y. Kim[4], T. Palacios[2], U. Ravaioli[1], [1]*University of Illinois, USA*, [2]*Massachusetts Institute of Technology, USA*, [3]*Lincoln Laboratory, USA*, [4]*IBM Research, USA*, "Atomistic Design of Multilayer Black Phosphorus Vertical Tunnel FETs"

P10 M. Macucci, P. Marconcini, *Universita di Pisa, Italy*, "Gate Bias Dependence of Flicker Noise in Graphene as a Result of Carrier Statistics" 125

P11 S. Soleimanikahnoj, I. Knezevic, *University of Wisconsin, USA*, "Band Structure of Zigzag Phosphorene Nanoribbons: A Tight-Binding Hubbard Model" 127

General Semiconductors

P12 C.-Y. Cheng, D. Vasileska, *Arizona State University, USA*, "Transport Modeling of 4H-SiC for Power Device Applications Using Full-Band Ensemble Monte Carlo Method"

P13 H. Kosina, M. Kampl, *TU Wien, Austria*, "Current Estimation in Backward Monte Carlo Simulations" 129

P14 A. Shaik[1], D. Brinkman[2], C. Ringhofer[1], D. Vasileska[1], [1]*Arizona State University, USA,* [2]*San Jose State University, USA*, "An Improved Unified Solver for Modeling Defect Dynamics in Materials" 131

P15 J. Wang, K.-C. Wang, T. Kubis, *Purdue University, USA*, "Design of Ultraviolet Light Emitting Diodes Based on Hexagonal Boron Nitride" 133

Thermal Transport

P16 Y. Guo, S. Volz, M. Nomura, *University of Tokyo, Japan*, "Coherent Heat Transport in Nanostructures by Numerical Solution of Quantum Kinetic Equation of Phonons" 135

Semiconductor Devices

P17 L. Maurer, M. Marshall, D. Campbell, L. Tracy, T.-M. Lu, D. Ward, S. Misra, *Sandia National Laboratories, USA*, "Modeling Transport in Phosphorus δ-Doped Silicon Tunnel Junctions" 137

P18 N. M. Shrestha[1], C.-H. Chen[1], Y.-J. Lee[2], Z.-M. Tsai[1], Y. Li[1], J.-H. Tarng[1], S. Samukawa[1,3], [1]*National Chiao Tung University,* [2]*Taiwan Semiconductor Ressearch Institute, Taiwan,* [3]*Tohoku University, Japan*, "Computational Study of AlGaN/GaN HEMTs with SiN/GaN Double-Cap Layer"

ISBN 978-3-9504738-0-3

P19 E. S. Skibinsky-Gitlin[1], F. M. Gomez-Campos[1], S. Rodriguez-Bolivar[1], J. E. Carceller[1], M. Caifano[2], [1]*UGR Grenada, Spain,* [2]*University of Leeds, UK*, "Electronic Mobility in a Periodic Superlattice of InSb Quantum Dots" 139

P20 D. Rossi, A. Di Carlo, M. Auf der Maur, *University of Rome Tor Vergata, Italy*, "The Multiparticle Drift-Diffusion Approach for Optoelectronic Devices" 141

ISBN 978-3-9504738-0-3

Electrical Manipulation of Electron and Hole Spins in Si Qubits

B. Venitucci, L. Bourdet, J. Li, Y.-M. Niquet
Univ. Grenoble Alpes, CEA, INAC-MEM-L_Sim, F-38000 Grenoble, France
yniquet@cea.fr

We review our recent results on the modeling of the electrical manipulation of electron and hole spins in silicon quantum dots. We focus on silicon-on-insulator (SOI) devices as an illustration (Fig. 1). Fast Rabi oscillations (up to 80 MHz) have indeed been measured in hole spin qubits [1], and Electric Dipole Spin Resonance (EDSR) has been demonstrated in electron devices despite the weak spin-orbit coupling (SOC) [2]. These devices are modeled with multi-bands **k.p** (holes) or tight-binding methods (electrons) (Fig. 2). The latter indeed account for valley and spin-orbit physics in the conduction band at the atomic scale. As for electrons, the calculations show that the coupling between spins and electric fields results from a subtle interplay between spin-orbit and valley interactions [2]. When the up spins of one valley anti-cross the down spins of the other, they get mixed by SOC, allowing for electrically driven spin transitions (Fig. 4). We argue, in particular, that SOC is enhanced by the very low symmetry of the “corner dots” formed in SOI devices (Fig. 3). We demonstrate that the valley splitting and the SOC can be tailored by front and back-gate electric fields; and we propose a manipulation scheme where an almost pure spin qubit (well protected from charge noise but hardly controllable electrically) can be transformed back and forth into a spin-valley qubit (or even a pure valley qubit) for fast electrical manipulation [3]. The physics of holes is very different. We show that the Rabi oscillations of holes are usually driven by a complex interplay between the motion of the dot as a whole in the electric field of the gate and the mixing of higher-lying excitations into the qubit states by the anharmonic components of the potential. These mechanisms can be described in a unified framework based on a gyromagnetic g-matrix and on its derivative with respect to the gate voltage [1, 4]. This g-matrix formalism can be used to model spin qubits at a very low computational cost (Fig. 5). As an illustration, we discuss the role of strains in spin qubits and show that silicon provides the best opportunities for fast hole spin Rabi oscillations owing to its very anisotropic valence band. This work was supported by the French ANR project MAQSi and the EU H2020 project MOSQUITO.

[1] A. Crippa *et al*., Physical Review Letters **120**, 137702 (2018).
[2] A. Corna *et al*., npj Quantum Information **4**, 6 (2018).
[3] L. Bourdet and Y.-M. Niquet, Physical Review B **97**, 155433 (2018).
[4] B. Venitucci *et al*., Physical Review B **98**, 155319 (2018).

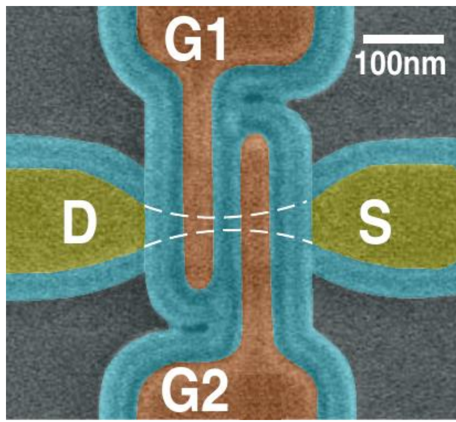

Fig.1: SEM image of a SOI device. The gates G1 and G2 control two quantum dots along a [110] Si nanowire outlined by the dashed white lines. The dot under G1 is used as a filter to measure the spin in the qubit under G2 through Pauli spin blockade of the source-drain (SD) current. The qubit is manipulated by radio-frequency pulses on G2 [1].

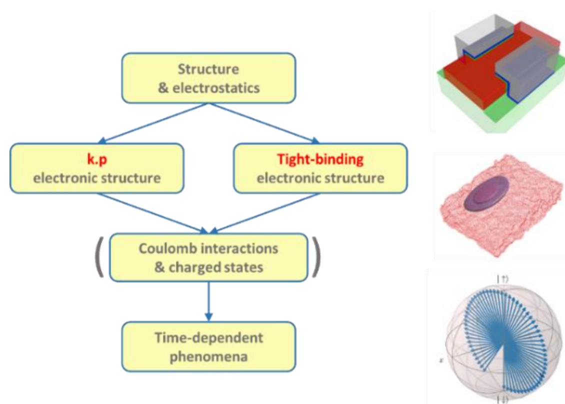

Fig. 2: Computational methodology developed for the qubits.

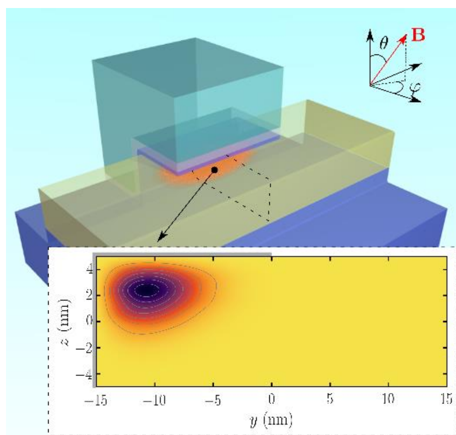

*Fig. 3: 3D model of a SOI device with a Si nanowire in yellow, SiO_2 in dark blue, and a partly overlapping gate in light blue. The location of the electron trapped under the gate is sketched in orange. A map of the squared wave function is plotted in the cross-section outlined by the dashed black lines. The orientation of the magnetic field **B** (see Fig. 5) is characterized by the angles θ and φ.*

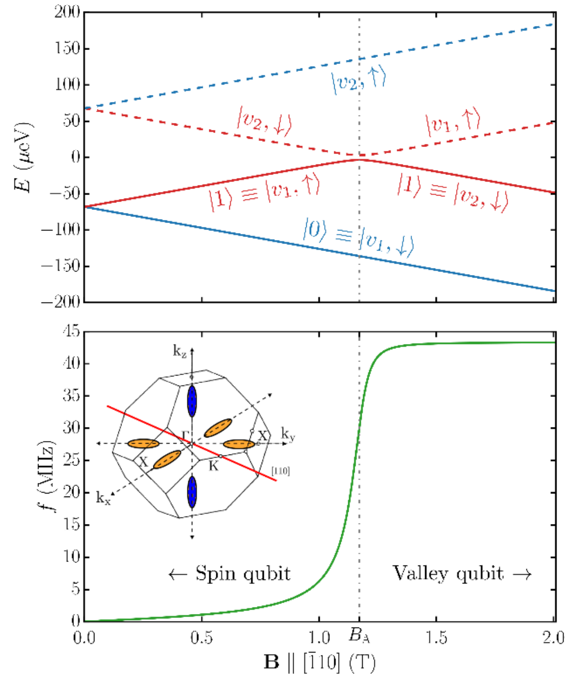

Fig. 4: (top panel) Single-particle energy levels in the conduction band of a thin Si quantum dot as a function of the magnetic field. At zero field, the degeneracy between the ±Z valleys is lifted by steep confinement at the Si/SiO_2 interface; the resulting v_1 and v_2 states are further split by the Zeeman interaction at finite magnetic field. The $|v_1,\uparrow\rangle$ state anti-crosses the $|v_2,\downarrow\rangle$ state around $B = B_A$ due to SOC; This enables electrically-driven Rabi oscillations between the lowest two states $|0\rangle$ and $|1\rangle$ as the dipole matrix element between $|v_1,\downarrow\rangle$ and $|v_2,\downarrow\rangle$ is finite. The calculated Rabi frequency is plotted in the lower panel [2, 3].

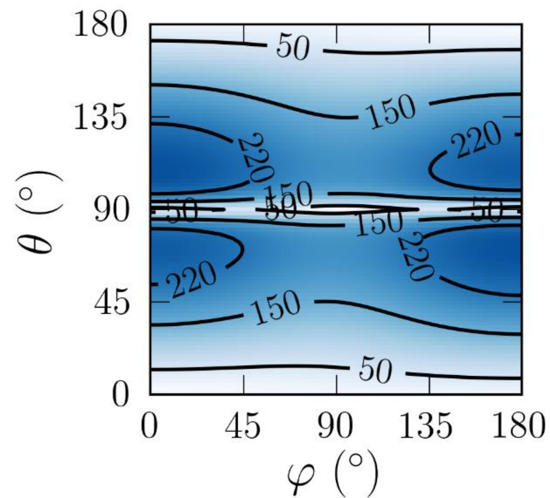

Fig. 5: Map of the Rabi frequency (MHz) of a heavy-hole spin qubit as a function of the orientation of the magnetic field, characterized by the angles θ and φ (see definition on Fig. 3) [4].

Sub-Harmonic Locked Oscillators for Neuromorphic Computing

M. Gal[1], Lukas Seitner[1], B. Radeleczki[1], W. Porod[2], G. Csaba[1]
[1]*Pazmany Peter Catholic University, Budapest, Hungary*
[2]*Department of Electrical Engineering and NDnano, University of Notre Dame, USA*
csaba.gyorgy@itk.ppke.hu

Oscillators are ubiquitous in the physical word and interconnected oscillators display complex, emergent dynamics behaviors. This makes them excellent candidates for non-Boolean computing models that may exploit their complex dynamics for computation [1]. The oscillator behaviors, however, are rather sensitive to the parameters of individual oscillators, and physical oscillators are always subject to manufacturing variations, making realization challenging.
A possible solution to this problem is using sub-harmonic injection locking (SHIL), i.e. pumping the oscillator with a frequency that typically is an n integer multiple of its natural frequency [2]. This stabilizes oscillator frequencies, and allows n number of distinct steady-state phases. The nonlinearity of the oscillations, and how strongly they are pulled toward the attractors, can be tuned by the strength of the pumping field.
In this work, we study ring oscillators and vanadium-oxide-based relaxation oscillators in SHIL-based computing systems. Both oscillators naturally support n=3,5 (odd harmonic) pumping, and we show how they can be redesigned for two-state systems. We study the construction of Hopfield-type networks using both ring oscillators and relaxation oscillators. Hopfield networks show excellent recognition capability with a basic Hebbian learning scheme, and we show an iterative algorithm for adjusting the weights to improve results. We will also demonstrate that adjustable coupling between ring oscillators can be achieved by simple, transistor-based interconnections.
SHIL-controlled relaxation and ring oscillators are very simple circuits, yet seem to be a promising hardware toolbox for realizing a number of computing functions. Importantly, SHIL control makes them much less susceptible to device-to-device parameter variations. This means that potentially large, complex computing circuits can be built from compact and imprecise circuit elements.

[1] Raychowdhury, Arijit, et. al. Computing With Networks of Oscillatory Dynamical Systems Proceedings of the IEEE (2018).
[2] Csaba, et. al. ”Neural network based on parametrically-pumped oscillators.” In Electronics, Circuits and Systems (ICECS), 2016 IEEE International Conference on, pp. 45-48. IEEE, 2016.

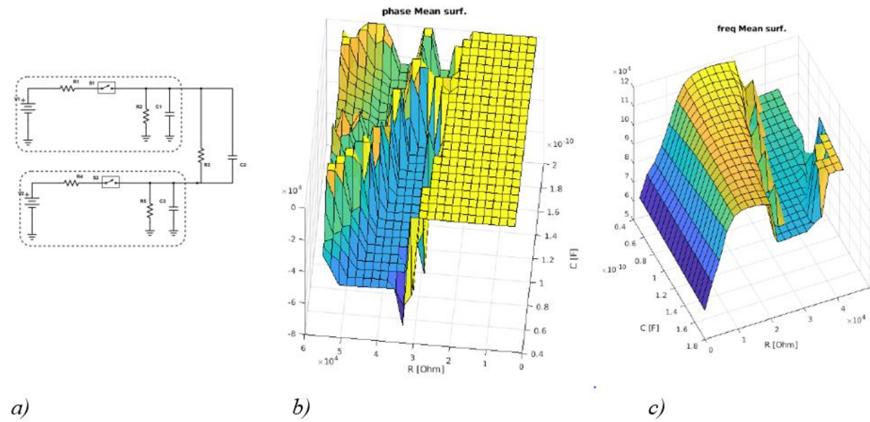

Figure 1. Synchronization regions for two VO2-based relaxation oscillators, interconnected by an RC element (a). Depending on the connections, various synchronized regions appear (b,c)

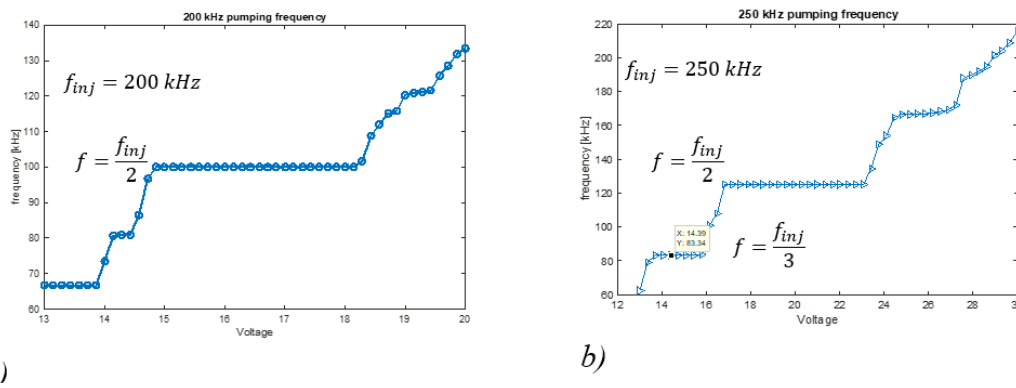

Figure 2. Relaxation oscillators act as voltage-controlled oscillators, and an externally injected oscillatory signal will injection-lock them to a fixed frequency. Here, the plateaus correspond to subharmonic locking to f/2 and f/3.

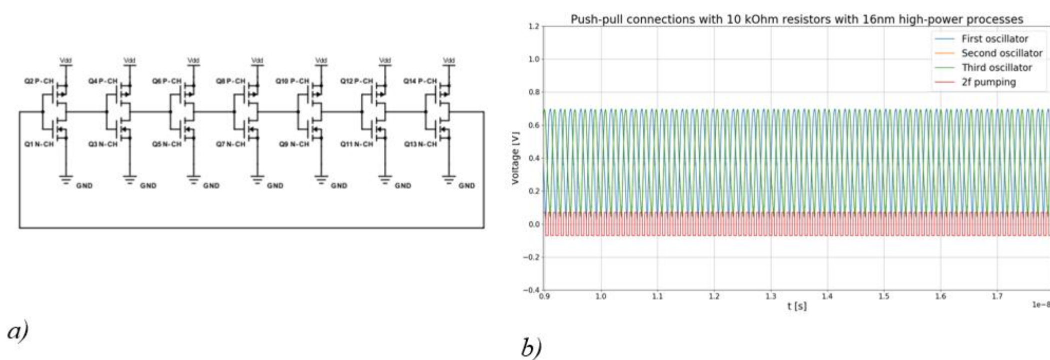

Figure 3. a) We designed a ring oscillator using highly asymmetric transistors, which can efficiently lock to 2f injection (b) – this network acts as a Hopfield network in the phase space.

Memcomputing: Leveraging Memory and Physics to Compute Efficiently

M. Di Ventra
Department of Physics, University of California San Diego, La Jolla, CA 92093-0319 USA
diventra@physics.ucsd.edu

It is well known that physical phenomena may be of great help in computing some difficult problems efficiently. A typical example is prime factorization that may be solved in polynomial time by exploiting quantum entanglement on a quantum computer. There are, however, other types of (non-quantum) physical properties that one may leverage to compute efficiently a wide range of hard problems. In this talk, I will discuss how to employ one such property, memory (time non-locality), in a novel physics-based approach to computation: *Memcomputing* [1, 2, 3, 4]. As examples, I will show the polynomial-time solution of prime factorization, the search version of the subset-sum problem [5], and approximations to the Max-SAT beyond the inapproximability gap [6] using polynomial resources and self-organizing logic gates, namely gates that self-organize to satisfy their logical proposition [5]. I will also show that these machines are described by a topological field theory, and compute via an instantonic phase, implying that they are robust against noise and disorder [7]. The digital memcomputing machines we propose can be efficiently simulated, are scalable and can be easily realized with available nanotechnology components. Work supported in part by MemComputing, Inc. (http://memcpu.com/) and CMRR.

[1] M. Di Ventra and Y.V. Pershin, Computing: the Parallel Approach, *Nature Physics* 9, 200 (2013).
[2] F. L. Traversa and M. Di Ventra, Universal Memcomputing Machines, *IEEE Transactions on Neural Networks and Learning Systems* 26, 2702 (2015).
[3] M. Di Ventra and Y.V. Pershin, Just add memory, *Scientific American* 312, 56 (2015).
[4] M. Di Ventra and F.L. Traversa, Memcomputing: leveraging memory and physics to compute efficiently, *J. Appl. Phys.* 123, 180901 (2018).
[5] F. L. Traversa and M. Di Ventra, Polynomial-time solution of prime factorization and NP-complete problems with digital memcomputing machines, *Chaos: An Interdisciplinary Journal of Nonlinear Science* 27, 023107 (2017).
[6] F. L. Traversa, P. Cicotti, F. Sheldon, and M. Di Ventra, Evidence of an exponential speed-up in the solution of hard optimization problems, *Complexity* 2018, 7982851 (2018).
[7] M. Di Ventra, F. L. Traversa and I.V. Ovchinnikov, Topological field theory and computing with instantons, *Annalen der Physik* 529,1700123 (2017).

Exponentially Adiabatic Switching in Quantum-dot Bits

S. S. Pidaparthi, C. S. Lent
Department of Electrical Engineering
University of Notre Dame
Notre Dame, IN 46556
lent@nd.edu

Active power dissipation is a crucial problem for nanoelectronics. Techniques currently employed to lower the power dissipation in CMOS processors include multicore architectures, dark silicon (turning off areas of the chip), and lowering clocking frequency. Clock frequencies have not increased much in the last decade for this reason. A more radical proposal is to alter the clocking waveforms and indeed the circuit architecture so that quasi-adiabatic switching can be achieved [1]. This can further lower the dissipated energy and may offer the next practical step in dissipation reduction. Adiabatic CMOS power reduction is *linear* in the switching time. Here we investigate a potential longer term approach to digital computation, quantum-dot cellular automata (QCA) [2]. We consider a ramped switching potential which flips the bit state of a quantum double dot. By solving the time-dependent Schrödinger equation, the excess energy deposited in the system during switching can be calculated. This energy must eventually be dissipated as heat. We show that this energy decreases *exponentially* with the switching time and demonstrate how an adiabaticity parameter can characterize the switching. We further examine the basic logical operations of a clocked three-dot QCA cell that functions as a latch [3]. Single molecule mixed-valence systems have been synthesized which target this functionality. [4] We calculate the excess energy of a WRITE operation, and both an ERASE and an ERASE WITH COPY. The results illustrate the effect of the Landauer principle connecting physical dissipation with logical reversibility.

[1] Athas, W.C., Svensson, L.J., Koller, J.G., Tzartzanis, N., Chou, E.Y.-C.: Low-power digital systems based on adiabatic-switching principles. IEEE Trans. VLSI Syst. 2 (4), 398−407 (1994).

[2] Lent, C.S.; Tougaw, P.D. A device architecture for computing with quantum dots. Proc. IEEE 85, 541–557 (1997).

[3] Orlov, A.O.; Kummamuru, R.; Ramasubramaniam, R.; Lent, C.S.; Bernstein, G.H.; Snider, G.L. A two-stage shift register for clocked quantum-dot cellular automata, J. Nanosci. Nanotechnol. 2, 351–355 (2002).

[4] Christie, J.A.; Forrest, R.P.; Corcelli, S.A.; Wasio, N.A.; Quardokus, R.C.; Brown, R.; Kandel, S.A.; Lu, Y.; Lent, C.S.; Henderson, K.W. Synthesis of a Neutral Mixed-Valence Diferrocenyl Carborane for MolecularQuantum-Dot Cellular Automata Applications. Angew. Chem. 127, , 15668–15671 (2015).

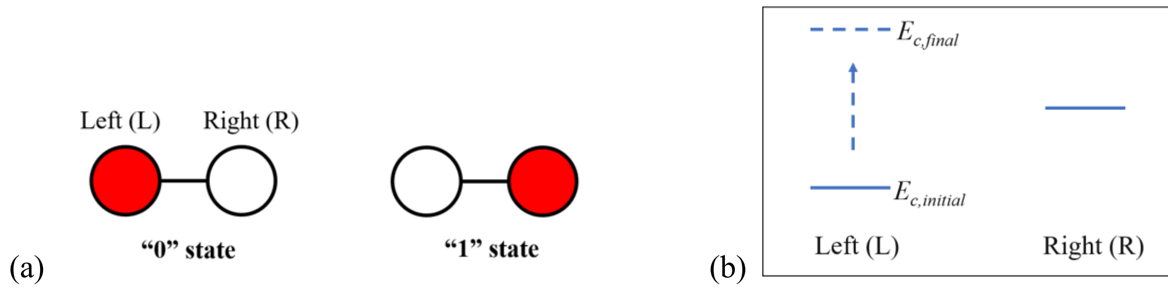

Figure 1. Switching a bit represented by a single charge in two quantum dots. (a) A charge on the left dot represents a binary 1 and a charge on the right represents a binary 0. The two dots are coupled by a Hamiltonian tunneling matrix element γ. (b) Switching can be accomplished by raising the potential energy of the left dot by an amount ΔE_c, from $E_{c,initial}$ to $E_{c,final}$ over a switching time T.

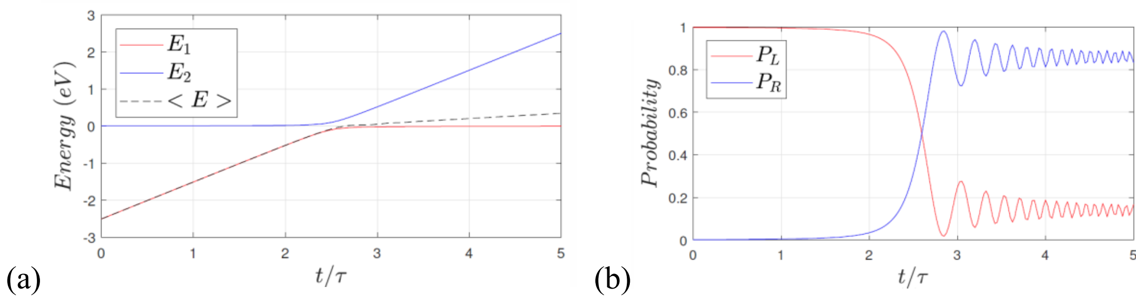

*Figure 2. Rapid switching of a two-dot system. The results shown are from a numerical solution of the time-dependent Schrodinger equation as the potential of the left dot is smoothly increased over time. The characteristic time is given by $\tau \equiv \pi\hbar / \gamma$. Here γ = 0.1 eV and $E_L = E_c$ is increased from -2.5 to +2.5 eV over a switching time of T = 5 τ. The right dot on-site potential is held constant. (**a**) The instantaneous energy eigenstates $E_1(t)$ and $E_2(t)$, showing the expected avoided level crossing. After the cross-over, the energy expectation value $\langle E \rangle$ is higher than $E_1(t)$. The difference between the two, E_{excess}, represents the energy deposited in the system during the switching event. (**b**) Probabilities are shown for the left and right dot occupancy. At time t = 2.5 τ, the charge transfers from the left dot to the right dot. Because the switching is very rapid however, ringing is evident.*

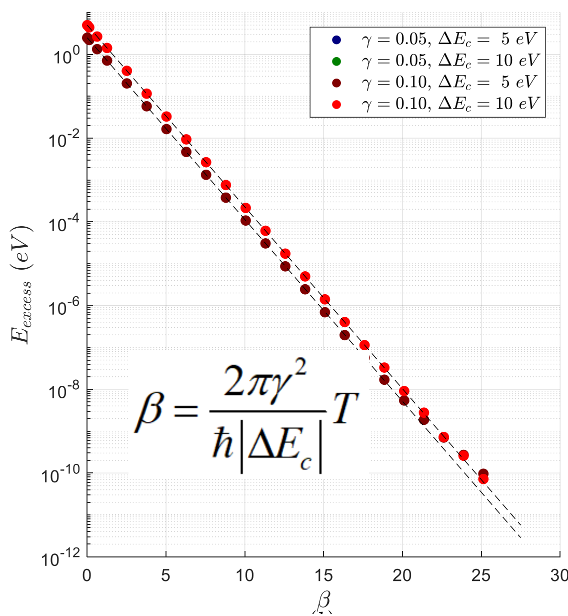

Figure 3. Exponential decrease in the excess energy deposited in the system due to switching. The adiabatic parameter β can be viewed as a scaled switching time which depends on the slope of the switching potential and the tunneling energy γ. As the switching time is increased the amount of excess energy decreases exponentially.

Eliminating Quantum Uncertainty in Quantum Electron Devices: Leveraging Classical and Quantum Computing

D. Pandey[1], L. Bellentani[2], M. Villani[1], G. Albareda[3], P. Bordone[2,4], A. Bertoni[4], X. Oriols[1]
[1]*Departament d'Enginyeria Electrónica, Universitat Autónoma de Barcelona, 08193-Bellaterra (Barcelona), Spain*
[2]*Dipartimento di Scienze Fisiche, Informatiche e Matematiche, Università degli Studi di Modena e Reggio Emilia, Via Campi 213/A, I-41125 Modena, Italy*
[3]*Max Planck Institute for the Structure and Dynamics of Matter and Center for Free-Electron Laser Science, Luruper Chaussee 149, 22761 Hamburg, Germany*
[4]*S3, Istituto Nanoscienze-CNR, Via Campi 213/A, 41125 Modena, Italy*
devashish.pandey@uab.cat

Today, there is a lively debate in the scientific community on whether quantum computing will offer better capabilities in the coming future compared to the existing classical computing. While some corporations and research centres are advocating the enormous potential of quantum computing, others are trying to push the limits of the classical computing strategies to its apex. Nowadays, classical and quantum computations are performed using quantum devices following three main steps: initial preparation of the quantum state, unitary evolution of the state and the final measurement of the state. The last step implies quantum uncertainties in outputs - due to the so-called wave function reduction - that causes inconveniences to the device engineers due to the undesired quantum noise [1] at the device output. This quantum noise can only be eliminated when the final state is an eigenstate of the observable of interest. In this conference, we will present a new protocol which ensures that the final state of a quantum device is an eigenstate of the current operator eradicating the quantum uncertainty in the practical implementation of the last measurement step for either classical or quantum computing. For a single electron, the measured current has an unavoidable quantum uncertainty. However, due to central limit theorem, when the number of electrons in the device becomes very large, the measured current due to all electrons (normalized to the number of electrons) approaches a single eigenvalue, without quantum uncertainty. Thus, the physical implementation of our protocol just requires increasing the number of involved electrons and normalizing the current. Its final success, however, requires that electrons behave as non-interacting quasi-particles [2]. Practical examples of the advantages of this protocol for classical (with resonant tunnelling diode (RTD)) and quantum (Mach-Zehnder interferometer (MZI)) computing will be discussed. In Fig. 1, we test how the effective number of particles required to ensure an acceptable low level of quantum noise depends on several device properties of a RTD (like transmission coefficient, doping, temperature, etc.). Similar arguments can be used in the context of current computation in a quantum computing device such as the MZI [3] (Fig. 2). In Fig. 3(a), the computation of the electrical current for a varying magnetic field is plotted which leads to Aharonov-Bohm oscillations in the device, which is a clear-cut signature of quantum interferences [3]. In Fig. 3(b), we plot the instantaneous current for different injection times (which is inversely proportional to the number of particles): the lower number of electrons, the noisier the device. In summary, we show the utility of a new protocol for device engineers, to minimize quantum uncertainty at the outputs of classical or quantum computing devices, at the price of involving a large number of transport electrons.

[1] X. Oriols et al, PRL **98**, 066803 (2007); D. Marian et al, PRL **116**, 110404 (2016)
[2] D.Pandey et al, *arXiv preprint arXiv:1812.10257* (2018)
[3] L Bellentani et al, Phys. Rev. B **97**, 205419 (2018)

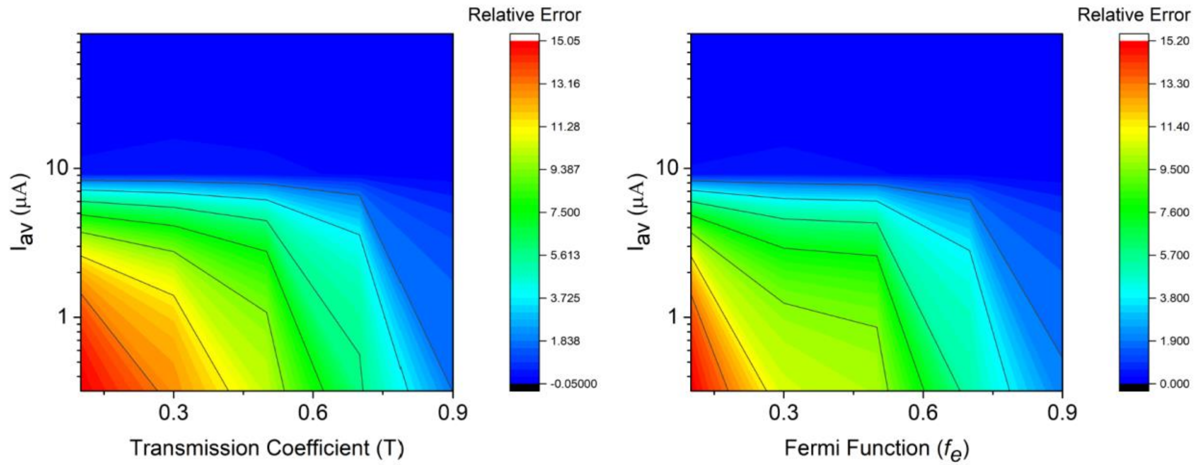

Figure.1 Plot of the relative noise in a Resonant tunneling device associated to the current with respect to the device transmission coefficient, temperature, doping and the electron saturation velocity. Figure (a) is plotted at a constant temperature while figure (b) is plotted with a constant transmission coefficient. As indicated in the text, the device with less electrons (pertaining to the low transmission coefficient, low fermi energy and low average current) is noisier.

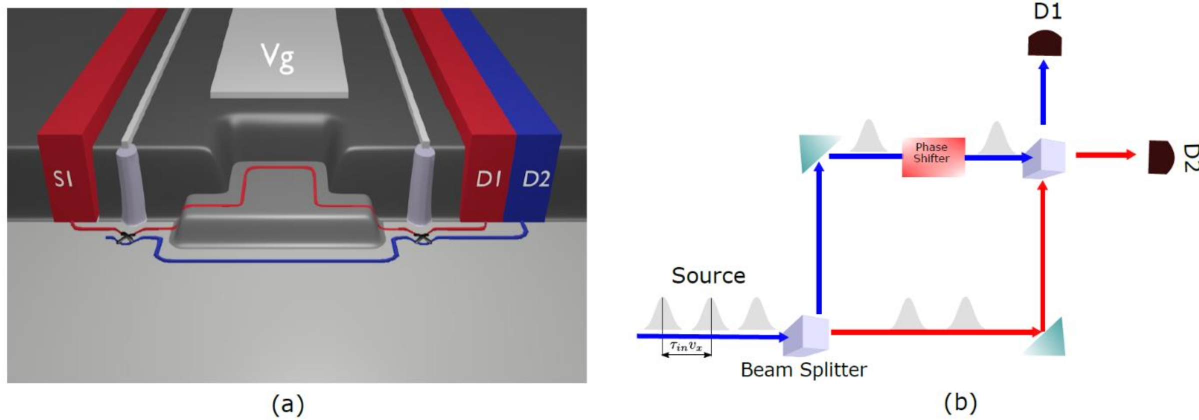

Figure.2 (a) 3D-view of the potential landscape generated by top gates in a realistic Mach-Zehnder interferometer. (b) Figure describing schematic of the device with the blue and red solid lines representing the different paths where the electrons are partitioned because of the beam splitter. The phase shifter is responsible for the interference of the wavepacket and the Aharonov-Bohm oscillations in Fig 3b.

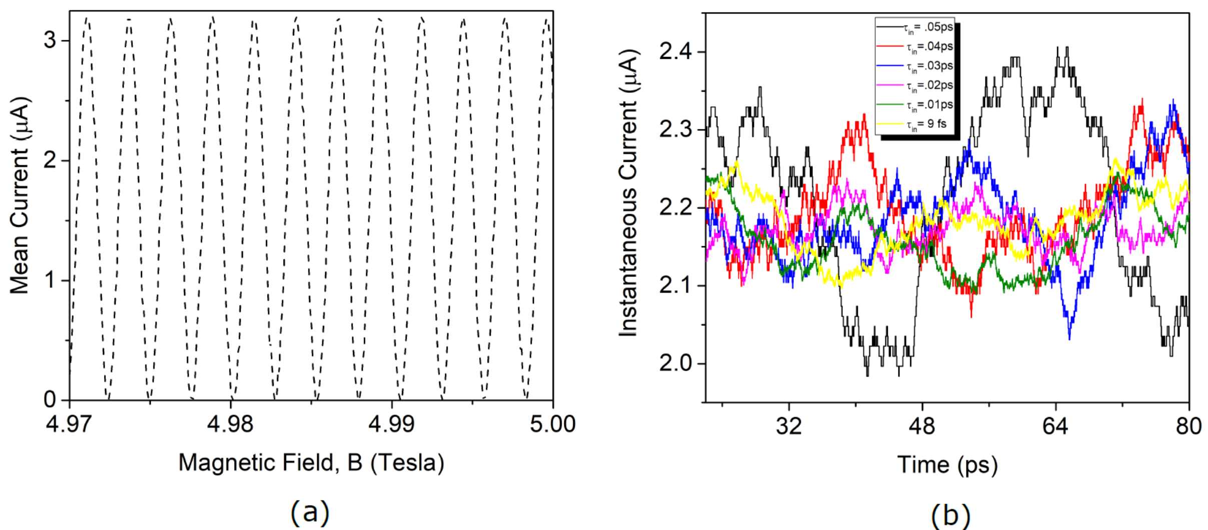

Figure.3 (a) The Aharonov-Bohm Oscillations of the mean current resulting due to the interference of the wavepackets at the output of the Detector 2 oscillating between the maximum and minimum limit of the mean current. (b) The normalized instantaneous current at the output of the detector 2 of the Mach-Zehnder interferometer with respect to the simulation time for a magnetic field of 1 T. The injection time varies from $9\ fs$ to $.05\ ps$ which has an inverse correspondence to the number of electrons in the device. The plots are normalized in terms of the minimum current obtained. As expected, the noise in the current reduces with the increase in the number of transport electrons due to the elimination of quantum uncertainty demonstrating the successful implementation of the protocol discussed in the text.

Hot Carrier Solar Cells: A New Approach

D. K. Ferry[1], I. R. Sellers[2], V. R. Whiteside[2], H. Esmaeilpour[2], M. B. Santos[2]
[1]*School of Electrical, Computer, and Energy Engineering*
Arizona State University, Tempe, AZ 85287-5706 USA
[2]*Department of Physics and Astronomy, University of Oklahoma, Norman, OK 73019*
Ferry@asu.edu

Hot carrier solar cells have been of interest as third generation cells since the work of Ross and Nozik [1]. In this approach, use of a structure which decreases the emission of phonons by the energetic photo-carriers, thus reducing their heat loss to the lattice, and use of an energy selective barrier which allows only the hot carriers to be transferred to the contacts of the device [2,3]. Unfortunately, this approach has been shown to lead to very low efficiency cells [4]. In most of these discussions, only the lowest valleys of the conduction band are considered, and higher lying satellite valleys are ignored. Thus, no account of using the higher valleys as metastable levels to maintain the hot carrier properties is considered. Since the scattering rate to the satellite valleys is generally much larger than that for intravalley phonon emission, the standard approach disregards an obvious method of maintaining the hot carrier properties of the photo-electrons. In this paper, I will describe how the use of the entire band structure for the absorber material can be used to give realistic, and conservative, estimates of achieving higher efficiencies for HCSC. We consider a p-n junction solar cell constructed with a heavily-doped p^+ layer followed by an n^- layer. The heavily-doped p-layer and lightly-doped n-layer assures that nearly all the depletion width of the junction is in the n-layer. We want the n-layer to be thinner than the depletion width, so that the electric field extends through this layer to a collector. A semi-infinite (in energy) collector is used; e.g., collection of only the hot carriers is achieved by a heterojunction with the collector layer having a larger band gap. When the photo-electrons transition from the absorber layer to the collector layer, a very large fraction of their kinetic energy is converted into potential energy of the band offset arising from the larger bandgap of the collector layer. The greatly reduced kinetic energy in this latter layer cannot emit large numbers of intravalley phonons and this further prevents significant energy loss by this mechanism. Here we use InAlAs for the absorber and AlAsSb for the other two layers, both lattice matched to InAs. We also discuss using InGaAs as the absorber for its greater solar collection efficiency.

[1] R. T. Ross and A. J. Nozik, J. Appl. Phys. **53**, 3813 (1982).
[2] H. Esmalelour *et al.,* Prog. Photovolt. Res. Appl. **24**, 591 (2016).
[3] J. A. R. Dimmock *et al.,* J. Opt. **18**, 074003 (2016),
[4] A. P. Kirk and M. V. Fischetti, Phys. Rev. B **86**, 165206 (2012).

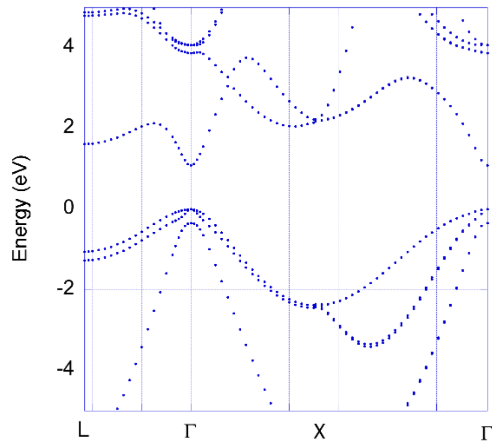

Fig.1: Band structure of $In_{0.65}Al_{0.35}As$ using non-local EPM with spin-orbing interaction included..

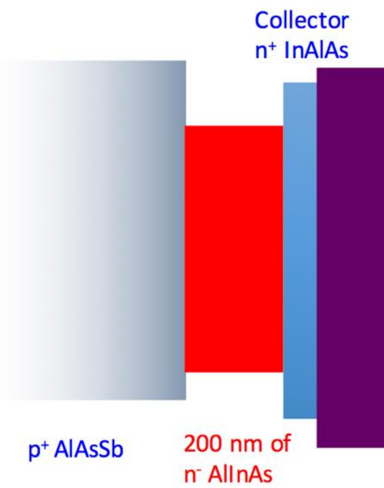

Fig.2: Structure of porposed HCSC..

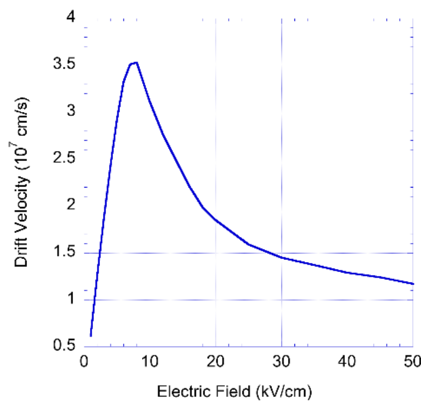

Fig.3: Drift velocity as a function of electric field when the material is continuously illuminated by solar radiation.

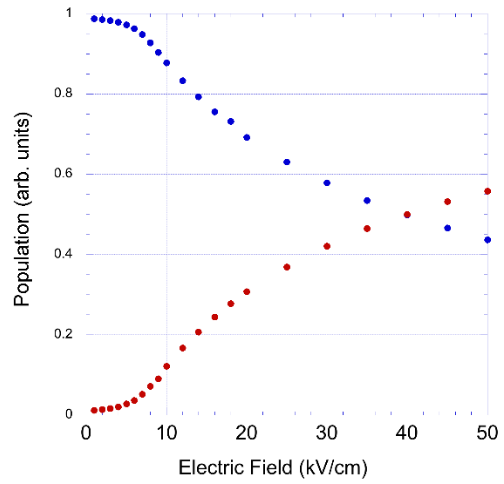

Fig.4: Population of the Γ and L valleys as a function of the electric field under continuous solar illumination.

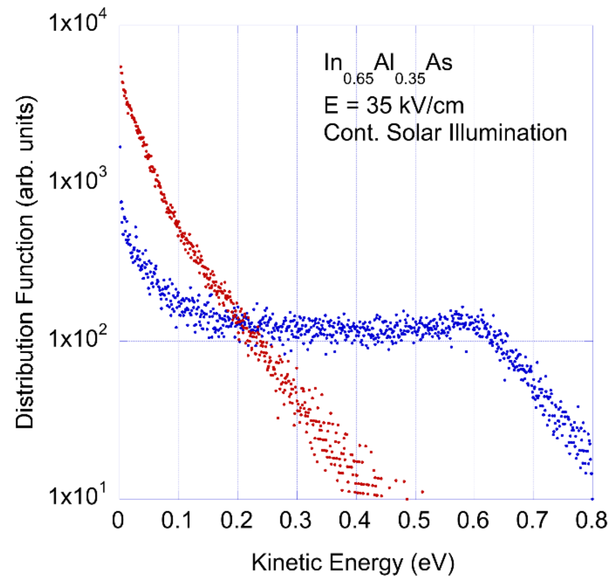

Fig.5 Carrier distribution function in the Γ and L valleys for an electric field of 35 kV/cm and continuous solar radiation.

DFT Simulations and Device Modelling of MXene/Perovskite Solar Cells

A. Di Vito[1], A. Pecchia[2], D. Rossi[1], M. Auf der Maur[1], A. Agresti[1],
S. Pescetelli[1], A. Pazniak[3], A. Di Carlo[1,3]
[1]Department of Electronics Engineering, University of Rome Tor Vergata, Via del Politecnico 1, 00133 Rome, Italy
[2]CNR-ISMN, Via Salaria Km 29.300, 00017 Monterotondo (Rome), Italy
[3]National University of Science and Technology NUTS-MISiS, Moscow, Russia
alessia.di.vito@uniroma2.it

Perovskite solar cells (PSC) have gained a key role in the field of renewable energy due to their high efficiencies and low production costs [1]. However, the effort in tuning the perovskite crystal morphology and interface properties, in order to improve the device performances, is still huge [2]. Among the solutions proposed so far, MXenes have emerged for the possibility of being incorporated within the perovskite layer resulting in an important improvement of the PSC efficiency [3].

In this study, we investigate the interaction between MXenes and perovskite, performing first-principles calculations in the framework of density functional theory. Here, we consider the interface between a $CH_3NH_3PbI_3$ thick layer, in its high temperature cubic phase, and a $Ti_3C_2T_x$ MXene layer, with the T_x functional group being F,O or/and OH. In particular, we analyze the electrostatic potential profile in the direction orthogonal to the interface and the electronic band structure of the system. We find that the functionalization of the MXene surface plays a crucial role in determining the electronic properties of the MXene/perovskite system. Specifically, the perovskite work function is strongly affected by the presence of the MXene layer and a shift of the Fermi level with respect to the perovskite band edge is observed. Interestingly, these effects depend on the MXene surface functional group: on the one hand, the OH group causes a reduction of the work function and an upward shift of the Fermi level, on the other hand, the O terminal group has the opposite effect. Parameters extracted from DFT have been used to model the PSC behavior using a Drift-Diffusion model. Comparison between simulations and experiments permits to outline the important role of the 2D MXenes in improving the performance of PSC through work function tuning.

[1] https://www.nrel.gov/pv/assets/pdfs/pv-efficiency-chart.20190103

[2] A. Agresti et al., ACS Energy Lett., **2**, 279 (2017).

[3] Z. Guo et al., Small, **14.47**, 1802738 (2018).

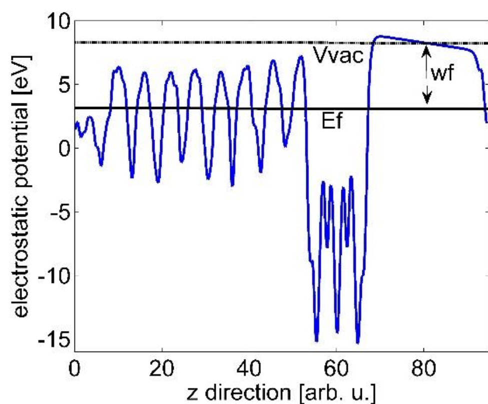

Fig.1: Electrostatic potential profile of $CH_3NH_3PbI_3/Ti_3C_2O_2$ heterojunction in the direction orthogonal to the interface.

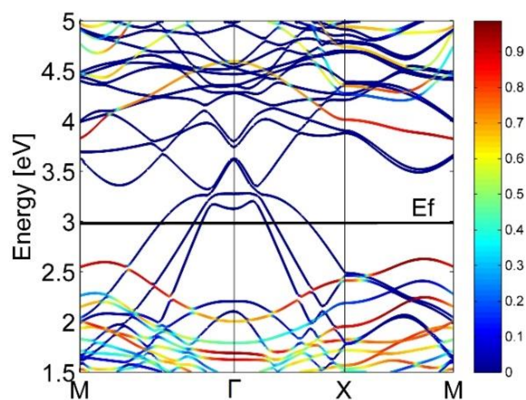

Fig.2: Projected band structure of $CH_3NH_3PbI_3/Ti_3C_2O_2$ heterojunction. The contribution from $CH_3NH_3PbI_3$ electronic orbitals is represented in red.

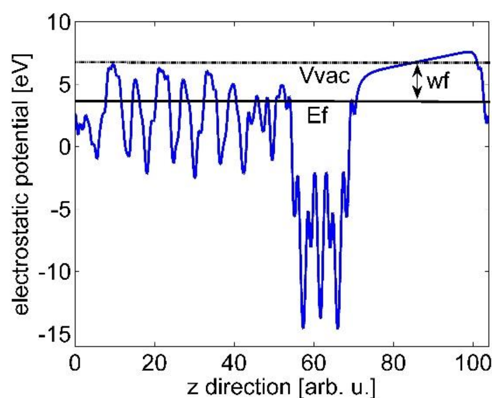

Fig.3: Electrostatic potential profile of $CH_3NH_3PbI_3/Ti_3C_2(OH)_2$ heterojunction in the direction orthogonal to the interface.

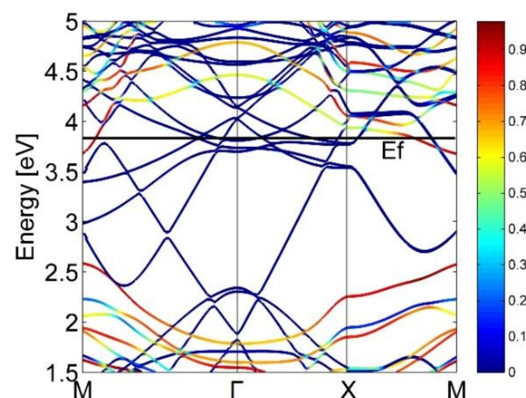

Fig.4: Projected band structure of $CH_3NH_3PbI_3/Ti_3C_2(OH)_2$ heterojunction. The contribution from $CH_3NH_3PbI_3$ electronic orbitals is represented in red.

Thermal Effects in Two-Dimensional Materials: The Role of 2D/3D Interfaces

Z. Akšamija
NanoEnergy & Thermophysics (NET) lab, Electrical and Computer Engineering
University of Massachsuetts Amherst, Amherst MA 01003
zlatana@engin.umass.edu

Two-dimensional (2D) materials have tremendous potential for next-generation nano- and optoelectronics. However, heat dissipation and its removal from hot spots in the monolayer remains a critical concern to the design of 2D-based devices [1]. Thermal currents flowing in an atomic layer can either dissipate through source/drain contacts in a transistor configuration, or through a supporting substrate via van der Waals (vdW) coupling to it. When a 2D material is supported by a substrate, the interfacial area formed between it and the substrate is often far larger than the lateral source/drain contact area. Thus, the majority of waste heat is removed across the 2D-substrate interface and then via the substrate. The thermal boundary conductance (TBC) between the 2D layer and substrate should be well characterized for reliable 2D device performance. Interfaces formed between 2D vdW materials and 3D substrates are fundamentally different than same-dimension 3D-3D and 2D-2D interfaces due to the presence of a vdW gap and the different dimensionalities of the phase spaces on either side of the interface. In this invited talk, I will review the progress in understanding lattice thermal transport, both in-plane and cross-plane, in 2D mono and few-layer materials. Then I will introduce my recent work aimed to tackle the question of selecting the best substrate for each 2D material from the point of view of heat dissipation.

Several recent papers measured the TBC between various monolayers and mostly the silicon dioxide (SiO_2) substrate, reporting a wide range of values due to inconsistent sample quality. Therefore, it is imperative to build predictive methods for quantifying the TBC between MLs and various substrates. Here, we use a combination of phonon dispersions from first-principles density functional perturbation theory simulations and our 2D-3D TBC model [2, 3]. We investigate the TBC between combinations of six atomic layers (h-BN, graphene, MoS_2, $MoSe_2$, WS_2, and WSe_2) and six substrates (SiO_2, AlN, GaN, 6H-SiC, diamond, and Al_2O_3). We show that TBC is higher for softer substrates with smaller speed of sound, but of the 6 substrates we compared, amorphous SiO_2 consistently produced higher TBC than crystalline substrates. Our work helps build a roadmap for quantifying the TBC between various 2D monolayers and their substrates and provides a framework for other 2D-3D interfaces to be studied.

[1] Yalon, E., et al., *Nano Letters* **17**(6), 3429–3433 (2017).
[2] Yasaei, P., et al., *Advanced Materials Interfaces* , 1700334 (2017).
[3] Correa, G. C., Foss, C. J., and Aksamija, Z. *Nanotechnology* **28**(13), 135402 (2017).

Phonon Thermal Transport in Nanostructured Materials

L. Lindsay
Materials Science and Technology Division, Oak Ridge National Laboratory, Oak Ridge, Tennessee 37831, USA
lindsaylr@ornl.gov

The management of heat and the understanding of heat transfer are ubiquitous challenges in numerous sciences and technologies, from models of Earth's thermal history to managing local hot spots in microelectronics. Computational materials physics is now playing an increasingly important role in developing fundamental insights into the lattice thermal conductivity of solids, a fundamentally important parameter that determines the utility of a material for energy-related applications including thermoelectricity, heat dissipation and manipulation, and thermal analogs to electronic components (e.g., thermal diodes and switches).

Here I will discuss a *predictive* method for modeling lattice dynamical properties and thermal conductivity: Peierls-Boltzmann transport coupled with density functional theory. Focus will be given to application of this method to nanostructured materials (e.g., 2D and layered vdW bonded systems, 1D chains), particularly as symmetry and dimensionality govern phonon interactions and transport. I will discuss phonon chirality and symmetry-based phonon scattering rules in 1D chains, invariance conditions for 2D materials, and the influence of anisotropy in bulk hBN and MoS_2.

This work was supported by the Department of Energy, Basic Energy Sciences, Materials Sciences and Engineering Division.

Nanoscale Heat Transfer via Ab-Initio Monte Carlo Simulation

B. Davier[1], J. Larroque[1], P. Dollfus[1], L. Chaput[2], S. Volz[3], D. Lacroix[2], J. Saint-Martin[1]
[1]*C2N, Univ. Paris-Sud, CNRS (UMR 9001), Université Paris-Saclay, Orsay, France*
[2]*LEMTA; Université de Lorraine, CNRS (UMR 7563), Vandoeuvre, France*
[3]*LIMMS, The University of Tokyo, CNRS (UMI 2820), Tokyo, Japan*
jerome.saint-martin@u-psud.fr

It is challenging to accurately model the heat transfer in devices of characteristic length close to the phonon mean free path, i.e. when the Fourier's heat transport formalism reaches its limits [1]. Additionally, if the lateral size of the structure also reaches the nanoscale, the role of the phonon reflections at the external interfaces becomes of high importance. A stochastic resolution of the Boltzmann's transport equation for phonons (pBTE) based on particle Monte Carlo (MC) algorithm is very efficient in terms of computational resources in the case of complex systems [2].

In this work, an original versatile particle MC simulator in which the material parameters, i.e. phonon dispersion and scattering rates, are parametrized by using ab initio calculation [3] is presented. It is a Full-band simulator since both dispersion and scattering rates are computed in the entire 3D Brillouin zone. To model the effect of rough external interfaces on the phonon transport, a combination of specular and diffuse phonon reflections at the external rough interfaces has been implemented in the phase space [4].

Rough nanowires and thin films schematized in Fig.1 were investigated. Cubic (Si3C) and hexagonal (Si2H) Silicon have been implemented in our MC code by using a Full-band approach, as illustrated for instance by equi-energy maps plotted in Fig 2. The effective thermal conductivity is plotted as a function of length and width in Fig. 3, illustrating the transition from a ballistic regime in short devices to a diffusive regime in long devices and the influence of the rough interfaces. In Fig. 4, the thermal conductivity of films of different phases and orientations of Si are investigated in terms of thermal conductivity and angular distribution of the density of states (DOS). It shows that the main direction of the thermal flux in Si3C is [100] though the flux along the directions [111] and [110] are also significant.

Finally, this coupling between MC and *ab-initio* methods overcomes the main limitation of the MC approach since it allows us to study of a large set of phases and materials along any transport direction without the use of any empirical parameter.

[1] D.G. Cahill, et al., J. App. Phys. **93**, 793 (2003)
[2] D. Lacroix, et al., Appl. Phys. Lett. **89**, 103104 (2006)
[3] L. Chaput, et al., Appl. Phys. Lett. **112**, 033104 (2018)
[4] B. Davier, et al, J. Phys.: Condens. Matter, **30**, 4959 (2018)

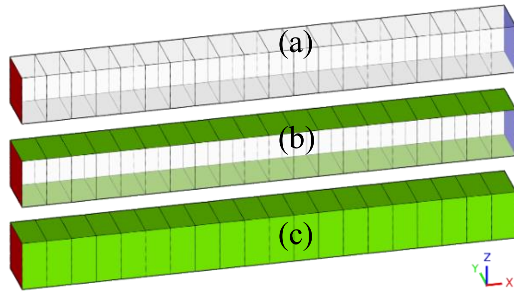

Fig.1: (a) CP nanofilm in cross-plane configuration, (b) IP nanofilm in in-plane configuration, (c) rough nanowire. Transparent/green faces for specular/rough boundaries.

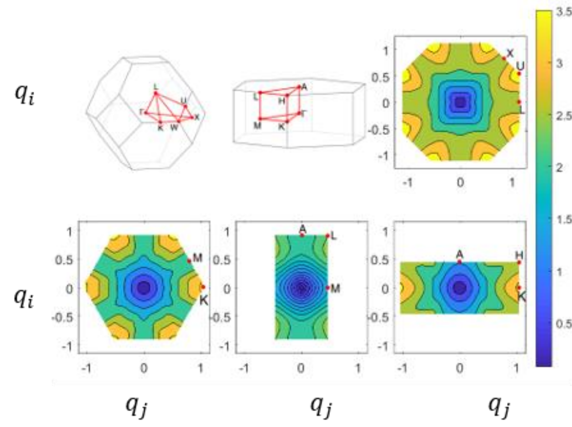

Fig.2: Schema of the BZ in (a) Si3C, (b) Si2H. Equi-energy maps in (c)the (110) plane of Si3C, (d),(e),(f) in planes of Si2H.

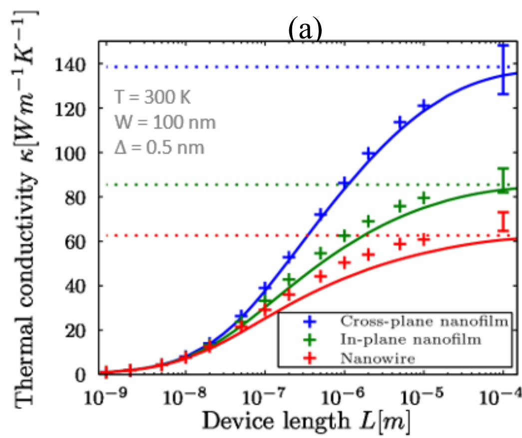

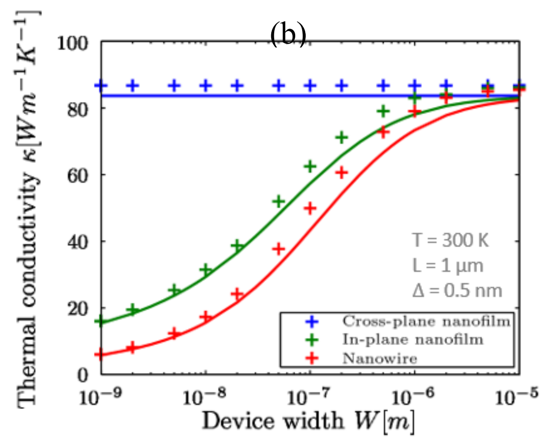

Fig.3: Thermal conductivity κ as a function of (a) length L and (b) width W for IP and CP nanofilms and for nanowires of [100] Si3C.. Dotted lines: long-device conductivity.

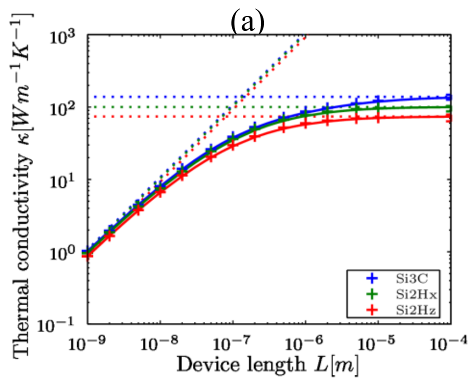

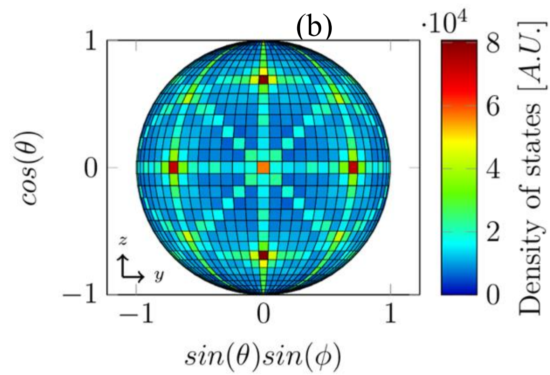

Fig.4: (a) Thermal conductivity as a function of length L for cross-plane nanofilms of Si3C, Si2Hx and Si2Hz. (b) Angular distribution of the DOS in Si3C. θ and ϕ: Polar and azimuthal angles.

Multi-Scale Thermal and Electrical Modeling of CMOS Devices and Circuits

R. Daugherty, D. Vasileska
Electrical and Computer Engineering, Arizona State University, Tempe, USA
rldaughe@asu.edu

This simulation work explores the thermal effects on electrical characteristics of CMOS devices and circuits using a multiscale dual-carrier approach. Simulating both electron and hole transport along with carrier-phonon interactions and thermal transport allows for the study of complementary logic circuits with device level accuracy regarding electrical performance and thermal effects. The electrical model is comprised of an ensemble Monte Carlo solution of the Boltzmann Transport Equation, coupled with a Poisson solver [1]; parametric iteration ensures current and voltage continuity in the circuit. The thermal model solves for carrier-phonon interactions in the device and phonon-phonon transport in interconnects [2]. This allows for modeling device behavior, analyzing circuit performance, and understanding thermal effects.

The electro-thermal approach is an improvement over de-coupled device simulators [3]. While initially developed to study individual NMOS devices, expanding this method for simulation of multiple NMOS devices in a tandem heater/sensor configuration allows for better comparison with experiments; figures 3-5 show the results [4]. Modeling PMOS devices necessitates the inclusion of hole transport and hole-phonon interactions. Finally, the analysis of CMOS logic circuits using this device simulation methodology uses parametric iteration. The device model treats contacts as Direclet boundaries, iteratively applying a fixed potential at each contact node then checking for current continuity. In simulating a CMOS inverter, the extracted voltage transfer curve shown in figure 6 demonstrates the procedure and efficacy of this methodology. This work demonstrates the effectiveness of the dual-carrier electrical solver in simulating CMOS circuits. Future work requires the coupling the dual-carrier electrical solver with the proven thermal solver to provide electro-thermal simulations of CMOS systems.

[1] C. Jacoboni, The Monte Carlo Method for Semiconductor Device Simulation. Wein ; New York: Wein ; New York : Springer-Verlag, 1989.

[2] E. Pop, S. Sinha and K. E. Goodson, "Heat Generation and Transport in Nanometer-Scale Transistors," Proc IEEE, vol. 94, (8), pp. 1587-1601, 2006.

[3] K. Raleva et al, "Modeling Thermal Effects in Nanodevices," Electron Devices, IEEE Transactions on, vol. 55, (6), pp. 1306-1316, 2008.

[4] Daugherty, R., & Vasileska, D. (2017). Multi-Scale Modeling of Self Heating Effects on Power Consumption in Silicon CMOS Devices. IMAPS January 2017, Vol. 2017, No. DPC, pp. 1-22.

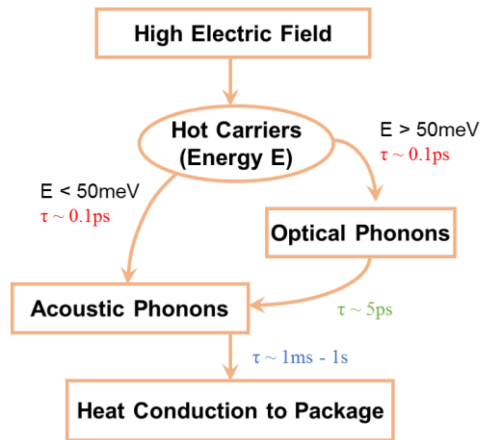

Fig.1: Overview of the thermal transport processes by which high energy carriers interact with phonons. Modeling the contribution of optical phonons requires device level simulation, while the wide variance in the time scales necessitates a multi-scale approach.

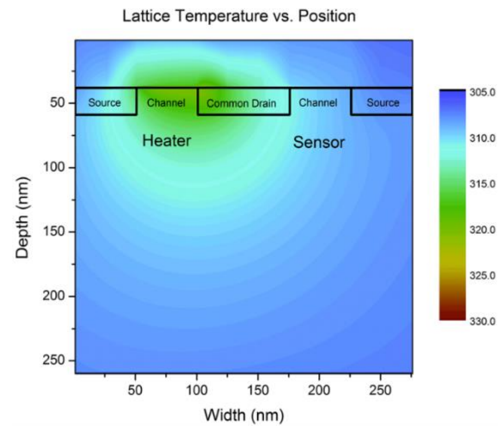

Fig.4 Comparison of experiment and simulation - simulated thermal profile of the lattice temperature in the active region of an NMOS device.

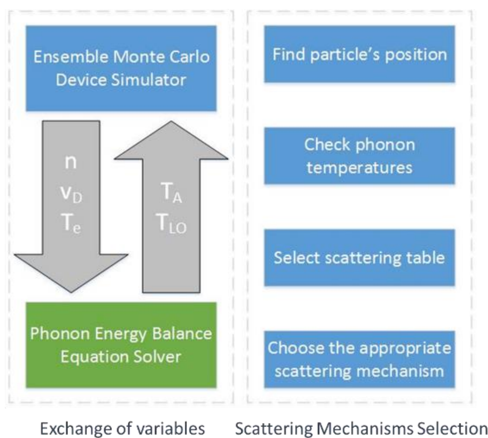

Fig.2: Coupling scheme to join the Monte Carlo/Poisson based electrical model with the energy balance carrier-phonon thermal transport model.

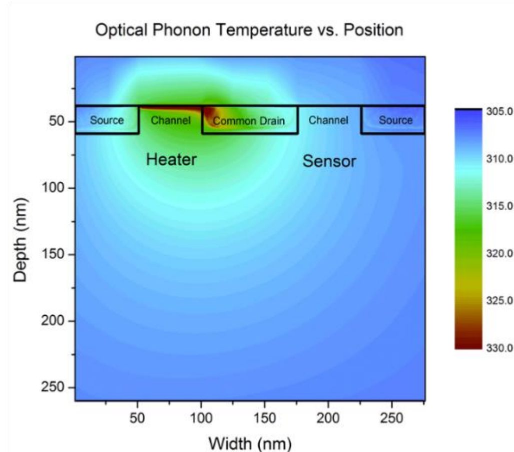

Fig.5 Comparison of experiment and simulation - simulated thermal profile of the optical phonons in the active region of an NMOS device.

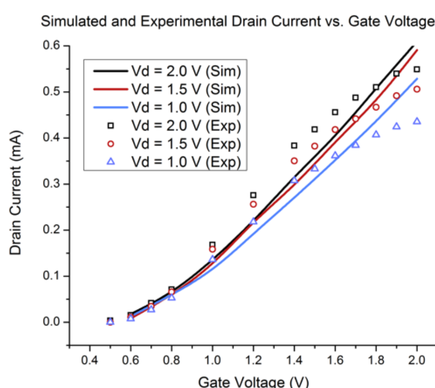

Fig.3: Comparison of experiment and simulation – IV characteristics of an NMOS active device paired with a common drain connected sub-threshold sensor.

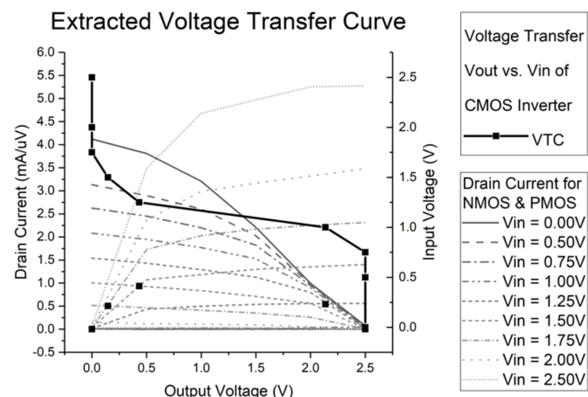

Fig.6: Voltage transfer curve of a simulated CMOS inverter. The output voltage is determined by treating contacts as Direchlet boundaries and looking for current continuity.

Thermal Boundary Resistance Predictions with Non-Equilibrium Green's Function and Molecular Dynamics Simulations

Y. Chu[1*], J. Shi[2*], K. Miao[1], Y. Zhong[2],
P. Sarangapani[1], X. Ruan[2], T. Kubis[1]
[1]School of Electrical and Computer Engineering, Purdue University,
West Lafayette, IN 47907, USA
School of Mechanical Engineering, Purdue University,
West Lafayette, IN 47907, USA
chu72@purdue.edu

Semiconductor heterostructures are widely used in the design of devices such as quantum cascade laser, transistors and thermoelectric devices. Scattering of thermal energy carriers at the interface between two solids results in thermal boundary resistance. Thermal boundary resistance was previously reported to be comparable to that of pure material with length of few to tens of nanometers [1] so that it cannot be neglected in systems of nanoscale. The non-equilibrium molecular dynamics (NEMD) method is often used to atomically model the thermal boundary resistance at interfaces since it has a good agreement with experiments [2]. The non-equilibrium Green's function (NEGF) method allows for atomic resolution and is widely accepted as one of the most consistent methods for transport properties in nanodevices in the presence of quantum phenomena including quantum confinement, tunneling, interferences, etc. However, the NEGF method has been used predominantly in the coherent (harmonic) phonon transport regime due to the fact that the inclusion of incoherent mechanisms usually requires solution of Green's functions and polarization graphs in the self-consistent Born approximation which entails a large numerical load [3]. In this work, a numerically highly efficient method to solve phonon transport in the NEGF framework including incoherent scattering phenomenologically (with Büttiker probes) is benchmarked against NEMD. For simplicity, the benchmark system is chosen to be an atomically resolved interface of Si/"heavy-Si". Nonzero interface resistance results in homogeneous structures that plague Landauer approaches [4] are absent in the presented NEGF approach. The thermal boundary resistance calculated by NEGF is compared with NEMD and shows good agreement. Subtle discrepancies of the methods are explained. Additional spectral transport information is extracted from NEGF, which shows that the different phonon modal contributions play an important role in thermal transport across the interface. This work confirms the reliability of scattered phonon NEGF and promotes its unique numerical and physical benefits for phonon transport nanodevice applications (full quantum mechanics, spectral approach compatible with periodicity, scalable method, etc.).

[1] E. S. Landry et al, *Phys. Rev. B*, vol. 80, no. 16, 2009. [2] P. K. Schelling et al, *Phys. Rev. B*, vol. 65, no. 14, 2002. [3] M. Luisier, *Phys. Rev. B*, vol. 86, no. 24, 2012. [4] G. Chen, *Appl. Phys. Lett.*, vol. 82, no. 6, 2003.

*These authors contribute equally to this work.

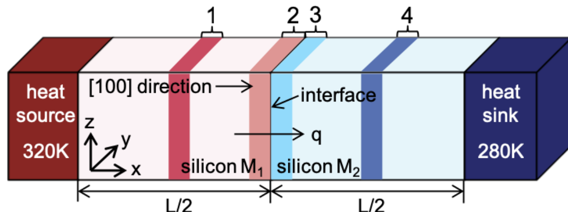

Figure.1: Simulation domain considered in this work. Left side is Si with mass M_1=28.085, right side is heavy Si with mass M2. Temperature in the heat source and hear sink are 320K and 280K, respectively. NEGF has semi-infinite leads while as NEMD has finite length reservoirs. Regions 1~4 marked by numbers are three atomic layers at middle of Si, left to the interface, right to the interface and middle of heavy Si, respectively.

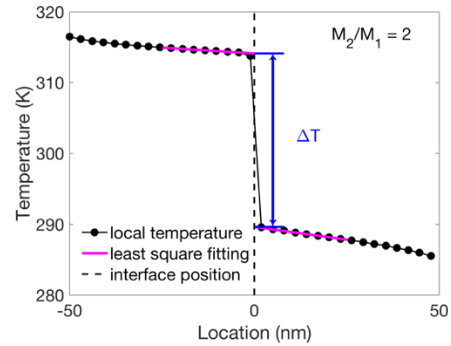

Figure.2: Schematic of extraction of the boundary thermal resistance. Linear fitting of local temperature inside Si and heavy Si, ΔT is obtained at the interface location. The thermal boundary resistance is equal to ΔT/q with q being the heat flux.

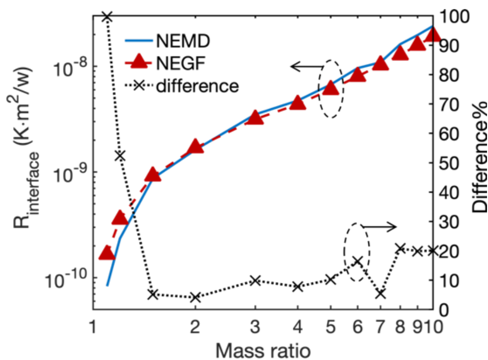

Figure.3: Thermal boundary resistance vs mass ratio calculated by two methods. Dashed line is percentage difference between the two methods defined as (NEGF-NEMD)/NEMD x 100%.

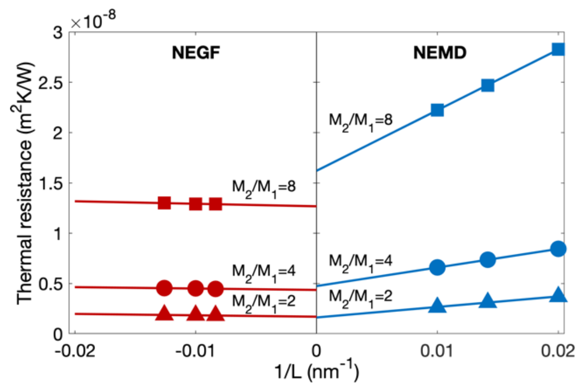

Figure.4: Linear extrapolation for NEGF and NEMD for three mass ratio values. NEMD results show a stronger dependence on the length of the device. True open boundary conditions of NEGF give virtually size independent results.

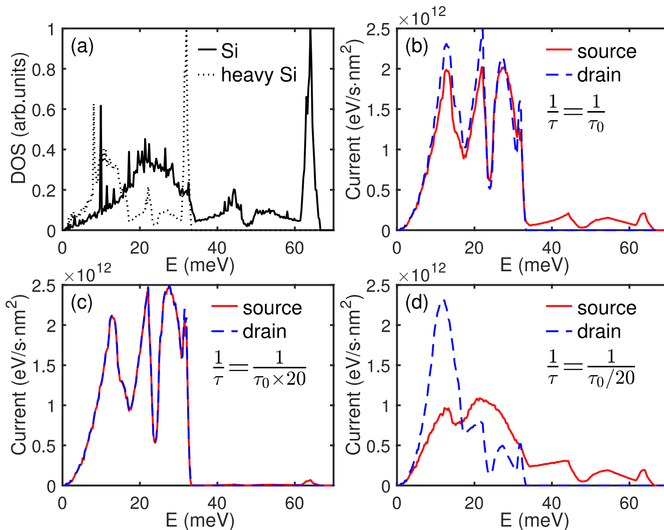

Figure.5: (a) Energy resolved (k integrated) DOS in Si and heavy Si leads. (b)~(d) Energy resolved (k integrated) net current of NEGF calculated with normal, artificially weak and artificially strong scattering strengths, respectively. The results reveal that stronger scattering increases inelastic processes and put the system in more pronounced local thermodynamic equilibrium.

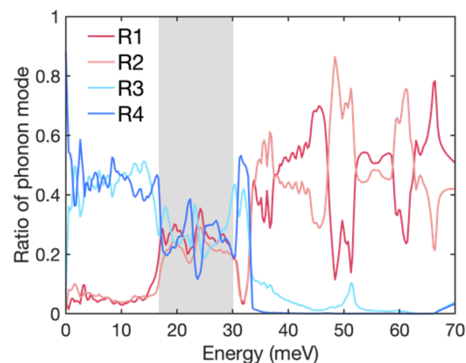

Figure.6: The ratio of the phonon mode in regions 1~4 is defined as $R_i = \|\phi_i(\omega)\|/\|\phi_{tot}(\omega)\|$, where i is the region index and $\|\phi_{tot}(\omega)\| = \sum_{i=1}^{4}\|\phi_i(\omega)\|$. The evenly distributed phonon modes around 20 meV (marked by the gray area) results in the highest current peak at 22 meV (see Fig. 5(b)) although having a low DOS and group velocity. This result shows that the different phonon modal contributions play an important role in determining the energy current flow across the interface.

Effect of Stacking Faults and Surface Roughness on the Thermal Conductivity of Si Nanowires

K. Vuttivorakulchai, M. Luisier, A. Schenk

Integrated Systems Laboratory, ETH Zürich, Gloriastrasse 35, CH-8092 Zürich, Switzerland

kvuttivo@iis.ee.ethz.ch

It has been shown experimentally that the thermoelectric figure of merit (ZT) of Si nanowires (NWs) can be improved by engineering their surface roughness (SR) [1]. If the reduction of the thermal conductivity exceeds the degradation of the power factor, the conversion efficiency increases. In addition to SR, a significant decrease of the thermal conductivity can originate from stacking faults (SFs), which naturally occur in III-V materials [2]. Recent calculations of phonon relaxation times due to scattering at SR and SFs resulted in excellent agreement with measured thermal conductivities of InAs NWs [3].

In this work, the thermal conductivity of ⟨111⟩-oriented Si NWs with SFs, as already studied in optical experiments [4], and SR is simulated based on density functional theory (DFT) [5]. The linearized Boltzmann transport equation (BTE) and the SR scattering model developed in Ref. [3] are first validated on Si NWs where experimental data for detailed roughness profiles exist [6] (Fig. 1). It is found that a Gaussian autocorrelation function of SR fits the measured thermal conductivity better than an exponential one (Fig. 1 (a)). For a NW with rough surface, a more than 80% decrease of the thermal conductivity is possible for specific roughness profiles (Fig. 1 (a)). When the autocorrelation length falls below a certain value, the thermal conductivity starts to increase. This behavior can be explained by the ratio between L and wave length λ_{ph} of the most contributing phonons. Long-wavelength phonons with $\lambda_{ph} >> L$ are hardly scattered by the SR potential.

As in the case of InAs NWs, comparable reductions of the thermal conductivity of Si NWs can be obtained with SFs instead of SR. The inclusion of SF requires the phonon band structure of a diamond-wurtzite (DMWZ) super-lattice, which represents an intermediate case between diamond (DM) and wurtzite (WZ) (Fig. 2). The average energy difference (ΔV) between DM and WZ phonon band structures is about 0.51 meV (Fig. 3 (a)). Different spatial distributions of the SF distance l_{sf} result in similar values of the thermal conductivity (Fig. 3 (b)). For the shortest possible distance between SFs along the NW, the room-temperature thermal conductivity reduces to ~25% of its ideal NW value (8 vs. 30 W/Km).

Our simulations show the general possibility of engineering ZT of Si NWs. However, it still has to be clarified how the power factor changes under the same conditions.

[1] A. I. Hochbaum et al., Nature, **451**, 163 (2008). [2] S. F. Karg et al., Nanotechnology, **25**, 305702 (2014). [3] K. Vuttivorakulchai et al., J. Appl. Phys., **124**, 205101 (2018). [4] Y. Li et al., Nanoscale **7**, 1601 (2015). [5] K. Vuttivorakulchai et al., ESSDERC, (IEEE, 2018), pp. 34-37. [6] J. Lim et al., Nano Lett., **12**, 2475 (2012).

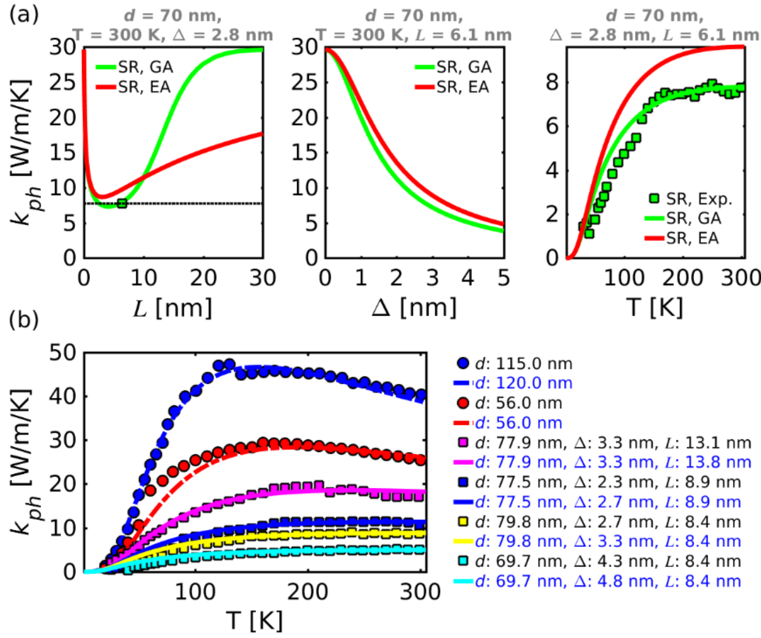

Fig.1: Thermal conductivity (k_{ph}) of Si NWs with Gaussian autocorrelation (GA) and exponential autocorrelation (EA) functions for SR. (a) k_{ph} as a function of the correlation lengths (L) (left), roughness heights (Δ) (middle), and temperature (T) *(right). The green-square symbols represent measured k_{ph} of a Si NW with a diameter (d) equal to 70 nm, Δ = 2.8 nm, and L = 6.4 nm from Lim et al. [6]. The black dotted-line indicates measured k_{ph} at 300 K. (b) k_{ph} of Si NWs with different d as a function of* T. *Lines or blue text in the legend represent simulated k_{ph} with GA function for SR. Symbols or black text are the experiments [1,6].*

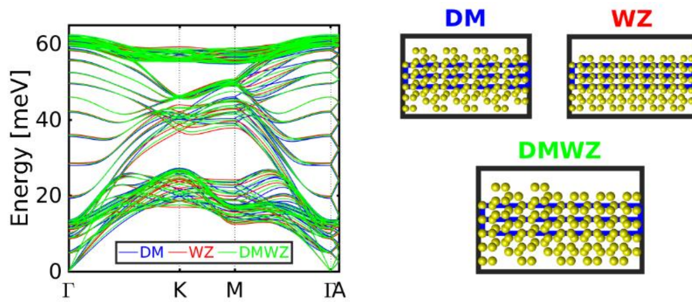

Fig.2: Left panel: DFT phonon band structures of bulk DM, WZ, and DMWZ lattices. Right panel: Hexagonal structures along the ⟨111⟩ *direction of DM and the* ⟨0001⟩ *direction of WZ. The blue solid lines are unit cells used for the computation of bulk phonon band structures with the same number of atoms in each cell.*

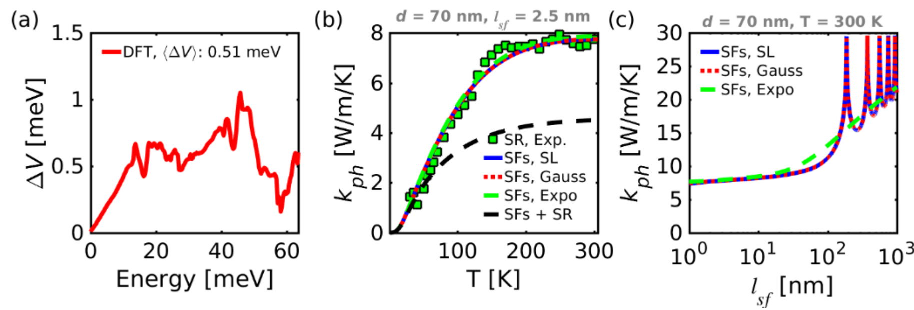

Fig.3: (a) Energy difference between DM and WZ phonon band structures as a function of phonon energy. The two (three) smallest cubic unit cells of DM (WZ) in ⟨111⟩ *(*⟨0001⟩*) direction are chosen with* 401×101×101 ***q****-point sampling. (b) k_{ph} of Si NWs with different l_{sf}-distributions, i.e. super-lattice (SL), Gaussian (Gauss) with standard deviation (σ) equal to 0.5 nm, exponential (Expo) as function of* T. *The black-dashed line is simulated k_{ph} of Si NW with SFs (exponential distribution of l_{sf}) and SR (d = 70 nm, Δ = 2.8 nm, and L = 6.1 nm). The green-square symbols are measured k_{ph} of a Si NW with d = 70 nm, Δ = 2.8 nm, and L = 6.4 nm from Lim et al. [6]. (c) k_{ph} of Si NWs with different distributions of SFs as function of l_{sf} at room temperature.*

Multiphysics Simulation of Nanostructured Thermoacoustic Loudspeakers

P. La Torraca[1], Y. Ricci[1], A. Falco[2], P. Lugli[2], L. Larcher[1]
[1]*Department of Sciences and Methods for Engineering,*
University of Modena and Reggio Emilia, Italy
[2]*Faculty of Science and Technology, Free University of Bozen-Bolzano, Italy*
paolo.latorraca@unimore.it

The recent advancements in the synthesis of solution-processed nanomaterials and the development of facile printing techniques allow the fabrication of nanostructures with unprecedented physical properties. The spray-coating deposition of solution-processed metallic nanowires enables for instance the fabrication of nanostructured layers, characterized by a low electrical resistance and an extremely low heat capacity [1]–[4], recognized as a promising solution for the development of efficient thermoacoustic (TA) loudspeakers [5]–[7]. The TA loudspeaker technology have long been studied but the models reported in literature are not fully adequate for the model-driven development of the technology, either lacking of a description of the device thermal behavior [8], [9], not accounting for the 3D geometry of the thermal and acoustic fields in air [10], [11], or neglecting the contribution of the heat losses due to convection and radiation [12]. In this work we present a multiphysics model of the TA loudspeaker transduction, overcoming the above limitations by considering the full electro-acoustic transduction as a sequence of two atomic processes: an electro-thermal transduction, describing all the involved thermal processes, and a thermo-acoustic transduction, accounting for the interaction between the thermal and acoustic fields. The model very accurately reproduces the response of nanostructured TA loudspeakers, providing a useful tool for further developing the technology.

[1] M. Bobinger et al., Phys. Status Solidi Appl. Mater. Sci. **214**, 1600466 (2017).
[2] M. Bobinger et al., Adv. Mater. Interfaces **4**, 1 (2017).
[3] M. Bobinger et al., 2017 IEEE 17th Int. Conf. Nanotechnol. (2017).
[4] M. Bobinger et al., IEEE Trans. Nanotechnol. **17**, 940 (2018).
[5] P. La Torraca et al., J. Appl. Phys. **121**, (2017).
[6] P. La Torraca et al., Adv. Mater. Technol. **3**, 1 (2018).
[7] P. La Torraca et al., 2018 IEEE 18th Int. Conf. Nanotechnol. (2018).
[8] M. Daschewski et al., J. Appl. Phys. **114**, (2013).
[9] S.S. Asadzadeh et al., J. Appl. Phys. **117**, (2015).
[10] L. Xiao et al., Nano Lett. **8**, 4539 (2008).
[11] H. Hu et al., Appl. Phys. Lett. **96**, (2010).
[12] H. Hu et al., AIP Adv. **4**, (2014).

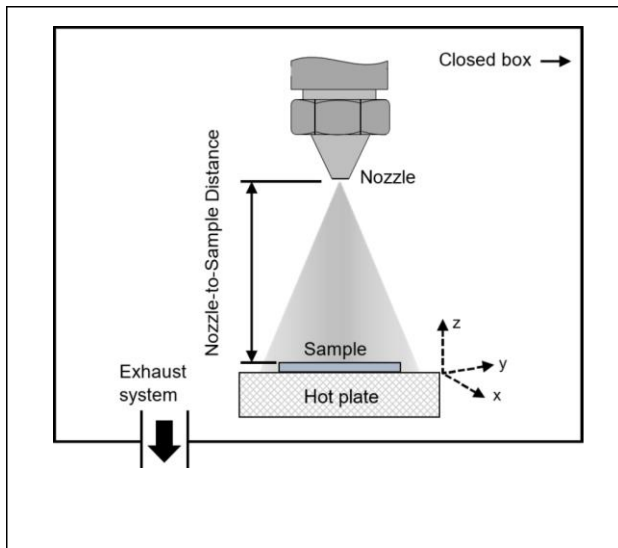

Fig.1: Schematic for a spray-coating setup that utilizes a spray gun, closed box, exhaust system and a movable hot plate.

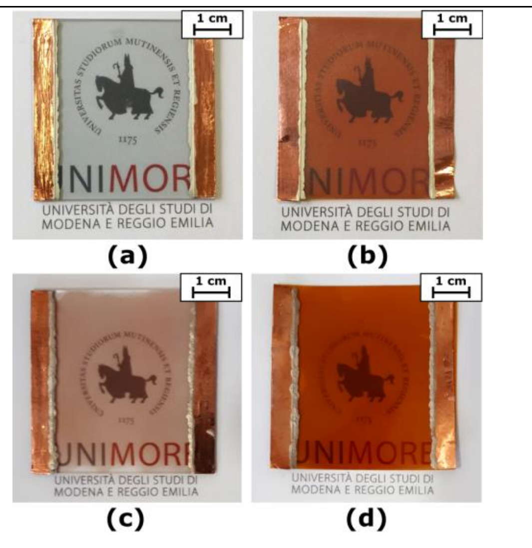

Fig.4: Thermoacoustic loudspeaker samples fabricated through spray coating of solution processed metallic nanowires: (a) silver nanowires deposited on glass; (b) silver nanowires deposited on Kapton; (c) copper nanowires deposited on glass; (d) copper nanowires deposited on Kapton.

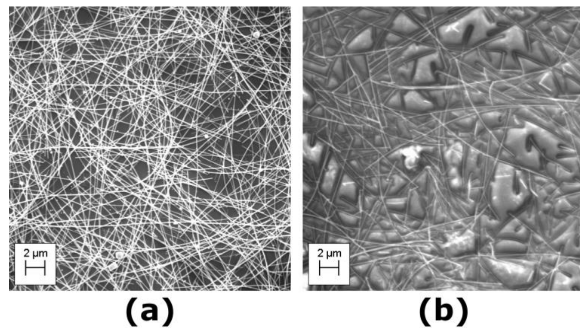

Fig.2: SEM-image of the conductive random network fabricated by spray-coating deposition of silver nanowires on glass (a) and Kapton (b).

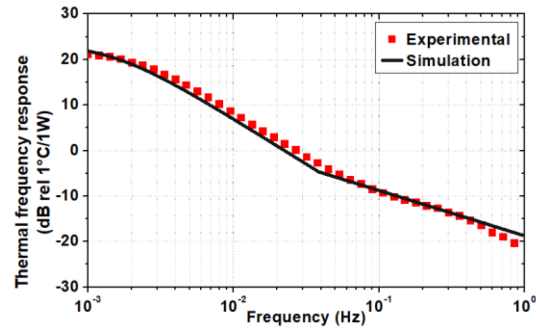

Fig.5 Experimental (colored symbols) and simulated (black solid line) thermal frequency response (power to temperature) of the TA loudspeaker sample made of silver nanowires on glass.

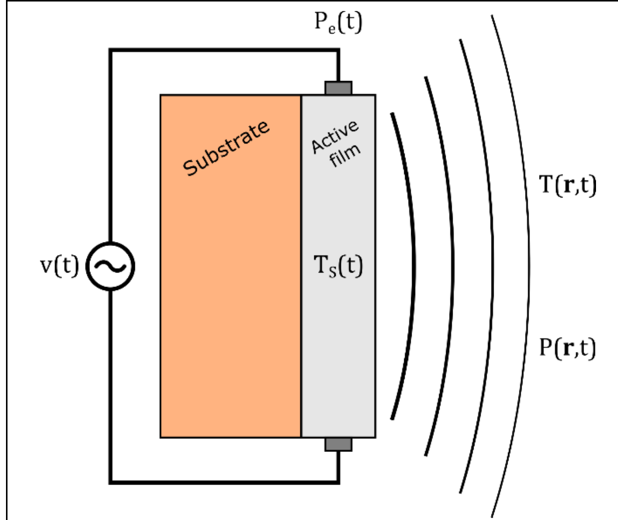

Fig.3: Structure of a solid substrate TA loudspeaker.

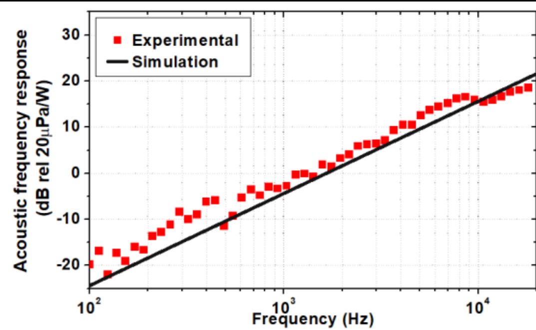

Fig.6 Experimental (colored symbols) and simulated (black solid line) acoustic frequency response (power to temperature) of the TA loudspeaker sample made of silver nanowires on glass.

Dynamic Thermal Interface Material (D-TIM) Simulation and Parameter Optimization Using Genetic Algorithm

M. Jo[1,2,4], E. Kirkor[6,7], S. Sinha[5,7], A. Scheeline[3,7],
P. Martin[1,2], U. Ravaioli[1,2]

[1]Beckman Institute for Advanced Science and Technology
[2]Department of Electrical and Computer Engineering, College of Engineering
[3]Department of Chemistry, College of Liberal Arts and Sciences
University of Illinois at Urbana-Champaign, Urbana, IL, USA
[4] Department of Electrical and Computer Engineering
Rose-Hulman Institute of Technology, Terre Haute, IN, USA
[5]Department of Electrical & Computer Engineering
[6]Department of Mathematics and Physics
University of New Haven, West Haven, CT, USA
[7]Anchor Science LLC
jo@rose-hulman.edu

Anchor Science LLC, led by Dr. Ewa Kirkor, invented D-TIM, which is a nanocomposite mixture of multi-wall carbon nanotubes and nano-graphites [1] shown in figure 1 (a). D-TIM is an adaptive thermal interface material that dynamically adapts its thermal conductivity with temperature and, as a result, the thermal conductivity of D-TIM increases as temperature increases unlike that of the state-of-the-art TIMs: this quality makes D-TIM a promising thermal interface material with faster and more efficient heat delivery.

To study the nature of D-TIM, we implemented a percolation theory-based simulation which incorporates resistive circuit network model [2]. The model takes into account the geometry of D-TIM sitting between CPU chip surface and heatsink. In addition, thermo-electric effect and variable range hopping conductance were employed to capture its thermal conductivity trend. Our simulation framework creates random D-TIM geometry based on mass ratio of D-TIM elements, simulates the temperature and potential change by updating the electric current and heat flux. Finally, it outputs the effective thermal conductivity of the system.

With the percolation theory-based simulation being our core physical engine, we use genetic algorithm to deduce the optimal parameter values that provide best fitness to the measurement data. This optimization algorithm makes us able to perform data-driven simulation by estimating the values of 45 parameters that include the thermal conductivity and electric conductivity for all elements and their contact properties. Simulation results with the optimized parameters show good agreement with the linear fit of the measurement data as in figure 5.

In this work, we present percolation theory-based simulation framework that captures and predict the effective thermal conductivity trend of D-TIM and the optimization procedure to reverse engineer the physical parameters for data-driven simulation.

[1] E. S. Kirkor, A. D. Schricker, S. K. Sinha, and A. Scheeline, U.S. Patent US 2014/0345843 A1 (2014)
[2] M. Jo, Ph.D. dissertation, University of Illinois at Urbana-Champaign (2018)

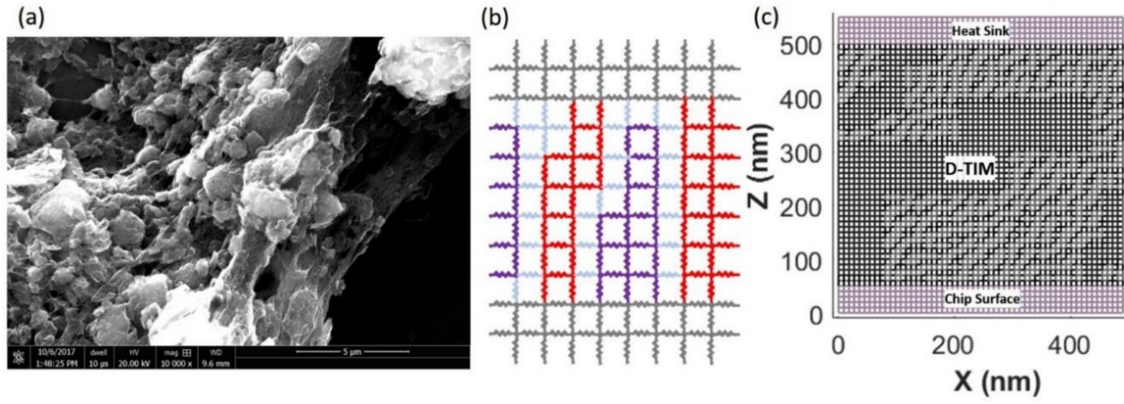

Fig.1: (a) Environmental Scanning Electron Microscope (ESEM) image of D-TIM sample. MWCNTs are tangled and covering the nGs. (b) Resistive network example for D-TIM percolation simulation. (c) Example of D-TIM percolation simulation setup.

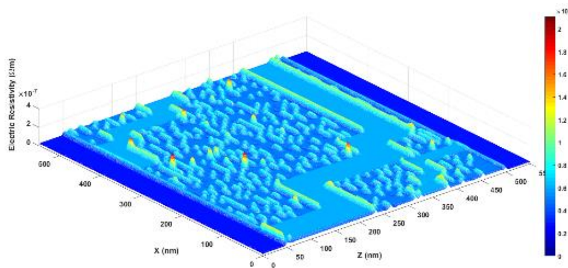

Fig.2: Electric resistivity ρ assigned to branches of D-TIM simulation. ρ_z, the vertical branches in the Z-direction.

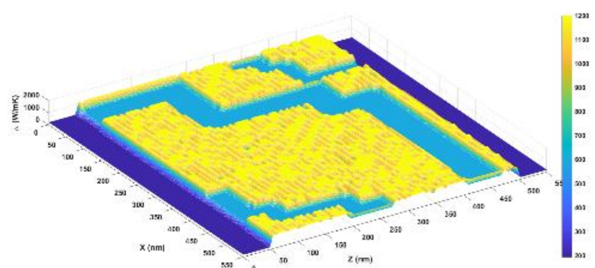

Fig.3 Thermal conductivity κ_z assigned to branches of D-TIM simulation.

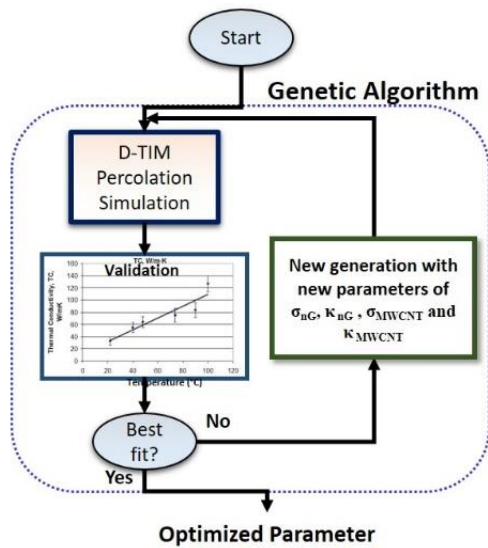

Fig.4: The pipeline for D-TIM parameter optimization using genetic algorithm.

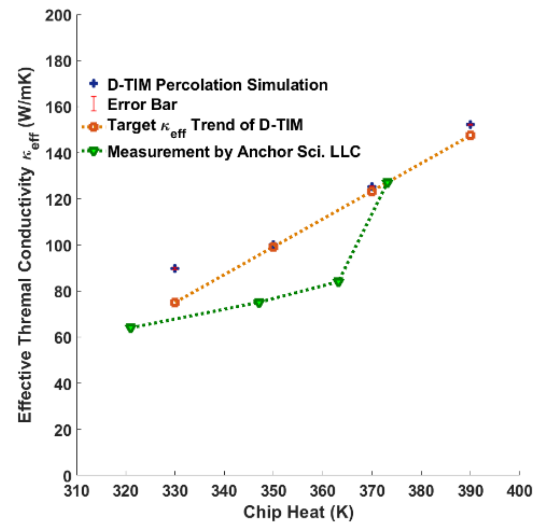

Fig.5: Simulation result of the effective thermal conductivity, using the optimized parameters by genetic algorithm.

Modeling of Nanowires with Superconducting Cladding

A. E. Antipov, G. W. Winkler, R. M. Lutchyn
Station Q, Microsoft Research, Santa Barbara, California 93106-6105, USA
andrey.antipov@microsoft.com

The initial theoretical proposal for the realization of Majorana bounds states in a condensed matter setup requires three simple ingredients: superconductivity, spin-orbit coupling and magnetic field. While this proposal is simple, the experiments are not, as they involve material science, fabrication steps, cooling, electrostatic control and actual measurements. The results of experiments are not unambiguous and allow for multiple interpretation by simple theoretical models. In order to bridge the gap one has to include peculiarities of experimental setup and engineer the modelling of systems supporting Majorana zero modes. In this talk I will show how the next generation of numerical models captures the effects of electric fields, disorder, orbital effects and how it can feedback and guide the ongoing experimental effort in the field.

[1] A.E. Antipov et al., Phys. Rev. X 8, 031041 (2018).
[2] arXiv:1902.07804
[3] arXiv:1810.04180

TCAD Based Performance Evaluation on Si NWTs

A. Asenov, T. Al-Ameri, V. Gerorgiev
The University of Glasgow, Glasgow, UK
Asen.aseno@glasgow.ac.uk

All Gate Around (AGA) silicon (Si) Nanowire Transistors (NWTs) have the ultimate electrostatic integrity and are considered as suitable candidates for 5nm CMOS technology and beyond [1]. Their operation is governed by strong quantum confinement effects and non-equilibrium quasi-ballistic transport. Therefore the Ensemble Monte Carlo transport simulations are the best vehicle for studying of their performance. Here we report a comprehensive EMC simulation study of NWTs suitable for 5nm CMOS technology generation. The quantum confinement effects are properly taken into account in the MC simulations using the effective quantum potential approach based both on the solution of the Poisson-Schrodinger (PS) equation and on the Density Gradient (DG) algorithm. The impact of the NWT cross sectional shape, channel orientation and strain are taken into consideration. The simulations are carried out with GARAND (Synopsys). Due to the heavy computational requirements only single NWT are simulated using the EMC approach. Multi-channel NWTs with complex contact arrangements are simulated using the Drift Diffusion (DD) approach meticulously calibrated to the EMC simulations. The study concludes with the optimal NWT design, meeting the requirements for the 5nm CMOS technology and beyond. The DD simulations are also used to evaluate the statistical variability in the multichannel NWTs.

The cross section of the single channel Si NWT used in the EMC simulations is illustrated in Fig.1. The quantum mechanical charge distribution in the cross section of the simulated NWTs with different shape is illustrated in Fig. 2. Fig. 3 presents the dependence of the mobile charge in the NWT channel as a function of the gate bias. A very interesting observation is that the largest amount of mobile charge is available in NWTs with elliptical cross section obeying the Golden Rule (GR) ratio as illustrated in Fig. 4. The EMC simulations also confirm that the GR NWT has the best drive current performance as illustrated in Fig. 5. The simulation domain for the multi-channel Si NWTs used in the DD simulations calibrated in respect of the EMC simulations are illustrated in Fig. 6. Results for the performance of the multi-channels NWTs will be presented at the conferences together with a comprehensive study of the corresponding variability.

[1] *J.-P. Colinge, FinFETs and Other Multi-Gate Transistors*. Boston, MA: Springer US, 2008

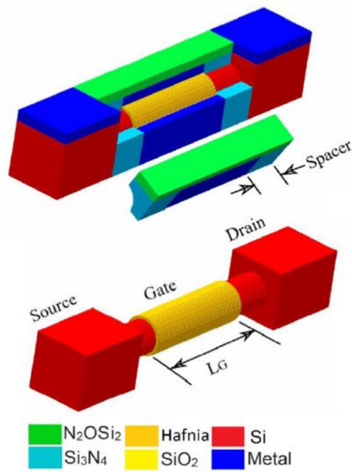

Fig.1: Cross section of the single channel Si NWT used in the EMC simulations.

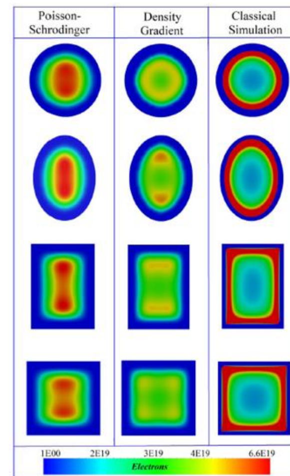

Fig2: quantum mechanical charge distribution in the cross section of the simulated NWTs with different shape.

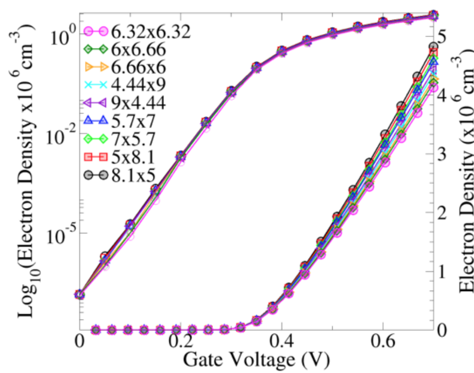

Fig.3: dependence of the mobile charge in the NWT channel as a function of the gate bias.

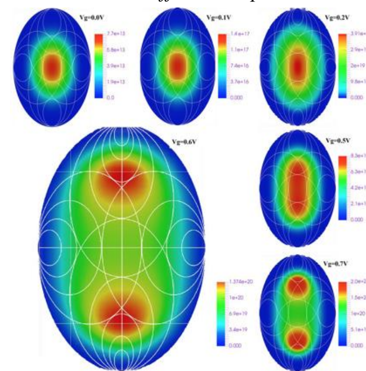

Fig.4 Normalized current as a function of the position x relative to silicon, for p=1, $\Gamma_N=\Gamma_0 \exp(-x/d)$, $\Gamma_F=\Gamma_0 \exp(-(d-x)/d)$, $T_2=T_1$, $\omega_L T_2 = \Gamma_0 T_2 = 10$,

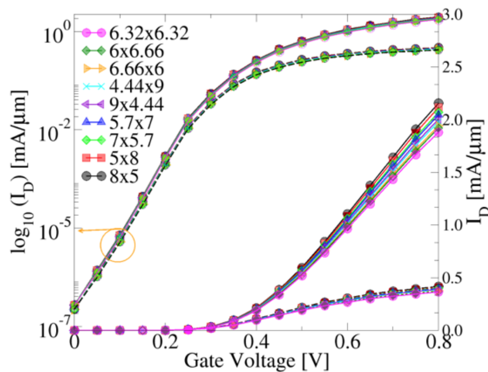

Fig.5: Current as a function the gate voltage for NWT with different cross section obtained from the EMC simulations.

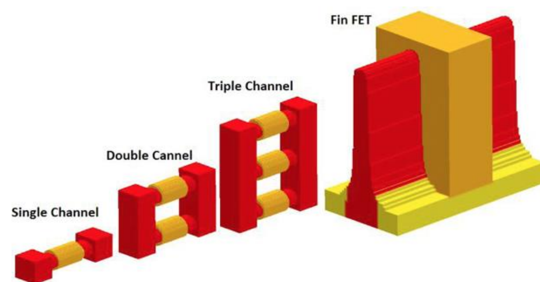

Fig.6: DD simulation domain for evaluating the performance of multichannel NWTs.

3D Schrödinger Equation Quantum Corrected Monte Carlo and Drift Diffusion Simulations of Stacked Nanosheet Gate-All-Around Transistor

K. Kalna[1], D. Nagy[2], A. J. García-Loureiro[2], Natalia Seoane[2]

[1]NanoDeCo Group, College of Engineering, Swansea University,

Swansea SA1 8EN, Wales, United Kingdom

[2]CITIUS, Universidade de Santiago de Compostela,

15782 Santiago de Compostela, Galicia, Spain

k.kalna@swansea.ac.uk

Nanosheet silicon channel transistors laterally stacked in pillars are one of the promising solutions for 5~nm technology nodes and beyond for logic applications [1]. The nanosheet transistor architecture with a wrap-around-gate (WAG) contact can deliver the same excellent electrostatic integrity as SOI FinFETs [2] or nanowire GAA FETs [3] while can deliver a larger on-current required by ITRS 2.0 prescriptions [4] and be fabricated with fewer deviations from the already established FinFET manufacturing. The most importantly, the fabrication of nanosheet FETs can overcome many of patterning challenges present in a nanoscale fabrication of stacked nanowires and closely stacked FinFETs [1].

In this work, we employ in-house 3D finite element (FE) Monte Carlo (MC) and drift-diffusion (DD) device simulation tools with quantum corrections to accurately model Si nanosheet transistors with the WAG illustrated in Figs. 1 and 2. The quantum corrections in the 3D FE MC simulations [5] use solutions of 2D Schrödinger equation (SchE) [6] assuming longitudinal and transverse electron effective masses in Si and wavefunctions penetrating into a surrounding high-κ dielectric layer [7,8]. The SchE is solved on 2D slices across the channel with a non-uniform distribution dependent on a gradient of electron density along the channel. The 3D FE MC simulations use Fermi-Dirac statistics in electron scattering with ionised impurities via static screening with a self-consistently calculated Fermi energy and electron temperature in real space of a device [8,9]. Two types of quantum corrections can be included in the 3D DD simulations: (i) 3D FE density gradient (DG) [10] which require calibration parameters and (ii) 2D SchE on slices along the channel as in the 3D FE MC simulations. The quantum corrections using eigenstates of the 2D SchE, $\psi_i(y,z;E_i)$, and eigenenergies, E_i, have been incorporated into the 3D FE DD simulations for this work. A quantum-mechanical electron density in Boltzmann approximation (6 equivalent valleys) can be obtained as [7]:

$$n_Q(y,z) = 6\frac{\sqrt{2\pi m^* k_B T}}{\pi\hbar}\sum_i |\psi_i(y,z;E_i|^2 \exp\left[\frac{E_{F_n}-E_i}{k_B T}\right]$$

where k_B is the Boltzmann constant, T is the electron temperature, and E_{F_n} is the electron quasi-Fermi level. The 2D quantum density, $n_Q(y,z)$, is interpolated using spline functions to a 3D device density domain, $n_Q(\boldsymbol{r})$. A quantum correction potential, $V_{qc}(\boldsymbol{r})$, reads [6]:

$$V_Q(\boldsymbol{r}) = k_B T\log[n_Q(\boldsymbol{r})] - V(\boldsymbol{r}) - k_B T\log[n_i^{\text{eff}}(\boldsymbol{r})]$$

where $V(\boldsymbol{r})$ is the potential energy, and $n_i^{\text{eff}}(\boldsymbol{r})$ is the effective intrinsic concentration.

A schematic cross-section of a stack with three Si nanosheet transistors with the WAG is illustrated in Fig. 1 which closely follows the 12 nm gate length nanosheet transistor reported in Ref. [1] by IBM, Samsung, and Global Foundries consortium. Fig. 2 shows a cross-section of three nanosheet transistors made of the outer metal gate and inner polysilicon gate closely surrounding a nanosheet *p*-type doped Si body covered with a high-κ dielectric layer [1]. The device has a Si channel with a 50 nm width and a height of 5 nm surrounded by a high-κ dielectric layer of a thickness of 1 nm and a dielectric constant of 3.9. We have then studied a performance of the nanosheet transistors when their width would be scaled down in order to reduce area of the CMOS to acquire a large transistor density on a chip. Fig. 3 illustrates quantum corrected electrostatic potential in cross-sections of a nanosheet FET scaled from a width of 50 nm to 30 nm, 10 nm, and 5 nm.

The comparison of the I_D-V_G characteristics obtained from 3D FE DD and MC simulations with experimental data are presented in Figs. 4-5 at a low drain bias of 0.0 V and a high drain bias of 0.7 V, respectively. The source/drain *n*-type doping has been reverse engineered using a Gaussian doping profile with a peak doping of 5×10^{19} cm^{-3} and a spread σ_x of 3.45 nm. The DD uses Caughey-Thomas doping dependent low-field electron mobility model combined with perpendicular (critical electric field) and lateral (saturation velocity) electric field models with a calibrated low-field mobility of 50.24 cm^2/Vs, a saturation velocity of 1.8×10^6 cm/s (1.7×10^7 cm/s), and a critical electric field of 1×10^6 V/cm (1×10^9 V/cm) at V_D = 0.05 V (V_D = 0.7 V), respectively. The interface roughness which plays a crucial role in multi-gate transistors at a high drain bias [5] assumes a RMS height of 1.5 nm and a correlation length of 1.7 nm. The DG quantum corrected DD exhibits only 2% difference between more accurate SchE quantum corrections used in DD and MC simulations while a difference between the SchE quantum corrected DD and MC simulations is nearly negligible. Figs. 6-8 show I_D-V_G characteristics at a high drain bias of 0.7 V when the width of Si nanosheet is reduced from 50 nm to 30 nm, 10 nm, and 5 nm. The respective reduction in the drain current normalised to a nanosheet circumference obtained from the 3D MC will be 10.7%, 34.2%, and 48.7% making the nanosheet width scaling below 30 nm meaningless.

[1] N. Loubet et al., Proc. IEEE VLSI Symp., Kyoto, Japan, 230-231, 2017.

[2] D. Nagy et al., IEEE J. Electron Devices Soc. **6**, 332-340, 2018.

[3] H. Mertens et al., IEDM Tech. Dig., 524-527, 2016.

[4] International Technology Roadmap for Semiconductors, http://www.itrs2.net/, 2019.

[5] M. Aldegunde and K. Kalna, Comput. Phys. Commun. **189**, 31-36, 2015.

[6] B. Winstead and U. Ravaioli, IEEE Trans. Electron Devices **50**, 440-446, 2003.

[7] J. Lindberg et al., IEEE Trans. Electron Devices **61**, 423-429, 2014.

[8] M. A. Elmessary et al., IEEE Trans. Electron Devices **63**, 933-939, 2016.

[9] A. Islam and K. Kalna, Semicond. Sci. Technol. **26**, 055007 (9pp), 2011.

[10] A. J. García-Loureiro et al., IEEE Trans. Comput-Aided Des. Integr. Circuits Syst. **30**, 841-851, 2011.

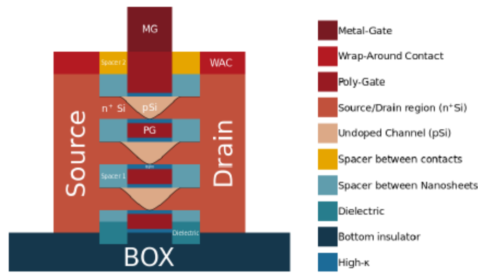

Fig. 1: Schematic cross-section of a typical Si nanosheet multi-gate transistor with three integrated nanosheets [1].

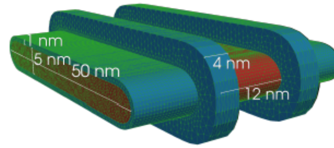

Fig. 2: A finite element mesh to accurately describe one nanosheet wrap-around channel multi-gate transistor.

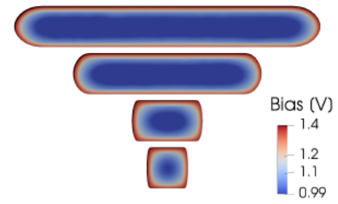

Fig. 3: Potential cross-section in the middle of the gate for nanosheet FETs with widths of 50, 30, 10 and 5 nm from top to bottom, respectively, at $V_D = 0.7$ V and $V_G = 1.0$ V.

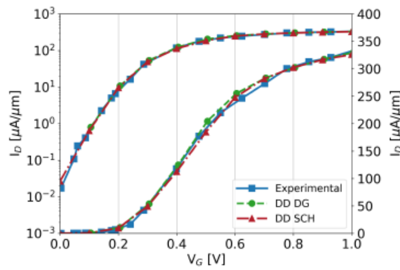

Fig. 4: I_D-V_G characteristics at V_D=0.05 V for the 12 nm gate length wrap-around channel nanosheet multi-gate FET comparing drift-diffusion simulations using density gradient (DD DG) and SchE (DD SCH) quantum corrections against experimental measurements [1].

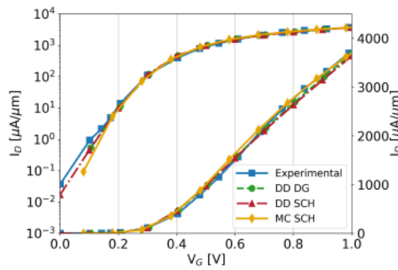

Fig. 5: I_D-V_G characteristics at V_D=0.7 V for the 12 nm gate length wrap-around channel nanosheet multi-gate FET comparing drift-diffusion simulations using density gradient (DD DG) and SchE (DD SCH) quantum corrections, and SchE quantum corrected Monte Carlo simulations (MC SCH) against experimental measurements [1].

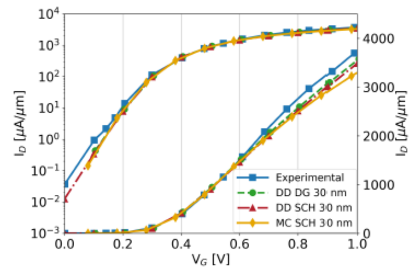

Fig. 6: I_D-V_G characteristics at V_D=0.7 V for the 12 nm gate length nanosheet FET obtained from Schrödinger Equation quantum corrected Monte Carlo simulations (MC SCH) with a nanosheet width reduced to 30 nm. The results from quantum corrected drift-diffusion simulations (DD DG and DD SCH) are for comparison.

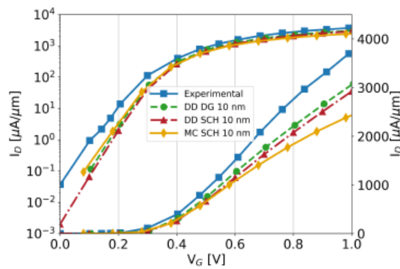

Fig. 7: I_D-V_G characteristics at V_D=0.7 V for the 12 nm gate length nanosheet FET obtained from SchE quantum corrected Monte Carlo simulations (MC SCH) with a nanosheet width reduced to 10 nm. The results from quantum corrected drift-diffusion simulations (DD DG and DD SCH) are for comparison.

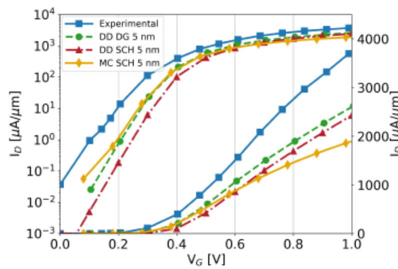

Fig. 8: I_D-V_G characteristics at V_D=0.7 V for the 12 nm gate length nanosheet FET obtained from SchE quantum corrected Monte Carlo simulations (MC SCH) with a nanosheet width reduced to 5 nm. The results from quantum corrected drift-diffusion simulations (DD DG and DD SCH) are for comparison.

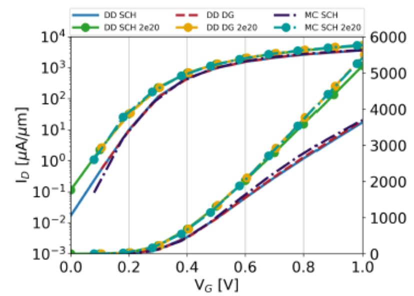

Fig. 9: I_D-V_G characteristics at V_D=0.7 V for the same nanosheet FET with a nanosheet width of 50 nm but assuming *n*-type S/D of 2×10^{20}cm^{-3} obtained from SchE quantum corrected MC simulations (MC SCH). The results from quantum corrected DD simulations (DD DG and DD SCH) are for comparison.

Quantum Transport Simulations of Gate-all-around Nanowire pFETs with Arbitrary Shaped Cross-section in the Presence of Hole-phonon Interaction

H. Lee, M. Shin

School of Electrical Engineering, Korea Advanced Institute of Science and Technology, Daejeon 34141, Republic of Korea

mshin@kaist.edu

Gate-all-around nanowire field-effect-transistors (GAA NW FETs) with the excellent electrostatic integrity are considered as a promising candidate for sub-10 nm CMOS technology. In order to assess the true potential of the devices, it is essential to capture the phonon scattering effects together with the quantum effects such as quantum confinement and tunneling. Although simulations of realistically sized devices including these effects have been extensively conducted for n-type transistors, those for p-type transistors are quite lacking. In this work, we have developed an efficient quantum transport simulator for p-type GAA NW FETs, which has the capabilities to include the hole-phonon scattering and handle arbitrary shaped cross-section. We have used the multiband k·p models to describe the valence bands. To faithfully represent an arbitrary shaped cross-section of NW, we have employed the finite element method (FEM) for a three-dimensional (3D) discretization of the k·p Hamiltonians and the Poisson equation as shown in Fig. 1. The hole-phonon interaction has been treated in the framework of the nonequilibrium Green's function (NEGF) method through the self-consistent Born approximation (SCBA) and assumed to be local. For efficient NEGF simulations, the size of the $k \cdot p$ Hamiltonians is reduced using the mode space approach [1] where the Bloch modes are sampled in energy and k space. We have developed an efficient scheme to calculate the hole-phonon self energy in the mode space which greatly reduce the computational cost of SCBA. See Fig. 2. for the flowchart. For validation of the simulator, we have compared the low-field hole mobilities of silicon NWs with those of the tight-binding (TB) full band simulations [2] and found that our results agree well with the TB results as shown in Fig. 3. Also, the inelastic scattering effects are seem to be captured correctly in Fig. 4. As an application, we have studied the impacts of the cross-section aspect ratio on the device performance of silicon pFET along the [110] transport direction in Fig. 5. Our simulator can be used as a practical tool for design and optimization of GAA NW pFETs.

[1] M. Shin et al., J. Appl. Phys, **119**, 154505 (2016).

[2] M. Luiser et al., IEDM Tech. Dig., pp. 8.6.1-8.6.4 (2010).

[3] A. Ziegler et al., SISPAD, pp. 25-28, (2017).

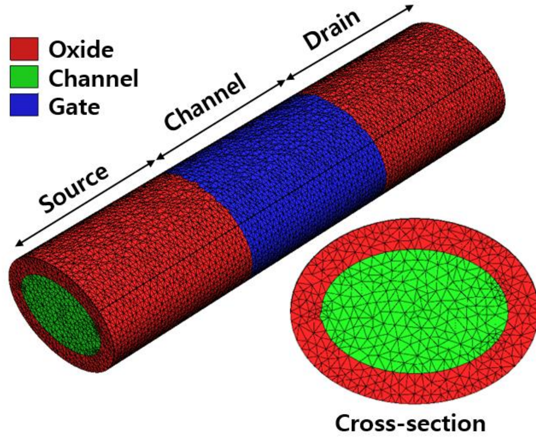

Fig.1: Schematic of GAA nanowire and the cross-section with the finite element mesh configuration.

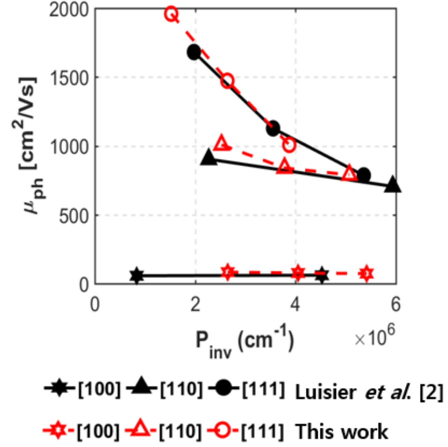

Fig.3: The low-field hole mobility μ_{ph} of a silicon nanowire as a function of hole inversion density P_{inv} at the top of the barrier at $V_{ds} = 10^{-4}$ V. The diameter of silicon nanowire is 3.0 nm and the source and drain lengths are 10.0 nm. The scaling parameters of the deformation potentials for phonon confinement effects were taken from Ref. [3].

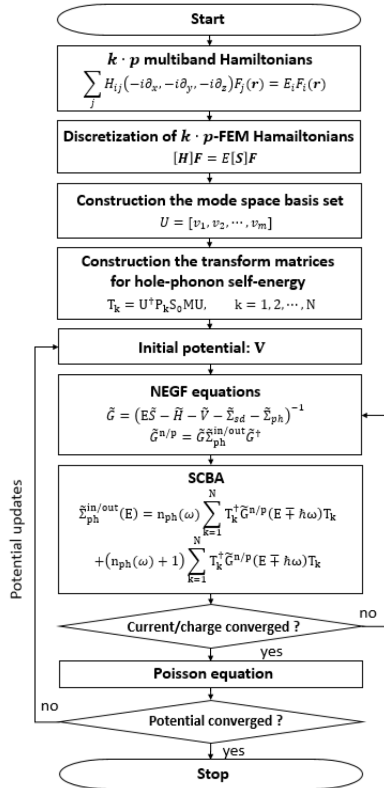

Fig.2: Flowchart of the overall simulation procedure. m is the number of modes and N is the number of the FEM nodes of the periodic layer. P_k is the orthogonal projection onto the subspace spanned by the multiband basis vectors of the k-th FEM node. S_0 is the overlap matrix and $n_{ph}(\omega)$ is the Bose-Einstein distribution of the phonon with frequency ω.

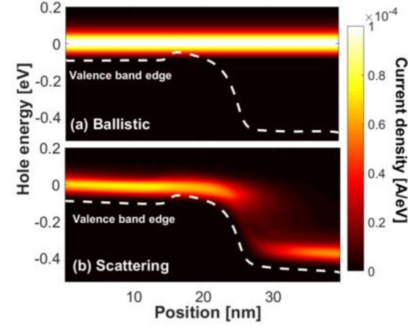

Fig.4: Current spectrum of a silicon NW pFET in (a) ballistic transport and (b) scattering transport at $V_{GS} = -0.4$ V and V_{DD} = 0.4 V. The NW diameter is 5.0 nm and the source, channel, and drain lengths are 15.0 nm, 10.0 nm, and 15.0 nm respectively.

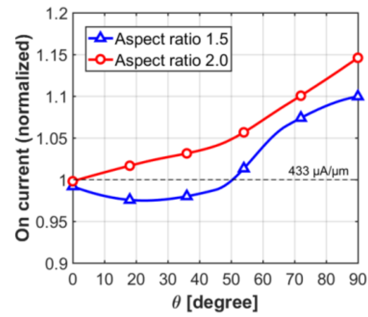

Fig.5: On-current of silicon NW pFETs as a function of θ where θ is the angle between the major axis of NW and (001) plane. The transport direction is <110>. The source-drain voltage is -0.4 V and the driving voltage is 0.4 V. The dashed line is the on-current of the device with the aspect ratio of 1.0. All devices have the same cross-section area as that of NW with the diameter of 5.0 nm.

Investigation of the Kink Effect in GaN HEMT Technology Using Fermi Kinetics Transport

N. C. Miller[1], M. Grupen[1], J. D. Albrecht[2]
[1]*Air Force Research Laboratory, Sensors Directorate,*
2241 Avionics Circle, WPAFB, OH, 45433, USA
[2]*Michigan State University, 428 S. Shaw Lane, East Lansing, MI, 48824, USA*
nicholas.miller.58@us.af.mil

High frequency, high power electronic components are required for a variety of commercial and Air Force applications. For example, wireless communication networks require RF power amplifiers for cellular base stations [1], and power switches are an important part of the electrical utility grid [2]. Because of its wide bandgap, high breakdown voltage, and large peak electron velocity, gallium nitride (GaN) is an attractive material for discrete power amplifier transistor technology. Moreover, GaN's ability to form heterostructures and the spontaneous and piezoelectric polarizations of the heterostructures can be exploited to construct high electron mobility transistors (HEMTs) containing highly conductive two-dimensional electron gas channels with large electron densities and high electron mobility.

Despite great strides in GaN HEMT development, this device can also exhibit certain operational in-stabilities. One type of instability is called the kink effect or drain current knee walkout. It is characterized by a sudden increase in drain current at high drain voltage [3]. Instabilities like these are on-going issues that must be addressed for advanced power-switching applications.

The work reported here investigated the GaN HEMT kink effect by including electron trap dynamics in a computational physics framework developed by the Air Force Research Laboratory (AFRL). These tools simulate devices by solving Maxwell's vector field equations coupled to nonlinear electron transport including electronic band structure, quantum mechanical scattering, and hot electron effects. Figures 1 – 3 depict simulation details, and Figure 4 compares simulated electron drift velocities with Monte Carlo results obtained from the literature [4]. Figures 5 and 6 show that results calculated by the AFRL transport solver compare favorably with measurements from the literature.

[1] M. Eron et al., IEEE Micro. Mag., **19**, 1, 16 (2018).

[2] S. Faramehr et al., Semicond. Sci. Technol., **29**, 025007-1 (2014).

[3] P. Roblin et al., IEEE Trans. ON Microwave Theory and Tech., **60**, 6, 1964 (2012).

[4] B. Benbakhti et al., IEEE Trans. Elect. Dev., **56**, 10, 2178 (2009).

[5] M. Wang and K. J. Chen, IEEE Elect. Dev. Let., **32**, 4, 482 (2011).

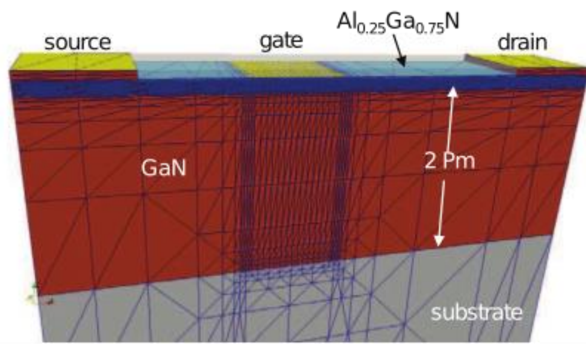

Fig.1: Simulated device structure similar to the GaN HEMT fabricated and characterized by Wang and Chen [5].

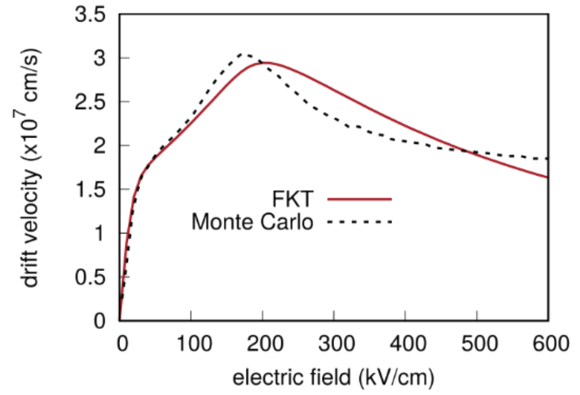

Fig.4: Electron drift velocity versus electric field computed with FKT using iso-energy integrals computed from GaN electronic band structure compared with Monte Carlo results [4].

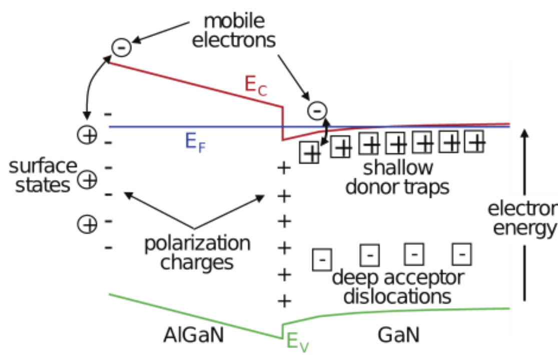

Fig.2: Polarization and defect charges typically located in a GaN HEMT.

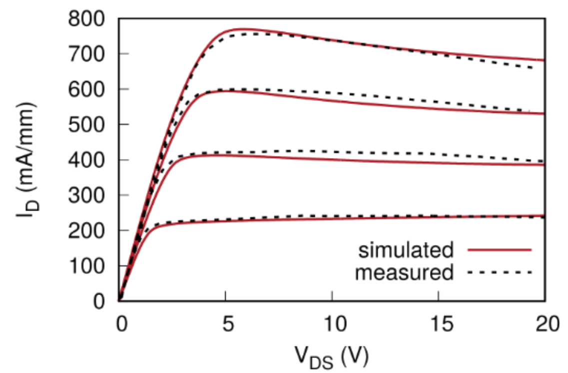

Fig.5: Drain current versus drain voltage for different gate biases. Measured data from Wang and Chen [5] under illuminated conditions and simulated with constant ionized trap density at GaN/AlGaN interface.

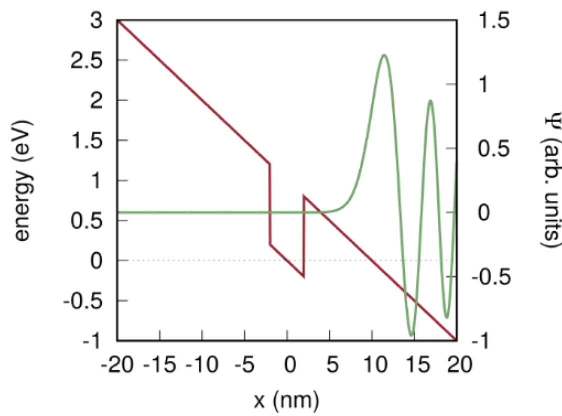

Fig.3: Airy function for an electron trap, approximated as a square potential well, in a constant electric field.

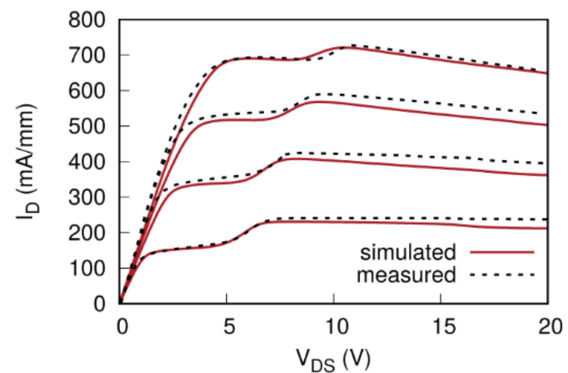

Fig.6: Drain current versus drain voltage for different gate biases. Measured data from Wang and Chen [5] without illumination and simulated with partially ionized GaN/AlGaN interface traps.

Prediction of Urbach Tails and Band Gap Narrowing in Bulk and Confined III-V Devices with Atomistic Non-Equilibrium Green's Functions

P. Sarangapani[1], Y. Chu[1], J. Charles[1], T. Kubis[1,2,3]

[1]*School of Electrical and Computer Engineering, Purdue University, West Lafayette, IN 47906, USA*

[2]*Network for Computational Nanotechnology, Purdue University, West Lafayette, IN 47906, USA*

[3]*Purdue Center for Predictive Materials and Devices, Purdue University, West Lafayette, IN 47906, USA*

charlesj@purdue.edu

High-doping induced Urbach tails and band gap narrowing play a significant role in determining the performance of tunneling devices and optoelectronic devices such as tunnel field-effect transistors (TFETs) [1][2], Esaki diodes and light-emitting diodes [3][4]. In this work, Urbach tails and band gap narrowing values are calculated explicitly for four candidate bulk and confined III-V devices (GaAs, InAs, GaSb and GaN) with scattering self-energies using the non-equilibrium Green's function approach in a multi-band tight binding basis. The scattering self-energies and subsequent scattering rates (Fig. 1 and Fig 2.) are solved using the self-consistent Born approach. Dominant non-local scattering mechanisms such as polar optical phonons and charged impurity scattering are considered with Lindhard screening. Predicted Urbach tails (Fig. 3) and band gap narrowing (Fig. 4) results are shown to agree well with available experimental data for a range of temperature and doping regimes. Dependence with doping is observed to be strongly dependent on confinement and screening. Guideline values for Urbach tail and band gap narrowing will be presented for ultra-thin body and nanowire devices.

[1] E. Lind, E. Memisevic, A. W. Dey, and L.-E. Wernersson, J. Electron Devices Soc. 3, 96 (2015).

[2] U.E. Avci, D.H. Morris, and I.A. Young, IEEE J. Electron Devices Soc. 3, 88 (2015).

[3] J. Geng, P. Sarangapani, K.-C. Wang, E. Nelson, B. Browne, C. Wordelman, J. Charles, Y. Chu, T. Kubis, and G. Klimeck, physica status solidi (a)215, 1700662 (2018).

[4] A. Laubsch, M. Sabathil, J. Baur, M. Peter, and B. Hahn, Trans. Electron Devices 57, 79 (2010).

[5] S. Johnson and T. Tiedje, „Journal of App. Phys. 78, 5609(1995).

[6] H. Yao and A. Compaan, App. Phys. Lett. 57, 147 (1997).

[7] H. Luo, W. Shen, Y. Zhang, and H. Yang, Phys. Cond. Matt. 324, 379 (2002).

[8] E. Harmon, M. Melloch and M. Lundstrom, App. Phys. Lett. 64, 502 (1994).

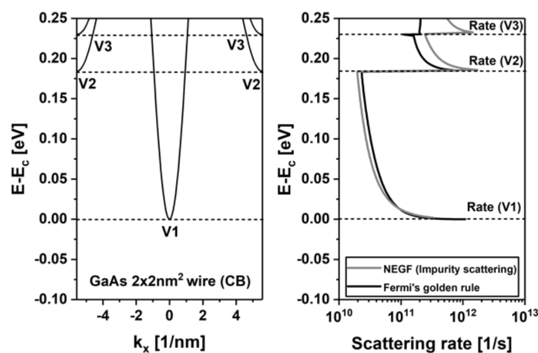

Fig.1: a) Conduction band profile of 2nmx2nm GaAs nanowire. b) Comparison of conduction band scattering rates obtained from NEGF against Fermi's golden rule for charged impurity scattering in 10-band sp3d5s* tight binding basis for a doping concentration of 2x10^{18} cm^{-3}. Screening length is set at 3 nm.

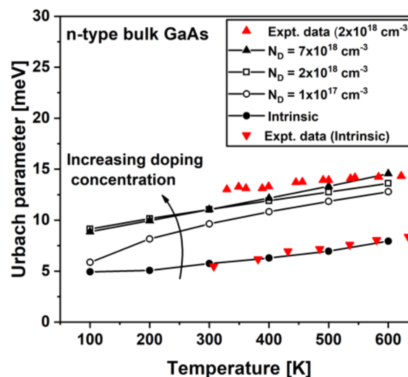

Fig.3: Variation of Urbach parameter as a function of temperature for n-type GaAs for different doping concentrations. Simulation results show good agreement with experimental data obtained from Ref. [5] for intrinsic case and for a doping concentration of 2x10^{18} cm^{-3}.

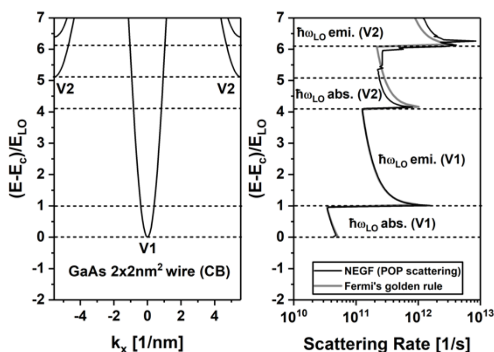

Fig.2: a) Conduction band profile of 2nmx2nm GaAs nanowire. b) Comparison of conduction band scattering rates obtained from NEGF against Fermi's golden rule for polar optical phonon scattering in 10-band sp3d5s* tight binding basis for a doping concentration of 2x10^{18} cm^{-3}. Screening length is set at 3 nm.

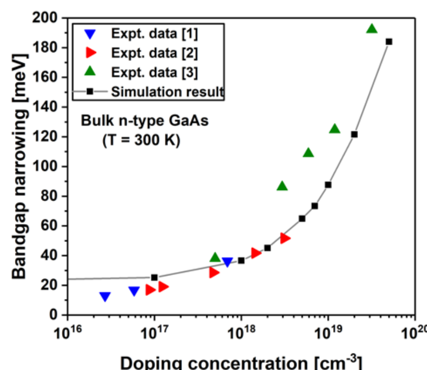

Fig.4: Variation of band gap narrowing of conduction band as a function of doping concentration for GaAs. Simulation results have been compared against a set of experimental results. Exp. data [1], Exp .data [2] and Exp. data [3]) obtained from Refs. [6], [7], and [8] respectively. Simulation results show very good agreement with available experimental data.

Temperature Affected Non-Equilibrium Spin Transport in Nanoscale $In_{0.3}Ga_{0.7}As$ Transistors

B. Thorpe[1], F. Langbein[2], S. Schirmer[1], K. Kalna[3]

[1]*College of Science (Physics), Swansea University, Swansea, SA2 8PP, UK*

[2]*School of Computer Science ¥& Informatics, Cardiff University, Cardiff CF24 3AA, UK*

[3]*NanoDeCo Group, College of Engineering, Swansea University, Swansea SA1 8EN, UK*

k.kalna@swansea.ac.uk

Electron spin offers extraordinarily attractive possibilities in the operation of semiconductor devices thanks to the speed and low energy consumption in its control [1, 2]. One application and future candidate for high performance computing and memory applications with ultra-low power consumption are spin field effect transistors (SpinFETs). Originally proposed by Datta-Das [3], spin transport in a hot electron transistor was demonstrated in [4].

In this work, 2D finite-element quantum-corrected ensemble Monte Carlo simulation code to model a realistic nanoscale $In_{0.3}Ga_{0.7}As$ MOSFET [6] (Fig. 1), designed on ITRS prescriptions [6], was augmented to incorporate electron spin-degrees of freedom and spin-orbit coupling to simulate electron spin transport in a realistic nanoscale device. The dimensions of the $In_{0.3}Ga_{0.7}As$ MOSFET are illustrated in Fig. 2. The device is similar to the Datta-Das SpinFET [3] but only the source electrode is ferromagnetic. The spin states are described by a spin density matrix: $\rho = \begin{pmatrix} \rho_{\uparrow\uparrow}(t) & \rho_{\downarrow\uparrow}(t) \\ \rho_{\uparrow\downarrow}(t) & \rho_{\downarrow\downarrow}(t) \end{pmatrix}$

where $\rho_{\uparrow\uparrow}$ and $\rho_{\downarrow\downarrow}$ are the population of spin-up and spin-down electrons, respectively, and the diagonal elements $\rho_{\downarrow\uparrow}$ and $\rho_{\uparrow\downarrow}$ represent the coherence. The spin degrees of freedom of the electrons are coupled to the orbital degrees of freedom described by the wavevector ***k*** via a spin-orbit coupling Hamiltonian. Dresselhaus and Rashba coupling are the two main contributions to spin-orbit coupling. Dresselhaus coupling is due to asymmetry in a crystal, given by the Hamiltonian

$$H_D = \Gamma_D \langle k_y^2 \rangle \ (k_z\sigma_z - k_x\sigma_x)$$

Rashba coupling is due to potential asymmetry in the quantum well, given by

$$H_R = \alpha_R \ (k_z\sigma_x - k_x\sigma_z)$$

This assumes that the channel is in the [001] direction, x is the transport direction along the channel, and z is the growth direction orthogonal to the quantum well. α_R and Γ_D are Rashba and Dresselhaus coupling constants, respectively, which are material, strain and temperature dependent/ We monitor the 3D magnetization components over varying drain and gate biases at fixed large gate (0.7 V) and drain biases (0.9 V), respectively, as shown in Figs. 4 and 5. Fig. 6 presents magnetization components as a function of temperature showing substantial increase in magnetization components of about 65% when lattice temperature drops from 300 K to 77 K due to a substantial reduction in electron-phonon scattering.

However, Figs. 8 and~9 demonstrate that increasing the source-to-gate and gate-to-drain spacers can enhance the spin recovery, reported initially in the 25 nm gate length $In_{0.3}Ga_{0.7}As$ MOSFET [7]. The polarisation of the electrons initially decays along the channel but surprisingly partially recovers as the electrons reach a high fringing electric field on the drain side of the gate. There they undergo highly non-equilibrium transport during their acceleration, limited mainly by emission of polar phonons. The drain electrode was deliberately chosen to be non-magnetic so that recovery of the magnetization cannot be attributed to existing polarized carriers inside the drain.

[1] D. D. Awschalom et al., Science **339**, 1174-1179, 2013.
[2] S. Wolf et al., Science **294**, 1488-1495, 2001.
[3] S. Datta and B. Das, Appl. Phys. Lett. **56**, 665-667, 1990.
[4] I. Appelbaum et al., Nature **447**, 295, 2007.
[5] A. Islam et al., IEEE Trans. Nanotechnol. **10** 1424-1432, 2011.
[6] Int. Technol. Roadmap for Semiconductors (ITRS 2.0) [http://www.itrs2.net/], 2015.
[7] B. Thorpe et al., J. Appl. Phys. **122,** 223903 (17pp), 2017.

Fig. 1: 3D model of the studied $In_{0.3}Ga_{0.7}As$ showing spin polarization of electrons along n-channel with 4% strain (red) and unstrained (purple).

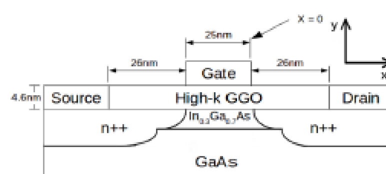

Fig. 2: Cross-section with dimensions of the 25 nm gate length, n-channel $In_{0.3}Ga_{0.7}As$ MOSFET.

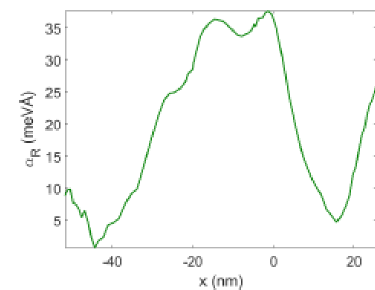

Fig. 3: Rashba coupling constant along the 25 nm gate length channel of $In_{0.3}Ga_{0.7}As$ MOSFET. The zero in the channel is set at the drain side of the gate.

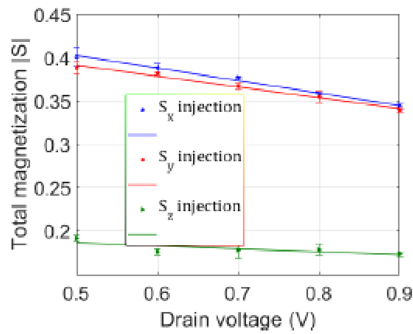

Fig. 4: Magnetization components of spin injection (averaged over 10 runs) vs. drain bias at V_G=0.7 V with indication of error in averages. The transport direction along the x-axis. The lines are only a guide to the eye.

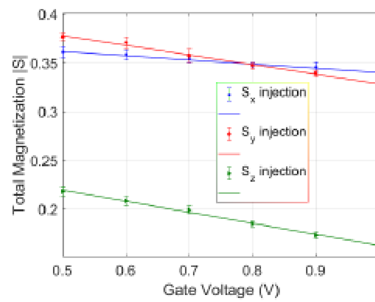

Fig. 5: Magnetization components of spin injection (averaged over 10 runs) vs. gate bias at V_D=0.9 V with indication of error in averages. The transport direction is along the x-axis.

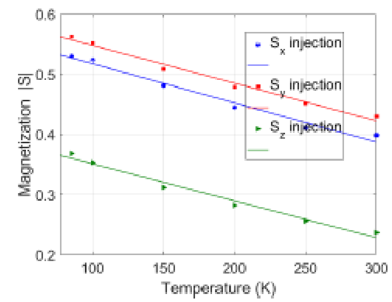

Fig. 6: Magnetization components of spin injection (averaged over 10 runs) vs. lattice temperature at V_G=0.7 V and V_D=0.9 V with errors in averages. The transport direction is along the x-axis.

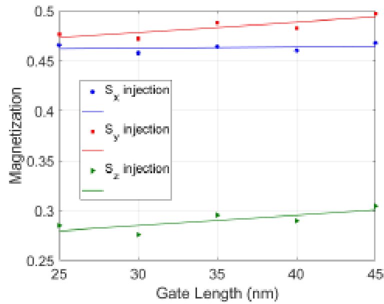

Fig. 7: Magnetization components (averaged over 10 runs) vs. the gate length of the transistor at V_G=0.7 V and V_D=0.9 V. The lines are only a guide to the eye.

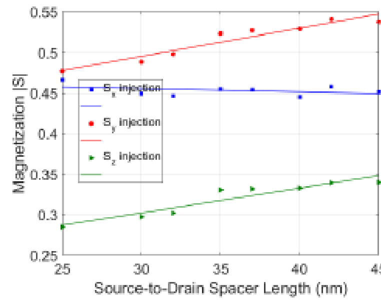

Fig. 8: Magnetization components (averaged over 10 runs) vs. the source-to-gate spacer of the transistor at V_G=0.7 V and V_D=0.9 V. The lines are only a guide to the eye.

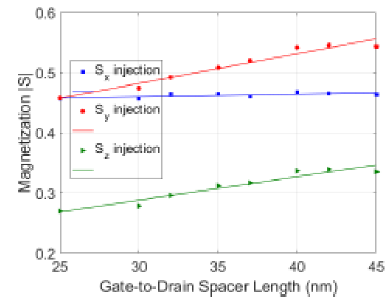

Fig. 9: Magnetization components (averaged over 10 runs) vs. the gate-to-drain spacer of the transistor at V_G=0.7 V and V_D=0.9 V. The lines are only a guide to the eye.

Atomistic Quantum Transport using Empirical Pseudopotentials

M. L. Van de Put, W. G. Vandenberghe,
A. A. Laturia, S. Chen, M. V. Fischetti
Department of Material Science and Engineering, The University of Texas at Dallas, Richardson, Texas, USA; vandeput.maarten@gmail.com

We have recently developed a technique to calculate ballistic electron transport through atomic structures using empirical pseudopotentials that is numerically tractable for devices containing more than a thousand atoms. [1] Our technique offers a competitive alternative to the commonly used tight-binding approximation.

To attain this efficiency, we exploit the Bloch waves of the underlying material. To do so, we consider atomic structures consisting of a repeated supercell, as shown in Fig. 1. Without external potentials, the solutions are Bloch waves that are calculated using a standard plane-wave empirical pseudopotential solver [2]. To account for the potential variations seen in devices, we employ the partition-of-unity method [3], where the wavefunctions are expanded using finite-elements shape-functions enhanced with the Bloch waves. The finite-element mesh, defined by nodes between each supercell (shown in Fig. 1), captures the device scale. The combination of Bloch waves captures the atomic scale within a supercell. Specifically, we use a limited set of Bloch-waves at high symmetry points. Use of the Galerkin method transforms the Schrödinger equation into a sparse generalized eigenvalue problem in the expansion coefficients. Thanks to the shape functions, the Hamiltonian contains only nearest neighbors coupling between adjacent nodes, resulting in a high computational efficiency and scalability.

The quantum transmitting boundary method (QTBM) is used to describe the open system in the presence of contacts and the travelling wavefunctions are calculated self-consistently with the Poisson equation. We have used our method to simulate various field-effect transistors (FETs) based on graphene nanoribbons (GNRs) and silicon nanowires (Si-NWs). We show, in Fig. 2, the structure and transfer characteristics of a GNR FET containing 960 atoms. For this device, we include the Bloch waves at the center and edge of the first Brillouin zone of 42 valence and 20 conduction bands. In Fig. 3, we demonstrate the accuracy of our method by reconstructing the complete band structure. Note that, unlike for methods based on envelope-functions [4], there are no spurious solutions in the energy range covered by the basis. A single self-consistent solution for the GNR FET in the off state (as shown in Fig. 4) is obtained in 20 minutes on a single CPU core, which is two orders of magnitude faster than a previous plane-wave approach [4]. In Fig. 5, we also show the transfer characteristics of an extremely scaled Si-NW FET with 2048 atoms, to demonstrate the generality of our method.

[1] M.L. Van de Put *et al.,* IEEE SISPAD 2018, 71-74 (2018)
[2] M.L. Van de Put *et al.*, J. Appl. Phys. **119**, 214306 (2016)
[3] I. Babuska and J.M. Melenk, Int. J. Numer. Meth. Eng. **40**, 727–758 (1998)
[4] J. Fang *et al.*, J. Appl. Phys. **119**, 035701 (2016)

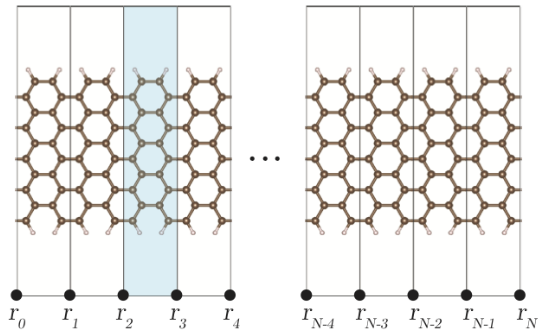

Fig. 1: The atomic structure of a graphene nanoribbon, where the supercells and nodes (r_i) are indicated. The Bloch waves are calculated assuming supercell periodicity, while the nodes are used to form a finite element basis describing the large-scale behavior of the system.

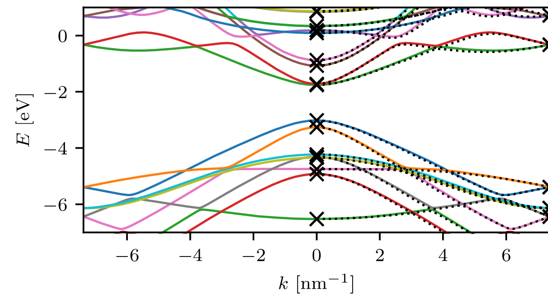

Fig. 3: The electronic band structure of the GNR ribbon shown in Fig. 2. The figure shows a comparison of the full empirical pseudopotential calculation (dashed black lines) to our method (colored lines) which uses only the Bloch waves at the indicated points (x).

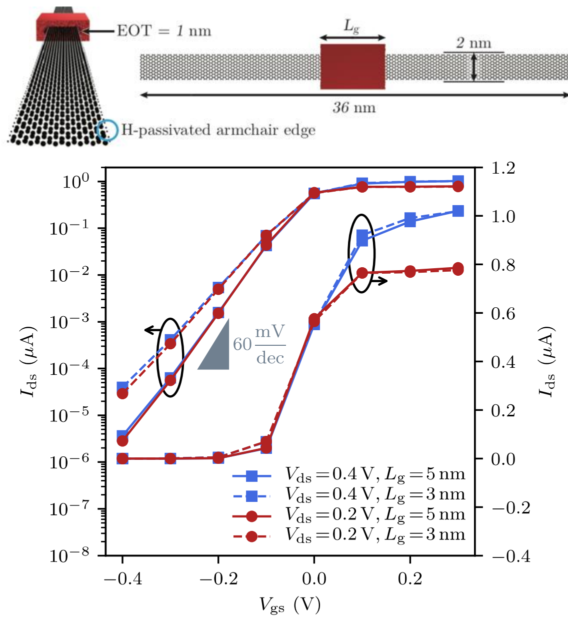

Fig. 2: *Top:* A three-dimensional depiction of the gate-all-around graphene nanoribbon field-effect transistor (GNR FET). Spheres indicate the position of carbon (black) and hydrogen (blue) atoms. *Bottom:* The transfer characteristics (I_{ds}– V_{gs}) of the GNR FET, shown above, at different drain-source bias (V_{ds}) and gate-lengths (L_g).

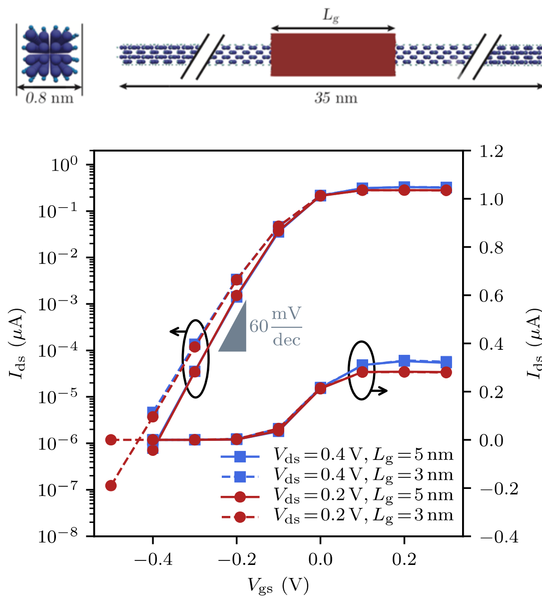

Fig. 5: *Top:* A three-dimensional depiction of the gate-all-around silicon nanowire field-effect transistor (Si-NW FET). Spheres indicate the position of silicon (dark blue) and hydrogen (light blue) atoms. *Bottom:* The transfer characteristics (I_{ds}– V_{gs}) of the Si-NW FET, shown above, at different drain-source bias (V_{ds}) and gate-lengths (L_g

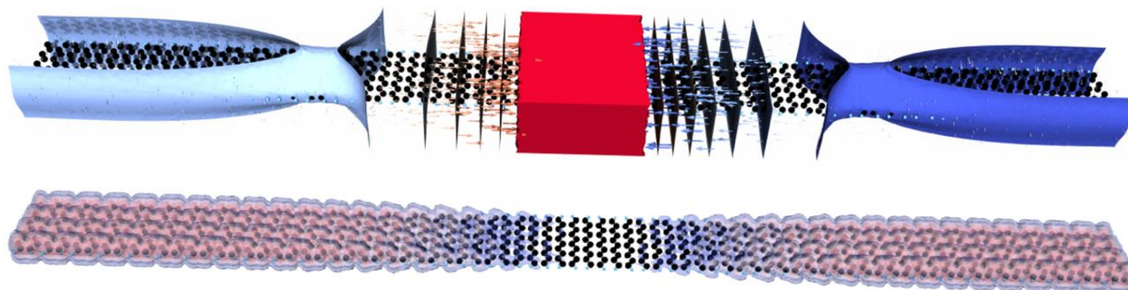

Fig.4: For the GNR FET of Fig. 2 in the off-state. *Top:* Shows the self-consistent potential and electric field, with the gate indicated in red. *Bottom:* Shows the free electron density, displaying spatial resolution well below the atomic scale. Spheres indicate the positions of the carbon (black) and hydrogen (blue) atoms.

Work-Function Engineering in Ultra-Scaled 2D-TFET Devices: An Atomistic DFT-NEGF Study

D. Stradi[1], P. Khomyakov[1], U. Vej-Hansen[1], M. Lee[1], J. Wellendorff[1], S. Smidstrup[1], K. Stokbro[1], A. Blom[2], S. Aboud[2]

[1]*Synopsys Denmark ApS, Fruebjergvej 3, 2100 Copenhagen, Denmark*

[2]*Synopsys, Inc., 690 E. Middlefield Road, Mountain View, CA 94043, USA*

Two-dimensional (2D) materials such as transition metal dichalcogenides (TMDs) have recently been included in the International Roadmap for Devices and Systems (IDRS) as promising channel materials for next-generation sub-10nm technology nodes [1,2]. In this contribution, we investigate the electrical characteristics of an ultra-scaled tunnel FET (TFET) device, where the channel is a heterojunction based on 2D semiconducting MoTe2 and SnS2 monolayers [3]. We characterize the electronic structure and the transport properties of the 2D-TFET device by means of density functional theory (DFT) combined with the non-equilibrium Green's function (NEGF) method [4] and with advanced electrostatic solvers, as implemented in the QuantumATK software [5]. We show how the electrical response of the device to electrostatic gates can be tuned by using an asymmetric contact scheme. The latter is analogous to that proposed for graphene-based photodetectors [6], where metals with different work functions have been used to contact the 2D channel. Our large-scale DFT-NEGF device simulations demonstrate that the electrical characteristics of ultra-scaled 2D devices can be engineered by an appropriate choice of the metallic electrodes, and highlight the importance of atomistic device simulations for the optimization of the electrical characteristics of future devices based on non-conventional semiconductors.

[1] G. Fiori et al. Nat. Nanotech. 9, 768 (2014).
[2] https://irds.ieee.org/images/files/pdf/2017/2017IRDS_MM.pdf
[3] A. Szabó, IEEE Electron Device Letters 36, 514 (2015).
[4] M. Brandbyge et al., Phys. Rev. B 65, 165401 (2002).
[5] S. Smidstrup et al., in preparation.
[6] F. Xia et al. Nature nanotechnology 4, 839 (2009).

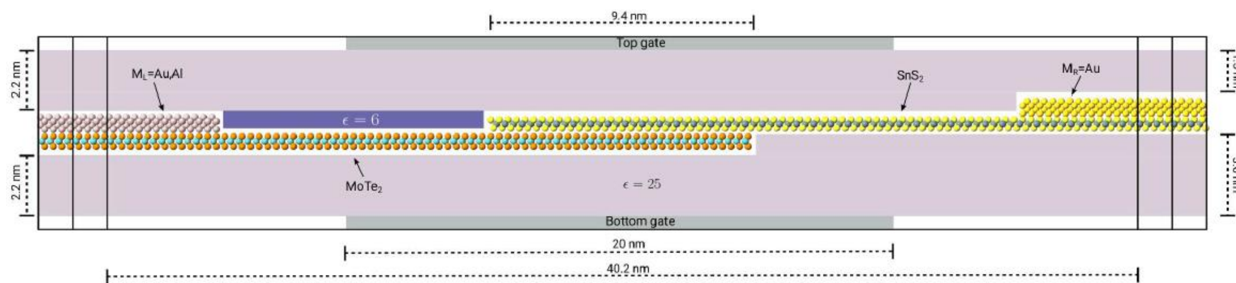

Fig. 1: Structure of the M_L/MoTe2/SnS2/M_R device. Mo, Te, Sn and S atoms are shown in cyan, orange, dark green and yellow. The atoms of the M_L (Au, Al) and M_R (Au) regions are shown in pink and yellow. The metallic gate regions (Top gate, Bottom gate) are shown as grey rectangles. The dielectric regions are shown as dark purple (ϵ = 6) or light purple (ϵ = 25) rectangles.

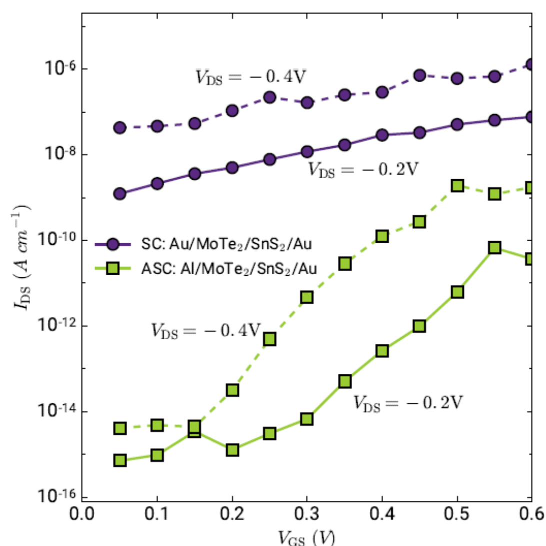

Fig. 2: I_{DS} vs. V_{GS} transconductance curves calculated for the symmetrically-contacted (SC, Au/MoTe2/SnS2/Au) device at V_{DS} = -0.2 V (purple circles, solid line) and V_{DS} = -0.4 V (purple circles, dashed line), and for the asymmetrically-contacted (ASC, Al/MoTe2/SnS2/Au) device at V_{DS} = -0.2 V (green squares, solid line) and V_{DS} = -0.4 V (green squares, dashed line).

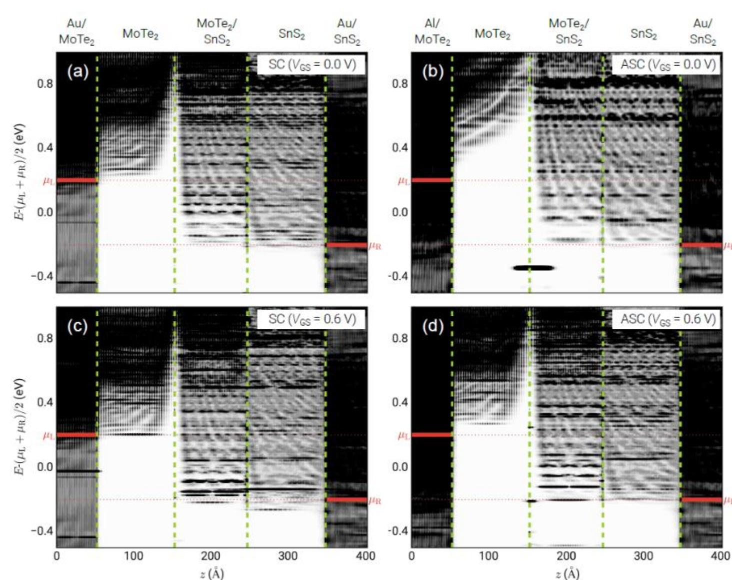

Figure 3: Projected local density of states (PLDOS) along the transport direction for the symmetrically-contacted (SC:Au/MoTe2/SnS2/Au) device at V_{DS} = -0.4V and V_{GS} = 0.0V (a) or at V_{GS} = 0.6V (c). (b,d) Same as (a,c), but for the asymmetrically-contacted (ASC: Al/$MoTe_2$/SnS_2/Au) device. The red solid lines indicate the position of the left and right chemical potentials. The green dashed lines mark the boundaries of the different device regions.

From Semiclassical to Quantum Transport Modeling Including Carrier Recombination and Generation

K.-C. Wang, S. H. Sureshbabu, X. Guo,
Y. Chu, T. Kubis
School of Electrical and Computer Engineering, *Purdue University,*
West Lafayette, IN 47907 USA
wang2366@purdue.edu

The non-equilibrium Green function (NEGF) method is capable of nanodevice performance predictions including coherent and incoherent effects. Typically, treating incoherent scattering, carrier generation and recombination in NEGF is computationally very expensive since it involves several nonlinear and highly dimensional integro-differential equations [1]. In contrast, drift-diffusion (DD) [2] models, with or without quantum corrections [3] have been the industrial standard for TCAD due to their efficiency. The Büttiker-probe model represents a good compromise between the accuracy of NEGF and the efficiency of heuristic thermalization models. In this work, the charge self-consistent NEGF Büttiker-probe model is expanded to include carrier recombination and generation effects. Several highlights are achieved with this method. First, atomic resolved recombination/generation effects such as Shockley-Read-Hall, radiative, and Auger recombination are incorporated into NEGF. Second, an alteration of the Büttiker-probe convergence criterion carefully satisfies the continuity equations – also in the presence of carrier recombination and generation. Note that atomically, energy and/or momentum resolved observables that give deep insight into the nanodevice physics and represent an important feature of NEGF are available just like with expensive self-consistent Born models. The new method is first benchmarked against charge self-consistent DD. A standard 20 nm GaN pn diode with $10^{20}/cm^3$ doping is constructed with 2 bands tight binding parameters from NEMO5's tool suit [4] and semiclassical parameters from Silvaco's Atlas tool suit. Current-voltage characteristics (Fig.1), bandstructures (Fig.2), density (Fig.3), and recombination profiles (Fig.4) compare very well. When carrier confinement effects are added to the pn junction with an $In_{0.13}Ga_{0.87}N$ quantum well, quantum transport capabilities are needed to cover the device behavior (Fig.5). These confinement effects enhance the recombination current as shown in Fig.6.

[1] J. Charles, et al., "Incoherent transport in NEMO5: realistic and efficient scattering on phonons," *J. Comput. Electron.*, vol. 15, no. 4, pp. 1123–1129, 2016.
[2] Y.-R. Wu, et al. , "Analyzing the physical properties of InGaN multiple quantum well light emitting diodes from nano scale structure," *Appl. Phys. Lett.*, vol. 101, no. 8, p. 83505, 2012.
[3] J. Geng, et al. , "Quantitative Multi-Scale, Multi-Physics Quantum Transport Modeling of GaN-Based Light Emitting Diodes," *Phys. Status Solidi*, vol. 1700662, p. 1700662, 2017.
[4] S. Steiger, et al., "NEMO5: A parallel multiscale nanoelectronics modeling tool," *IEEE Trans. Nanotechnol.*, vol. 10, no. 6, pp. 1464–1474, 2011.

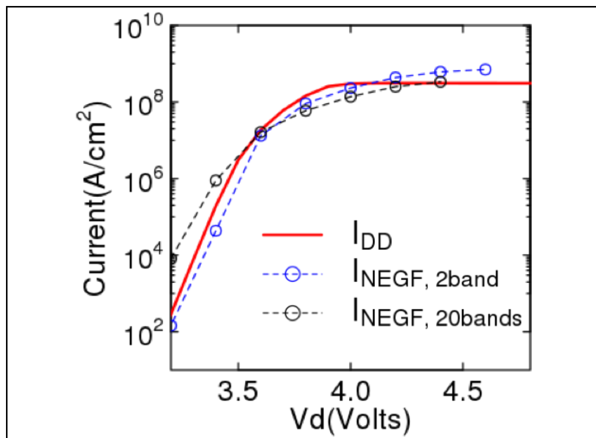

Fig.1: Current-voltage characteristics predicted within quantum transport of NEMO5 and drift diffusion(DD). The current densities match well in a two band model. The better resolution of the 20band results of NEMO5 yield more pronounced deviations.

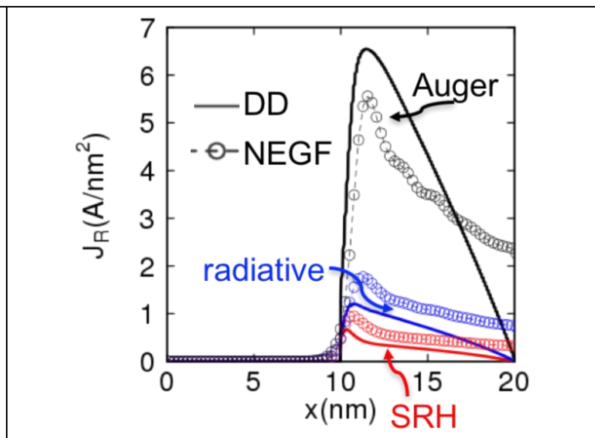

Fig.4: Recombination rates at Vd=3.6V for quantum transport (NEMO5) and drift diffusion(DD). The good agreement is consistent with the carrier comparison of Fig.3.

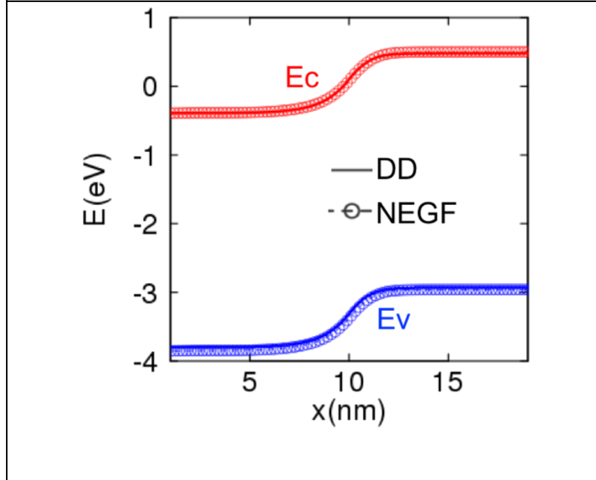

Fig.2: Band diagram (Ec, Ev) comparison between drift diffusion(DD) and NEGF at Vd=3V. Excellent agreement between the two models is observed.

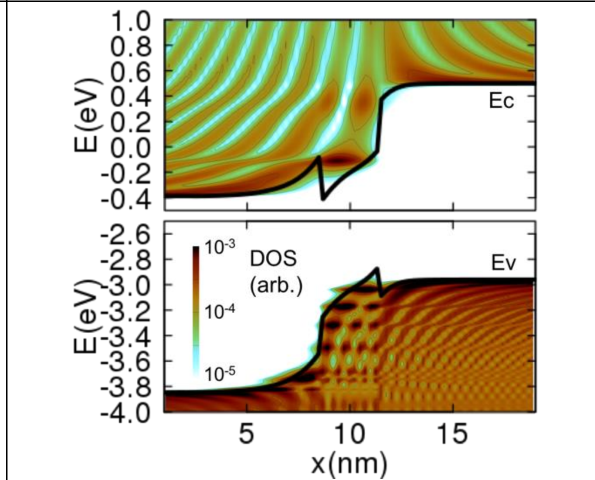

Fig.5: Energy resolved density of states (contour) and band edges (lines) of the pn junction with a quantum well at Vd=3V at the Gamma point. Confined states illustrate the need for quantum transport in nanodevice predictions.

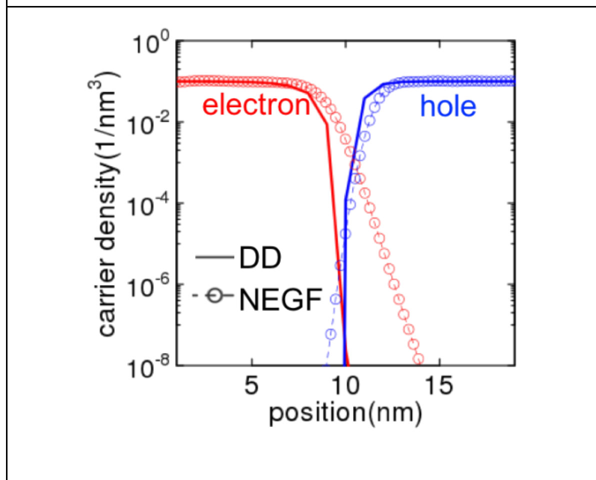

Fig.3: Hole and electron density comparison between drift diffusion(DD) and NEGF at Vd=3V. NEGF predicts a higher minority carrier concentration, presumably since NEGF avoids local equilibrium assumptions.

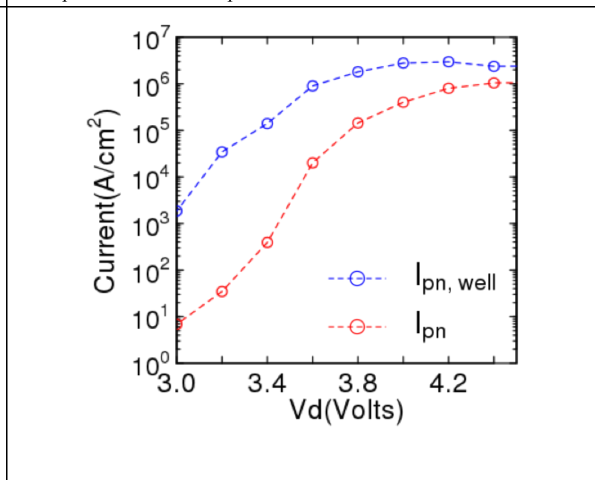

Fig.6: IV curve comparing the standard pn diode case with the same diode added by a quantum well (pn, well). A larger recombination induced by additional carriers in the well increases the total current.

Simulation Tool for Coupled Quantum Transport and Electrodynamics

M. King, F. Karimi, S. Schmidt, I. Knezevic
Department of Electrical and Computer Engineering,
University of Wisconsin-Madison, Madison, WI 53706, USA
michelle.king@wisc.edu

Accurate simulation of light-matter interaction at the nanoscale requires a computational approach that combines quantum transport and electrodynamics, self-consistently and at every time step. Here we present the development of a new tool for this purpose — Quantum Transport and Electrodynamics Simulation Tool (QuTEST) — which self-consistently couples a full-wave finite-difference time-domain (FDTD) electrodynamics solver for the potentials with a density-matrix-based quantum transport solver. A schematic of the coupling is depicted in Fig. 1. The current density $\boldsymbol{J}$ and charge density ρ are calculated from the density matrix and inputted back into the FDTD; FDTD produces the vector potential $\boldsymbol{A}$ and scalar potential Φ, both of which are needed in the density-matrix equation of motion.

The non-traditional 3D FDTD formulation for the potentials is implemented by discretizing Maxwell's equations for $\boldsymbol{A}$ and Φ in the Lorentz gauge [1]. Calculations on a simple current source are depicted in Fig. 2 and show excellent agreement between analytical results and numerical calculation in our implementation. The rigorous density-matrix formalism for quantum transport is based on a Markovian master equation that preserves the positivity of the density matrix [2,3] and it employs the calculated $\boldsymbol{A}$ and Φ in the Hamiltonian. We are currently developing the coupled simulation and, at conference time, we will present the results obtained on several sample systems (e.g., the bowtie antenna).

[1] C. J. Ryu, A. Y. Liu, W. E. I. Sha, and W. C. Chew, J. Multiscale and Multiphys. Comput. Techn., **1**, 40-47 (2016).
[2] O. Jonasson, F. Karimi, I. Knezevic, Journal of Computational Electronics **15**, 1192-1205 (2016).
[3] F. Karimi, A.H. Davoody, and I. Knezevic, Phys. Rev. B **93**, 205421 (2016).

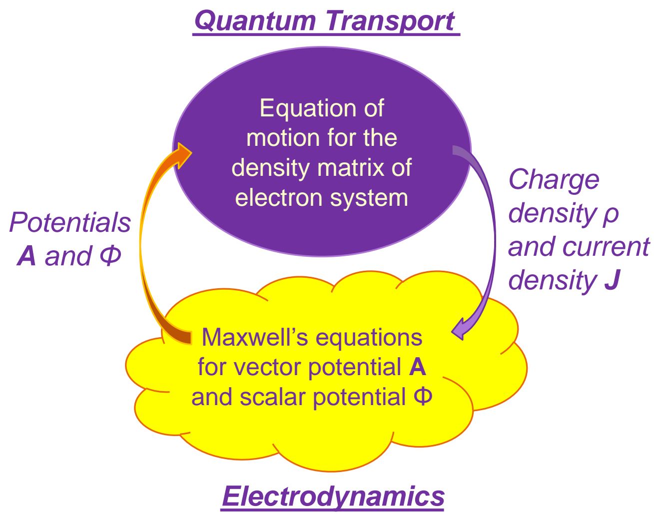

Fig. 1: Schematic illustrating the self-consistent coupling between the full-wave electrodynamic solver for vector potential ***A*** *and scalar potential* Φ *and the density-matrix based quantum transport solver, which produce current density* ***J*** *and charge density* ρ *for the coupled simulator.*

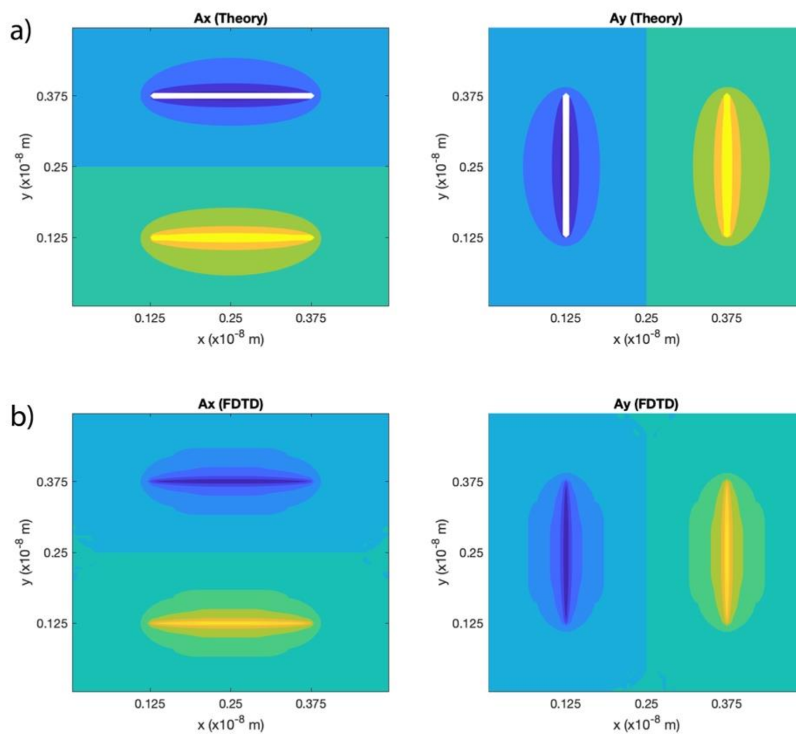

Figure 2: Contour plot of relative magnitudes of magnetic vector potential ***A*** *(yellow: high; blue: low) for a square wire with constant current density* ***J*** *flowing counter-clockwise around the wire, as calculated a) analytically and b) from FDTD for the potentials within the Lorentz gauge.*

An Efficient Method for Atomistic-Level Non-Equilibrium Green's Function Simulations of Field-Effect Transistors involving Heterojunctions

Y. Ahn, B. Kim, M. Shin
School of Electrical Engineering, Korea Advanced Institute of Science and Technology, Daejeon 34141, Republic of Korea
mshin@kaist.edu

The device structure consisting of heteromaterials is being widely considered for the future field-effect transistors (FETs) such as tunneling FETs (TFETs) and Schottky barrier FETs. In order to properly describe the band gap and band offsets and to naturally capture the interface effects at heterojunctions, it is essential to model the heterostructure FETs in the atomistic level. Therefore, a density functional theory (DFT) based approach is called for. A recently developed framework where the DFT and non-equilibrium Green's function (NEGF) parts are performed sequentially provides a practical simulation platform [1], but when it comes to its application to heterostructure FETs, the large size of the junction Hamiltonians becomes the main obstacle to efficient NEGF simulations. This work presents a methodology to reduce the computational burden in the NEGF part. The main idea is to employ the recursive Green's function (RGF) method [2] for homogeneous unit cells and the R-matrix method [3] for the junction parts in a heterostructure FET, respectively (Fig. 1), to calculate the retarded Green's functions. For this purpose, we have extended the R-matrix algorithm to open boundary device. To assess the computational efficiency of the proposed RGF+R-matrix approach, we have measured the elapsed CPU time (Fig. 2) for calculating the retarded Green's functions of four two-dimensional heterostructures. The calculated transmission functions for the four heterostructures (Fig. 3) show the exactness of the computed retarded Green's functions. Our RGF+R-matrix method is numerically efficient for atomistic-level NEGF simulations of hetero-FETs. As an application, the self-consistent simulations of NEGF and Poisson equation have been performed for germanane/InSe vertical TFET (Fig. 4) using the RGF+R-matrix approach. It can be seen in Fig. 5 that the band-to-band tunneling occurs when the conduction band is lowered below the valence band, leading to the onset of the ON-state region. The approach of this work can be applied to the device having heterojunction of three-dimensional materials, surface roughness, and atomic vacancies or dopants.

[1] M. Shin et al., J. Appl. Phys., **119**, 154505 (2016).
[2] A. Svizhenko et al., J. Appl. Phys., **91**, 2343 (2002).
[3] G. Mil'nikov et al., Phys. Rev. B, **79**, 235337 (2009).

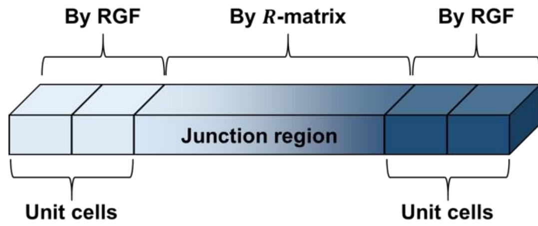

Fig.1: The concept of RGF+R-matrix method. RGF is used for the matrix calculations related to the homogeneous unit cells, while R-matrix is applied to those for the junction regions.

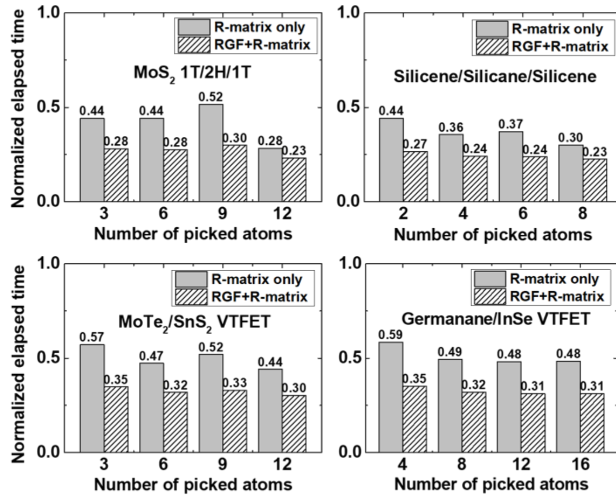

Fig.2: The elapsed CPU time per energy grid for calculating retarded Green's functions of four two-dimensional heterostructures. 1.0 is the reference elapsed time when the RGF method is used only.

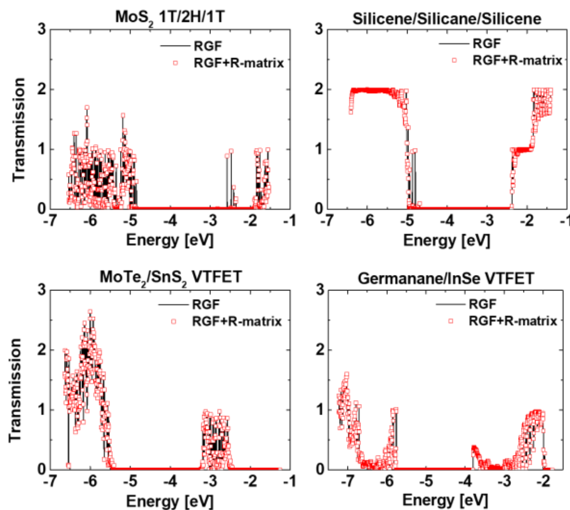

Fig.3: The transmission functions of the simulated heterostructures.

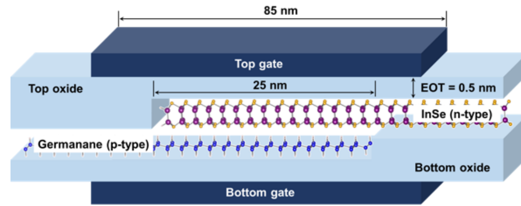

Fig.4: Schematic of the simulated germanane/InSe vertical TFET.

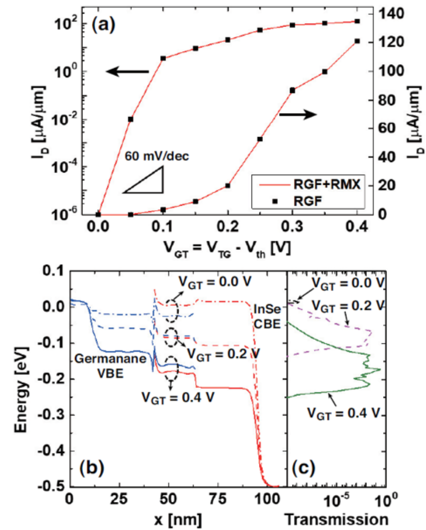

Fig.5 (a) Transfer characteristics of the simulated germanane/InSe vertical TFET at drain voltage of 0.4 V and top gate voltage (V_{TG}) of -0.8 V. Threshold voltage (V_{th}) is defined such that off-state current is 10^{-6} μA/μm. (b) Band edge profile and (c) transmission (log scale) of the simulated vertical TFET at various top gate voltages. V_{GT} denotes V_{TG}-V_{th}.

Subdomain Algorithm for the Numerical Solution of the Liouville-von-Neumann-Equation

L. Schulz, D. Schulz

Chair for High Frequency Techniques, TU Dortmund, Germany

lukas.schulz@tu-dortmund.de

For the numerical simulation of quantum electronic devices sophisticated methods are desirable. The numerical solution of the Wigner Transport Equation (WTE) is preferable for engineering applications [1,2,3]. On the one hand, transient effects can be analyzed in a straightforward manner. On the other hand, scattering mechanisms can be implemented in detail. Unfortunately, conventional methods utilized for a numerical solution of the WTE tend to pose problems [2].

To begin with, the conventional discretization schemes cannot adequately include coherent effects resulting in an overestimation of the diffusion effect [4] as these are based on upwind difference schemes. Furthermore, by the utilization of these schemes, the drift operator is not interacting with the inflow boundary conditions, whereas this is a prerequisite [2]. Additionally, the drift operator represents a highly oscillating function, when considering heterostructure devices, leading to a worse convergence behavior with respect to the Fourier integrals. As a result, large computational errors are subject to these drawbacks.

In order to address these aspects, an approach based on the formulation of an exponential operator combined with the finite volume discretization technique has been developed for the numerical solution of the Liouville-Von-Neumann-Equation (LVNE) in center-mass coordinates, χ and ξ [5]. On the basis of the discretized diffusion operator with regard to the ξ-direction, a transformation of the statistical density matrix is carried out allowing a definition of the inflowing and outflowing waves. With regard to the continuity conditions at the interfaces, the real space formulation is preferable.

Here, a concept is proposed allowing the utilization of arbitrary basis functions as well as allowing the application of a subdomain approach for a highly efficient solution of the LVNE. Indeed, when an orthogonal set of exponential functions is applied to form the transformation matrix, the WTE is formally obtained from the discretized equation and, therefore, the corresponding advantages with regard to the implementation of scattering mechanisms can be preserved. Furthermore, the conventional coupling between the discretized real space and the discretized phase space can be effectively avoided. Along with this procedure more flexible and efficient solutions are enabled.

The approach is verified with the numerical simulation of a simply structured resonant tunneling diode (RTD) on the basis of the AlGaAs/GaAs material system as demonstrated in Fig.1-6. Finally, a novel approach for a highly efficient solution of the LVNE combined with an in-depth analysis with regard to the WTE is presented.

[1] J. Weinbub et al., Appl. Phys. Rev., doi: 10.1063/1.5046663 (2018)

[2] D. Schulz et al., J. Quantum Electron., 8700109, doi: 10.1109/JQE.2015.2504086 (2016).

[3] W. R. Frensley, Phys. Rev. B., 1570, doi: 10.1103/PhysRevB.36.1570 (1987).

[4] C. Carey et al., Appl. Math. Modelling, doi: 10.1016/0307-904X(93)90048-L (1993).

[5] K. Khalid et al., Trans. Nanotechnol., doi: 10.1109/TNANO.2017.2747622 (2017)

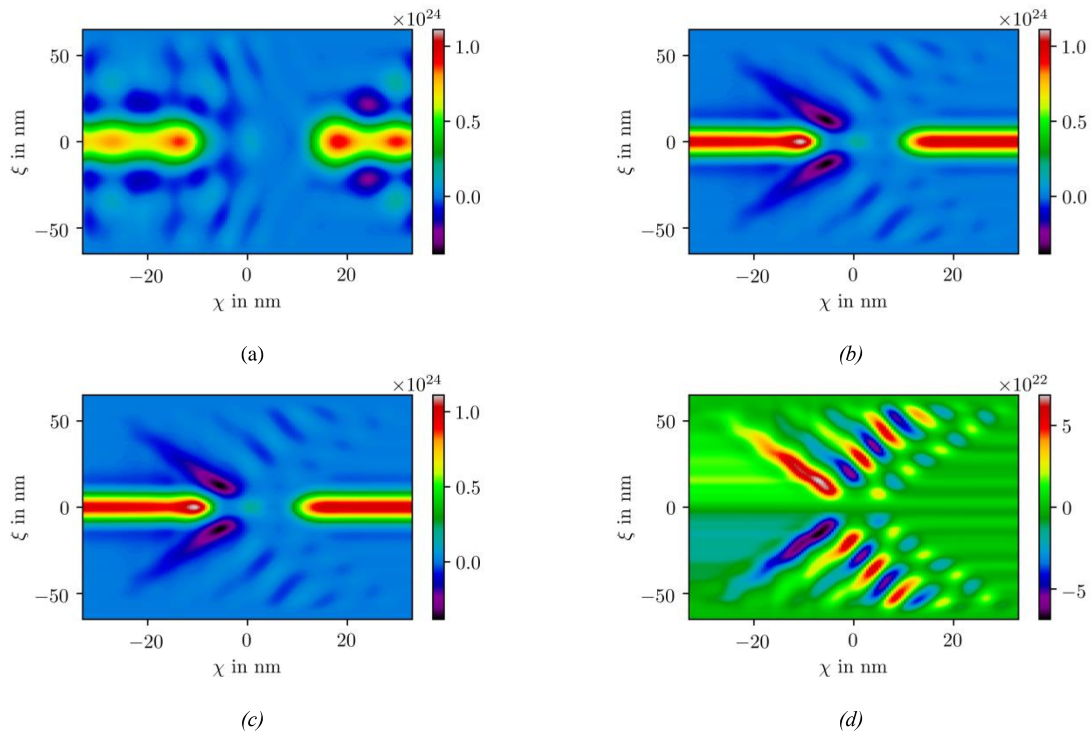

Fig.1: Real part of the statistical density matrix for the RTD for the non-equilibrium case shown for an external bias of -0.15V and for different subdomain dimensions. For the demonstration an exponential basis is applied so that the expansion coefficients are inherently linked with the values of the discretized Wigner function. The discretized statistical density matrix obtained for the use of N=250 basis functions is depicted in (c), which corresponds to the full set of basis functions, whereas the subdomain dimensions N=10 and N=50 are shown in (a) and (b), respectively. As apparent from the numerical solution in (b), N=50 basis functions are sufficient for a convergence of the statistical density matrix. As a consequence, the number of basis functions can be drastically reduced in comparison to standard methods. The computation time as well as the computational resources can be effectively reduced. The imaginary part of the statistical density matrix obtained from the subdomain solution is shown in (c).

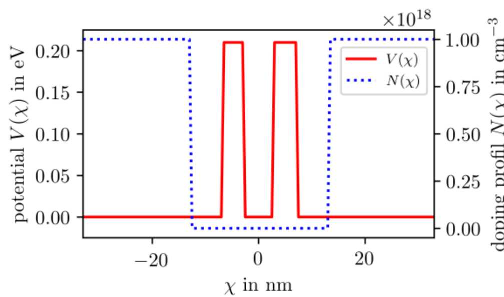

Fig.2: Conduction band diagram V and doping concentration N of the RTD.

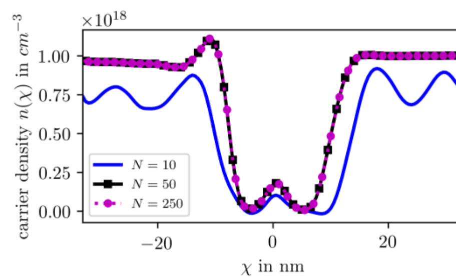

Fig.3: Carrier densities calculated from the values of the corresponding statistical density with regard to different subdomain dimensions N as shown in (a), (b) and (c).

Linking Wigner Function Negativity to Quantum Coherence in a Nanowire

Mauro Ballicchia[1,2], David K. Ferry[3], Mihail Nedjalkov[2], Josef Weinbub[4]
[1]*Department of Information Engineering, Università Politecnica delle Marche, Italy*
[2]*Institute for Microelectronics, TU Wien, Austria*
[3]*School of Electrical, Computer, and Energy Engineering, Arizona State University, USA*
[4]*Christian Doppler Laboratory for High Performance TCAD at the Institute for Microelectronics, TU Wien, Austria*
josef.weinbub@tuwien.ac.at

Quantum information and quantum communication are both strongly based on concepts of quantum superposition and entanglement. Entanglement allows distinct bodies, that share a common origin or that have interacted in the past, to continue to be described by the same wave function until evolution is coherent. When two bodies interact in a quantum manner, they become entangled, which implies that they are now described by a single wave function and are no longer two distinct bodies. Even after they have ceased to interact and have moved some distance away, they remain entangled until some decoherence process acts upon them [1,2]. So, there is an equivalence between coherence and entanglement. However, in experiments, one must face the fact that entanglement is difficult to measure. There is no physical variable whose Eigenvalue yields the entanglement. Hence, researchers have investigated for years to devise measures of entanglement [3]. Most of these, however, do not provide a clear visualization of the entanglement. But, it has been demonstrated that the Wigner function does provide a clear visualization of entanglement [1], and is used intensely today in optics [2]. Expanding upon this notion (and based on a recently formulated Wigner coherence theory [4]), we discuss the relation between quantum coherence and quantum interference and the negative parts of the Wigner quasi-distribution, using the Wigner signed-particle formulation [5]. A straightforward physical problem consisting of electrons in a nanowire interacting with the potential of a repulsive dopant placed in the center of it creates a quasi-two-slit electron system that separates the wave function into two entangled branches, as indicated in Fig. 1. The analysis of the Wigner quasi-distribution establishes that its negative part, Fig. 2, is principally concentrated in the region behind the dopant between the two entangled branches, maintaining the coherence between them. Moreover, quantum interference is shown in this region both in the negative and in the positive part, shown in Fig. 3. Fig. 4 (using a rotated viewpoint) illustrates how this effect is produced by the superposition of Wigner functions evaluated at points of the momentum space that are symmetric with respect to the initial momentum of the injected electrons. This shows that a Wigner signed-particle approach enables to analyze coherence and entanglement in nanoelectronics devices as it allows to directly reconstruct the Wigner quasi-distribution.

[1] D. K. Ferry, M. Nedjalkov, *The Wigner Function in Science and Technology* (IOP, 2018)

[2] J. Weinbub, D. K. Ferry, Appl. Phys. Rev. **5**, 041104 (2018)

[3] R. Horodecki *et al.*, Rev. Mod. Phys. **81**, 865 (2009)

[4] P. Ellinghaus *et al.*, Phys. Stat. Sol. RRL **11**, 1700102 (2017)

[5] M. Ballicchia *et al.*, Appl. Sci. **9**, 1344 (2019)

Acknowledgments. The financial support by the Austrian Science Fund (FWF) project FWF-P29406-N30, the Austrian Federal Ministry of Science, Research and Economy, and the National Foundation for Research, Technology and Development is gratefully acknowledged. The computational results presented have been achieved using the Vienna Scientific Cluster (VSC).

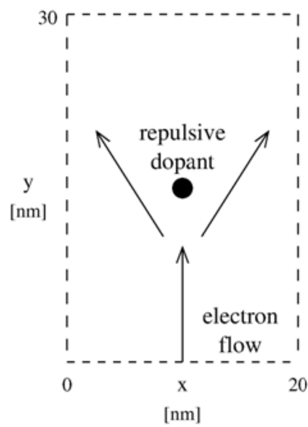

Fig.1: Experimental setup.

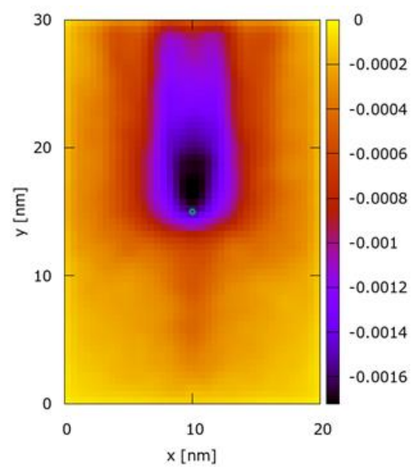

Fig.2: Spatial distribution of the negative part of the Wigner distribution.

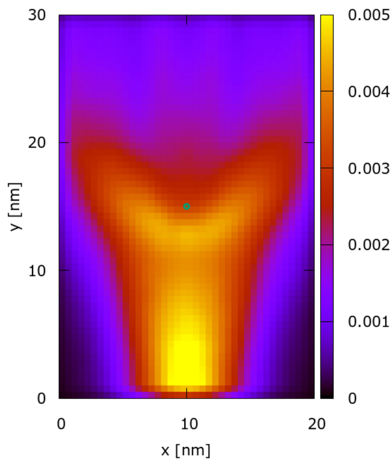

Fig.3: Spatial distribution of the positive part of the Wigner distribution.

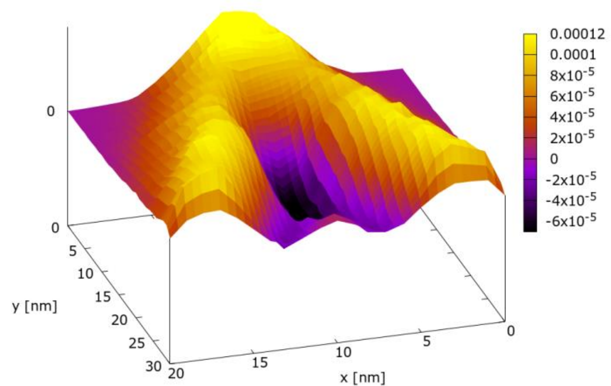

Fig.4 Sum of the Wigner quasi-distribution in the points (k_{x1}, k_{y1}) = $(0.26\ nm^{-1}, 0.89\ nm^{-1})$ and (k_{x2}, k_{y2}).= $(-0.26\ nm^{-1}, 0.89\ nm^{-1})$.

Empirical Pseudopotentials for 3D and 2D Materials: A Unified Approach

A. A. Laturia, M. L. Van de Put, M. V. Fischetti, W. G. Vandenberghe
Department of Material Science and Engineering, The University of Texas at Dallas, Richardson, Texas, USA, 75080
wxv101020@utdallas.edu

Local empirical pseudopotential (EP) are used to compute the electronic band structure of various semiconductors, and have also been used to study electronic transport [1]. In this method, the potential of each atomic species is described by a pseudopotential $V_{\mathrm{EP}}(\boldsymbol{r})$. Given the EP and the position of each atom, the Schrödinger equation can be solved and the electronic band structure $E_n(\mathbf{k})$ (where n is the band index, and $\mathbf{k}$ is the electron wavevector) can be determined.

Whereas EPs are available for diamond and zinc-blende materials [2], they are specified in terms of form-factors, $V_{\mathrm{EP}}(G)$, at specific reciprocal lattice vectors $\mathbf{G}$. These enable the calculation of the band structure for unstrained bulk materials. However, to calculate the band structure of strained materials, we need the full wavevector dependence of the EPs, $V_{\mathrm{EP}}(q)$, given by smooth functions of the wavevector magnitude q. Historically, many different empirical interpolating functions have been used for the construction of these EPs [3-6]. Here we propose a common functional form for the EPs of different materials. We also present an automated method that optimizes the parameters of the EPs to accurately reproduce the bulk band structure of various 3D and 2D materials.

The functional form in reciprocal space for the EPs we propose is constructed as the sum of cosine waves that vanishes at a specified cut-off wavevector q_{cut}:

$$V_{\mathrm{EP}}(q) = \frac{1}{2(N-1)}\left[a[1] + a[N]\cos\left(\frac{\pi(N-1)q}{q_{\mathrm{cut}}}\right) + 2\sum_{n=2}^{N-1} a[n]\cos\left(\frac{\pi(n-1)q}{q_{\mathrm{cut}}}\right)\right]\Theta(q_{\mathrm{cut}} - q) \quad (1)$$

The coefficients $a[n]$ are determined by the discrete cosine transform of the EP parameters $V[q_i]$, with N wavenumbers, q_i equally spaced from 0 to q_{cut}. $V[q_N]$ is fixed at 0 and the other $V[q_i]$ are varied until an optimized solution is found. In Eq. 1, $\Theta(q)$ is the Heaviside step function so that $V(q)$= 0 for $q > q_{\mathrm{cut}}$. Using this definition, $V(q)$ represents a cosine-based interpolation of the parameters $V[q_i]$ within q_{cut}.

These pseudopotential parameters are optimized to match a reference band-structure which we generate from first principles [7] using hybrid functionals [8] in our study. Optimum values of $a[n]$ for a given material are determined using the Broyden–Fletcher–Goldfarb–Shanno algorithm, a quasi-Newton based optimization algorithm [9]. During this optimization, the EP with trial parameters is used for the calculation of the electronic band structure (E_i) using the procedure described in Ref. 1. The difference between the calculated band structure and the reference band structure is quantified by an objective function (d_{obj}) defined as:

$$d_{\mathrm{obj}} = \sqrt{\frac{\Sigma_i w_i (E_i^2 - E_{\mathrm{ref}}^2)}{\Sigma_i w_i}}$$

where i runs over all bands and a selected number of $\mathbf{k}$ points, and w_i represent weights that are chosen such that the band structure is primarily matched in the region of interest, i.e. close to the bandgap for electronic transport purposes. The trial parameters are optimized until a minimum value of d_{obj} is obtained. In Figs.1-4, we show the EP and the band structures corresponding to the optimized set of parameters for bulk Si and phosphorene (monolayer black phosphorus). These calculated band structures reproduce the respective reference band structures very well yielding d_{obj} ≈10 meV. We are thus able to establish an automated, unified workflow for the EP construction of both three- and two-dimensional materials.

[1] M. L. Van de Put, A. A. Laturia, M. V. Fischetti and W. G. Vandenberghe, in Proc. 2018 SISPAD, pp. 71-74 (2018).
[2] M. L. Cohen, T. K. Bergstresser, Phys. Rev. **141**, 789 (1966).
[3] S.B. Zhang, C. Y. Yeh, A. Zunger, Phys. Rev. B **48**, 11204 (1993).
[4] P. Friedel, M. S. Hybertsen, M. Schlüter, Phys. Rev. B **39**, 7974 (1989).
[5] Y. Kurokawa, S. Nomura, T. Takemori, Y. Aoyagi, Phys. Rev. B **61**, 12616 (2000).
[6] K. Mäder and A. Zunger, Phys. Rev. B **50**, 17393 (1994).
[7] G. Kresse and J. Hafner, Phys. Rev. B **47**, 558 (1993); ibid. **49**, 14 251 (1994).
[8] A. V. Krukau, O. A. Vydrov, A. F. Izmaylov, and G. E. Scuseria, J. Chem. Phys. **125**, 224106 (2006).
[9] J. Nocedal and S. J. Wright, "Numerical Optimization" (Springer, New York, 2006).

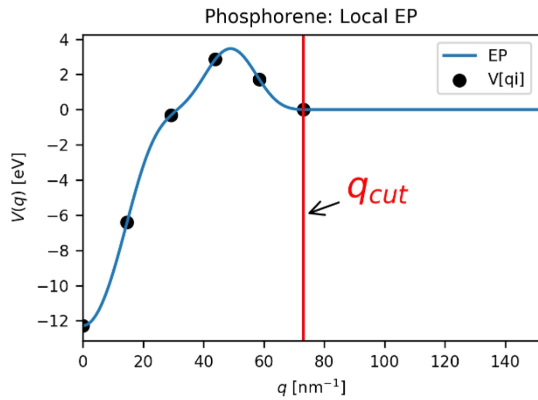

Fig.1: Local empirical pseudopotential (EP) for phosphorene in reciprocal space. This EP is optimized for a 15 Ry energy cutoff. The black dots represent the optimized EP parameters $V[q_i]$ *and* q_{cut} *represents the reciprocal lattice vector cut-off calculated from the energy cutoff.*

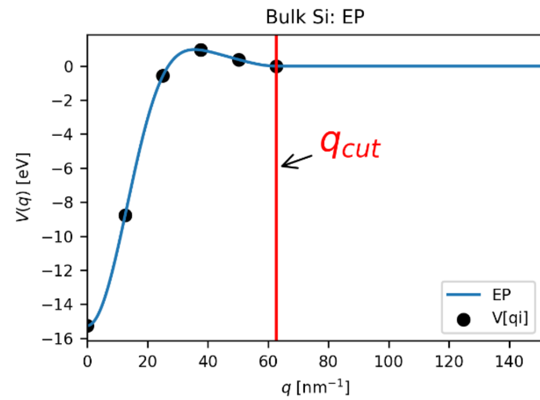

Fig.2: Local Empirical Pseudopotential (EP) for bulk Si in reciprocal space. This EP is optimized for 11 Ry energy cutoff. The black dots represent the optimized EP parameters $V[q_i]$ *and* q_{cut} *represents the reciprocal lattice vector cut-off calculated from the energy cutoff.*

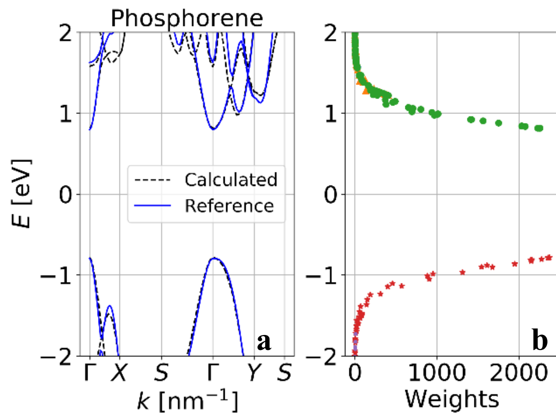

Fig.3: ***a****: Electronic band structure for phosphorene calculated at 120 k-points. The blue curve represents the reference band structure obtained from first principles and the dashed black curve represents the band structure calculated using EP given by Eq. 1.* ***b****: Weight distribution used for finding the optimized EP.*

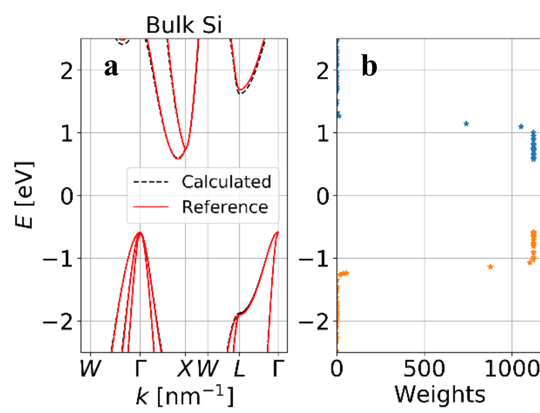

Fig.4: ***a****: Electronic band structure for bulk Si calculated at 100 k-points. Red curve represents the reference band structure obtained from first principles and the dashed black curve represents the band structure calculated using the EP given by Eq. 1.* ***b****: Weight distribution used for finding the optimized EP.*

*This work is supported by the National Science Foundation (NSF Grant #1710066)

Thermoelectric Properties of Complex Bandstructure Materials by Coupling DFT to Boltzmann Transport Equation Including All Energy Dependences

P. Graziosi, C. Kumarasinghe, N. Neophytou
School of engineering, University of Warwick, UK
Patrizio.Graziosi@warwick.ac.uk

Thermoelectricity has recently experienced a large growth due to the discovery of a large number of complex bandstructure materials with unprecedented performance. Performance prediction for thermoelectric (TE) materials requires extracting DFT bandstructures and computation of TE coefficients using Boltzmann transport (BTE). The constant relaxation time approximation is employed due to complexities in accurately computing scattering rates.

In this work, we describe the construction of an advanced simulator, which couples generic bandstructures (e.g. from DFT) with BTE, utilizing the full numerical energy/momentum/valley dependences of all states in the extraction of the relaxation times. We provide much more predictive capabilities and accuracy, but also consider all scattering mechanisms (phonons, ionized impurities (IIS), alloy, nanostructuring, etc.) independently. We start the simulation by interpolating the E(k) (if needed-using linear/quadratic/Fourier, etc. methods). We then sample the Brillouin zone using Delaunay triangulation (Fig. 1a) to extract the k-points at the transport used energy grid, i.e. k(E). Iso-energy surfaces are shown in Fig. 1b for Si and 1c for TiCoSb. We then compute the scattering rates using Fermi's Golden rule. In Fig. 2 we show validations of our code with measured data for Si and GaAs mobilities, and Si and the half-Heusler NbCoSn TE power factors (PFs). (PF discrepancies occur due to lack of experimental details).

In Fig. 3 we show the bandstructures of 4 half-Heuslers, typical promising TE materials. They possess multi-valleys with complex energy surfaces (Fig. 3e). To illustrate the importance of accurate treatment of the scattering rates, Fig. 4 shows the PF vs T of TiCoSb, under 3 different scattering rate scenarios: a) constant τ=20 fs – black line (matches mobility data at 300 K), b) scattering rate ~ 1/T (typical for ADP - acoustic phonon scattering), c) full energy dependence ADP+IIS (red line). In Fig. 5 we show the PF for the 4 half-Heuslers of Fig. 3, and in Fig. 6 we compare 2 of them using constant τ, and proper $\tau(E)$ with acoustic/optical phonons. Evidently in Fig. 4-6, the PF values, trends, and rankings between the materials are different.

Thus, our results indicate that proper scattering considerations can alter the outcomes of large efforts currently being undertaken in materials screening to rank the TE potential of hundreds of materials. The code we develop can significantly assist for proper materials evaluation.

[1] J. Zhou et al., Nature Comm. **9**, 1721 (2018); [2] G. Sun et al., J. Mater. Sci. Chem. Eng, **3**, 78 (2015); [3] T. Sekimoto et al. Materials Transactions, **47**, 1445 (2006); [4] M. A. Kouacou et al., J. Phys.: Condens. Matter, **7**, 7373 (1995); [5] He et al., APL Materials **4**, 104804 (2016).

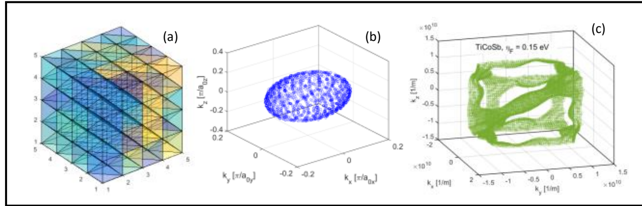

*Figure 1(a) 3D Delaunay triangulation sampling of the Brillouin Zone and extraction of the **k** points at each transport needed energy E for each band of an arbitrary bandstructure. Examples of iso-energy surfaces extracted using the code: (b) **k** points of an ellipsoid of the Si conduction band. (c) **k** points of an energy surface from the TiCoSb half-Heusler material. Strong deviations from parabolic/non-parabolic shapes are evident, indicating the need for full numerical description.*

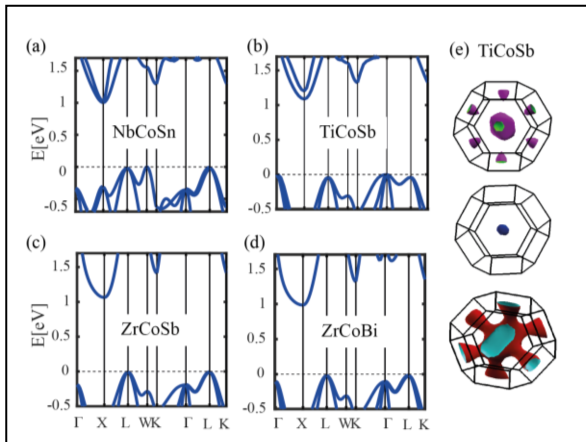

Figure 3: Bands and Fermi surfaces of representative half-Heulser alloys used in the study. Evidently, multi-band materials with complex energy surfaces call for full numerical implementation of details in transport rate description.

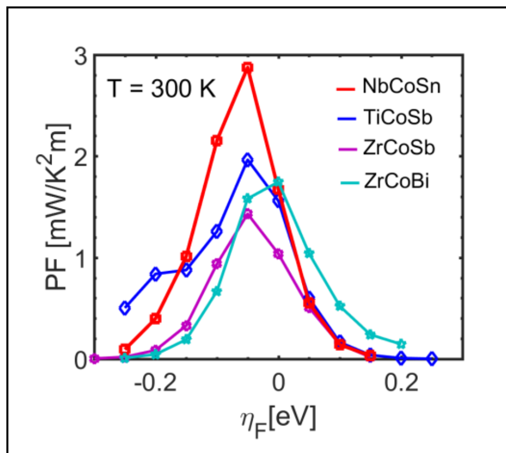

Figure 5: PF versus distance between the Fermi level and the band edge for selected p-type half Heuslers alloys, considering ADP and ODP energy dependent scattering rates. The results are shown for 300 K. Parameters are extracted from references [1]-[3].

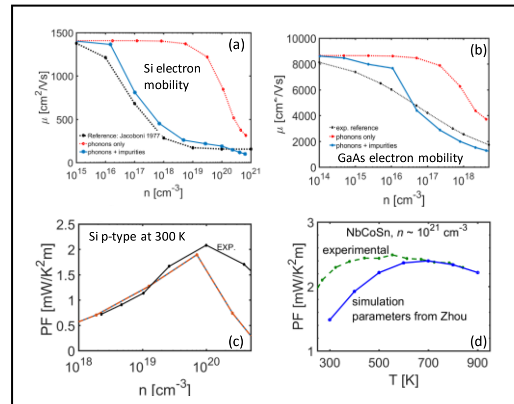

Figure 2: Validation of the simulator constructed for: (a) the mobility of Si conduction band, using phonon-limited and phonon plus ionized impurity scattering calculations. The black-dashed line is experimental data. (b) Same for GaAs. (c) TE power factor for Si (simulation vs experiment) and (d) NbCoSn, experimental data (green) from [5].

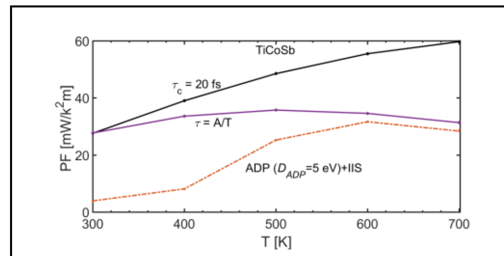

Figure 4: The PF of TiCoSb calculated using three different scattering rate considerations. a) Constant τ=20fs (chosen to match the experimental mobility at 300 K [4])-black line, (b) a τ~1/T as in the ADP case (purple line) that matches the PF of (a) at 300 K, (c) energy dependent τ including ADP + impurities (IIS). Evidently, different scattering physics considerations give different values and trends.

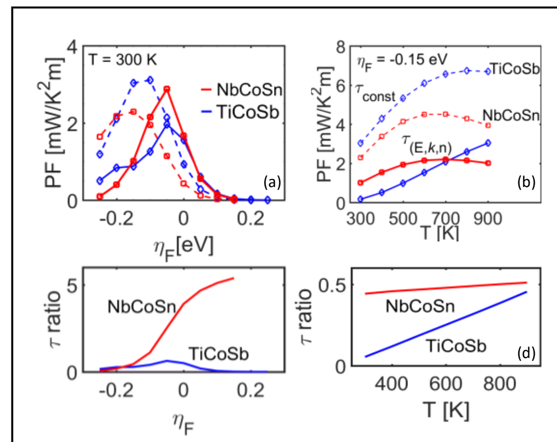

Figure 6: Comparison of constant τ (dashed lines) and τ(E) for the PF of Co-based half-Heuslers, (including ADP and ODP scattering-solid lines) versus (a) ηF, (b) T. (c, d) comparison of the constant τ needed in order to match τ(E) compared at each case. A constant τ leads to significant deviations among different materials, T, and carriers concentrations

Impact of Electron-Phonon Scattering on Optical and Electrical Properties of Perovskite Material

B. Galvani[1], A. Delamarre[2], D. Suchet[3], M. Bescond[4],
F. Michelini[1], M. Lannoo[1], J.-F. Guillemoles[3], N. Cavassilas[1,5]
[1]*AMU, CNRS, Université de Toulon, IM2NP - UMR 7334, Marseille, France*
[2]*C2N – UMR 9001, Palaiseau, France*
[3]*CNRS, IPVF – UMR 9006, 91120 Palaiseau, France*
[4]*LIMMS, CNRS-IIS, UMI 2820, University of Tokyo, Tokyo, Japan*
[5]*NextPV, LIA, CNRS-RCAST/U. Tokyo-U. Bordeaux, Tokyo, Japan*
benoit.galvani@im2np.fr

Perovskite materials are suitable for solar applications due to their excellent carrier transport properties [1,2]. However, behaviors controlling the carrier mobility, measured experimentally from 1 to 100 cm²/V.s [3,4], are not yet well understood. In this polar material it is generally assumed that interaction with polar optical phonon is important. However, rotations of the CH_3NH_3 matrix could also have an impact. From a formalism point of view, such rotations are very close to the polar phonon interaction, but with unknown parameters. In this work, we present a numerical study of electrical and optical properties modified by scattering. Using a non-equilibrium Green functions model [5] we obtain 196 cm²/V.s for the electron mobility. In order to fit the wide range of the experimental mobility we modify and assume four values of the coupling strength with the idea to mimic the CH_3NH_3 rotations. With this model we calculate the local density-of-states (DOS) in a perovskite-based device (Fig.1) which can be compared to the ballistic counterpart (Fig.2). Scattering tends to induce a broadening in the bandgap, that decrease exponentially in the latter. Fig. 3 and 4 respectively show the optical absorption and emission spectra for the four scattering couplings. Modifications with stronger scattering are both absorption and emission occurring at energies lower than the bandgap (1.55 eV). More important, we report Fig. 5 a decrease of the absorption/emission ratio inducing a reduction of the solar cell efficiency. We finally propose an analytical model of the DOS deep in the bandgap which is in good agreement with numerical results (Fig. 6).

[1] A.S. Chouhan et al., C.A.Physics, Vol 17, 10, p1335-1340 (2017).
[2] D.Webber et al., Appl. Phys. Lett. 111, 121905 (2017).
[3] Mei, Y et al., MRS Communications. 5. 1-5. 10.1557/mrc.2015.21 (2015).
[4] Dong Shi et al., Science 30, Vol. 347, Issue 6221 (2015).
[5] N.Cavassilas et al., Journal of Renewable and Sustainable Energy, 6, 011203 (2014).

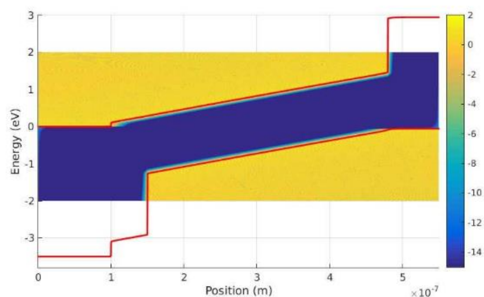

Fig.1: Log of local density of states as a function of energy and position in a perovskite-based solar cell, calculated without electron-phonon interaction.

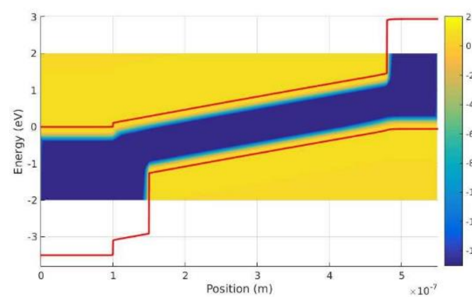

Fig.2: Log of local density of states as a function of energy and position in a perovskite-based solar cell, calculated with electron-phonon interaction (corresponding to a electron mobility = 86cm²/V.s)

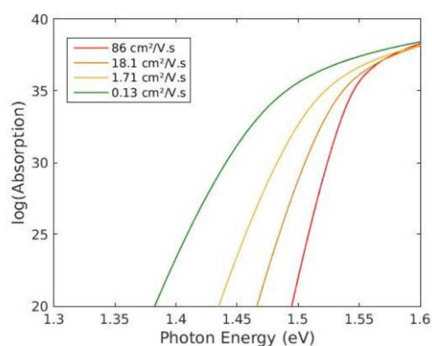

Fig.3: Log of absorption vs photon energy in the studied perovskite device, calculated for 4 different values of electron mobility (corresponding to 4 different values of electron-phonon scattering strength)

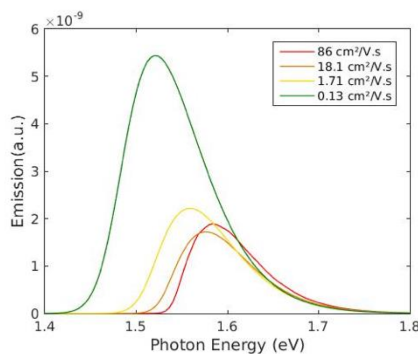

Fig.4 Emission vs photon energy in the studied perovskite device, calculated for 4 different values of electron mobility (corresponding to 4 different values of electron-phonon scattering strength)

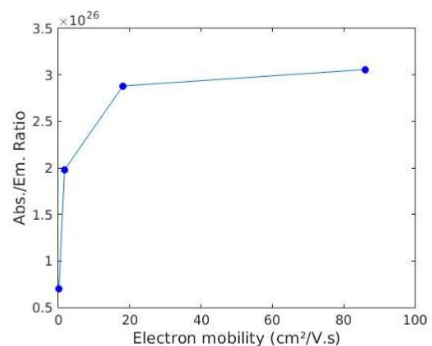

Fig.5: Absorption/emission ratio plotted as a function of electron mobility

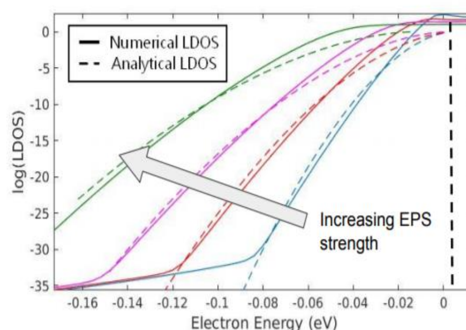

Fig.6: Log of local density of states close to the conduction band edge at the middle of the studied device. Plain lines correspond to self-consistent calculations. Dashed lines correspond to the analytical model.

A Gauge-Invariant Wigner Equation for General Electromagnetic Fields

M. Nedjalkov[1,2], J. Weinbub[3], M. Ballicchia[1],
S. Selberherr[1], I. Dimov[2], D. K. Ferry[4], K. Rupp[1]
[1]*Institute for Microelectronics, TU Wien, Austria*
[2]*IICT Bulgarian Academy of Sciences, Sofia, Bulgaria*
[3]*Christian Doppler Laboratory for High Performance TCAD,*
Institute for Microelectronics, TU Wien, Austria
[4]*School of Electrical Computer and Energy Engineering, Arizona State University, USA*
nedjalkov@iue.tuwien.ac.at

Wigner quantum mechanics is standardly formulated in near electrostatic conditions with a scalar potential ϕ gauge used to define the Wigner potential V_w. Theories, aiming to generalize this picture for the case of magnetic field **B** usually involve the choice of a particular gauge. The latter enters the Wigner function f_w via the canonical momentum **p**, obtained from the Weyl map of $\hat{\mathbf{p}} = -i\hbar\nabla$. In contrast, the kinetic momentum $\mathbf{P} = \mathbf{p} - e\mathbf{A}(\mathbf{r})$, where **A** is the vector potential, is a physical quantity and thus is gauge-invariant. Furthermore averages of generic physical quantities depend on the kinetic momentum and thus can be easily obtained from $f_w(\mathbf{P})$. This inspired some theories [1],[2], where a variable change is performed to obtain f_w in terms of **P**. Alternative theories involve the transform

$$f(\mathbf{P},\mathbf{x}) = \int \frac{d\mathbf{s}}{(2\pi\hbar)^3} e^{-\frac{i}{\hbar}\mathbf{s}\cdot\mathbf{P}} e^{-\frac{i}{\hbar}\frac{e}{2}\mathbf{s}\cdot\int_{-1}^{1} d\tau \mathbf{A}\left(\mathbf{x}+\frac{\mathbf{s}\tau}{2}\right)} \rho\left(\mathbf{x}+\frac{\mathbf{s}}{2}, \boldsymbol{x}-\frac{\mathbf{s}}{2}\right) \tag{1}$$

which generalizes the Weyl map to obtain a kinetic momentum quantum theory directly from the density operator [3],[4]. The transform, which can be obtained by using the Baker-Campbell-Hausdorff formula, has been introduced six decades ago [5] by Stratonovich using an intuitive approach involving the characteristic function of the momentum. The corresponding evolution equations for f_w derived in the framework of these theories depend on the electromagnetic fields (EM), but not on the potentials. However, these fields appear as pseudo-differential operators: The position dependence of **E** and **B** is replaced by an expression containing the $\nabla_{\mathbf{p}}$ operator. This gives rise to compact mathematical forms, but is a serious computational problem, as e.g the order of the equation with respect to the momentum derivatives varies with the position dependence of the EM fields, hampering any numerical approach. We derive an equation for general, inhomogeneous, and time-dependent EM conditions, which has an explicit mathematical structure with clearly defined differential and integral operations. The equation depends on the EM fields only, but in a nonlocal way: terms such as $\int_{-1}^{1} d\tau(\mathbf{sB})_F\ (\mathbf{P},\mathbf{x},\tau)$ where $(\mathbf{sB})_F$ is the Fourier transform $e^{-(i/\hbar)\mathbf{s}\cdot\mathbf{P}}$ of $\big(\mathbf{s}\times \mathbf{B}(\mathbf{x}+\mathbf{s}\tau/2)\big)$ (and similarly for **E**) act as integral operators on the f_w in the same way as V_w. For homogeneous magnetic fields the equation simplifies to a local action of **B**:

$$\left[\frac{\partial}{\partial t} + \frac{\mathbf{P}}{m}\cdot\frac{\partial}{\partial \mathbf{r}} + e\frac{\mathbf{P}}{m}\times\mathbf{B}\cdot\frac{\partial}{\partial \mathbf{P}}\right] f_w(\mathbf{r},\mathbf{P},t) = \int d\mathbf{P}'\, V_w(\mathbf{P}-\mathbf{P}',\mathbf{r}) f_w(\mathbf{r},\mathbf{P}',t) \tag{2}$$

Here, the potential V which defines V_w is determined by **E**. As a generic application we repeat the emblematic simulations of magnetic field governed tunneling through a single barrier [6]. The ViennaWD stochastic simulator based on the signed particle approach [7] has been modified to account for accelerating forces and applied for obtaining the simulation data.
In the experiment coherent electrons are injected from the bottom boundary towards the barrier marked by the blue lines, Figure 1.

Classical particle simulation results are conveniently used as a reference frame for the quantum effects, analyzed in the figure captions. The derived equation presents a computationally feasible task for the important case of homogeneous magnetic fields (**B** = *const*). The inhomogeneous terms imply presence of non-local effects.

Acknowledgment: The financial support by the Austrian Science Fund (FWF) through the projects P29406-N30 and P29119-N30, by the Bulgarian National Science Fund (NSF) project DN 12/5-2017, by the Austrian Federal Ministry of Science, Research and Economy, and by the National Foundation for Research, Technology and Development are gratefully acknowledged. The computational results have been obtained by using the Vienna Scientific Cluster (VSC).

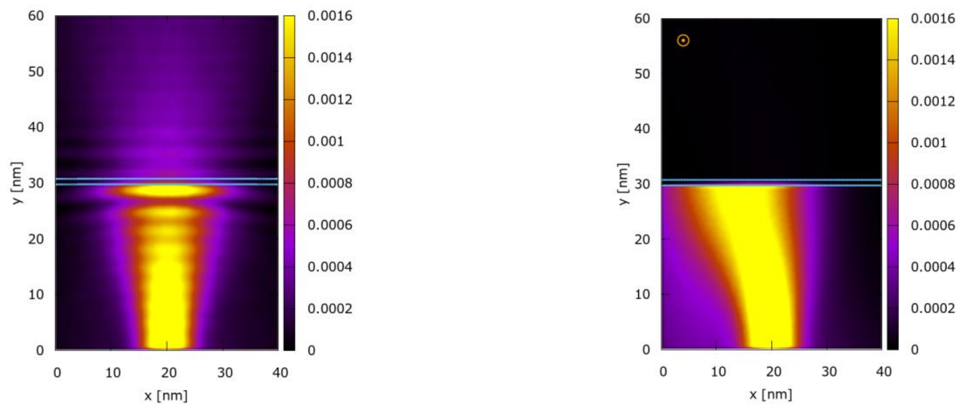

*Fig.1: Electron density [a.u] around a 0.2 eV barrier. The left picture shows the symmetry of the quantum density for **B**=0. Two important properties are demonstrated: (i) interference effects reveal the wave nature of the evolution, in particular the finite density after the barrier is due to tunneling; (ii) the non-locality of the potential, which affects the electron density far before the barrier. In contrast, on the right picture, classical electrons with energy less than 0.2 eV (the here presented case) are back scattered locally by the barrier. The magnetic field of **B** = 6T breaks the symmetry by bending the electron trajectory. In this case there is no wave-like transport and no tunneling; all particles are reflected back from the barrier.*

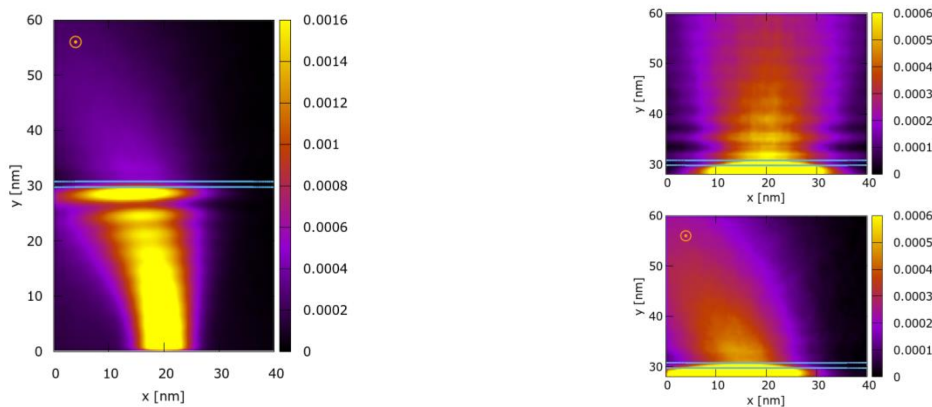

*Fig.2: The quantum density [a.u.] for **B**=6T (left) and the zoom of the density above the barrier with **B**=6T (right, bottom) and without magnetic field (right, top) show that even if the electric field action is still non-local the coherence of the transport is affected by the magnetic field.*

[1] R. Kubo, J. Phys. Soc. Jpn. **19**, 2127 (1964)
[2] I. B. Levinson, Sov. Phys. JETP **30**, 362 (1970)
[3] O. T. Serimaa, J.Javanien S. Varro, Phys. Rev. A **33**, 2913 (1986)
[4] H. Haug, A. P. Jauho, *Quantum Kinetics in Transport and Optics of Semiconductors* (Springer, 2018)
[5] R. Stratonovich, Dokl. Akad. Nauk SSSR **109**, 72 (1956)
[6] N.C. Kluksdahl, A.M. Kriman, D.K. Ferry, Springer Series in Solid State Sciences **87**, 335 (1989)
[7] P. Ellinghaus, Ph. D. Dissertation, Technische Universität Wien 2016.

Robust Magnetic Field Free Switching Scheme for Perpendicular Free Layer in Advanced Spin Orbit Torque Magnetoresistive Random Access Memory

R. Orio[1], A. Makarov[2], S. Selberherr[2], W. Gös[3],
J. Ender[1], S. Fiorentini[1], V. Sverdlov[1]
[1]*Christian Doppler Laboratory for Nonvolatile Magnetoresistive Memory and Logic at the*
[2]*Institute for Microelectronics, TU Wien, Austria*
[3]*Silvaco Europe Ltd., Cambridge, United Kingdom*
{orio|sverdlov}@iue.tuwien.ac.at

The continuous increase in performance and speed of modern integrated circuits is steadily supported by miniaturization of the complementary metal-oxide semiconductor (CMOS) devices. However, a rapid increase of dynamic and stand-by power due to transistor leakages becomes a pressing issue. A promising way to overcome this issue is to introduce non-volatility in circuits. The development of an electrically addressable non-volatile memory combining high speed and high endurance is essential to achieve this goal. To reduce the energy consumption in particularly CPUs, one can replace the SRAM in hierarchical multi-level processor memory structures with a non-volatile memory [1]. Spin-orbit torque magnetoresistive random access memory (SOT-MRAM) combines non-volatility, high speed, and high endurance and is thus perfectly suited for applications in caches. However, its development is still hindered by the need of an external magnetic field for deterministic switching of perpendicularly magnetized layers [2].

We demonstrate that the fast (sub-500ps), deterministic, and magnetic field free switching of a perpendicularly magnetized rectangular recording layer achieved by employing two orthogonal short (100ps) current pulses of duration T_1 and T_2 running through the two heavy metal lines NM1 and NM2 of thickness l and widths w_1 and w_2 in a cross-bar array shown in Fig.1 is extremely robust with respect to the pulse synchronization failure. It yields a large confidence window for the time delay τ (positive or negative) between the two pulses.

Similar to the set-up suggested earlier [3], the NM2 line has an incomplete overlap with the free layer (Fig.1). The magnetization dynamics is described by the Landau-Lifshitz-Gilbert equation supplemented with the SOTs generated by the currents $I_{1,2}$ and acting on the free magnetic layer of the thickness $d = 2$nm:

$$\frac{\partial \mathbf{m}}{\partial t} = -\gamma \mathbf{m} \times \mathbf{H}_{\mathrm{eff}} + \alpha \mathbf{m} \times \frac{\partial \mathbf{m}}{\partial t} + \gamma \frac{\hbar}{2e} \frac{\Theta_{SH} I_1}{M_S d w_1 l} [\mathbf{m} \times (\mathbf{m} \times \mathbf{y})] \Theta(t) \Theta(T_1 - t)$$
$$- \gamma \frac{\hbar}{2e} \frac{\Theta_{SH} I_2}{M_S d w_2 t} [\mathbf{m} \times (\mathbf{m} \times \mathbf{x})] \Theta(t - T_1 - \tau) \Theta(T_2 + T_1 + \tau - t), \quad (1)$$

where $\mathbf{m}$ is the position-dependent magnetization $\mathbf{M}$ normalized by the saturation magnetization M_S, γ is the gyromagnetic ratio, α is the Gilbert damping, e is the elementary charge, ħ is the reduced Plank constant, and Θ_{SH} is an effective Hall angle. $\mathbf{H}_{\mathrm{eff}}$ includes the exchange, anisotropy (see Table 1), demagnetization, and random thermal field at 300K.

The duration of the “Write pulse 1” of 100μA is fixed to $T_1 = 100$ps. T_2, τ, and I_2 of “Write pulse 2” vary. When NM2 has a full overlap w_2 of 52.5nm with the free layer, the switching by the two consecutive 100μA pulses is robust *only*, if the second pulse is either short (50-70ps) or long (>1ns) (Fig.2). The switching becomes fully deterministic for a broad range of the “Write pulse 2” duration T_2 if either the current through NM2 is increased to I_2=200μA (Fig.3) or the overlap of NM2 with the free layer is reduced to ~1/3 (Fig.1), for the same I_2=100μA current (Fig.4). The “Write pulse 1” puts the magnetization of the free layer in-plane perpendicular to the “Write pulse 1” direction (Fig.2, Fig.3). Depending on the “Write pulse 2” polarity, the corresponding SOT slightly tilts the magnetization in-plane towards the left or right end of the rectangle. Then the magnetization experiences the shape anisotropy field, which plays the role of the external field to complete the switching 100% reliably. Fig.5 shows that the switching is extremely robust with respect to the delay τ, which proves the scheme suitable for practical implementation.

[1] O. Golonzka *et al*. Proceedings of the 2018 IEDM, 36.2.1 (2018).

[2] S. Fukami, T. Anekawa, C. Zhan, and H. Ohno, Nature Nanotechnology **11**, 621 (2016).

[3] V. Sverdlov, A. Makarov, and S. Selberherr, J.Systemics, Cybernetics and Informatics **16**, 55 (2018).

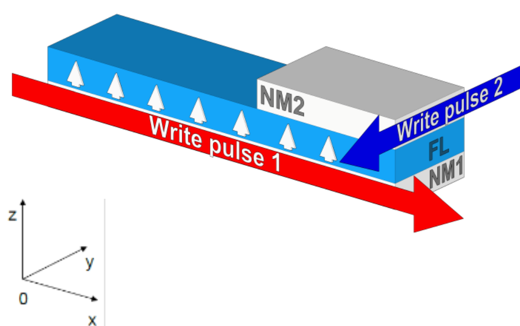

Fig.1 Schematic structure of the two-pulse switching scheme applied to the perpendicularly polarized magnetic free layer (FL).

Name	Value
Saturation magnetization M_S	4×10^5 A/m
Exchange constant A	2×10^{-11} J/m
Perpendicular anisotropy K	2×10^5 J/m^3
Gilbert damping α	0.05
Spin Hall angle Θ_{SH}	0.3
Free layer dimensions	52.5×12.5×2nm^3
NM1: w_1×l	12.5nm×3nm
NM2: w_2×l	5-52.5nm×3nm

Table 1 Parameter values used in the simulations. They correspond to CoFeB FL on tungsten (NM1 and NM2).

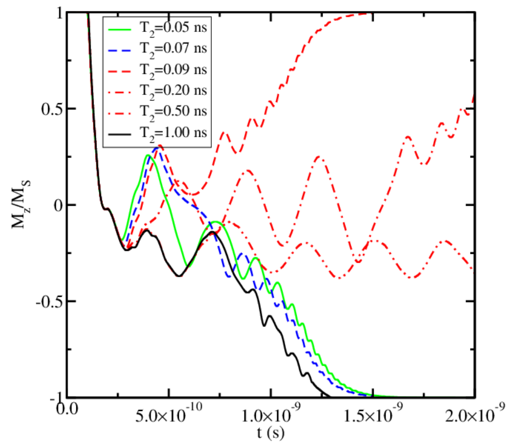

Fig.2 $m_z(t)$ for NM2 fully overlapping with FL averaged for 20 realizations. $I_1=I_2=100\mu A$. For 70ps<T_2<1ns the switching fails (shown in red).

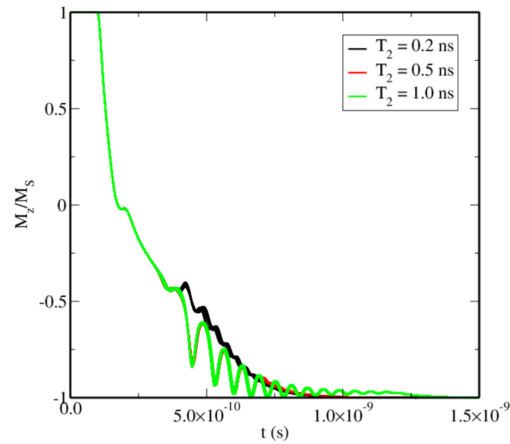

Fig.3 20 realizations of magnetization switching for NM2 fully overlapping with FL (w_2=52.5nm) similarly to Fig.1, but with I_2 increased to 200µA.

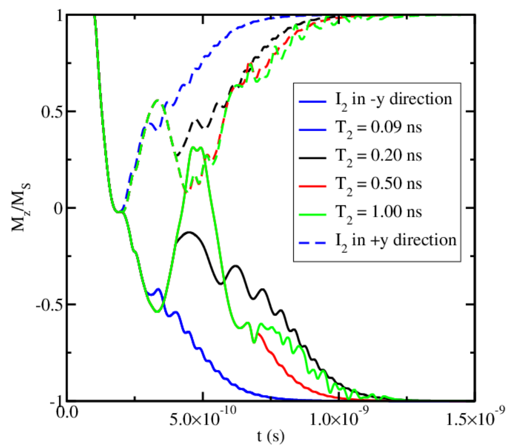

Fig.4 Average of 20 realizations of $m_z(t)$, with $m_z(0)=1$ for NM2=12.5nm, $I_1= I_2=100\mu A$, several T_2, and τ=0. I_2 along –y reliably switches m_z while I_2 of the opposite polarity brings it to the initial state.

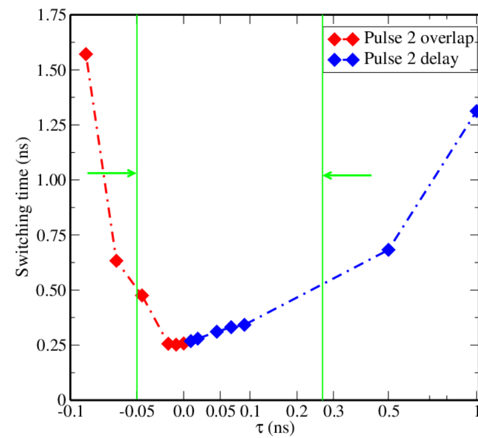

Fig.5 Robust switching at pulse delays between -90ps<τ<1ns (defined in (1)), for $w_1=w_2$=12.5nm and equal Write pulses 1,2 ($I_1=I_2=100\mu A$, $T_1=T_2$=100ps). Sub 0.5ns switching is obtained at -50ps<τ<250ps.

Acknowledgments. The financial support by the Austrian Federal Ministry for Digital and Economic Affairs and the National Foundation for Research, Technology and Development is gratefully acknowledged.

A Mechanism of Electroforming in SiO_2 Based ReRAM Devices Facilitated by Electron Injection

J. Cottom[1], M. Munde[1,2], A. Shluger[1]

[1]*Department of Physics and Astronomy, UCL, Gower St., London, WC1E 6BT*

[2]*Materials Science Center and Faculty of Physics (WZMW), Philipps University Marburg, Hans-Meerwein-Straße, 6, 35043 Marburg, Germany*

a.shluger@ucl.ac.uk

The TiN/SiO_2/TiN stack (Fig.1) described in [1] is used as a model system to study the mechanisms of electroforming is SiOx based resistive random access memory devices (ReRAM) using density functional theory (DFT) and atomistic modelling. The bulk system (far from the interface) is approximated as stoichiometric amorphous (a)-SiO_2 whereas the SiO_2/TiN interface is considered explicitly and constructed using DFT simulations (Fig. 3,4). It has previously been demonstrated that electron injection can facilitate the creation of Frenkel defects in a-SiO_2 at structural precursor sites composed of wide O-Si-O bond angles [2]. These sites act as deep electron traps (Fig. 2) and can accommodate up to two extra electrons. Trapping of two electrons at intrinsic sites results in weakening of Si-O bonds and emergence of efficient bond breaking pathways for producing neutral O vacancies and interstitial O_i^{2-} ions with low activation barriers [2]. Inside the a-SiO_2 film, a low barrier for migration (Fig. 5) of the O^{2-} ion ($\approx$ 0.2 eV) is further reduced by bias application. These barriers are further reduced at the TiN/SiO_2 interface facilitating diffusion of O_i^{2-} from the bulk towards the interface coupled to a lowering of the incorporation energies for the O_i^{2-} as a function of the distance from the interface. The charge transition level for the O_i (0/--) moves towards that of the TiN Fermi level as the O_i approaches the interface. This results in a transfer of the electrons to the TiN electrode at the interface. Once the interstitials arrive at the interface, there is an initial ‘oxidation’ of the interface *via* the formation of a TiO layer (Fig. 6), preferably at Ti-interface sites, in accordance with the transition electron microscopy and electron energy loss spectroscopy observations [3]. The Ti-O bonds (Fig. 6) are strong and show high barriers (> 1.2 eV) for dissociation and migration along the surface. Once the interface Ti-sites are occupied, O_i are incorporated at or in the layers directly below the interface or diffuse inside TiN via grain boundaries and desorb into gas [1].

[1] A. Mehonic, et al., Adv. Materials, **28**(34), 7486-7493 (2016)

[2] D. Z. Gao, et al., Nanotechnology, **27**(50), 505207 (2017)

[3] M. S. Munde, et al., Scientific Reports, **7**, 9274 (2017)

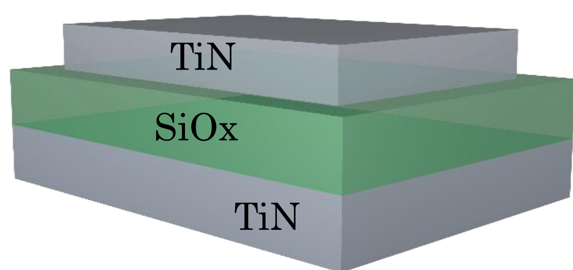

Fig.1: Symmetric MIM design TiN/SiOx/TiN structure used for unipolar resistive switching [1].

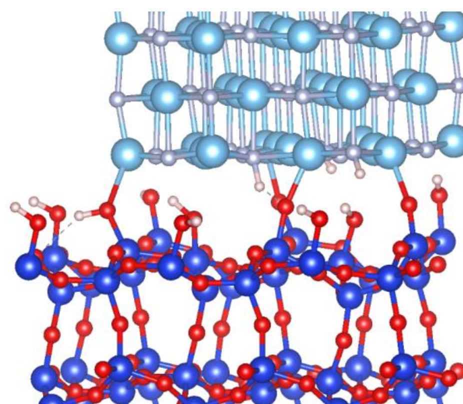

Fig.4: The model of SiO2/TiN stack where the SiO2 surface is partially hydroxylated, forming silanols (H is shown in white, Si-blue and O-red).

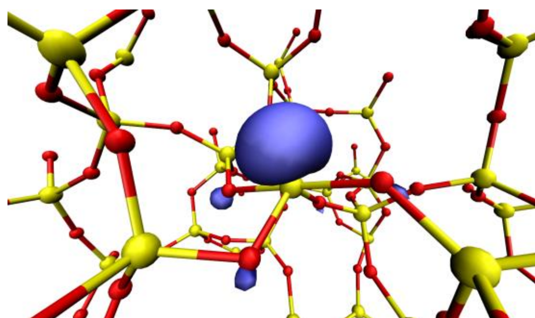

Fig.2: The electron density distribution (blue) of two electrons trapped at a Si atom (yellow) in amorphous SiO2 structure. The O-Si-O angle after trapping is 176°.

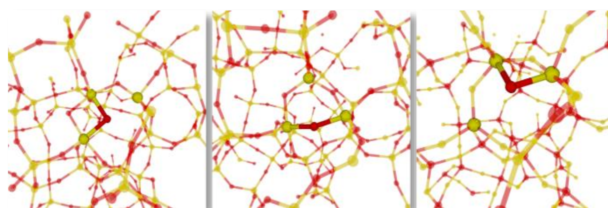

Fig.5 Sequence of atomic configurations corresponding to the interstitial O^{2-} diffusion in a-SiO_2. The middle configuration corresponds to the barrier point. The average barrier for diffusion is about 0.2 eV.

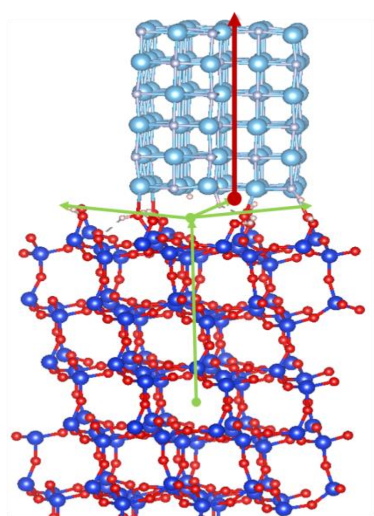

Fig.3: The model of SiO_2/TiN stack. SiO2 is represented by the α-cristobalite crystalline structure. Red arrows indicate the directions of O interstitial ion diffusion considered in simulations.

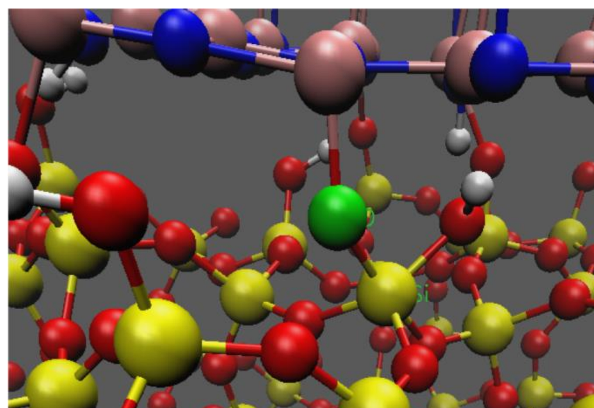

Fig.6: Close-up of the interface between a-SiO_2 and TiN showing the formation of Ti-O-Si bond .

Hopping in a Multiple Ferromagnetic Terminal Configuration

V. Sverdlov[1], S. Selberherr[2]
[1]*Christian Doppler Laboratory for Nonvolatile Magnetoresistive Memory and Logic at the*
[2]*Institute for Microelectronics, TU Wien, Austria*
{sverdlov|selberherr}@iue.tuwien.ac.at

The Coulomb repulsion results in strong correlations between the contacts at tunneling transport through a trap or a small quantum dot. If the dot Fermi energy is below the Fermi energies in the source and the drain and if the Coulomb charging energy to add an electron at the dot is larger than the transport window, the regime of the Coulomb blockade is realized. In a three-terminal transistor-like configuration the potential and the energy of the dot can be modified by coupling it capacitively to the gate electrode. Then the current can flow, when the dot energy level with one extra electron is brought within the transport window, and a single-electron transistor is realized [1]. The transport blockade can also be due to another intrinsic electron property, the electron spin. The Pauli, or spin, blockade is due to the Pauli exclusion principle forbidding two electrons with the same spin projection to occupy the same quantum state. Spin correlations induced by the Pauli blockade result in a large magnetoresistance between the normal and the ferromagnetic terminals [2]. The value of non-zero spin at the trap is determined by the polarization of the drain electrode relative to the magnetic field. In the case when there are several ferromagnetic terminals e1, e2, e3 shown in Fig.1 the spin correlations and thus the currents through each junction are determined by the generalized equations (1) and (2).

$$\frac{d}{dt}n = \Gamma_S(1-n) - \Gamma_D n - \Gamma_D \mathbf{p_D s} \ , \Gamma_{S(D)} = \sum_i \Gamma_{S(D)i} \quad (1)$$

$$\frac{d}{dt}\mathbf{s} = \Gamma_S(1-n)\mathbf{p_S} - \Gamma_D \mathbf{s} - \mathbf{p_D}\Gamma_D n + [\mathbf{s} \times \boldsymbol{\omega}_L] \ , \mathbf{p}_{S(D)} = \frac{1}{\Gamma_{S(D)}}\sum_i \mathbf{p}_{S(D)i}\Gamma_{S(D)i} \quad (2)$$

Table 1 outlines the derivation of the equations starting with the equation for full density matrix including electrodes [3], and (1) and (2) are obtained by tracing irrelevant variables out [3]. For simplicity we assume all absolute values of electrode polarizations $|\mathbf{p}_i|=p$ and transition rates $|\Gamma_{S(D)i}| = \Gamma$ equal. The direction of $\mathbf{p}_1$ is fixed (Fig.1), $\mathbf{p}_2$ can be parallel or anti-parallel to $\mathbf{p}_1$, $\mathbf{p}_3$ forms an angle Θ with $\mathbf{p}_1$. The junction currents are positive if flowing from the trap to the corresponding electrode, so the condition $I_1 + I_2 + I_3 = 0$ is always satisfied. First, we consider the case, when the current flows from the electrodes e1 and e3 into e2. If $\mathbf{p}_1=\mathbf{p}_2$, a strong current I_2 modulation is observed with Θ (Fig.2). If $\Theta=0$, $\mathbf{p}_3=\mathbf{p}_1=\mathbf{p}_2$, only spins with one projection are injected and absorbed, and the current is maximal. For $\mathbf{p}_3=-\mathbf{p}_1=-\mathbf{p}_2$ ($\Theta=\pi$) the current is minimal due to the spin blockade because of a non-zero spin at the trap. As the spin value is determined by $\mathbf{p}_2$, the minimum current value depends on p. This also explains the current behavior, when the orientation of $\mathbf{p}_2$ is altered to $\mathbf{p}_2 = -\mathbf{p}_1$ shown in Fig.3. Now the current is minimal at $\mathbf{p}_3=\mathbf{p}_1=-\mathbf{p}_2$. This is due to the spin injection orientation from e1 and e3 on the trap anti-parallel to $\mathbf{p}_2$. Due to the spin anti-parallel to the magnetization of e2, the electron cannot escape to e2 and dwells long at the trap.

As another electron cannot enter the occupied trap, the current is long blocked, which results in minimal average current (Fig.3). Now we consider the situation, when the current flows from e1 into e2 and e3, $\mathbf{p}_2$ is anti-parallel to $\mathbf{p}_1$: $\mathbf{p}_2 = -\mathbf{p}_1$. Fig.4 demonstrates that at Θ=0 ($\mathbf{p}_1 = \mathbf{p}_3$) the current I_3 is maximal, while I_2 is the smallest. This is expected as the spins injected from e1 go with no problem into e3, the magnetization of which is parallel to e1, while they go onto e2 rarely because of their anti-parallel orientation. If now one thinks of a current switch based on the spin blockade, it is desirable to have a configuration of fixed magnetization shown as in Fig.1. Then the current I_2 is small for polarization p close to one (Fig.3, Fig.4). The current I_3 is large when it flows into e3 in Fig.4, while it is suppressed in Fig.3, where it flows away from e3. Such a behavior is achieved, when the rate Γ_3 changes sign, for example, when it depends on voltages on e2 and e3. S*ingle spin* switch-like characteristics shown in Fig.5 are then realized.

[1] S. Bakhvalov *et al.*, Sov.Phys.JETP 68, 581 (1989).

[2] N.J. Harmon and M. E. Flatte, Phys.Rev.B 98, 035412 (2018).

[3] R. Haberkorn, Molecular Phys. 32, 1491 (1976).

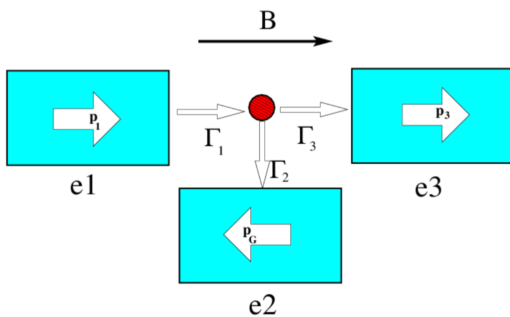

Fig.1 A three ferromagnetic terminal configuration. Electron transport is due to spin-dependent hopping.

$$i\frac{\partial}{\partial t}\mathfrak{R} = \frac{1}{\hbar}[\boldsymbol{\mathcal{H}},\mathfrak{R}] - 2\sum_i \Gamma_{Di}\{\wp_{\boldsymbol{Di}},\mathfrak{R}\} + \sum_i \Gamma_{Si}\wp_{Si}(1-n),$$

$\mathfrak{R}$*-full density matrix including terminals [3];*

$\boldsymbol{\mathcal{H}}$*-impurity Hamiltonian, n-trap occupation;*

$\wp_{D,Si}$*-projection on i-th drain-source magnetization*

$[\boldsymbol{\mathcal{H}},\mathfrak{R}] = \boldsymbol{\mathcal{H}}\mathfrak{R} - \mathfrak{R}\ \boldsymbol{\mathcal{H}},\ \{\wp,\mathfrak{R}\} = \wp\mathfrak{R} + \mathfrak{R}\ \wp,$

Tr –partial trace over terminals' degrees

ρ *=Tr* $\mathfrak{R}$ *describes only the trap (including spin):*

$$i\frac{\partial}{\partial t}\rho = \frac{1}{2\hbar}[\boldsymbol{B\sigma},\rho] - \sum_i \Gamma_{Di}\left\{\frac{I}{2} + \boldsymbol{p}_{Di}\boldsymbol{\sigma},\rho\right\} + \sum_i \Gamma_{Si}\left(\frac{I}{2} + \boldsymbol{p}_{Si}\boldsymbol{\sigma}\right)\boldsymbol{\sigma}(1-n)$$

Table 1 Sketch of a derivation of the master equation for the density matrix on the trap generalized to multiple terminals.

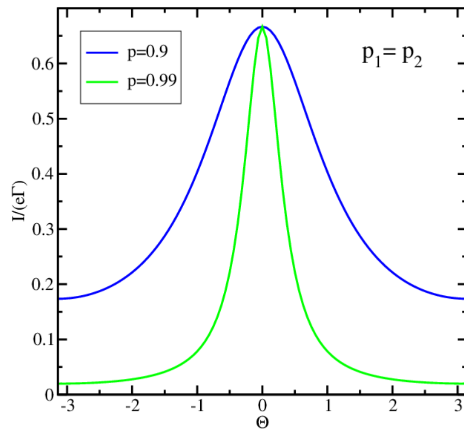

Fig.2 Current I_2, as a function of Θ, for $\boldsymbol{p_1}$=$\boldsymbol{p_2}$, when Γ_3 allows transport from e3 to the trap.

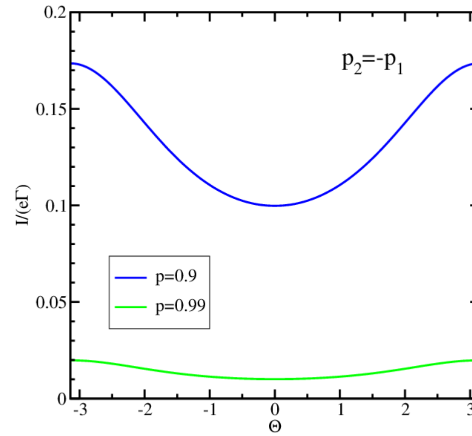

Fig.3 Current I_2 for $\boldsymbol{p_1}$=-$\boldsymbol{p_2}$, for other conditions similar to Fig.2. I_2 is reduced for $\boldsymbol{p_3}$=$\boldsymbol{p_1}$=-$\boldsymbol{p_2}$.

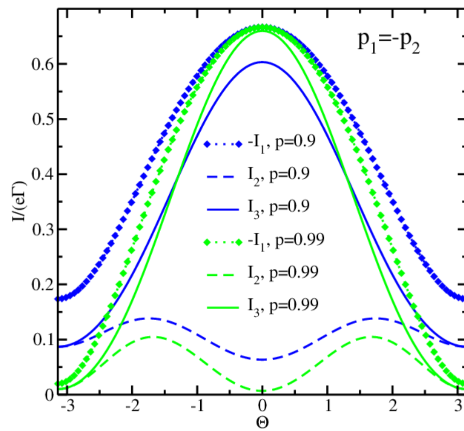

Fig.4 Current I, when Γ_3 allows transport from the trap to e3. I_3 is the highest and I_2 is the smallest, when $\boldsymbol{p_3}$=$\boldsymbol{p_1}$=-$\boldsymbol{p_2}$.

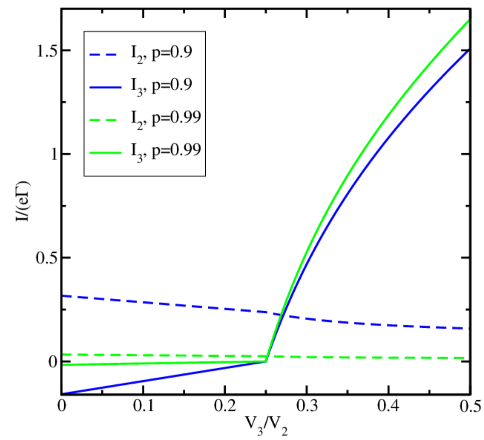

Fig.5 Switch-like characteristics are realized, if Γ_3 yields transport from e3 to the trap for V_3 <0.5 V_2 and from the trap to e3 for V_3 <0.5 V_2.

Acknowledgments. The financial support by the Austrian Federal Ministry for Digital and Economic Affairs and the National Foundation for Research, Technology and Development is gratefully acknowledged.

First Principles Insights into Spintronic and Spin-Orbitronic Phenomena in Magnetic Nanostructures

M. Chshiev
Univ. Grenoble Alpes, CEA, CNRS, INAC-Spintec, Grenoble, France
mair.chshiev@cea.fr

Ab initio insights are provided into spin-orbit coupling based phenomena such as perpendicular magnetic anisotropy (PMA) [1-6] and Dzyaloshinskii-Moriya interaction (DMI) [7-10] at interfaces comprising transition metals, insulators, or graphene. First, the nature of PMA at Fe|MgO interfaces is unveiled by evaluating orbital and layer resolved contributions to PMA in Fe/MgO interfaces and MTJs with different interfacial conditions [1-3] (Fig. 1). Mechanisms of the optimization of effective anisotropy as well as of its electric field control are discussed [4-6]. Next, the main features and microscopic mechanisms of DMI behavior are elucidated in Co/Pt and other Co/heavy metal bilayers [7,8] (Figs. 2-4). Furthermore, several approaches for DMI enhancement and manipulation will be presented including, in particular, physical mechanisms of DMI behavior in Pt/Co/MgO structures [8,9] allowing observation of room temperature skyrmions [9]. The behavior of PMA and DMI will then be addressed for nanostructures comprising Co/graphene interfaces [10,11] (Figs. 5,6) which may be of strong interest for graphene spintronics [12,13].

[1] B. Dieny and M. Chshiev, Rev. Mod. Phys. **89**, 025008 (2017)
[2] H. X. Yang. M. Chshiev, A. Manchon et al, Phys. Rev. B **84**, 054401 (2011)
[3] A. Hallal, H. X. Yang, B. Dieny, and M. Chshiev, Phys. Rev. B **88**, 184423 (2013)
[4] A. Hallal, B. Dieny, and M. Chshiev, Phys. Rev. B **90**, 064422 (2014)
[5] F. Ibrahim, H. X. Yang, A. Hallal, B. Dieny, and M. Chshiev, Phys. Rev. B **93**, 014429 (2016)
[6] F. Ibrahim, A. Hallal, B. Dieny, and M. Chshiev, Phys. Rev. B **98**, 214441 (2018)
[7] H. X. Yang, A. Thiaville, S. Rohart, A. Fert, and M. Chshiev, Phys. Rev. Lett. **115**, 267210 (2015)
[8] H. X. Yang, O. Boulle, V. Cros, A. Fert & M. Chshiev, Scientific Reports **8**, 12356 (2018)
[9] O. Boulle et al, Nature Nanotechnology **11**, 449 (2016)
[10] H. X. Yang, A. D. Vu, A. Hallal, N. Rougemaille, J. Coraux, G. Chen, A. K. Schmid, and M. Chshiev Nano Lett. **16**, 145 (2015)
[11] H. X. Yang, G. Chen, A. A. C. Cotta, A. T. N'Diaye, S. A. Nikolaev, E. A. Soares, W. A. A. Macedo, K. Liu, A. K. Schmid, A. Fert & M. Chshiev, Nature Materials **17**, 605 (2018)
[12] S. Roche et al, 2D Materials **2**, 030202 (2015)
[13] H. X. Yang, A. Hallal, X. Waintal, S. Roche and M. Chshiev, Phys. Rev. Lett. **110**, 046603 (2013)

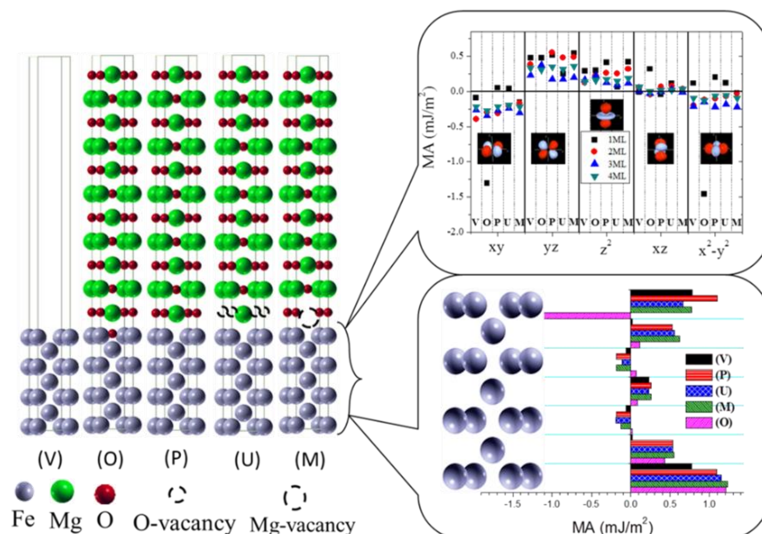

Fig.1: Layer- and orbital-resolved anisotropy contributions for crystalline structures: (V) Fe/vacuum, (O) overoxidized Fe7/MgO, (P) pure Fe7/MgO11, (U) underoxidized Fe7/MgO, and (M) Mg vacancy in Fe7/MgO11. From Refs. [1,3].

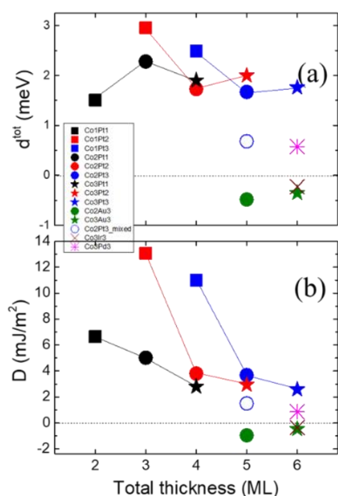

Fig.2: (a) Microscopic (d^{tot}) and (b) Micromagnetic (D) DMI coefficients for the Co/Pt, Co/Ir, Co/Au, Co/Pd bilayers as a function of the total number of atomic layers.

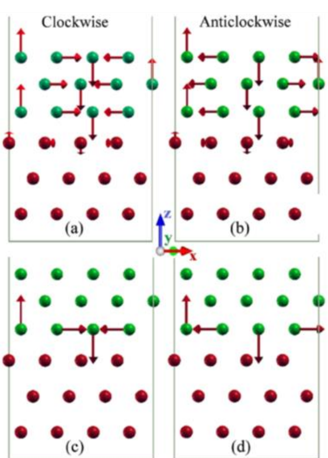

Fig.3: Examples of (a),(c) clockwise (CW) and (b),(d) anticlockwise (ACW) spin configurations to calculate the DMI hcp(0001)Co/fcc(111)Pt bilayers. Green and red correspond to Co and Pt.

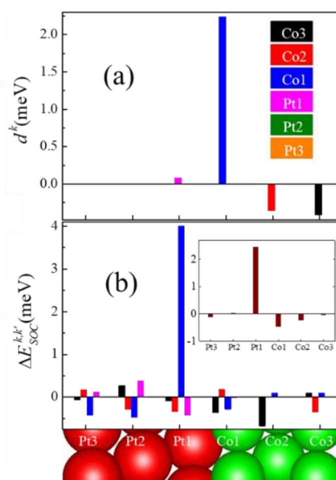

Fig.4: (a) Layer resolved DMI coefficient d^k vs layer k and (b) the corresponding localization of the associated SOC energy source in the atomic sites of all layers k'.From Ref. [7]

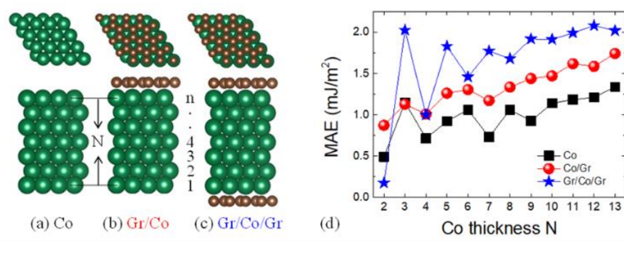

Fig.5: Top and side view of (a) bare Co slab, (b) Co on graphene, and (c) Gr/Co/Gr, respectively. (d) Magnetocrystalline anisotropy energy as a function of Co thickness N (monolayers).

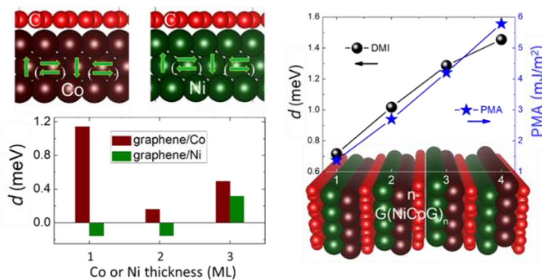

Fig.6: Top- and side-view of graphene on a hcp Co(0001) and on a fcc Ni(111) surfaces. DMI coefficient as a function of Co(Ni) thickness. DMI and PMA for multilayers of graphene/[Co/Ni/graphene]$_n$ as a function n.

Voltage Sensor of Sodium Channels: Natural Nanotechnology

B. Eisenberg[1,2]
[1]*Department of Applied Mathematics, Illinois Institute of Technology, Chicago IL 60616*
[2]*Department of Physiology and Biophysics, Rush University, Chicago IL 60612*
Bob.Eisenberg@gmail.com

Voltage signals in biology are binary 'action potentials' that propagate meters in nerve fibers $\text{diameter} = 10^{-6}\text{m}$ and coordinate contraction in skeletal muscle and the heart. These signals are conducted by ions, not electrons. Ions are massive so movement is dominated by friction. Ionic signals require continual regeneration to travel meters, much as electron signals require regeneration to travel $> 10^6$ m through oceans in submarine cables. Regeneration in nerve fibers is provided by ion channel proteins, particularly sodium channels, that convert the gradient of chemical potential of sodium into electric current. Sodium is much more concentrated outside than inside cells, 0.14 vs. ~ 0.05 Molar. Sodium channels are proteins with a hole down their middle embedded in a thin $2 \times 10^{-9}\text{m}$ lipid membrane that is nearly an ideal dielectric. Sodium channels are closed at rest but respond to small positive going signals by opening, allowing sodium ions to carry current across the otherwise insulating membrane. The response of the sodium channel to voltage is a crucial determinant of the speed of signaling in nerves, and of the regularity of the heart beat. Evolution has created an atomic machine called the voltage sensor to open sodium channels as voltage goes positive. Every atom's location is known in crystals of the channel protein. Channel structures are a triumph of anatomical science but structures do not contain chemical potentials to energize function, nor do they conduct currents or action potentials. A model and a theory are needed for that.

We [1] constructed an electromechanical model showing how the voltage sensor responds to potential as positively charged atoms (of the arginine side chains of the protein) are pulled through a dielectric plug. Arginine movement creates a voltage and time dependent displacement current in a nonlinear capacitor. That displacement current flows into ionic solutions outside the nerve and can be collected with great fidelity by amplifiers in a voltage clamp apparatus. The resulting 'gating currents' have been studied in hundreds of papers [2].

Few atomic scale machines, or changes in shape of proteins, are known in such experimental detail, although conformation changes control a large fraction of biological processes. Our one dimensional model includes essential structural details and accounts for many, but not all of the features of gating currents observed in experiments.

[1] T.-L. Horng, R.S. Eisenberg, C. Liu, and F. Bezanilla, Biophysical Journal, **116**, 270 (2019)

[2] F. Bezanilla, and E. Stefani Methods in Enzymology, **293**, 331(1998); F. Bezanilla, Nat Rev Mol Cell Biol **9** 323 (2008); F. Bezanilla and E. Perozo Adv. Protein Chem., **63,** 211 (2003)

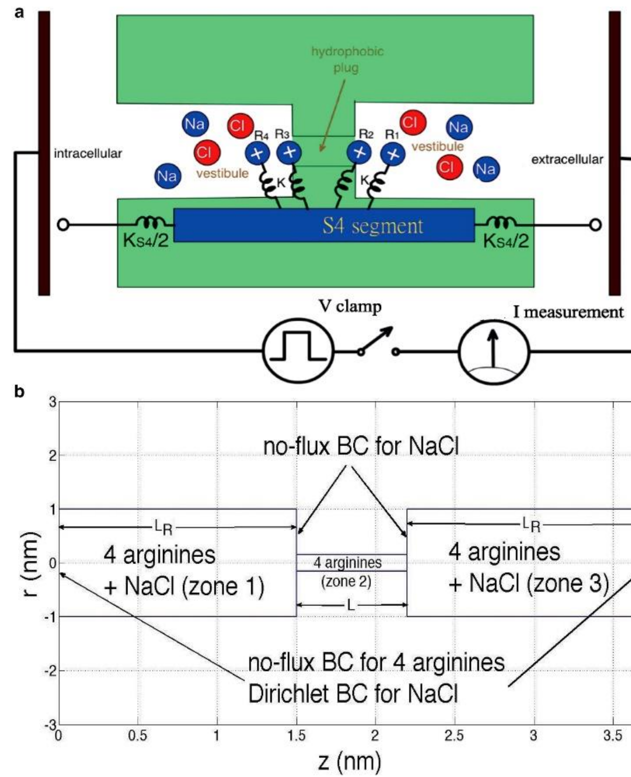

Fig. 1 Setup of Voltage Sensor and Gating Current Estimation from ref. [1]

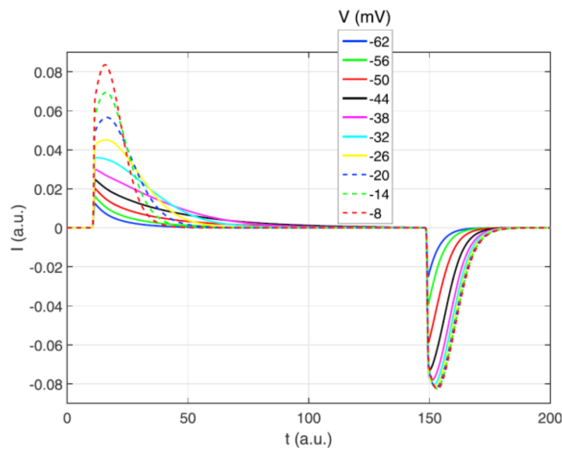

Fig. 2 Gating current response to rectangular voltage V, from ref. [1]

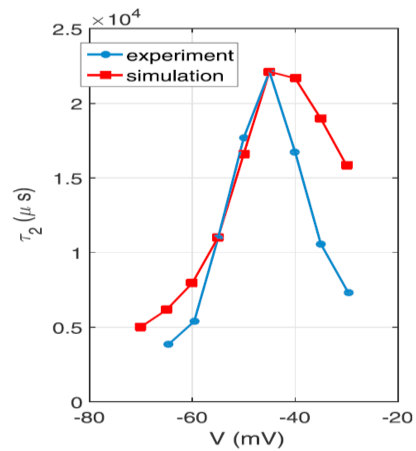

Fig.3: Experiment vs. Simulation. OFF Time constant τ_2 vs. Voltage V, from ref. [1]

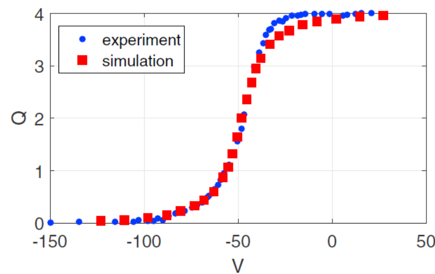

Fig. 4. Charge Q vs. Voltage V, from ref. [1]

Using nanoHUB.org in Research and Education – A Hands-on Tutorial

G. Klimeck, A. Strachan, T. Faltens,
B. Hallberg, L. K. Zentner, M. G. Zentner, M. Hunt
Network for Computational Nanotechnology, Purdue University, West Lafayette, IN 47906
gekco@purdue.edu

If you had access to interactive modeling and simulation tools that run in any browser, could you introduce interactive learning into your classes? If you had easy access tools, which need no installation, could you use them to help guide your experiments? If you did not have to worry about compute cycles, would you benchmark your own tools against other state-of-the-art approaches? If you had your own tools and could easily share them with the community, would you do it? This tutorial will provide an overview of these processes and their impact as they are supported on nanoHUB.org today.

Recently we have begun to deploy Jupyter notebooks within nanoHUB. nanoHUB provides its users with a secure Jupyter installation with a large number of installed mathematical and graphical packages. Users can develop their own scripts in python or octave and deploy their own codes. More complex codes can also be installed in nanoHUB and called as a service. All the Rappture-based tools in nanoHUB can be called as a service in the Jupyter notebooks as well.

Annually, nanoHUB provides a library of 5,500+ learning resources to over 1.4 million users worldwide. Its 500+ simulation tools, free from the limitations of running software locally, are used in the cloud by over 16,000 annually. Its impact is demonstrated by 2,180+ citations to nanoHUB in the scientific literature with over 30,900 secondary citations, yielding an h-index of 82 and by a median time from publication of a research simulation program to classroom use of less than 6 months [1]. Cumulatively, over 35,600 students in over 1,500 formal classes in over 185 institutions have used 210 nanoHUB simulation tools. *The **Web of Science and Google Scholar** now both **list nanoHUB simulation tools** as proper publications giving credit to the tool authors.*

nanoHUB.org is a virtual nanotechnology user facility funded by the National Science Foundation and supports the National Nanotechnology Initiative with a highly successful cyber-infrastructure. nanoHUB.org has been supported by the U.S. National Science Foundation since 2002 to serve the nanotechnology community.

[1] Krishna Madhavan, Michael Zentner, Gerhard Klimeck, "Learning and research in the cloud", *Nature Nanotechnology* 8, 786–789 (2013); doi:10.1038/nnano.2013.231

Fig.1: (a) annual nanoHUB user map superposed on NASA's world at night. Red circles designate users viewing lectures, tutorials, or homework assignments. Yellow dots are users of simulation. Green dots indicate authors of over 2,180 scientific publications citing nanoHUB. Dot size corresponds to the number of users, and lines show author-to-author connections proving intense research collaboration networks. (b) U.S. enlarged. (c) a collage of typical nanoHUB interactive tool sessions and 3D-rendered interactively explorable results (quantum dots, carbon nanotubes, nanowires).

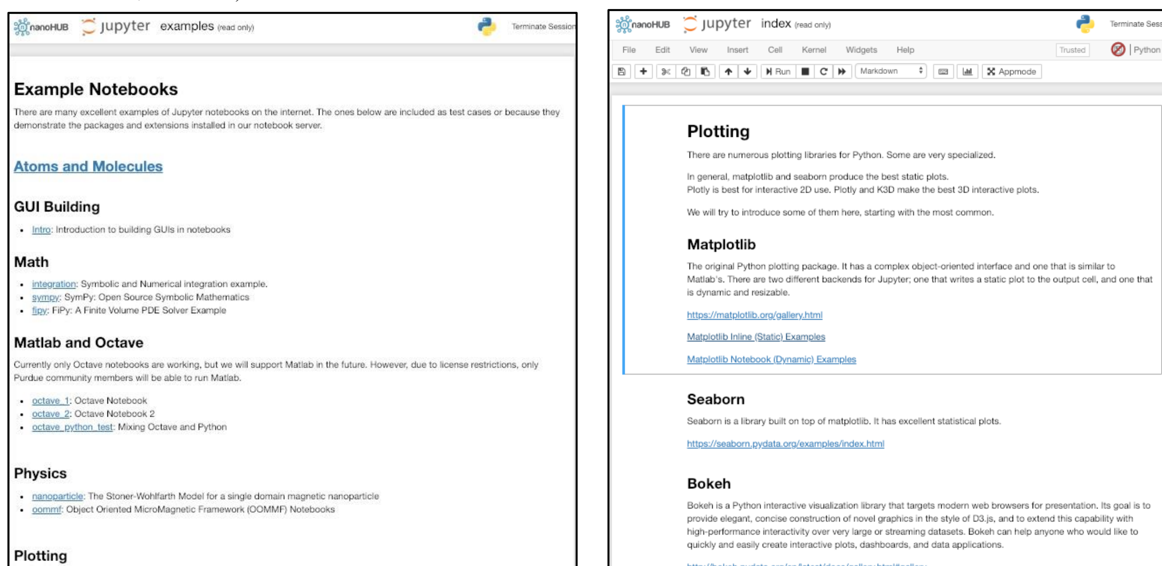

Fig.2: nanoHUB provides its users with a secure Jupyter installation with a large number of installed mathematical and graphical packages. Users can develop their own scripts in python or octave and deploy their own codes. More complex codes can also be installed in nanoHUB and called as a service. All the Rappture-based tools in nanoHUB can be called as a service in the Jupyter notebooks as well. Computational cycles and 24/7 operation as a service to these Jupyter notebooks is provided for nanoHUB users. (left) Example notebooks. (right) Tutorials for plotting libraries in Jupyter.

Towards a Simulation Framework for Coupled Microwave and Micromagnetic Structures

D. Connelly[1], G. Csaba[2], G. H. Bernstein[1], A. Orlov[1],
J. Chisum[1], W. Porod[1]
[1]*Department of Electrical Engineering, University of Notre Dame, USA*
[2]*Pazmany Peter Catholic University, Budapest, Hungary*
dconnel7@nd.edu

In electromagnetic models, magnetic materials are almost always included by means of a permeability function, which is treated as a macroscopic material parameter. This approach is overly simplistic if complex, nonlinear magnetization dynamics take place in the magnetic material – the magnetization dynamics, in general, depend on the frequency and amplitude of the electromagnetic excitation, the external magnetic field, and on the geometry of the magnetic material.

This motivates the development of our simulation framework, schematically shown in Fig. 1, where an electromagnetic model is coupled to a full micromagnetic model of the magnetic material. We study a coplanar waveguide on top of a low-damping magnetic film (YIG). The joint electromagnetic and micromagnetic problem is split into an electromagnetic domain and a micromagnetic domain. The problem is initially solved in HFSS to find incident fields upon the magnetic film. A micromagnetic simulator (OOMMF) then is used to solve for the magnetic material's response (scattered fields), and the result is integrated with the electromagnetic solution to obtain the complete solution. In order to reduce the computational requirement of this co-simulation framework, the electromagnetic domain was reduced to solving a 2D cross-section. The micromagnetic domain solved for the scattered fields along the top surface of the film's cross-section (1D line). An angular spectrum expansion is used to extend that solution to the entire 2D cross-section. The total field is the sum of the incident and scattered fields and can be processed to solve for the overall electromagnetic/micromagnetic response of the structure.

The magnetic film acts as a tunable, nonlinear and frequency dependent inductance [1], coupled to the waveguide. There are a number of device proposals [2] that exploit magnetization dynamics for computing and signal processing. These typically use waveguides for generating magnetic excitations, and the waveguide may also sense the magnetization dynamics. Our study intends to lay the groundwork for the simulation and design of such devices, and we present an example shown in Fig. 2.

[1] Paul, Clayton R., Inductance: Loop and Partial, John Wiley & Sons, 2011.
[2] Papp, Ádám, Wolfgang Porod, Árpád I. Csurgay, and György Csaba. "Nanoscale spectrum analyzer based on spin-wave interference." Scientific Reports 7, no. 1 (2017): 9245.

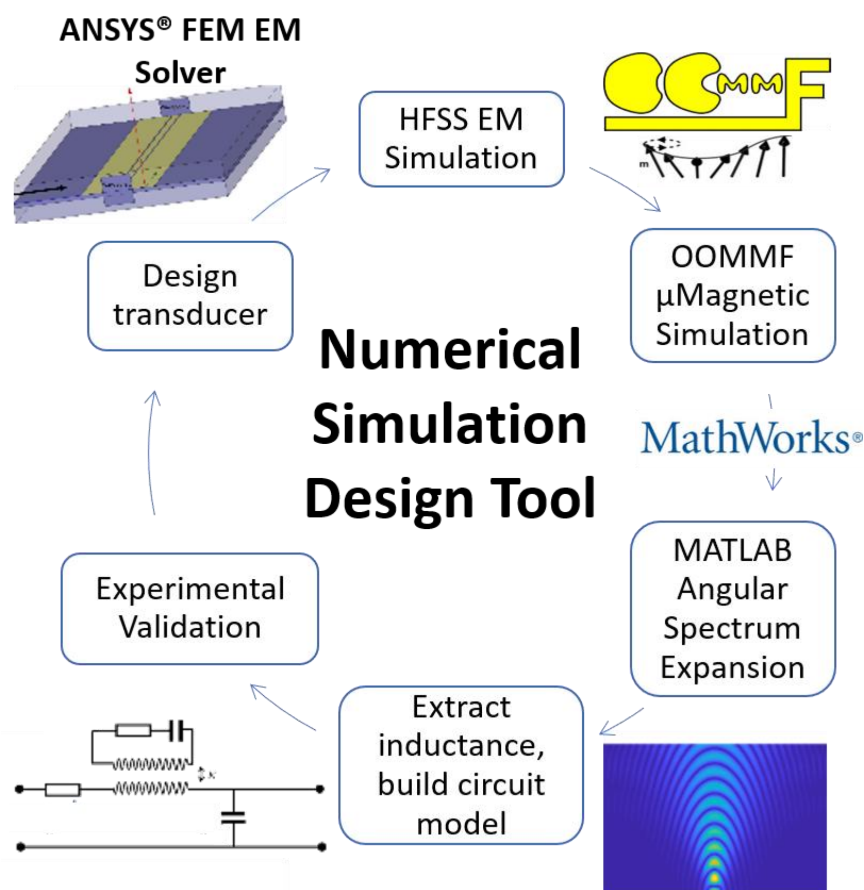

Fig. 1. The numerical simulation design tool flow chart.

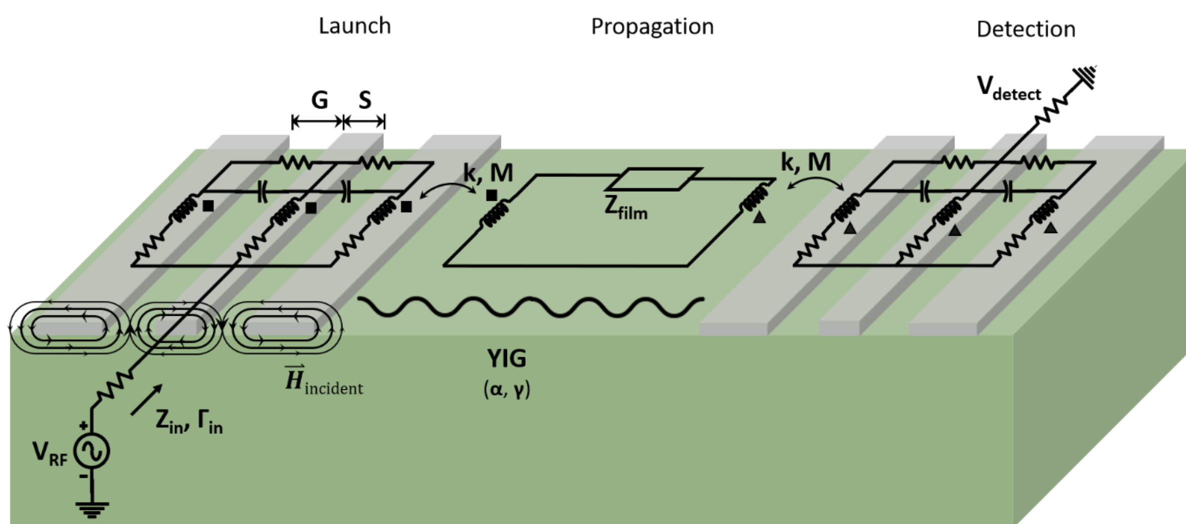

Fig. 2. As a concrete example of our simulation framework, we study structures consisting of coplanar waveguides on top of magnetic films (YIG in this case) to launch, propagate, and detect spin waves. The magnetic fields due to the microwave signal on the waveguide excite spin waves in the magnetic film, and this coupling can be modeled as an inductive coupling. The microscopic simulations provide the parameters for a circuit model for the transmission line and its effect on the magnetic film. This circuit model is schematically superimposed on the physical structure.

A Multi-Physics Model to Study Defect Assisted Transport in Amorphous Barrier Layers

P. Muralidharan, S. M. Goodnick, D. Vasileska
Electrical, Computer and Energy Engineering, Arizona State University, Tempe, USA
pmuralid@asu.com

It is already well established that good surface passivation at the heterointerface in silicon heterojunction solar cells (SHJSC's) leads to high open circuit voltages (V_{oc}'s) and fill factors (FF's), and ultimately to high conversion efficiencies [1][2]. Hence, high device performance is obtained by using carrier selective contact (CSC) structures to optimize collection of photogenerated carriers [3]. In SHJSC's, CSC's usually consist of a transparent conducting oxide (TCO) and a doped (n or p type) hydrogenated amorphous silicon layer [a-Si:H(n/p)] on top of a crystalline silicon (c-Si) absorber (see Fig. 1). Traditionally, passivation layers based on intrinsic hydrogenated amorphous silicon [a-Si:H(i)] have been used between the doped a-Si:H and the c-Si in the highest efficiency cells, to create a low recombination contact.

In this work we use a combination of drift-diffusion (DD), ensemble Monte Carlo (EMC) and kinetic Monte Carlo (KMC) simulations to study the effect of defect assisted transport (DAT) of photogenerated holes through hydrogenated amorphous silicon [a-Si:H(i)] passivation layers. We then correlate the effect of DAT on the overall device performance of SHJSC. At first the DD simulation is conducted for the entire SHJSC to determine its J-V characteristics and band profiles. We extract the valence band, hole quasi-Fermi level and electric field for the DD simulation for various device operating points (maximum power point is of particular interest). EMC is used to determine the incident carrier distribution on the barrier. Along with analytical distributions for a-Si:H [4], the KMC domain is set up to simulate the interaction of discrete carriers with discrete defects [5][6]. The KMC method uses probabilistic distributions of various physical mechanisms to ascertain the behavior of the system [7].

Our simulations indicate that multi-phonon injection is the primary process via which photogenerated holes are injected into the a-Si:H(i) passivation layer. Defect to defect (hopping) transitions is the prominent mode of transport within the a-Si:H(i) barrier. Lastly, for collection of photogenerated holes, Poole-Frenkel emission is dominant for thin a-Si:H(i) layers (< 10 nm) whereas the defect emission is dominant for thicker layer (> 10 nm).

[1] S. de Wolf et al., Green, **2**, 7–24, 2012.

[2] M. Taguchi et al., Prog. Photovoltaics Res. Appl., **13**, 481–488, 2005.

[3] A. Cuevas et al., IEEE 42nd Photovolt. Spec. Conf., no. 1, pp. 1–6, 2015.

[4] R. . Street, Hydrogenated Amorphous Silicon. 1991.

[5] P. Muralidharan et al., Phys. Status Solidi C, **12**, 1198–1200, 2015.

[6] P. Muralidharan et al., IEEE 42nd Photovolt. Spec. Conf., 743–758, 2015.

[7] G. C. Jegert, PhD Thesis, 2011.

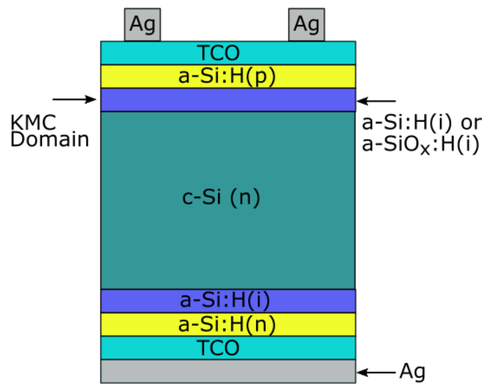

Fig.1: Schematic diagram of a silicon heterojunction solar cell. Drift-diffusion simulations are conducted for the entire cell, whereas the kinetic Monte Carlo simulation is limited to the a-Si:H(i) layer.

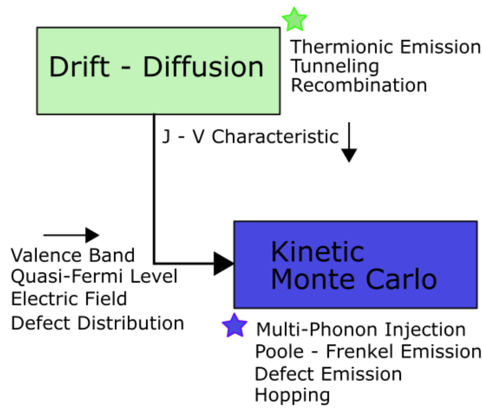

Fig.2: Flow-chart of simulation methodology.

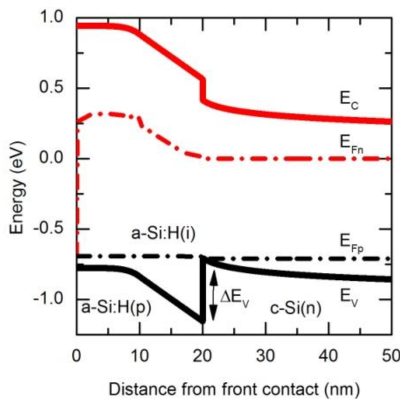

Fig.3: Energy band diagram of a SHJSC with a 10 nm thick a-Si:H(i) passivation layer at maximum power point (~ 0.693 V).

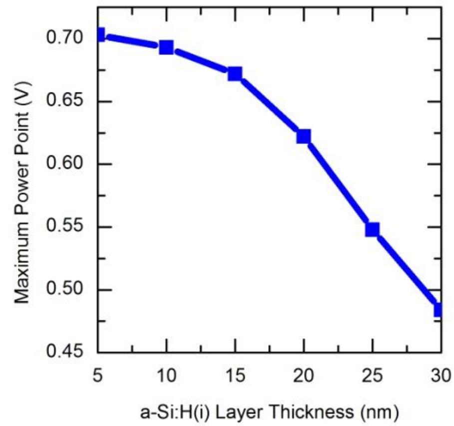

Fig.4: Maximum power point of a SHJSC vs. a-Si:H(i) thickness.

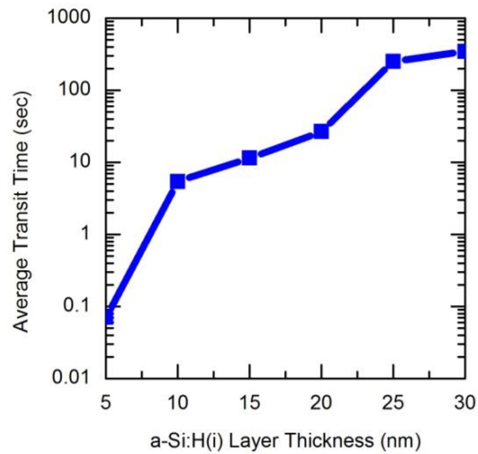

Fig.5 Average transit time (τ) for photogenerated holes to cross the a-Si:H(i) layer vs. a-Si:H(i) layer thickness at 300 K.

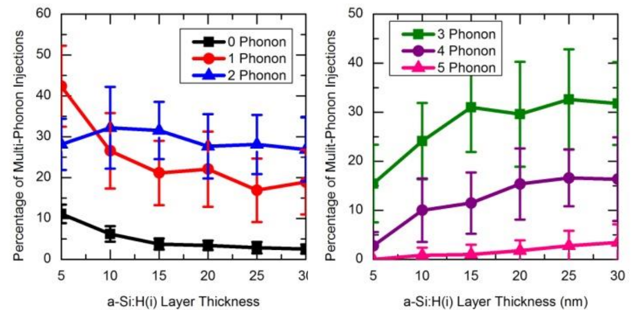

Fig.6: Percentage of phonon transitions for injection into the a-Si:H(i) barrier vs. a-Si:H(i) thickness.

Multiphysics Simulations for the Design of IR and THz Nanoantennas

G. P. Szakmany, G. H. Bernstein, A. O. Orlov, W. Porod
Department of Electrical Engineering, University of Notre Dame, Notre Dame, IN 46556
gszakman@nd.edu

The operating principle of antenna-coupled nanothermocouples (ACNTCs) is based on the wave nature of the IR radiation. A nanoantenna receives the incident radiation, and the radiation-induced antenna currents heat the hot junction of a NTC at the center of the antenna, generating a DC voltage. The thermal response of the devices is inversely proportional to the heat loss to the substrate and the lead lines of the NTC (Fig. 1). In this work, we design thermal insulations for ACNTCs operating at 0.6 THz and 28.3 THz by using COMSOL Multiphysics Simulation Software to reduce these heat losses and increase the device response. The devices are simulated in receiving antenna mode with a unidirectional coupling of the electromagnetic wave module to the heat-transfer module by an electromagnetic-heat-source boundary condition.

Previously, ACNTCs for 0.6 THz were fabricated on a high-resistivity Si wafer [1]. The thermal conductivity of Si is about 100 times larger than SiO_2. By inserting a thin layer of SiO_2 (1 μm to 6 μm) between the antenna and the Si substrate, the heat loss can be significantly reduced (Fig. 2). The resonant antenna length, l, depends on the dielectric constant and the thickness of the material surrounding the antenna. COMSOL simulations were used to determine l for various SiO_2 thicknesses (Fig. 2). The meshing of such simulations is challenging due to the large geometry differences between the antenna and the substrate (Fig. 3a). By varying the antenna length to determine l, the geometry and the mesh changes, resulting in simulation artifacts. We created a geometry independent mesh by constructing the antenna from small domains (Fig 3b), and its length was changed by assigning air or antenna material to each domain. So, the geometry, and hence the mesh, were fixed.

The heat loss to the lead lines can be eliminated by using a primary and secondary antenna structure, as shown in Fig. 4, for a suspended ACNTC operating at 28.3 THz [2]. The thermal resistance around the hot junction is increased because the wider lead lines of the NTCs are located farther away. In addition, both the primary and secondary antennas resonate and heat the hot junction more effectively than a single dipole antenna. Figure 5 shows the resonant antenna length of the primary and secondary antennas obtained by COMSOL simulations. Figure 6 shows the simulated temperature profiles along the antenna. In our presentation, we will discuss the simulation methods and results in detail.

[1] G. P. Szakmany, A. O. Orlov, G. H. Bernstein, W. Porod, IEEE Trans. Terahertz Sci. Technol. **7,** 582 (2017).

[2] G. P. Szakmany, A. O. Orlov, G. H. Bernstein and W. Porod, J. Vac. Sci. Technol., B **36** , 052203 (2018).

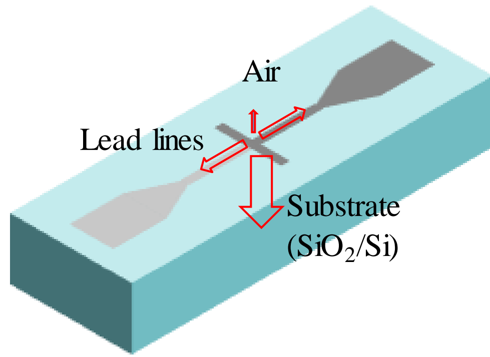

Fig.1: Heat loss of the antenna by air, lead lines, and substrate. The substrate and lead line effects are the strongest, and can be reduced by thermal insulation.

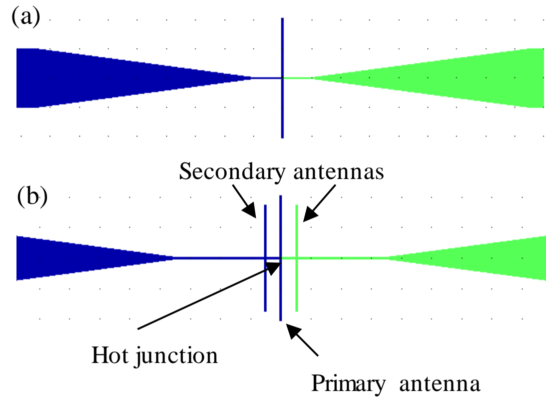

Fig.4:.Schematic of the ACNTC (a) with single dipole antenna, (b) with the antenna structure constructed from a primary and secondary antennas.

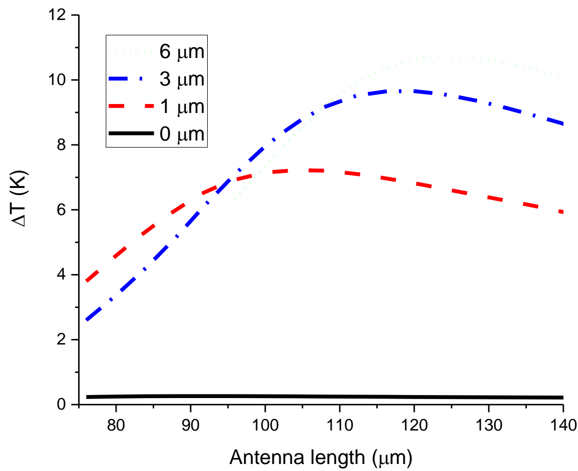

Fig.2: Temperature increase as a function of antenna length for various oxide thicknesses. ΔT on SiO_2 is about 50 times larger compared to devices on a Si substrate. The resonant antenna length changed from 92 µm to 125 µm.

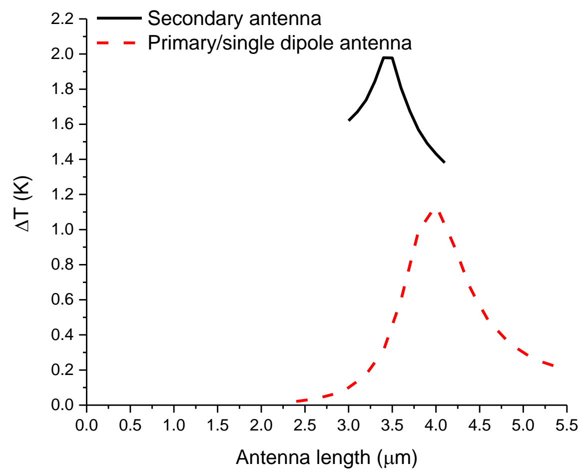

Fig.5. Resonant antenna length of the primary and secondary antennas. The temperature increase at the hot junction is about twice for the antenna structure with primary and secondary antennas as for a single dipole antenna.

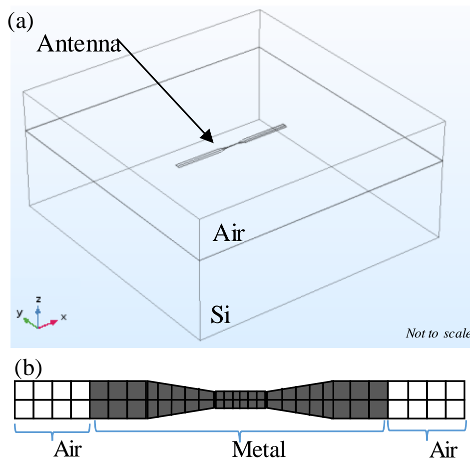

Fig.3: (a) Schematic of the antenna for simulations. (b) The antenna model for geometry-independent meshing. Metal (grey) and air (white) material properties are assigned to each domain to vary the length of the antenna while keeping the mesh the same. .

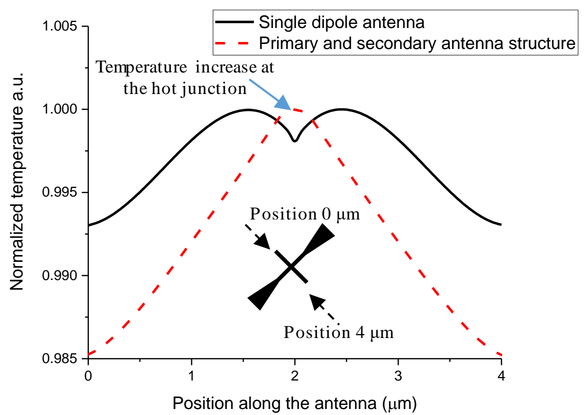

Fig.6: Normalized temperature profiles along the antenna. The heat loss to the lead lines for a single dipole antenna is indicated by the temperature drop at the center, while it is eliminated by using the secondary antenna structure.

Finite-Difference Time-Domain Study of Phonon Dynamics and Rough-Interface Scattering in Nanostructures

L. Avazpour, S. Soleimanikahnoj, S. Suri, I. Knezevic
Department of Electrical and Computer Engineering,
University of Wisconsin-Madison, Madison, Wisconsin 53706, USA
Laleh.Avazpour@wisc.edu

The advancements in the growth of heterostructures with high-quality interfaces arise from the need for high-performance electronic devices. However, systems with multiple interfaces suffer from low thermal conductivity owing to a complex and still insufficiently understood interplay of interface scattering and phonon-dispersion modification. In this work, we introduce a finite-difference time-domain (FDTD) simulation technique for the analysis of elastic-wave scattering at a rough interface between dissimilar elastic solids [1]. We tease out the effects of interface morphology (rms roughness and correlation length) and the mismatch between the materials' elastic properties on the refraction/transmission and mode localization near the interface.

The model system is a lateral interface between single-layer graphene and hBN [3]. In Figs. 1 and 2, we present the time progression of the energy-density profile for a normally incident longitudinal wave packet. The rms roughness is 1.23 nm, the wavelength equals 10 rms, and the autocorrelation length equals rms roughness in Figure 1 and is 1/2 of the rms roughness in Figure 2. The smaller correlation length leads to more transmitted energy and less reflection. Moreover, at a smaller correlation length, more energy remains localized at the interface. The results of this study on phonon transport across junctions between dissimilar materials can be used to develop simplified interface-scattering models to be used in the design of functional nanomaterials with desired thermal properties.

[1] L. N. Maurer, S. Mei, and I. Knezevic, Phys. Rev. B **94**, 045312 (2016).
[2] K.V. Zakharchenko, M.I. Katsnelson, and A. Fasolino, Phys. Rev. Lett. **102**, 046808 (2009).
[3] F. Kargar, Z. Barani, R. Salgado, B. Debnath, J.S. Lewis, E. Aytan, R.K. Lake, and A.A. Balandin, ACS Appl. Mater. Interfaces **43**, 37555 (2018).

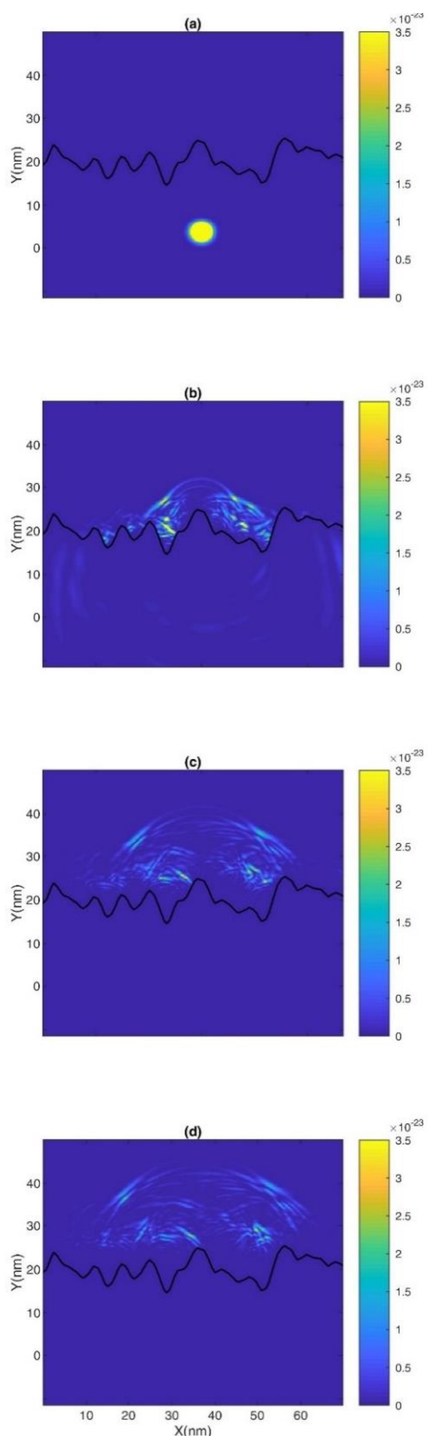

Fig.1: Energy-density profile (yellow: high; blue: low) after a scattering event at the interface between graphene and hBN. A longitudinal wave packet was injected toward the interface from the bottom and center with normal incidence. The rms roughness of 1.23 nm, autocorrelation length equals rms roughness, and the wavelength is 10 times the rms roughness. The results are plotted at a) 0, b) 2, c) 4 and d) 5 ps.

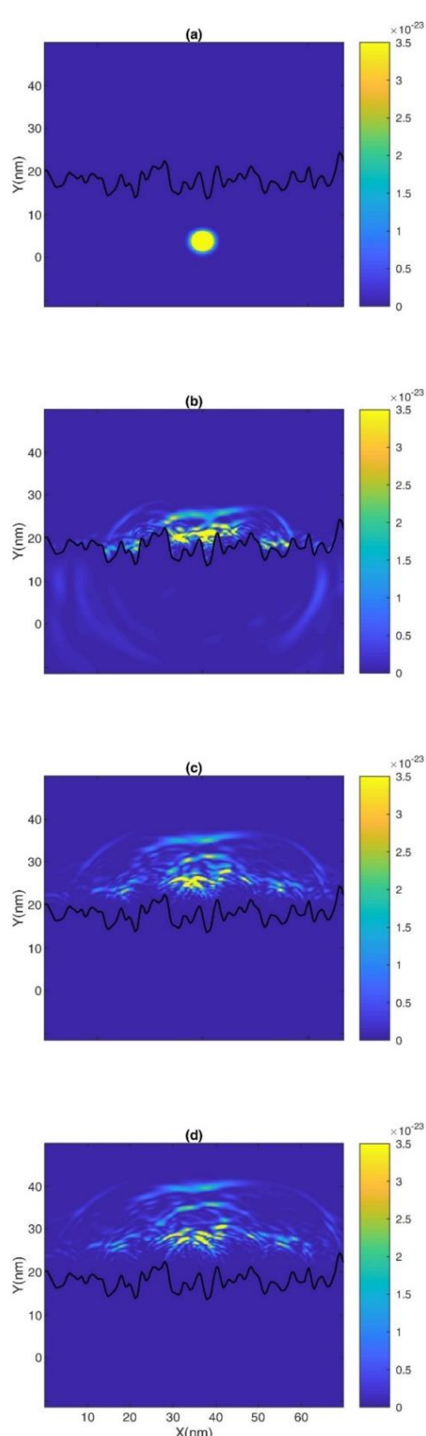

Fig.2: Energy-density profile (yellow: high; blue: low) after a scattering event at the interface between graphene and hBN. A longitudinal wave packet was injected toward the interface from the bottom and center with normal incidence. The rms roughness of 1.23 nm, autocorrelation length equals half of rms roughness, and the wavelength is 10 times the rms roughness. The results are plotted at a) 0, b) 2, c) 4 and d) 5 ps.

A Two-Particle Monte Carlo Method for Carrier Transport in the Presence of Electron-Electron Scattering

H. Kosina[1], G. Indalecio[2]

[1]*Institute for Microelectronics, TU Wien, Austria*

[2]*CITUS, University of Santiago de Compostela, Spain*

kosina@iue.tuwien.ac.at

The Boltzmann collision operator taking into account electron-electron scattering (EES) is nonlinear in the single-particle distribution function. Numerical solution of the resulting nonlinear Boltzmann equation requires an iterative method. In terms of the two-particle distribution function, however, the scattering operator is linear. We have formulated a kinetic equation for the two-particle distribution function and derived Monte Carlo (MC) algorithms for the numerical solution of that equation [1].

The stationary transport problem for a uniform electric field is solved by a two-particle MC algorithm. A pair of trajectories is traced for a long period of time and quantities of interest can be computed by several methods: time-averaging, sampling at equidistant time steps, and before-scattering sampling. Fig. 1 shows the electron distribution functions in bulk silicon. The nonequlibrium distributions are broadened due to EES especially at low temperatures.

The transient transport problem for a bulk semiconductor is solved by an ensemble MC algorithm. The time evolution of an ensemble of particle pairs is computed, and quantities of interest are obtained as ensemble averages. As a transient problem we analyzed the mixing of a hot and a cold carrier ensemble. The energy of the hot ensemble relaxes faster in the presence of EES (Fig. 2). The effect of EES on the velocity overshoot is shown in Fig. 3.

The stationary algorihtm has been extended to non-uniform electric fields. We calculate the energy distributions for a potential profile proposed in [2]. At room temperature a slight enhancement of the high energy tail is observed (Fig. 4), which, however, is less pronounced than that reported in [2].

The novelty of the proposed method is that the problem to be solved is linear. Storing and iteratively updating the single particle distribution is not required by this method.

[1] G. Indalecio and H. Kosina. Monte Carlo Simulation of Electron-electron Interactions in Bulk Silicon. Book of Abstracts of “The 12th International Conference on Scientific Computing in Electrical Engineering (SCEE)”, 97 – 98 (2018)

[2] P. A. Childs and C. C. C. Leung. A one-dimensional solution of the Boltzmann transport equation including electron-electron interactions. Journal of Applied Physics 79, 222 (1996)

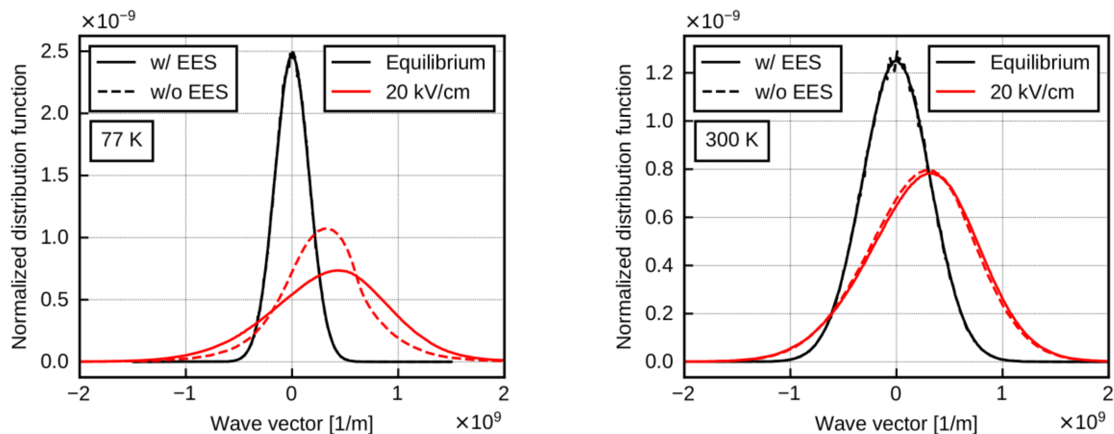

Fig.1: Effect of EES on the bulk distribution function at 77K (left) and 300K (right) in thermal equilibrium and non-equilibrium.

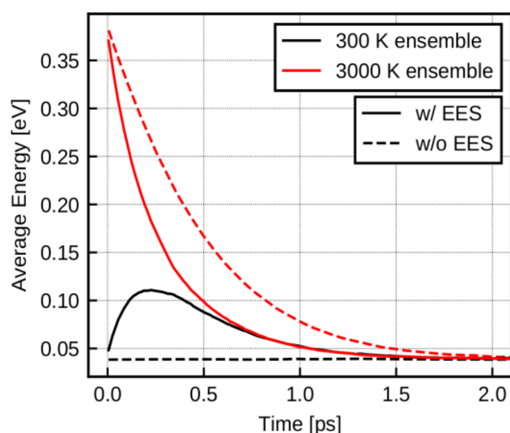

Fig.2: Enhancement of energy relaxation due to EES. The initial two-particle distribution function assumed is a aproduct of a cold Maxwellian at 300K and a heated Maxwellian at 3000K.

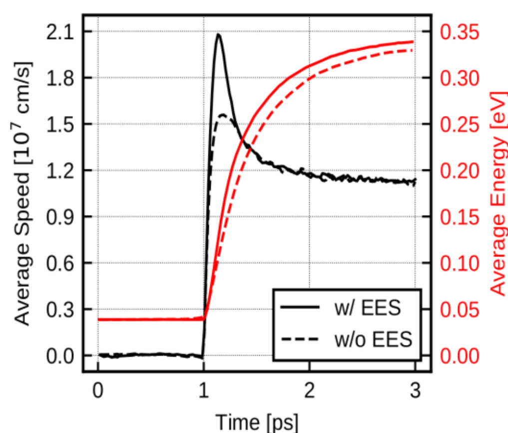

Fig.3 Effect of EES on the velocity overshoot (black line) and the energy transient (red line). An electric field step of 50kV/cm is applied at 1 ps. Lattice temperature is 300K.

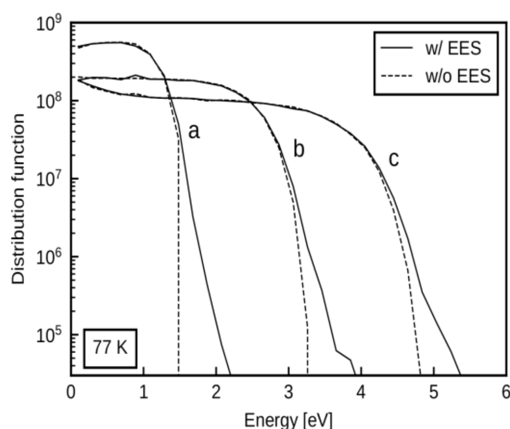

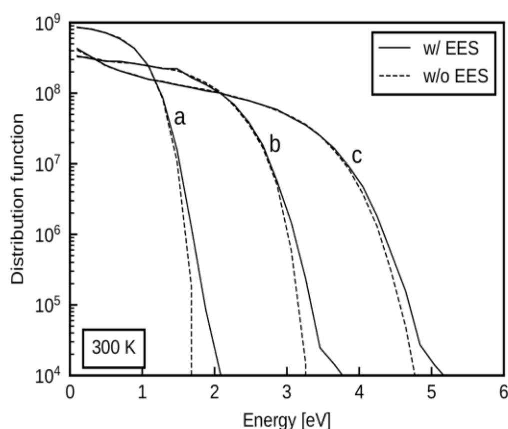

Fig.4: Enhancement of the high energy tail due to EES. The potential profile and three lateral positions reported in [2] have been used.

Electron Transport in Strained $In_{0.64}Al_{0.36}As$

I. Welland, D. K. Ferry
School of Electrical, Computer, and Energy Engineering
Arizona State University, Tempe, AZ 85287-5706 USA
ferry@asu.edu

The ternary semiconductor InAlAs has proven to be useful in a variety of device applications. Recently, it has become useful in hot carrier solar cells [1], particularly for cells with materials lattice matched to InAs [2]. We use a series of methods to examine the band structure and transport properties of the electrons in $In_{0.64}Al_{0.36}As$ is strained to the InAs lattice constant. We demonstrate that it has reasonably good properties for use in third generation hot carrier solar cells, both as a barrier and as the active absorber layer. These properties include the band structure, mobility, hot carrier velocity, and distribution functions of the electrons in various valleys under continuous solar irradiation. In particular, we evaluate the low field properties using Rode's method and the hot carrier properties are determined with ensemble Monte Carlo simulations that examine all three relevant valleys of the conduction band, including the transfer of carriers between these valleys. The band structure determined by empirical pseudopotential methods, including non-local and full zone spin-orbit splitting. Then, we examine the low field mobility and Hall factors as a function of lattice temperature. Finally, we turn to a careful examination of the hot electron properties with the ensemble Monte Carlo procedure.

[1] Hirst L C, *et al.*, 2014 *IEEE J. Photovolt*. **4** 1526
[2] Esmalelpour H, *et al.,* 2017 *J. Appl. Phys*. **121** 235301

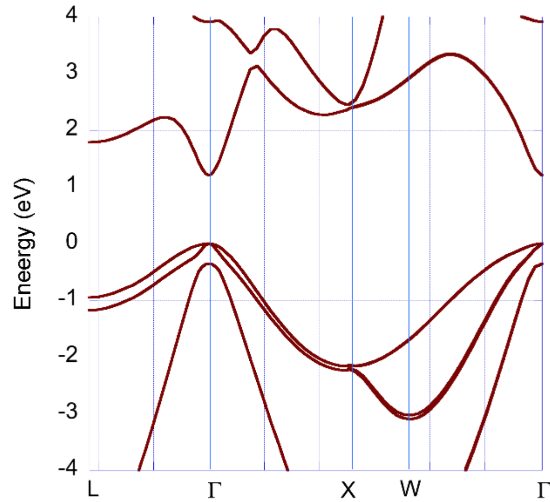

Fig.1: Band structure of $In_{64}Al_{36}As$ strained to the InAs lattice constant.

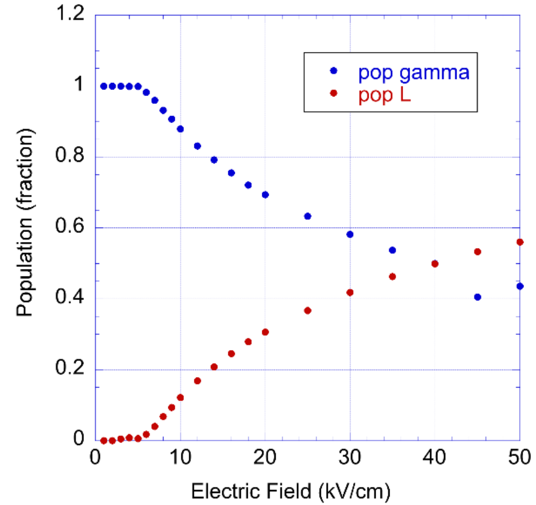

Fig.4: Relative populations of the Γ and L valleys of the conduction band as a function of the electric field.

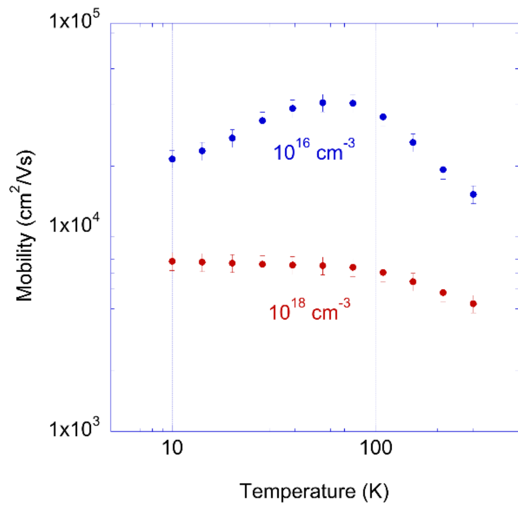

Fig.2 Electron mobility as a function of temperature for a doping density of $1x10^{18}$ cm^{-2}.

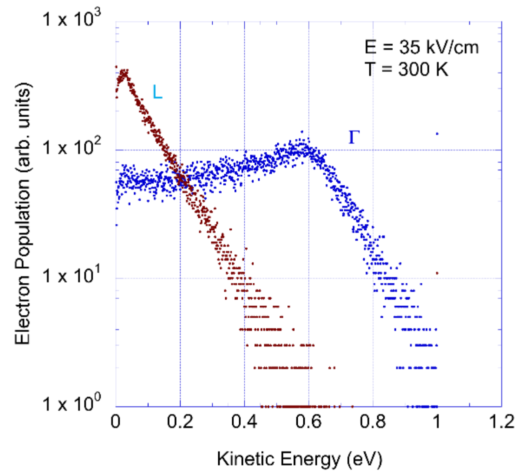

Fig.5 Population of the Γ and L valleys of the conduction band as a function of the kinetic energy of the carriers at 35 kV/cm..

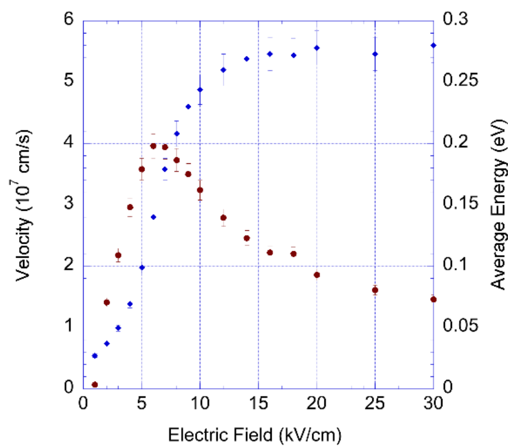

Fig.3: Electron velocity and average ener as a function of electric field for a carrier density of $1x10^{18}$ cm^{-2}.

In Pursuit of the Next Wonder 2-D Materials: An *ab initio S*tudy

M. Luisier[1], C. Klinkert[1], C. Stieger[1],
A. Szabo[1], Y. Lee[1], D. Campi[2], N. Marzari[2]

[1]*Integrated Systems Laboratory, ETH Zurich, 8092 Zurich, Switzerland*
[2]*Laboratory of Theory and Simulation of Materials, EPFL, 1015 Lausanne, Switzerland*
mluisier@iis.ee.ethz.ch

Daily progresses are made in the exfoliation and growth of high-quality two-dimensional (2-D) monolayers, in their reliable transfer onto different substrates, in the clean deposition of oxide dielectrics on top of them, in the incorporation of metallic contacts with low resistances, and in their chemical doping. A very appealing outlet of 2-D materials is the replacement of Si FinFETs, the currently manufactured transistor technology, at the end of Moore's scaling law. In effect, 2-D single-layer crystals benefit from their planar atomic structure that provides an excellent electrostatic control. This, in turn, allows to effectively turn off switches made out of them, even with gate lengths below 15 nm. Here, the most promising 2-D semiconductors as next-generation transistors beyond Si FinFETs will be identified via *ab initio* device simulations. A recently produced database containing more than 1,000 relatively easily exfoliable 2-D candidates [1] will be used as starting point. Not all materials are suitable for logic applications.

The transistor structure depicted in Fig. 1 has been chosen as benchmark to compare different 2-D channel materials. To model the "current vs. voltage" characteristics of the investigated components, an *ab initio* quantum transport approach has been developed. Its workflow is shown in Fig. 2. Starting from the atomic positions and lattice vectors found in the database of Ref. [1], the primitive unit cell of the considered 2-D material is constructed and its electronic structure calculated with a density functional theory (DFT) tool, e.g. VASP [2] or Quantum ESPRESSO [3]. By transforming the plane wave results into a set of maximally localized Wannier functions with the Wannier90 software [4], a Hamiltonian matrix in a localized orbital basis is obtained. It can be inserted into a quantum transport solver [5] to compute the figures of merit of transistors similar to the one in Fig. 1. Selected results are presented in Fig. 3. They demonstrate the existence of materials capable of producing high ON-currents for both n- and p-type device configurations. More than 100 2-D monolayers have so far been modeled.

Acknowledgment: This work was supported in part by the MARVEL National Centre of Competence in Research of the Swiss National Science Foundation and in part by ETH Zürich under Grant ETH-32 15-1. The authors like to thank PRACE for providing them access to Piz Daint at Swiss National Supercomputing Centre, Lugano, Switzerland, under Project pr28.

References: [1] N. Mounet et al., Nature Nano. **13**, 246 (2018). [2] G. Kresse et al., Phys. Rev. B **54**, 11169 (1996). [3] P. Giannozzi et al., J. Phys.: Condens. Matter **21**, 395502 (2009). [4] N. Marzari et al., Phys. Rev. B **56**, 12847, (1997). [5] M. Luisier et al., Phys. Rev. B **74**, 205323 (2006).

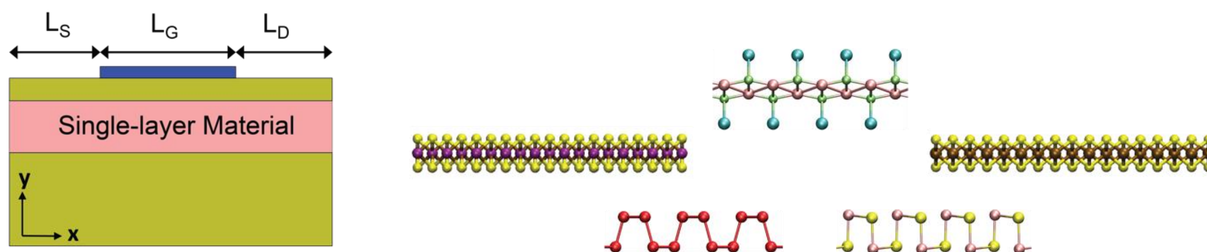

Figure 1: (left) Schematic view of a single-gate field-effect transistor with a 2-D monolayer as channel material. In this study, the gate length L_G ist set to 15 nm, the source and drain extensions measure L_S=L_D=12.5 nm each and are doped with a donor (N_D) or acceptor (N_A) concentration of 5e13 cm^{-2} for n- and p-type devices, respectively. The oxide separating the channel from the gate contact is assumed to be a 3nm thick HfO_2 layer with a relative dielectric constant ε_R=20. All simulations are performed at room temperature and include a phenomenological dissipative scattering mechanism to ensure convergence at high V_{GS} and to remove unphysical negative differential resistance behavior. (right) Example of 2-D monolayer crystals used in this work.

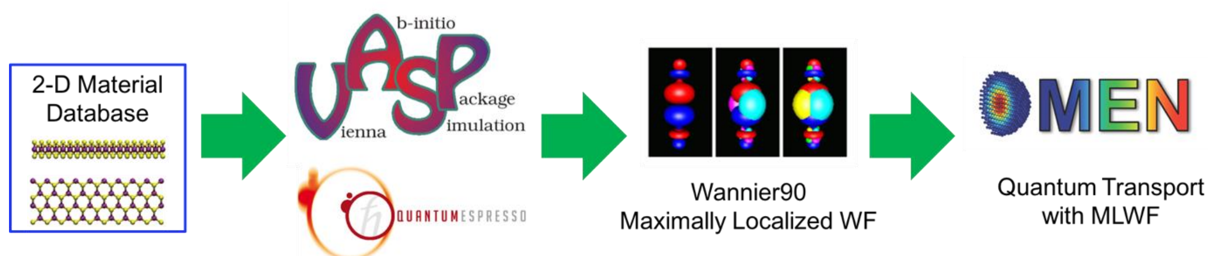

Figure 3: Illustration of the developed computational scheme to simulate the single-gate transistors from Fig. 1. Starting from a recently produced 2-D materials database that contains more than 1,800 monolayer candidates [1], the electronic structure of the selected crystal is calculated with density functional theory (DFT), e.g. with VASP [2] or Quantum ESPRESSO [3], for its primitive unit cell. The plane-wave results are converted into a set of maximally localized Wannier functions (MLWF), which gives rise to a Hamiltonian matrix with short range interactions. The latter is finally passed to a quantum transport solver called OMEN [5] to obtain the "current vs. voltage" characteristics of the considered transistor samples.

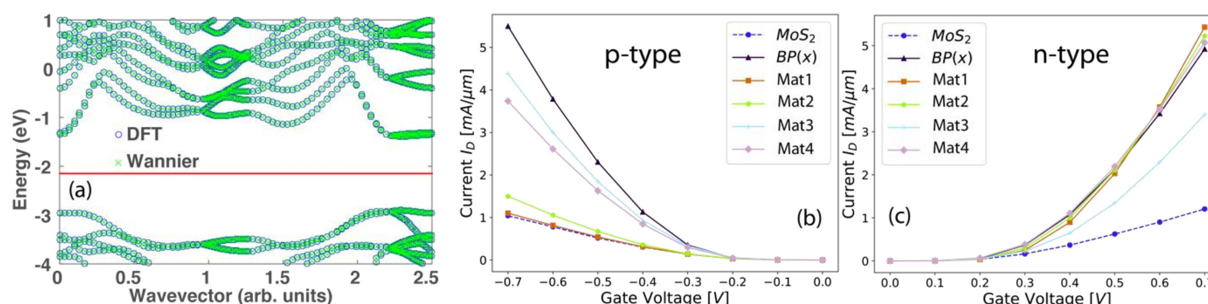

Figure 2: (a) Bandstructure of a single-layer 2-D material (P_8Si_4) as computed with density functional theory (blue circles) and after a transformation into MLWFs (green crosses). An excellent agreement between both methods is obtained. The red line in the middle of the band gap indicates the Fermi level. (b) I_D-V_{GS} transfer characteristics at V_{DS}=0.7 V of p-type single-gate 2-D transistors as in Fig. 1 with different 2-D monolayers as channel materials. The OFF-current of all devices is set to 0.1 μA/μm. The I-V characteristics of MoS_2 (dashed curve with circles) and black phosphorus (black curve with triangles) are given as references. They are compared to the those of transistors based on four other 2-D materials from the database of Ref. [1]. While none of them outperforms black phosphorus, at least two of them deliver promising ON-current values. (c) Same as (b), but for n-type transistors. All considered 2-D materials exhibit significantly higher ON-currents than MoS_2.

Intricacies and Limitations of the ab-initio Determination of Electronic Transport Properties in Two-Dimensional Materials

G. Gaddemane[1], M. L. Van de Put[1], W. G. Vandenberghe[1],
S. Gopalan[1], E. Chen[2], M. V. Fischetti[1]
[1]*Department of Material Science and Engineering, The University of Texas at Dallas, Richardson, Texas, USA*
[2]*Taiwan Semiconductor Manufacturing Company Ltd., Hsinchu, Taiwan*
gautam.gaddemane@utdallas.edu

Two-dimensional (2D) materials have gained wide interest in the field of electronics as a potential channel material in field-effect transistors (FET). The ability of these materials to confine carriers to atomically thin layers provides excellent electrostatics and reduces short channel effects. In addition, their layered nature also reduces/eliminates deviations from ideality, such as surface roughness, dangling bonds, and interface. However, experimental research on these materials is still in the early stages, and most of the predictions are based on theoretical studies. The lack of experimental information, and timely progress made in *ab-initio* ("first principles") methods to calculate band structures, phonon dispersion, and electron-phonon interactions, have made them a popular tool to calculate carrier transport properties of monolayer 2D materials.

Recently we have reported on the electron-phonon scattering rates (see Figs. 1 and 2), mobility (see Table 1) and high-field characteristics of phosphorene [1], silicene and germanene [13,14]. In addition, in Fig. 1 (c), we show our most recent results for the scattering rates in molybdenum disulfide (MoS_2). Throughout our investigations, we have found a large discrepancy among the *ab-initio* predictions of carrier transport properties. Fig. 3 shows the spread of the calculated mobilities found in literature, ranging 20-26,000 $cm^2/(V{\cdot}s)$ for phosphorene [1-6], 130-410 $cm^2/(V{\cdot}s)$ for MoS_2 [7-11], and 0.01-250,000 $cm^2/(V{\cdot}s)$ for silicene and germanene [9,12-16]. Within our precise full-band Monte-Carlo method, we also see discrepancies in the predicted scattering rates (shown in Fig. 1) and mobilities (listed in Table 1) between different well-known *ab-initio* packages.

In this work, we analyze critically the discrepancies we find for the materials listed above. We detail the computational and physical aspects of the various models used in literature. We analyze the underlying causes of the disagreement (ignoring anisotropy, elastic approximation, a coarse discretization) and provide the key ingredients to a precise transport model. With this transport model, we compare different *ab-initio* packages and comment on the reliability of *ab-initio* methods to accurately predict electronic transport properties in novel 2D materials.

[1] G. Gaddemane *et al.,* Phys. Rev. B **98**, 115416 (2018).
[2] B. Liao *et al*., Phys. Rev. B **91**, 235419 (2015).
[3] Z. Jin *et al.,* Appl. Phys. Lett. **109**, 053108 (2016).
[4] A. N. Rudenko *et al*., Phys. Rev. Lett. **116**, 246401 (2016).
[5] Y. Trushkov and V. Perebeinos, Phys. Rev. B **95**, 075436 (2017).
[6] J. Qiao *et al*., Nature Comm. **5**, 4475 (2014).
[7] T. Gunst *et al.,* Phys. Rev. B **93**, 035414 (2016).
[8] W. Li, Phys. Rev. B **92**, 075405 (2015).
[9] X. Li *et al.,* Phys. Rev. B **87**, 115418 (2013).
[10] K. Kaasjberg *et al.,* Phys. Rev. B **85**, 115317 (2012).
[11] T. Sohier *et al.,* Phys. Rev. Materials **2**, 114010 (2018).

[12] W. Zhang *et al*., Nano Research **7**, 1731 (2014).
[13] M. V. Fischetti *et al*., Phys. Rev. B **93**, 155413 (2016).
[14] G. Gaddemane *et al.,* J. Appl. Phys. **124**, 044306 (2018).
[15] Z.G. Shao *et al*., J. Appl. Phys. **114**, 093712 (2013).
[16] X.S. Ye *et al.*, RSC Advances **4**, 21216 (2014).

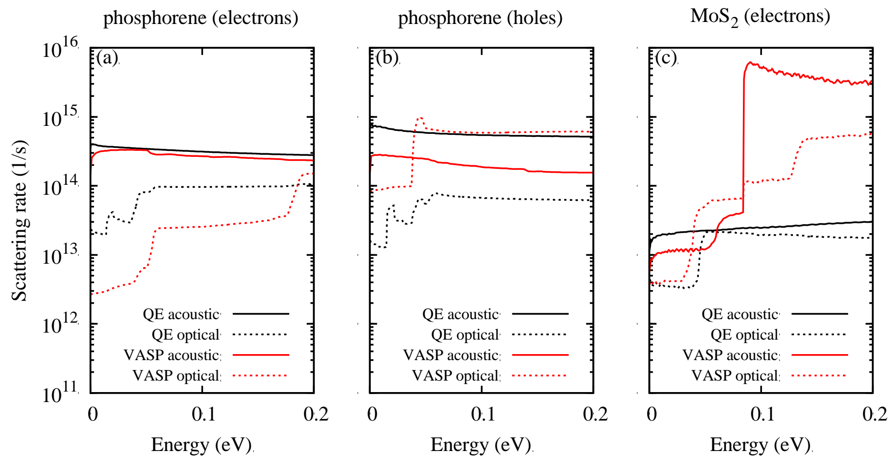

Fig. 1: Carrier-phonon scattering rates at 300K for (a) phosphorene electrons, (b), phosphorene holes, and (c) MoS_2 electrons.

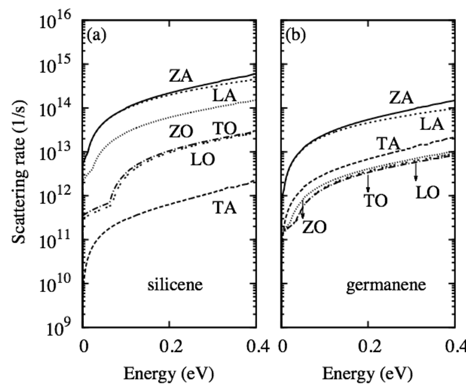

Fig. 2: Electron-phonon scattering rate in (a) silicene, and (b) germanene at 300 K with a 1 nm cutoff for the ZA phonon wavelength.

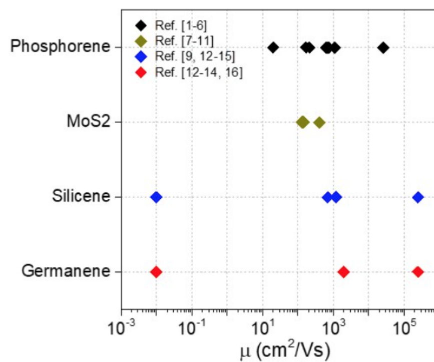

Fig. 3: Spread of the reported mobilities in literature for various 2D materials. Note that the x-axis has a logarithmic scale.

	***Ab-initio* method**	$\mu \left(\frac{cm^2}{V \cdot s}\right)$
Phosphorene (electrons)	VASP	20
	QE	21
Phosphorene (holes)	VASP	19
	QE	19
Silicene (electrons)	VASP	~10^{-3}
	VASP with cutoff*	700
Germanene (electrons)	VASP	~10^{-3}
	VASP with cutoff*	2300
MoS_2 (electrons)	VASP	137
	QE	127

Table 1: Low-field carrier mobility μ for various 2D materials, calculated using the full band Monte Carlo method. VASP: Vienna Ab initio Simulation Package, PHONOPY and our own code, uses the finite difference approach. QE: QUANTUM ESPRESSO, uses Density Functional Perturbation Theory. Details are given in Ref. [1]. *: 1 nm cutoff is assumed for the ZA-phonon wavelength in silicene and germanene

Acknowledgements: This work has been supported in part by the Taiwan Semiconductor Manufacturing Company, Ltd (TSMC) and the Semiconductor Research Corporation (SRC nCORE).

Second-Order Optical Nonlinearity in MoS_2 Nanoislands from Density-Matrix Calculations

F. Karimi, I. Knezevic

Department of Electrical Engineering, University of Wisconsin-Madison

Madison, Wisconsin 53706, USA

karimi2@wisc.edu

Nonlinear optics has many applications in nanophotonics, such as frequency combs and optical modulators. The feasibility and efficiency of these applications are contingent upon nanoscale materials with a sufficiently large optical nonlinearity. As a result, there is ongoing research in the pursuit of nanomaterials and nanostructures with a high nonlinear optical susceptibility. The second-order optical susceptibility vanishes in most materials owing to their centrosymmetric structure. The synthesis of noncentrosymmetric nanostrucutres promises to enhance the optical nonlinearity. Following recent advances in the chemical vapor deposition processes [1], nanoscale equilateral-triangle-shaped islands of transition-metal dichalcogenides, such as MoS_2, WS2, and WSe2, can be accurately synthesized. Owing to the broken centrosymmetry in these nanotriangles, the second-order optical susceptibility is nonzero. Here, we employ the density-matrix approach to calculate the second-order optical susceptibility of MoS_2 nanotriangles at mid-infrared to near-infrared frequencies [2-4]. We show that the second-order optical susceptibility maximizes at plasmon resonances as well as two-photon (intraband) resonances. The two-photon resonances are only dependent on the size of the nanotriangles; however, the plasmon resonances can be tuned via the carrier density. We show that by aligning the plasmon resonances and two-photon resonances, the second-order optical susceptibility can increase up to 10^{-6} mV^{-1}.

[1] S. Xie et al., Science **359**, 1131 (2018).

[2] R. W. Boyd, *Nonlinear optics*, Elsevier (New York) (2008).

[3] F. Karimi, A.H. Davoody, and I. Knezevic, Physical Review B **93**, 205421 (2016).

[4] F. Karimi, A.H. Davoody, and I. Knezevic, Physical Review B **97**, 245403 (2018).

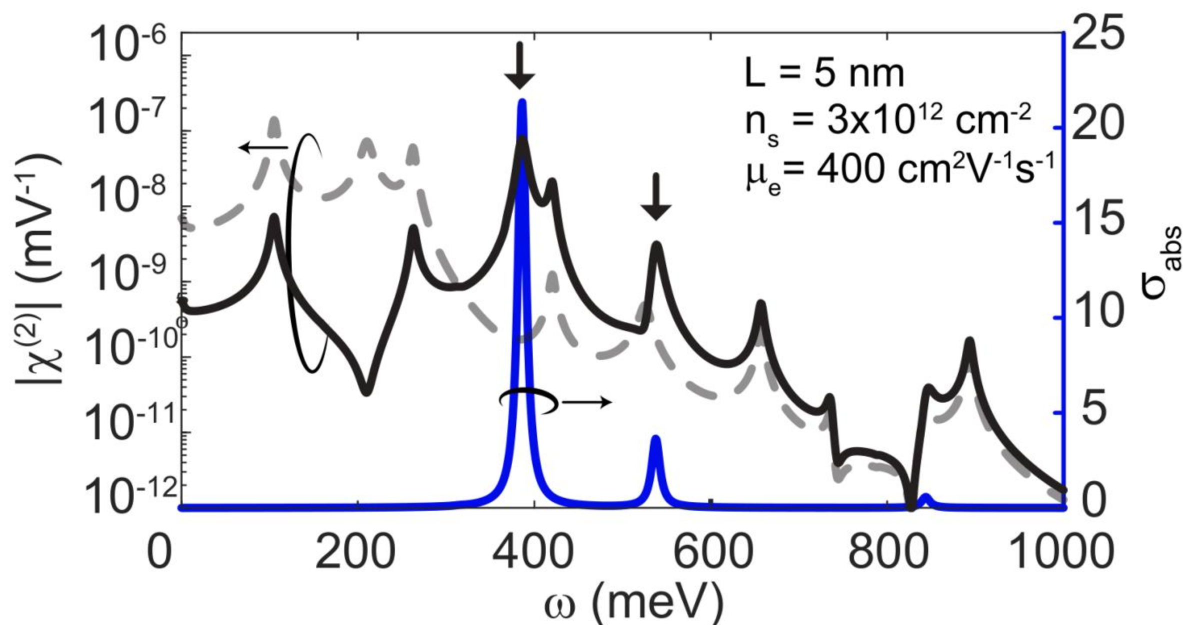

Fig.1: The second-order optical susceptibility with respect to the external field (solid black) and the self-consistent field (dashed black) for a nanotriangle with the side length of 5 nm, electron density of $3x10^{12}$ cm^{-2}, and electron mobility of 400 $cm^2V^{-1}s^{-1}$. The loss function is shown by the blue curve.

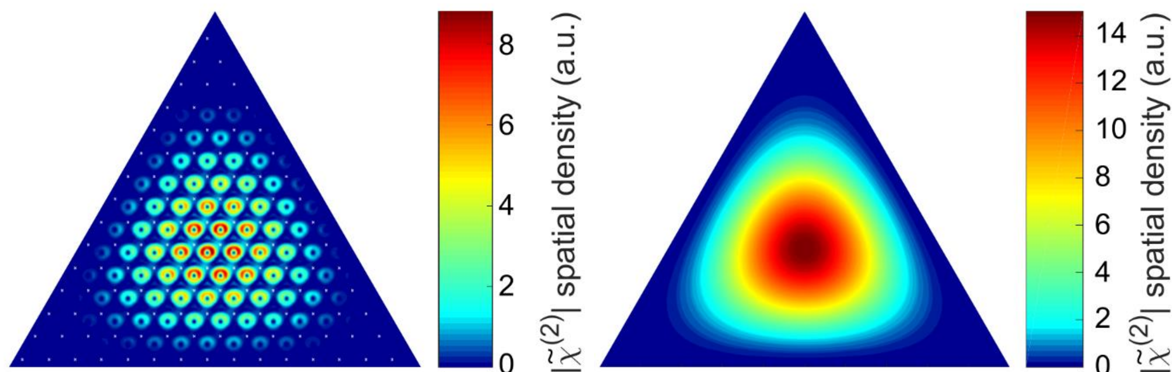

Fig.2: Spatial profile of the second-order optical susceptibility at the plane of Mo atoms and at the plasmon resonance frequency of 380 meV, calculated within the envelope function approximation with (left) and without (right) the Bloch wave function included. The nanotriangle has the side length of 5 nm, electron density of $3x10^{12}$ cm^{-2}, and electron mobility of 400 $cm^2V^{-1}s^{-1}$. The white crosses in the left figure denote the location of S atoms.

Drain-Backgate-Enhanced TFET Based on In-Plane $MoTe_2/MoS_2$ Heterojunction

J. Choukroun[1], D. Logoteta[1,2], M. Pala[1], P. Dollfus[1]
[1]*C2N, CNRS, Univ. Paris-Sud, Université Paris-Saclay, Palaiseau, France*
[2]*Dipartimento di Ingegneria dell'Informazione, Università di Pisa, Pisa, Italy*
philippe.dollfus@u-psud.fr

Thanks to their ability to yield subthreshold swings (*SS*) below the thermionic limit of 60 mV/dec at room temperature [1], Tunnel Field Effect Transistors (TFETs) are recognized to be a promising avenue for the scaling of power supply. However, since TFETs rely on band-to-band tunneling (BTBT), the on-state current I_{ON} they provide is often severely lower than that of MOSFETs, which limits their possible applications [2]. Encouraging experimental results have been obtained for III-V TFETs [3], but the use of 2D materials offers the advantage of using electrostatic doping of leads via backgates, and a better control of the heterojunction interface. Vertical and in-plane heterojunction TFETs based on 2D materials have demonstrated promising results [4]. Recently, we have shown that TFETs based on in-plane heterostructures of transition metal dichalcogenides (TMDs) may offer both excellent SS and high I_{ON}, particularly in the case of strained $MoTe_2/MoS_2$ system [5] that provides appropriate "broken gap" configuration of bandstructure. However, the performance of this device depends on the gate length and the SS strongly degrades when reducing the gate length below 20 nm.

Here, we propose a new design of this in-plane heterojunction TFET (see Fig. 1), where top gate and drain backgate are interconnected and both used to control the current through the device. TMDs were modeled with an atomistic 11-band tight-binding (TB) model including strain effects due to lattice mismatch between $MoTe_2$ and MoS_2 [6]. These TB Hamiltonians were introduced in an NEGF solver to compute the quantum transport (here in the ballistic approximation) self-consistently coupled to 2D Poisson's equation. As shown in Fig. 2, excellent *I-V* characteristics are obtained with SS as low as 5 mV/dec. More importantly, this performance is nearly independent of channel length, in contrast with standard TFET with same materials (Fig. 3). This Drain-Backgate Enhanced (DBE) TFET indeed provides an excellent control of the off-state whatever the channel length, as illustrated by LDOS pictures of Fig. 4.

[1] D. Esseni et al., Semicond. Sci. Technol. **32**, 083005 (2017).
[2] U. E. Avci et al., IEEE J. Electron Devices Soc. **3**, 88-95 (2015).
[3] A. W. Dey et al., IEEE Electron Device Lett. **34**. 211-213 (2013).
[4] Y. Gong et al., Nat. Mater. **13**, 1135-1142 (2014).
[5] J. Choukroun et al., Nanotechnol. **30**, 025201 (2019).
[6] S. Fang et al., Phys. Rev. B **98**, 075106 (2018).

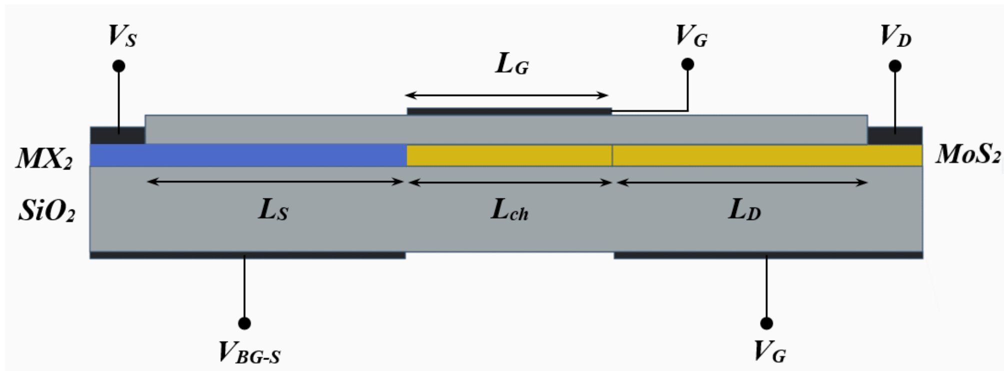

Fig.1: Device architecture for the considered DBE in-plane heterojunction TFETs. $MoTe_2$ is used for the source, and MoS_2 for channel and drain. 3.35 nm-thick SiO2 is used as a buried oxide, and a high-κ dielectric (EOT = 0.44 nm) as the top gate oxide. The same voltage is applied to the drain backgate and the top-gate so that $V_{BG-D} = V_G$.

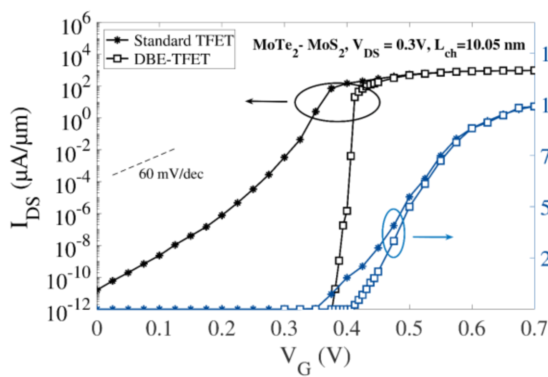

Fig. 2. I_D-V_{GS} characteristics of $MoTe_2/MoS_2$ standard-TFET and DBE-TFET with channel length L_{ch} = 10.05 nm for V_{DS} = 0.3V.

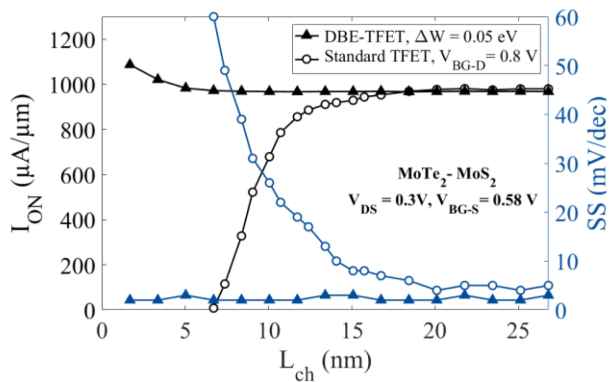

Fig. 3. Channel length dependence of I_{ON} and SS in standard-TFET and DBE-TFET (V_{DD} = 0.3 V).

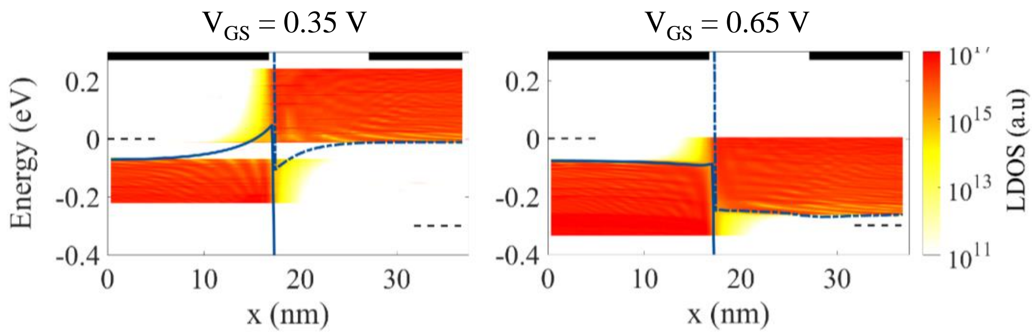

Fig. 4. LDOS, top of valence band (full lines) and bottom of conduction band (dotted lines) in DBE-TFET (L_{ch} = 10.05 nm) at V_{GS} = 0.35 V (left, off-state) and V_{GS} = 0.65 V (right, on-state), for V_{DS} = 0.3 V.

Fano Resonance in Ultra-Thin Body Double-Gate MOSFETs

P. B. Vyas[†], M. L. Van de Put[*], M. V. Fischetti[*]

[†] *Department of Electrical Engineering,* [*]*Department of Materials Science and Engineering*

The University of Texas at Dallas, 800 W. Campbell Rd., Richardson, TX 75080, USA

pbv130130@utdallas.edu

We report the numerical prediction of the Fano interference [1] phenomenon in ultra-thin body (UTB) double-gate (DG) MOSFETs. Fano interference has previously been reported in quantum waveguides [2] and coupled quantum dot systems [3]. Therefore, our observation of this purely quantum phenomenon in a realistic CMOS device structure presents a novel and intriguing case. Antiresonance is seen in the transmission spectra of electrons injected ballistically into the device at the energies of the quasi-bound states in the channel.

The device structure is shown in Fig. 1. Ballistic electron-transport in the device is simulated by solving the Schrödinger and Poisson equations self-consistently [4] in the two-dimensional plane of the device using the effective mass approximation. We follow the popular Quantum Transmitting Boundary method [5] to enforce *open* boundary conditions. Our self-consistent scheme bears resemblance to the method proposed by Fischetti [6].

Figures 2(a) and 2(b) show the transmission coefficient and local density-of-states (LDOS) in the simulated device. The LDOS distribution highlights the presence of quasi-bound states in the channel, while sharp dips of the transmission-coefficient plot indicate the occurrence of antiresonance at these bound-state energies. At a sufficiently high gate bias, the simulated current-density distribution in the device (Fig. 5(a)) shows the presence of channel inversion. At resonating frequencies, destructive interference between electrons traveling through the two coupled inverted channels causes the antiresonance 'dips' to appear in the transmission spectra. In the presence of this Fano interference, vortices are seen in the overall current density (Fig. 5(b)) at cryogenic temperatures. Moreover, when asymmetry is introduced by applying an unequal gate bias in this case, the transmission dips broaden (Fig. 3) and vortices in the current appear even at room temperature (Fig. 5(c)). We thus conjecture that, under the right conditions, the phenomenon can be observed experimentally. Finally, we will investigate if the antiresonance persists in the presence of electron-phonon scattering, modeled by incorporating the solution of Pauli's master equation into our self-consistent scheme.

[1] U. Fano, Phys. Rev. **124**, 1866 (1961).
[2] W. Porod *et al*., Phys. Rev. B **48**, 8495 (1993).
[3] K. Kobayashi *et al*., Phys. Rev. B **70**, 035319 (2004).
[4] P. B. Vyas *et al*., 2018 SISPAD, 1 (2018).
[5] C. S. Lent and D. J. Kirkner, J. Appl. Phys. **67**, 6353 (1990).
[6] M. V. Fischetti, J. Appl. Phys. **83**, 270 (1998).

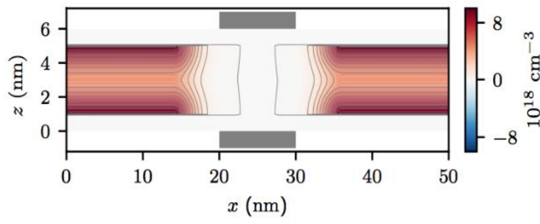

Fig. 1: Doping profile of 10 nm *UTB DG nMOS. The white region and the grey patches at the top and bottom represent the 1 nm thick gate oxide and gate terminals, respectively.*

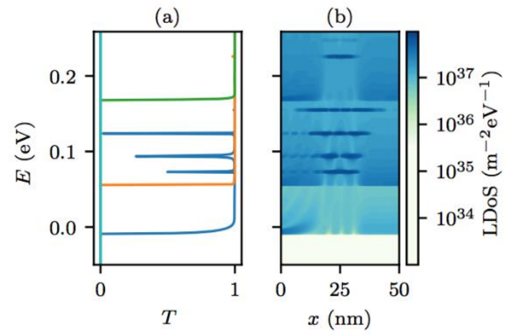

Fig. 2: (a) Transmission coefficient (T) vs. injection energy (E), (b) LDOS averaged over device thickness. The darker regions correspond to the quasi-bound states.

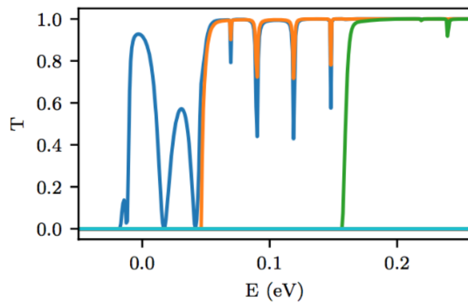

Fig. 3: Antiresonance features in the transmission spectra broaden in the presence of an asymmetric gate bias. The potential difference between the gates is 0.4 V.

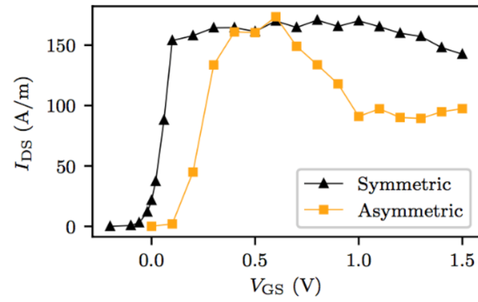

Fig. 4: Transfer characteristics of the device with equal (symmetric) and unequal (asymmetric) gate biases applied. Potential difference between gates is 0.4 V *for the latter case.*

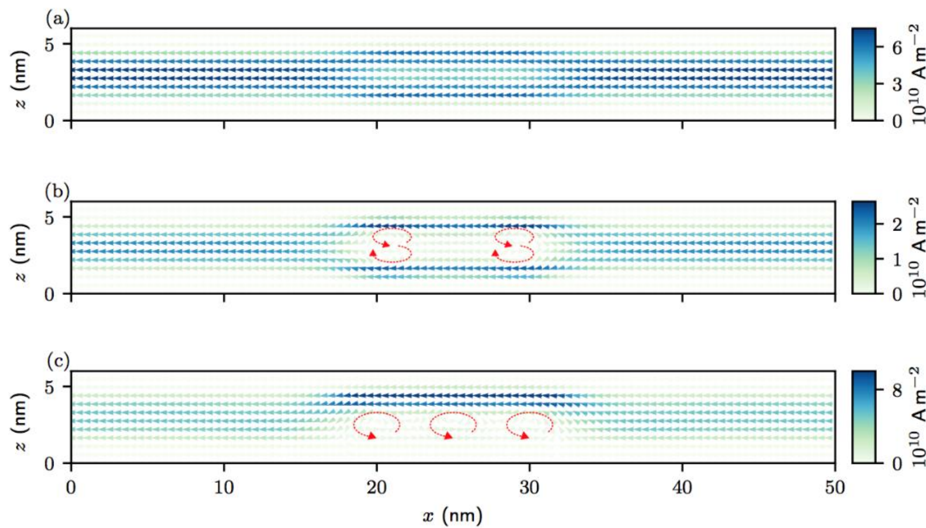

Fig. 5: Current-density distribution in (a) device with symmetric gate bias at 300 K*, (b) device with symmetric gate bias at 10* K*, and (c) device with asymmetric gate bias at 300* K*. The red arrows highlight the direction of vortices in the current density. V_{DS}=10* mV.

Full Quantum Time-Dependent Simulation of Electron Devices with Linear 2D Band Structures: Holes or Electrons with Negative Kinetic Energy?

Z. Zhan[1,2], X. Kuang[1], E. Colomés[2],
D. Pandey[2], S. Yuan[1], X. Oriols[2]
[1]*School of Physics and Technology, Wuhan University, Wuhan 430072, China*
[2]*Departament d'Enginyeria Electrònica, Universitat Autònoma de Barcelona, 08193, Bellaterra (Barcelona), Spain*
zhenzhanh@gmail.com, xavier.oriols@uab.cat

During the past years, two-dimensional (2D) materials have been extensively explored to minimize some fundamental challenges encountered in the new-generation of transistors. Some novel physical phenomena, Klein tunneling for example, make the accurate modeling of 2D materials different from that of traditional bulk ones, and need to be properly tackled and flexibly adopted to the device simulator [1,2]. In this conference, a Monte Carlo time-dependent solution of the Dirac equation is presented for full (DC, AC, transient and noise) quantum simulations of electron devices with linear band 2D materials, like graphene in Fig.1 [3,4].

In order to simplify the computational burden of the electron device simulation, carriers with positive kinetic energy are considered as electrons in the conduction band (CB) while carriers in the valence band (VB) are traditionally modelled with the concept of holes (absence of electrons). However, the use of holes in linear 2D materials implies an unphysical treatment of the Klein tunneling process by an *artificial* electron-hole generation, see Fig.2(c). The instantaneous total current $\mathrm{I(t)}$ in the *artificial* Klein tunneling process in Fig.2 (c) is different from that in Fig.2 (b). Consequently, it introduces unphysical results at high-frequency outputs. For instance, the transit time $t_e - t_G$, which determines the cut-off frequency of graphene transistors [5], is much shorter than that of the physical value $t_e - t_0$ in Fig.2(b). This problem simply disappears when treating carriers in the VB as electrons with negative kinetic energy.

In conclusion, the injection of electrons with positive and negative kinetic energies are mandatory to properly simulate the high-frequency electron device characteristics with Klein tunneling in gapless materials like graphene. Numerical results in Figs.3-5 validate the correctness of this *natural* Klein tunneling treatment, which has been implemented in home-made BITLLES simulator (by defining the wave nature of electrons as a bispinor solution of the Dirac equation and its particle nature as a Bohmian trajectory) to study quantum transport for DC, AC and transient in graphene field effect transistors (GFETs).

[1] E. Colomes, Z. Zhan, D. Marian and X. Oriols, Phys. Rev. B, **96**, 075135 (2017).

[2] http://europe.uab.es/bitlles

[3] X. Oriols, Phys. Rev. Lett., **98**, 066803 (2007).

[4] Z. Zhan, X. Kuang, E. Colomes, D. Pandey, S. Yuan and X. Oriols, submitted.

[5] Z. Zhan, E. Colomes and X. Oriols, IEEE Trans. Electron Devices, **64**, 2617 (2017).

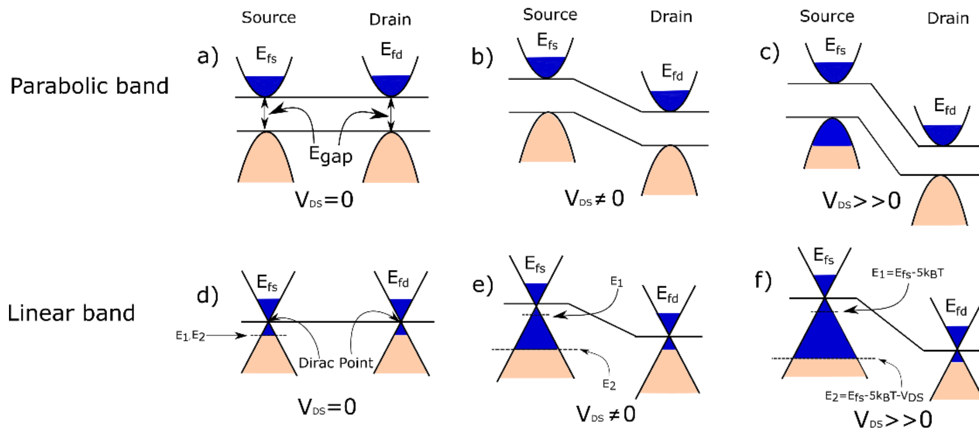

Fig.1: Schematic representation of the energy band structure as a function of the source and drain position for a device with applied bias. The figures (a), (b)and (c) correspond to a device with parabolic CB and VB separated by an energy bandgap E_{gap} with different bias conditions, while the (d), (e) and (f) correspond to a gapless material with linear CB and VB.

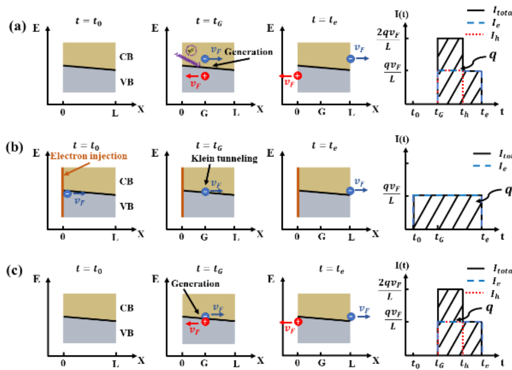

Fig,2: Schematic representation of (a) electron-hole generation due to light absorption, (b) Klein tunneling process modeled by one electron injected from the source, traversing from VB to CB, and arriving at the drain contact, (c) Klein tunneling modeled as an electron-hole generation at time t_G at $x = G$. The processes depicted in (a) and (b) provide the correct instantaneous current plotted in the right column. However, when modeling high-frequency properties, unphysical predictions results from the treatment of the Klein tunneling in inset (c).

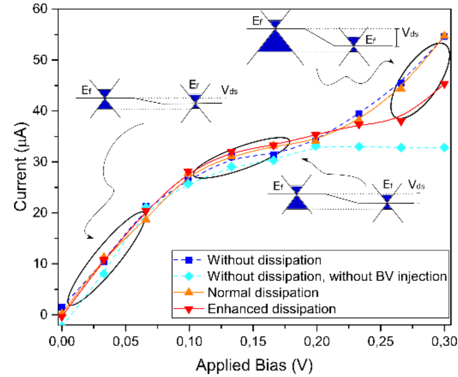

Fig4: Current-voltage characteristic for four dual-gate FETs. The dashed lines depict the ballistic transport where the dark blue (square) one represents graphene injection (electrons injected from both CB and VB) current-voltage characteristic and the light blue (diamond) line represents only electrons injected from the CB. In the orange solid curve, dissipation due to acoustic and optical phonons are taken into account. The red solid line represents enhanced scattering

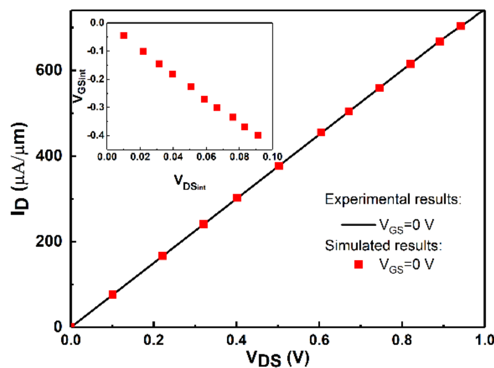

Fig.3: The current-voltage characteristic for a GFET computed (red square) from BITLLES simulator compared with experimental results (black lines). The red square in the inset corresponds to the intrinsic gate-source voltage $V_{GS_{int}}$ and drain-source voltage $V_{DS_{int}}$ used to simulate the drain current I_D in the BITLLES simulator. The simulation and experimental results show quantitative agreement.

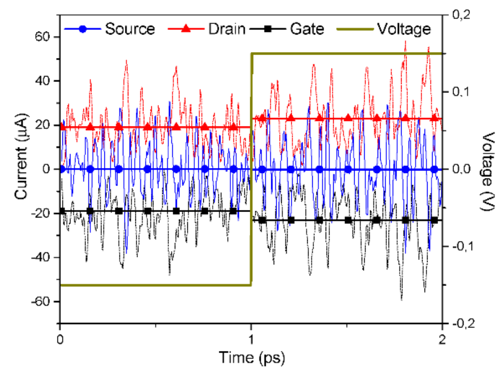

Fig.5: The transient current in a dual-gate FET. Initially both (top and bottom) gate voltages are set to $V_{bg} = V_{tg} = -0.15\ V$, at time $t = 1\ ps$ these values are changed to $V_{bg} = V_{tg} = 0.15\ V$.

A Mathematical Extension to Knudsen Diffusion Including Direct Flux and Accurate Geometric Description

L. F. Aguinsky[1], P. Manstetten[2], A. Hössinger[3],
S. Selberherr[2], J. Weinbub[1]
[1]Christian Doppler Laboratory for High Performance TCAD at the
[2]Institute for Microelectronics, TU Wien, Gußhausstraße 27-29/E360, 1040 Wien, Austria
[3]Silvaco Europe Ltd., Compass Point, St Ives, Cambridge PE27 5JL, United Kingdom
aguinsky@iue.tuwien.ac.at

As device designs become three-dimensional, modern semiconductor manufacturing technology must evolve to enable high aspect ratio (AR) features [1]. One critical challenge in high AR processing is the depletion of neutral species towards the bottom of a feature. In deposition cases, depletion manifests itself as a decline in step coverage [2], while in etching it is linked to AR dependent etching [3]. The defining characteristic of neutral species transport is isotropic reflections on the surface [2], which motivates two common modeling approaches: Radiosity [4] and Knudsen diffusion [2]. Radiosity is the exact formulation of the net exchanges between all surfaces, including a particle source. However, it requires the inversion of a matrix describing these exchanges. Otherwise, the Knudsen diffusion approach rests on physically-motivated approximations to the mass balance to provide a coarser but more insightful description, enabling an intuitive understanding of the effects of the parameters. We propose an extension to the standard Knudsen diffusion approach (Figs.1,2) by including the direct flux from a source and a geometric factor. The direct flux stems from the radiosity approach but avoids the costly matrix inversion by disregarding reflections. The geometric factor is obtained from an integral over the whole geometry performed at each differential cross section. It allows for a more accurate description of the indirect flux due to reflections. We verify this novel approach (Fig.3) against our reference radiosity model for a finite cylinder [4], obtaining good agreement (Fig.4). We show that the infinite cylinder approximation, used in standard Knudsen diffusion [2], fails near the extremities of finite cylinders (Fig.5) and that the hydraulic diameter approximation for rectangular trenches [5] has inadequate asymptotic behavior (Fig.6).

Acknowledgments. The financial support by the Austrian Federal Ministry of Science, Research and Economy, and the National Foundation for Research, Technology and Development is gratefully acknowledged.

[1] C.G.N. Lee et al., J. Phys. D: Appl. Phys. **47**, 273001 (2014).
[2] A. Yanguas-Gil, Growth and Transport in Nanostructured Materials (Springer, 2017).
[3] K. Ishikawa et al., Jpn. J. Appl. Phys. **56**, 06HA02 (2017).
[4] P. Manstetten et al., Solid-State Electron. **128**, 141 (2017).
[5] M. Ylilammi et al., J. Appl. Phys. **123**, 205301 (2018).

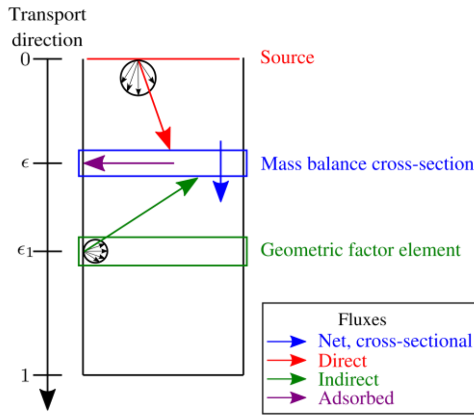

Fig.1: Schematic representation of the model. The goal is to obtain the net, cross-sectional flux through the mass balance volume (blue) by balancing the direct (red), adsorbed (purple), and indirect (green) fluxes. The complete indirect flux contribution is obtained by integrating over all ϵ_1 (green elements).

Extended Knudsen diffusion

Standard Knudsen diffusion

$$\tilde{j}(\epsilon) = F_D(\epsilon) + g(\epsilon) \times \tilde{D}_{Kn} \times \frac{d\psi}{d\epsilon}$$

$$\frac{d\tilde{j}}{d\epsilon} = k \times \psi(\epsilon)$$

$\tilde{j}$: Normalized, net, cross-sectional flux
ψ : Normalized concentration
ϵ : Normalized axial distance
F_D : Direct flux
g : Geometric factor
$\tilde{D}_{Kn}$: Normalized Knudsen diffusivity
k : Surface adsorption rate

Fig.2: Schematic representation of the system of ordinary differential equations modeling neutral transport. The colors relate to Fig.1. We note the differences between our model and the standard Knudsen diffusion approach [2]: The presence of direct flux and the geometric factor. The adsorbed flux is modeled by a volumetric sink term, as in [2].

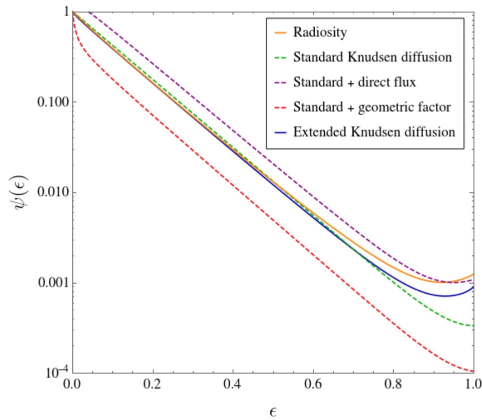

Fig.3: Comparison of the local concentration between different approaches for a cylinder of AR 50 and sticking 1%. We note that the full extended Knudsen diffusion approach is required for more accurately matching radiosity [4] over most of the feature.

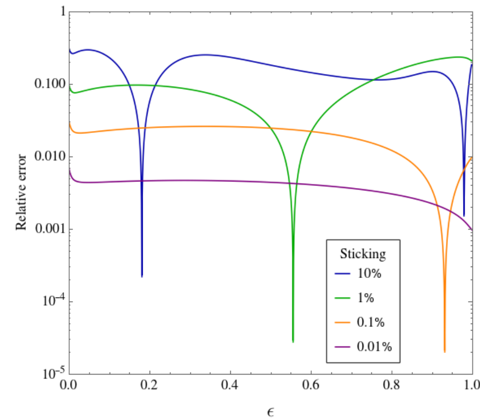

Fig.4: Local relative error, defined as the relative difference between the extended Knudsen diffusion and radiosity [4] results, for a cylinder of AR 50 and varying sticking. Here, we showcase how our model produces adequate results even in high sticking regimes.

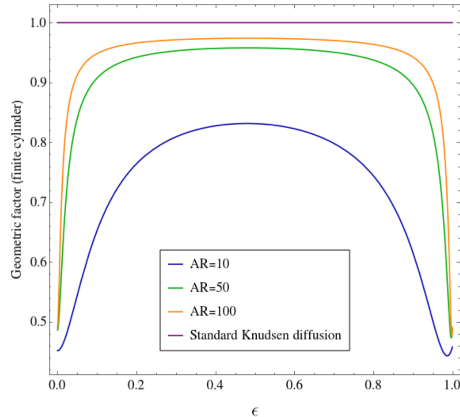

Fig.5: Geometric factor as a function of axial distance ϵ for a finite cylinder of sticking 1% and varying ARs. Our model highlights significant discrepancies in the standard approach [2] for the extremities of the cylinder even for high ARs.

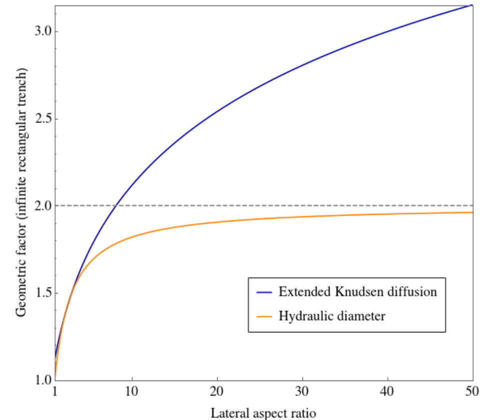

Fig.6: Geometric factor for a rectangular trench of infinite length, for each lateral AR, given by our model and by the hydraulic diameter approximation [5]. Our model has divergent asymptotic behavior. This is expected, as the problem is intrinsically three-dimensional.

TCAD Analysis of Leakage Currents in the Ballistic Regime

P. Aguirre, S. Sant, A. Schenk
Integrated Systems Laboratory, ETH Zurich, Gloriastrasse 35, CH-8092 Zurich, Switzerland
adelia@iis.ee.ethz.ch

Introduction: In this work it is demonstrated how ballistic mobility (μ_b) models [1,2] affect the leakage currents in ultra-short FETs using a semi-classical device simulator [3,4]. Method: The test device and relevant parameters are shown in Fig. 1. Ballistic I_D-V_{GS} characteristics obtained from the quantum-transport tool QTx [5] served as reference. Source-to-drain tunneling (STDT) which dominates the sub-threshold current at ultra-short gate lengths [6] was simulated by the default "Non Local Tunneling" (NLT) model implemented in [4]. Two μ_b-models where used to better match the ON-current (I_{ON}) with the QTx reference. The first has a ballistic electron velocity (v_b) dependent on the quasi-Fermi potential (QFP) ψ_n [1,2]. In the second, v_b is a function of the electron density n_{TOB} at the top of the source-to-drain potential barrier [1]. A leakage mechanism inherent in DG transistors and FinFETs is the floating-body effect (FBE) [7] caused by band-to-band tunneling (BTBT) and affected by Shockley-Read-Hall (SRH) recombination. Models available in [4] were used in the TCAD simulations.
Results: Fig. 2a shows that the $v_b(n_{TOB})$-model can well reproduce the quantum-ballistic I_{ON}, but the sub-threshold current becomes corrupted. This can be traced back to the deformation of $\psi_n(x)$ (see Fig. 2b). As the STDT rate of the NLT model is computed with the local QFPs at the classical turning points (x_t) for each tunnel path, the deformed $\psi_n(x)$ artificially suppresses the tunnel current. The red curve in Fig. 3 was obtained by a post-processing calculation of the STDT current using the contact Fermi levels in the NLT model instead of $\psi_n(x_t)$. This removes the artifact in the deep sub-threshold range (first two points), but quickly leads to deviations from the self-consistent TCAD solution which contains the ordinary drift-diffusion current. The ballistic velocity models also impact the BTBT rates which locally depend on the QFPs (see Fig. 5a). The transfer curves in Fig. 4 (with BTBT+SRH added to STDT) exhibit the additional FBE-induced leakage current. The stronger sensitivity of the BTBT rate to the $v_b(n_{TOB})$-model as compared to the $v_b(\psi_n)$-model can be traced back to a stronger deformation of $\psi_n(x)$ in the channel-drain junction where the electron BTBT rate is maximal (Fig. 5b). The relative effect is not much changed even at an extreme rate of $\sim 10^{32}$ cm^{-3}s^{-1} (see Fig. 6).

[1] P. Aguirre et al., Solid-States-Electronics, accepted, 2019. [2] O. Penzin et al., IEEE T-ED **64,** 2017. [3] M. Ieong et al., IEDM, 1998. [4] Synopsys Inc., Sentaurus Device User Guide, V-2016.03, 2016. [5] M. Luisier et al., Jour. Appl. Phys. **100**(4), 043713, (2006). [6] F. Heinz et al., Jour. Appl. Phys. **100**(8), 084314, 2006. [7] S. Sant et al., IEEE T-ED **65** (6), 2578-2584, 2018.

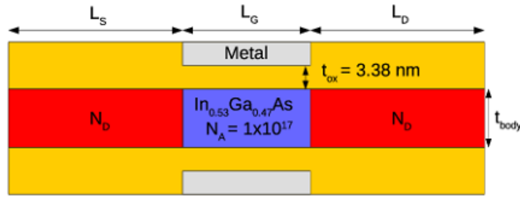

Fig.1: Schematic of an $In_{0.53}Ga_{0.47}As$ double-gate (DG) ultra-thin-body FET. Parameters: $N_D = 5x10^{19}\ cm^{-3}$, $L_S = 20$ nm, $L_G = 11.5$ nm, $t_{body} = 4.2$ nm, and $m_e = 0.0678\ m_0$.

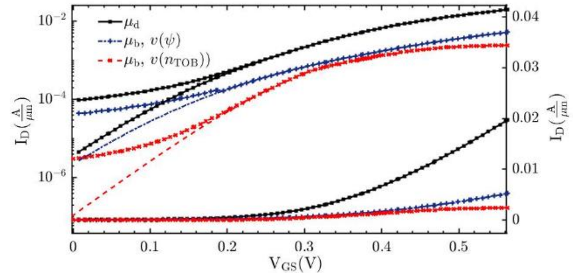

Fig.4: I_D-V_{GS} characteristics at $V_{DS} = 1$ V of the device depicted in Fig. 1 for different electron mobilities ($\mu_d = 1x10^3\ cm^2/Vs$, $\mu_b[v(\psi_n)]$, and $\mu_b[v(n_{TOB})]$) with $m_e = 0.0678\ m_0$, $m_h = 0.446\ m_0$, and SRH lifetimes $\tau_e = \tau_h = 1$ ns. The actual band gap of $E_G = 1.7$ eV caused by the strong confinement was lowered to $E_G = 0.7$ eV in order to enhance the effect of BTBT. Curves without BTBT are shown for comparison (dashed and dot-dashed lines).

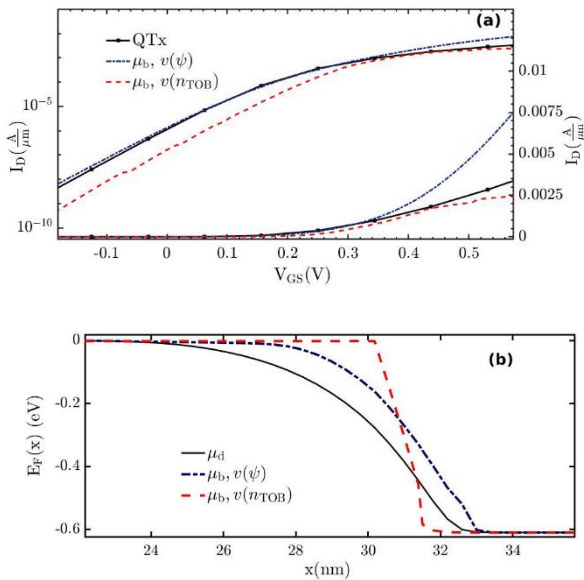

Fig.2: (a) I_D-V_{GS} characteristics at $V_{DS} = 0.61$ V of the device depicted in Fig. 1 with a tunnel mass $m_t = m_e$. (b) Fermi energy profiles $-e\psi_n(x)$ for different electron mobilities ($\mu_d = 1x10^3\ cm^2/Vs$, $\mu_b[v(\psi_n)]$, and $\mu_b[v(n_{TOB})]$), all extracted at $V_{GS} = -0.2$ V and $V_{DS} = 0.61$ V.

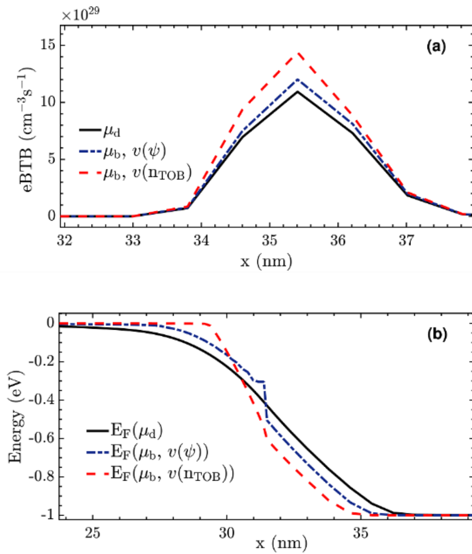

Fig.5: (a) Electron BTBT rates for different electron mobilities ($\mu_d = 1x10^3\ cm^2/Vs$, $\mu_b[v(\psi_n)]$, and $\mu_b[v(n_{TOB})]$) extracted at $V_{GS} = 0$ V and $V_{DS} = 1$ V. Parameters are the same as in Fig. 4. (b) Corresponding profiles of the electron Fermi energy $-e\psi_n(x)$.

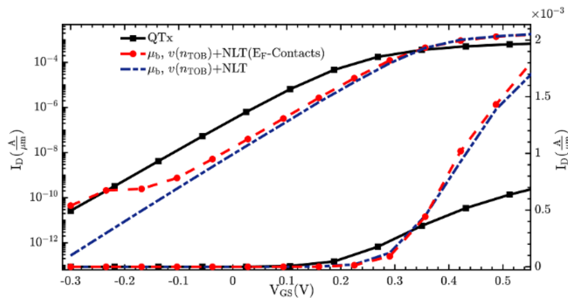

Fig.3: I_D-V_{GS} characteristics at $V_{DS} = 50$ mV of the device depicted in Fig. 1 with a tunnel mass $m_t = m_e$. The red curve was obtained by a post-processing calculation of the STDT current using the contact Fermi energies in the NLT model instead of local QFPs.

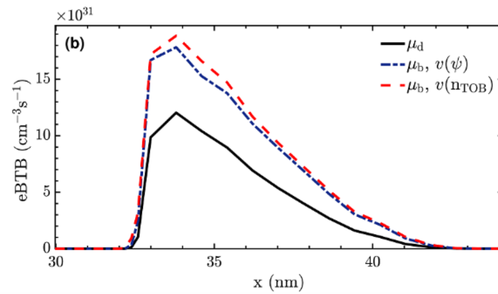

Fig.6: Electron BTBT rates for different electron mobilities ($\mu_d = 1x10^3\ cm^2/Vs$, $\mu_b[v(\psi_n)]$, and $\mu_b[v(n_{TOB})]$) extracted at $V_{GS} = 0$ V and $V_{DS} = 2.5$ V.

Fast Volume Evaluation on Sparse Level Sets

X. Klemenschits, S. Selberherr, L. Filipovic
Institute for Microelectronics, TU Wien
Gußhausstraße 27-29/E360, 1040 Vienna, Austria
klemenschits@iue.tuwien.ac.at

Implicit surface representations such as the level set method, as often applied in process simulations [1], usually only represent the interfaces between materials, rather than the full volume of a material itself. This limits the accurate representation of diffusion and the effects of chemical reactions taking place inside a material. Therefore, diffusive processes cannot be modelled directly, but demand regular conversions to a volume representation, requiring computationally costly algorithms. As an alternative, we propose a fast ray tracing algorithm to evaluate the effective volume of a material layer directly on the implicit surface with sub-grid resolution, eliminating the need for a costly volume conversion. Our algorithm is implemented in ViennaTS [2], a level set powered topography simulator. As a relevant application, a polymer stabilisation step, a so-called N_2 flash, performed during gate stack etching [3], was simulated. This fabrication step reduces the volume of a thin layer proportionally to the initial layer volume [4]. Therefore, the volume of the material to be reduced must be known to model this process accurately. Diffusion processes simulated by ray tracing, monitor the path each incoming particle takes through the volume of a material. This is computationally costly due to the large number of rays needed to describe the process. A bottom-up approach [5], where rays are reversely followed from the bottom interface and counted on the top interface, can be used instead, which is shown in Fig. 1. The combination of the path length and distribution of rays on the top interface provides an approximation of the volume accessible to particles diffusing from the top surface. Normalising the length of the rays, as shown in Fig. 2, gives an approximation of the effective volume of the material below each surface point. The effect of the normalisation for the trench geometry shown in Fig. 3, can be seen in Fig. 4, which highlights the discrepancy between pure ray counts per surface element and the effective volume. The simulation of the N_2 stabilisation process step, using the three test geometries, shown in Fig. 3 and Fig. 5, is able to adequately describe the etch process. The developed method can also be applied to a variety of diffusive and volume-dependent processes, such as ion implantation or oxidation without the need for compute-expensive volume extraction. The results of the simulation of a diffusion limited deposition process are shown in Fig. 6.

[1] S. Osher and J. A. Sethian, J. Comput. Phys., **79**(1), p. 12-49, (1988).
[2] ViennaTS. [Online]. Available: http://www.iue.tuwien.ac.at/software/viennats
[3] X. Klemenschits, S. Selberherr, and L. Filipovic, in Proc. EUROSOI-ULIS, pp.1-4, 2018.
[4] O. R. Bengoetxea, Ph.D. dissertation, Université Grenoble Alpes, 2016.
[5] P. L. Manstetten, Ph.D. dissertation, Technische Universität Wien, 2018.

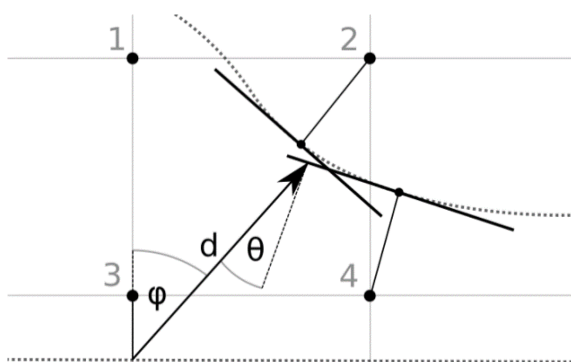

Fig.1: Ray tracing on an implicit surface by approximating the surface using discs [2] shifted from each grid point to the surface by the level set value in the direction of the normal vector. A ray with start and intersection angles of φ and θ, respectively, travels a distance d. The number of rays and their properties are stored in the data structure for each grid point of the top level set.

$$\bar{d}_i = \sum_{j=0}^{N} d_j cos^n(\theta_j) cos^m(\phi_j)$$

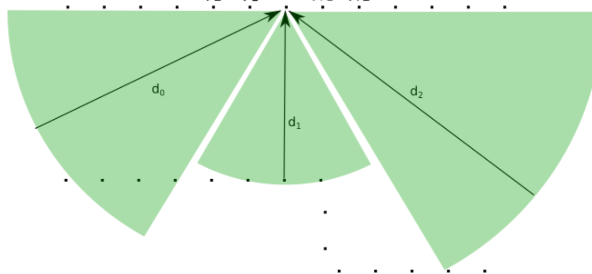

Fig.2: Normalisation of ray distances via power cosine distributions of the start and intersection angle. The powers were chosen as n=m=2 for minimum simulation time while still providing reliable results. The dots correspond to the active level set points, used to define the location of the surface when sparse level set methods are used.

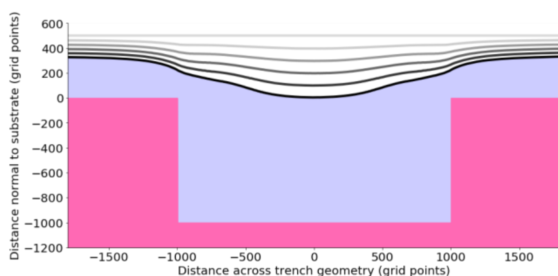

Fig.3: Surface evolution of a thin passivation layer during an N_2 flash process step, obtained from volume dependent etch models. The evolution of the top level set above a trench geometry is shown from light grey as the initial surface to dark grey for the final profile. The substrate and the thin layer are shown in pink and blue respectively.

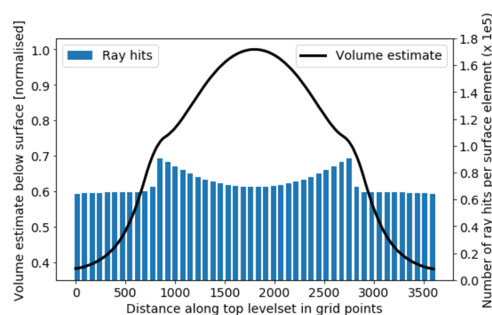

Fig.4: Volume estimate of a trench geometry underneath a plane, given in Fig. 3. The estimated volume (black line) is shown in comparison to the number of rays incident on the surface (blue bars), highlighting the strong effect of the angle dependence on the final profile, which adequately balances the abrupt increase of ray hits due to the sharp edge in the geometry.

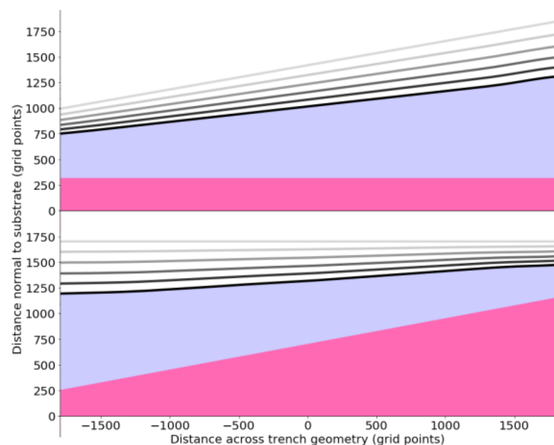

Fig.5: Comparison of two thin layers (blue) on a substrate (purple) during the N_2 flash process, with linearly increasing thickness. Areas with higher volume reduce quicker than those with less volume. The evolution of the top layers' locations over time is shown from light grey for the initial surface to dark grey for the final profile.

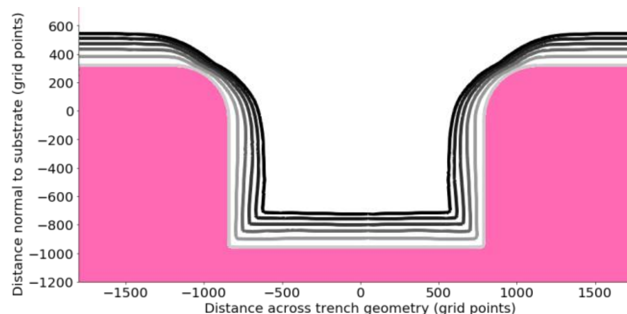

Fig.6: Surface evolution of diffusion limited growth, achieved by considering the volume particles have to diffuse through, in order to react with the surface below. The reacting substrate is shown in purple while the time evolution of the material growing above is shown from light grey to dark grey for the final profile.

Effects of Repulsive Dopants on Quantum Transport in a Nanowire

M. Ballicchia[1,2], M. Nedjalkov[1], J. Weinbub[3]
[1]Institute for Microelectronics, TU Wien, Austria
[2] Department of Information Engineering, Università Politecnica delle Marche, Italy
[3] Christian Doppler Laboratory for High Performance TCAD at the
Institute for Microelectronics, TU Wien, Austria
ballicchia@iue.tuwien.ac.at

We present an analysis of quantum coherent transport inside a nanowire in presence of a repulsive dopant [1]. In particular, we focus on the current that flows inside the nanowire and which depends on the potential energy of the dopant. The latter is modeled by a screened Coulomb potential centered in the middle of the wire. The electron evolution has been studied by using the Wigner transport equation:

$$\left[\frac{\partial}{\partial t} + \frac{\mathbf{p}}{m} \cdot \nabla_r\right] f_w(\mathbf{r}, \mathbf{p}, t) = \int d\mathbf{p}' \, V_w(\mathbf{p} - \mathbf{p}', \mathbf{r}) f_w(\mathbf{r}, \mathbf{p}', t) \quad . \tag{1}$$

Pure states corresponding to Gaussian wave packets are injected from the bottom contact, which in particular avoids the decoherence effects characterizing ohmic contacts [2]. The chosen formalism allows to treat both the quantum and the classical evolution in the same framework, allowing to conveniently highlight the quantum effects. A stochastic reformulation of the Wigner transport model named the signed-particle approach is used [3]. In this formulation the Wigner function is modeled by numerical particles that evolve in the phase space along forceless Newtonian trajectories as suggested by the left-hand side of (1). The quantum effects are governed by the Wigner potential V_w, obtained from the electric potential of the dopant. V_w determines the generation of couple of particles, with opposite sign. The Wigner function in the phase space cells is given by the sum of the sign of the particles inside, legitimizing the annihilation of particles with opposite sign in the same cell. The current density inside the nanowire can be determined as the first order moment of the Wigner function,

$$\mathbf{J}(\mathbf{r}, \mathbf{p}, t) = n(\mathbf{r}, t) \;\; \mathbf{v}(\mathbf{r}, t) = \frac{1}{m} \int \mathbf{p} f_w(\mathbf{r}, \mathbf{p}, t) d\mathbf{p} \quad . \tag{2}$$

Fig. 1a) and Fig 1b) show the current density inside the nanowire in the classical and in the quantum case, respectively, with a 0.35 eV dopant. In contrast to the classical case, where the current density after the dopant is established by the boundary reflection, the quantum current is distributed due to a complicated interplay of reflection, nonlocal action of V_w, and tunneling effects [1]. As a consequence, the total current inside the nanowire is higher in the quantum case, as shown in Fig. 2. However, both the classical and the quantum case offer lower currents as compared to the case where no dopant is present. In Fig. 3, we show the decrease of the current with the increase of the dopant potential. Fig. 4 shows the ratio between the quantum and the classical current that starts from 1.0, in absence of the dopant, to around 1.1 (a 10% increase) for a 0.35 eV dopant.

The research particularly illustrates why a global treatment is needed to model quantum current transport as the results can be different for closed physical setups as illustrated by the considered density and current behavior.

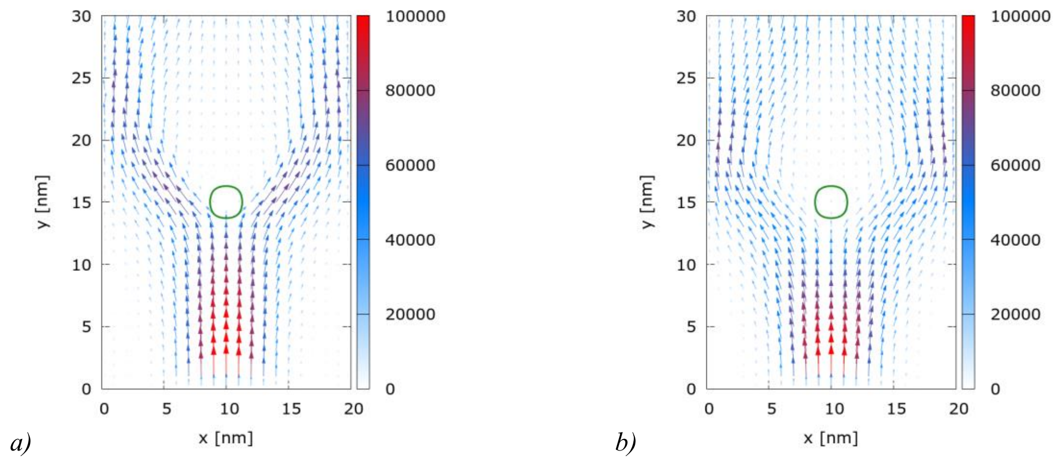

Fig.1: Current density around a dopant with a 0.35 eV peak potential energy, that is represented by the green 0.15 eV isoline: a) classical evolution, b) quantum coherent evolution.

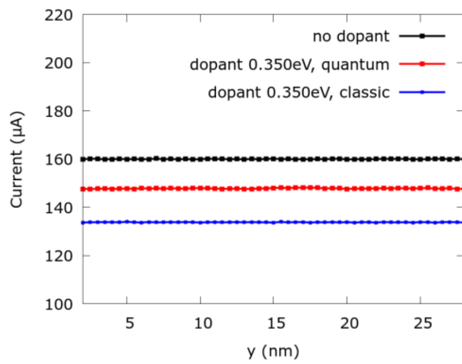

Fig.2: Current inside the nanowire without dopants (black) and with a 0.35 eV repulsive dopant placed in the center: quantum case (red), classical case (blue).

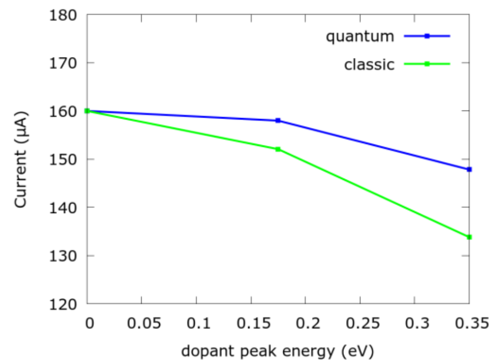

Fig.3: Classical and quantum current inside the nanowire as function of the potential energy of the repulsive dopant

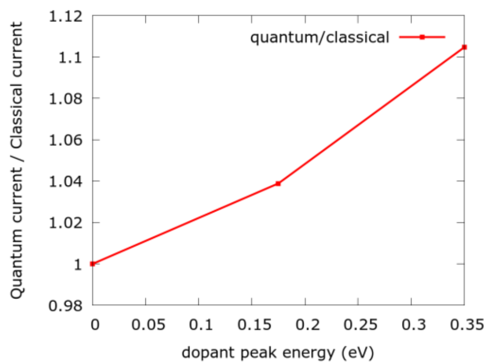

Fig.4: Ratio between quantum and classical current as function of the potential energy of the (repulsive) dopant.

Acknowledgment: The financial support by the Austrian Science Fund (FWF) project FWF-P29406-N30, the Austrian Federal Ministry of Science, Research and Economy, and the National Foundation for Research, Technology and Development is gratefully acknowledged. The computational results presented have been achieved using the Vienna Scientific Cluster (VSC).

[1] M. Ballicchia, J. Weinbub, M. Nedjalkov, Nanoscale **10**, 23037 (2018)

[2] I. Knezevic, Phys. Rev. B **77**, 125301 (2008)

[3] P. Ellinghaus, Ph.D. Dissertation, Technische Universität Wien (2016)

Mobility Modeling of Split-gate GaN Nanowires

V. N. Kumar[1], D. Vasileska[1]
[1]School of Electrical, Computer and Energy Engineering,
Arizona State University, Tempe, AZ-85281
vkumar21@asu.edu

This work aims to develop a low-field electron mobility model for GaN nanowires. Nanowires being quasi-1D systems exhibit transport properties significantly differing from their bulk counterparts. Investigation of electron – phonon scattering mechanisms in confined systems is necessary to provide insight into transport dynamics. The split-gate nanowire considered in this work consists of an AlGaN/AlN/GaN heterostructure and two gates as shown in Figure 1. Application of a negative potential at the split-gates creates a 2D potential well at the AlN/GaN heterointerface. A self-consistent 2D Schrödinger-Poisson solver is implemented which determines the subband energies and the corresponding wavefunctions of the confined system. Figures 2 and 3 show the confining potential superimposed over electron density profiles in the nanowire. Figure 4 shows the lowest 15 subband energies with their corresponding line densities. Three scattering mechanisms: acoustic phonon scattering, polar optical phonon scattering and piezoelectric scattering are considered to account for the electron phonon interactions in the system. Overlap integrals and 1D scattering rate expressions are derived for all the mechanisms listed. A generic one-dimensional Monte Carlo solver is also developed. Due to the high optical phonon energy in GaN, piezoelectric scattering is the only electron-phonon scattering mechanism found to be dominant at low fields. Steady state results for subband velocity and subband energies from the 1D Monte Carlo solver are extracted to determine the low field mobility of the GaN nanowires. The results for phonon limited electron mobility predicted by the model (3140 cm^2/V.s) are consistent with experimental results for a similar highly intrinsic, pure AlGaN/GaN radial nanowire [1]. Figure 5 compares the electron mobility determined from the model for various temperatures versus the experimental results of a similar highly intrinsic AlGaN/GaN nanowire. Since this structure uses split-gates to achieve electrostatic confinement in the x-direction, interface-roughness scattering is a factor only along the y-direction. The interface roughness scattering, combined with the quantum confined stark effect due to the presence of high electric field at the AlN/GaN interface, will play a role at lower temperatures [2]. The contribution of total interface roughness scattering to the electron mobility at lower temperatures is currently being studied and will be presented at the conference.

[1] Y. Li, J. Xiang, F. Qian, S. Gradecak, Y. Wu, H. Yan, D. A. Blom and C. M. Lieber, "Dopant-free GaN/AlN/AlGaN radial nanowire heterostructures as high electron mobility transistors," *Nano letters,* vol. 6, no. 7, pp. 1468-1473, 2006.

[2] R. K. Jana and D. Jena, Stark-effect scattering in rough quantum wells," Applied Physics Letters 99, 012104 (2011), https://doi.org/10.1063/1.3607485.

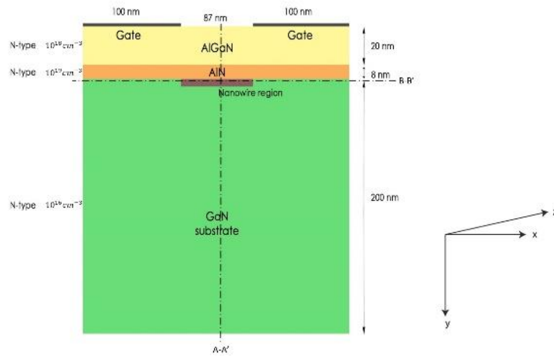

Fig.1: The split-gate nanowire structure used in this work.

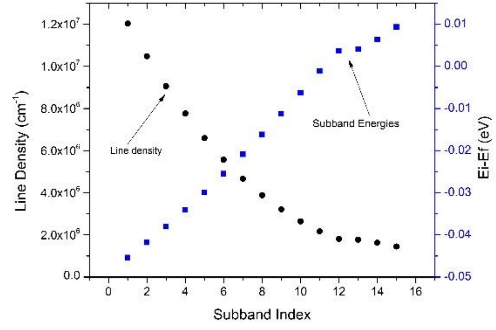

Fig 4: Subband energies and line densities of the lowest 15 subbands in the nanowire.

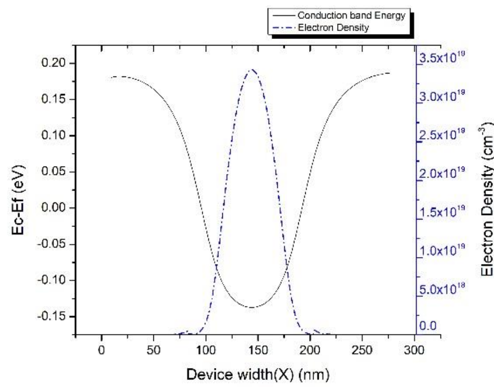

Fig.2: Conduction band profile and Electron density along x axis (Cutline A-A').

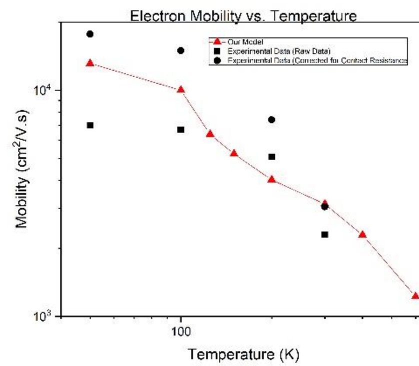

Fig 5. Comparison of electron mobility obtained by this model with the experimental results taken from Ref. [1].

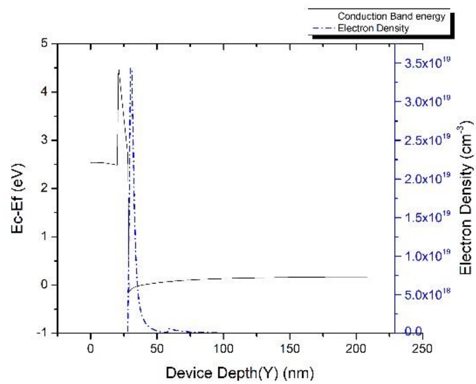

Fig 3. Conduction band profile and Electron density along y axis (Cutline B-B')

Random Telegraph Noise of Gate-All-Around Silicon Nanowire MOSFETs Induced by Single Charge Trap

S. R. Kola, Y. Li*

Parallel and Scientific Computing Laboratory, Department of Electrical and Computer Engineering, National Chiao Tung University, Ta-Hsueh Rd. 1001, Hsinchu 300, Taiwan

ymli@faculty.nctu.edu.tw

We for the first time study random telegraph noise (RTN) of cylindrical shape gate-all-around silicon nanowire (GAA Si NW) metal-oxide-semiconductor field effect transistors (MOSFETs) with spacer induced by acceptor-type single-charge trap for sub-7-nm technologies. For GAA NW MOSFETs, the trap position dependence on the RTN magnitude (($\Delta I_D/I_D$) ×100%) in channel is observed. The impact of RTN located middle of the channel is significant. The reduction of on-state current of the explored device with and without spacer are 9.3% and the gate capacitance can be reduced up to 18.56%. Gate-all-around silicon nanowire MOSFET is a promising device for sub-7-nm technology nodes owing to its ultimately electrostatic controllability and good short channel effects (SCE) immunity [1-3]. In this work, we study the transfer characteristic (I_D-V_G) and gate capacitance (C-V) of device with spacer. Random telegraph noise influenced by acceptor-type single charge trap (SCT) presenting at different positions along the channel [4-6] between silicon and silicon dioxide for N-type GAA Si NW MOSFET devices by using an experimentally validated 3D device simulation under the similar parameters settings. The magnitude of RTN induced by cylindrical-type SCT along the channel is estimated for the nominal GAA Si NW MOSFET and the device with spacer. At the drain due to band-to-band tunneling the reduction of RTN is caused. By extracting SCE parameters, we discuss characteristic variability induced by SCT. We observe that the magnitude of RTN is high at the SCT middle (i.e., B of Fig. 1(a)) position to source and drain. Figures 1(c) and (d) illustrate the simulated structures for nominal and with spacer GAA Si NW MOSFETs devices. Figures 1(a) and (b) show the positions of SCTs and cross-section view of the channel respectively. The density of interface trap (D_{IT}) is greater than 10^{12} cm^{-2}. This simulation is examined by solving 3D quantum-mechanically corrected transport model which is valid by nonequilibrium green function (NEGF) [1]. We express the simulation results, evaluate I_D-V_G electrical characteristics variability due to spacer is shown in Fig. 2; here, the SiO_2 acts as low-□□dielectric material. The spacer acts like capacitor. The reduction of on-state current of the explored device with and without spacer are 9.3%. Similarly, for the C-V analysis, the capacitance varies largely due to dielectric charging and discharging, which we can clearly observe from Fig. 3. However, for realistic nano-CMOS technologies, the dependence of RTN not only on device geometry but also the trap's location and energy. Figures 4 and 5 illustrate the amplitude of the RTN in the presence of SCT (by calculating the deviation $\Delta I_D/I_D$ x 100%.) due to trapping/de-trapping in different location for nominal device and the device with spacer, respectively. The amplitude of RTN decreases with increasing V_G due to the low charge carriers. Finally, The RTN amplitude is large when SCT is placed at the position B. As listed in Tab. 1, we compare the magnitudes of RTN for the nominal GAA Si NW MOSFET and the device with spacer, respectively, at the off-state for both doped and undoped channels. Notably, for the device with spacer and undoped channel, the large magnitude of RTN is observed for the trap at position B. In summary, we have investigated the SCT induced RTN; and, for device with spacer and undoped channel, the magnitude of RTN is high when the trap is located at middle of the channel.

This work was supported in part by Ministry of Science and Technology (MOST) of Taiwan under Contracts No. MOST-107-2221-E-009-094 and No. MOST-106-2218-E-009-149.

[1] Y. Li et al., IEDM, pp. 887-890, 2015.
[2] W.-L. Sung and Y. Li, IEEE T ED, vol. 65, pp. 2638-2646, 2018.
[3] D. Nagy et al., IEEE J EDS, vol. 6, pp. 332-340, 2018.
[4] P. Su et al., ICICDT, vol. 26, pp. 61-64, 2012.
[5] S.-C. Hsu and Y. Li, Nanoscale Res. Lett., vol. 9, 2014, 633, 2014.
[6] Y. Li and H.-W. Cheng, Solid-State Electron., vol. 77, pp. 12-19, 2012.

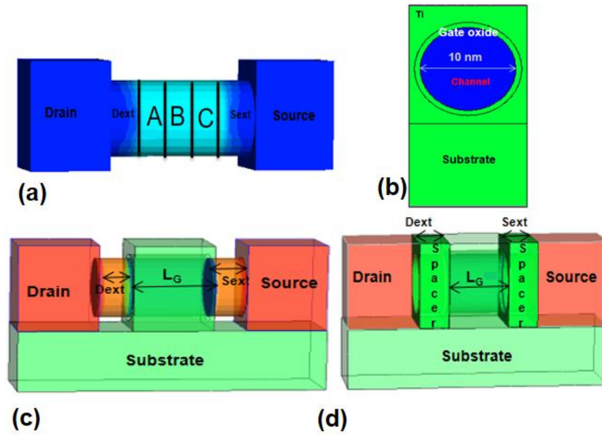

Fig. 1: (a) The single charge trap is located at different position along the channel on the interface of Si/SiO_2. (b) The cross-sectional view at the middle of the channel. (c) and (d) are the 3D simulated structures of the GAA NW MOSFET without/with spacer.

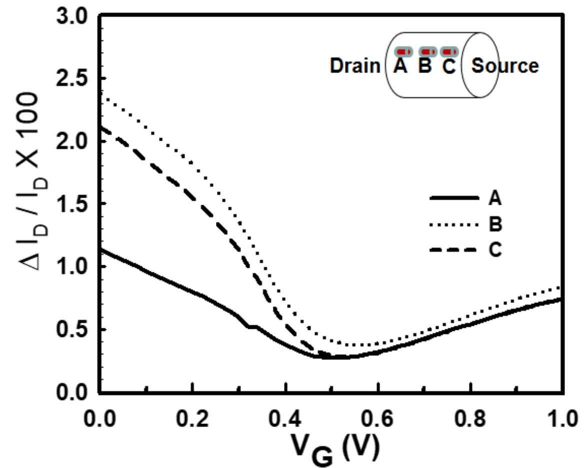

Fig. 4: The comparison of calculated magnitude (%) of the random telegraph noise in the presence of the acceptor-type single charge trap at different locations in the channel for nominal GAA NW MOSFET under V_D=0.01 V.

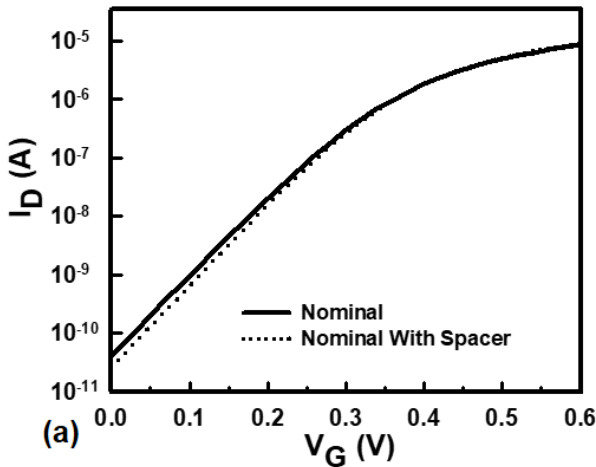

Fig. 2: I_D-V_G plots of electrical characteristics comparison (i.e., nominal device (solid line) and device with spacer (dot)) under the biasing of V_D=0.6 V and the same settings of parameters for both devices.

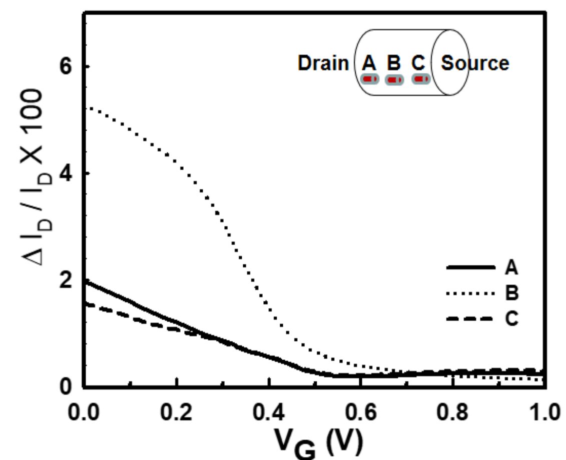

Fig. 5 The comparison of calculated magnitude (%) of the random telegraph noise in the presence of the acceptor-type single charge trap at different locations in the channel for with spacer GAA NW MOSFET under V_D=0.01 V.

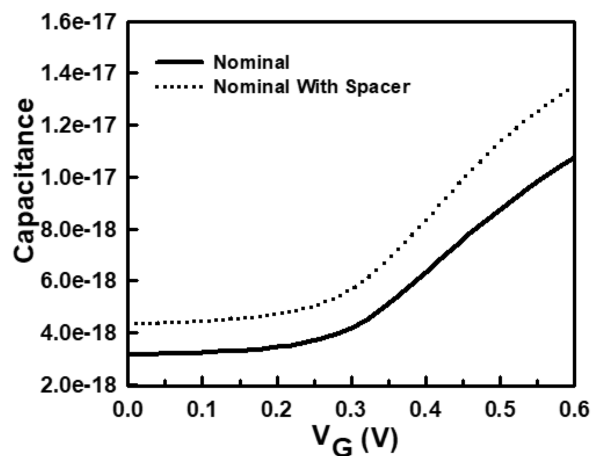

Fig. 3: C-V comparison of the simulated devices (i.e., nominal device (solid line) and device with spacer (dot)) under the similar parameters and biasing condition of V_D=0.6 V.

Tab. 1: List of calculated magnitudes of RTN (%) comparison in the presence of the acceptor-type SCT placed in different position along the channel for the nominal and with spacer GAA NW MOSFETs under the doped and undoped channel, with similar biasing conditions and device settings.

Type of Device	SCT Position		
	A	B	C
Without spacer & doped channel	1.095	2.310	2.280
Without spacer & undoped channel	1.290	2.390	2.380
Spacer & doped channel	2.000	5.200	1.560
Spacer & undoped channel	2.200	5.300	1.620

Monolayer Tungsten Disulfide with Transition Metal Doping

C.-Y. Chen[1,2], Y. Li[1,2,3]
[1]*Parallel and Scientific Computing Laboratory;* [2] *Institute of Communications Engineering;*
[3]*Department of Electrical and Computer Engineering, National Chiao Tung University, 1001 Ta-Hsueh Rd., Hsinchu 300, Taiwan*
ymli@faculty.nctu.edu.tw

In this work, monolayer tungsten disulfide (mWS_2) doped by various 3d transition metals (TM), with two different concentrations, 7.13×10^{13} and 2.85×10^{14} cm^{-2}, are studied by density-functional-theory simulation. Not like many studies assuming substitutional doping sites [1-2], we considered two interstitial (I−) and two substitutional (S−) sites. Then, the work function, the charge transfer, and the projected local density of state are accordingly discussed.

This study uses Vienna ab initio Simulation Package (VASP) [3] to calculate structure relaxation and electronic properties under spin-polarized density functional theory (DFT). Perdew-Burke-Ernzerhof (PBE) is used as an exchange-correlation function since our intensive accuracy test before [4-5], as shown in Fig. 1. The cutoff kinetic energy is 500 eV; the force acting on each atom of relaxed structure is smaller than 0.01 eV/A°; the energy difference is less than 10^{-6} per atom.

Figure 2 shows the simulation flow. The calculated band structures of Fig. 2(a) bulk and Fig. 2(b) monolayer WS_2 are verified with experimental results. To determine the most stable site with lowest formation energy, four possible doping sites, two interstitial (I−) and two substitutional (S−) sites, are discussed. The formation energy is determined with the formula in Fig. 3. The interstitial site, I−T, has the lowest formation energy for all TM dopant in this study, as shown in Fig. 4.

The formation energy for all TM dopant are listed in Tab. I. The calculated magnetic moments are listed in Tab. II, doping with scandium (Sc) and copper (Cu) results in large change of magnetic moment, about 61.7% and 89% reductions, as doping concentration increases. Figure 5 plots the work function of TM-doped mWS_2 with respect to two concentrations. The titanium (Ti)-doped mWS_2 has the lowest work function while zinc (Zn)-doped has the highest work function. Doping with Sc possesses the largest range of modulation of work function, about 1.63 eV, among different doping species. The difference between conduction band and fermi energy is discussed in Fig. 6. Ti-doped mWS_2 behaves metal; Sc, manganese (Mn), and Chromium (Cr) are suitable for n-type dopant; and nickel (Ni) and Zn are for p-type dopant.

Acknowledgement: This work was supported in part by the Ministry of Science and Technology (MOST), Taiwan, under grants MOST 106-2221-E-009-149, MOST 106-2622-8-009-013-TM, 107-2622-8-009 -011-TM, 107-2221-E-009-094, and MOST 107-3017-F-009-001, and the "Center for mmWave Smart Radar Systems and Technologies" under the Featured Areas Research Center Program within the framework of the Higher Education Sprout Project by the Ministry of Education (MOE) in Taiwan.

References:

[1] Y. Wang et al., Sci. Rep., **6**, 24153 (2016).
[2] C. Huang et al., Journal of Semiconductors, **38**, 033004 (2017).
[3] G. Kresse et al., Phys. Rev. B, Condens. Matter, **47**, 558 (1993).
[4] Y.-C. Tsai et al., Int. Conf. Simul. Semicond. Process. Devices (SISPAD), pp. 169–172 (2017).
[5] Y.-C. Tsai et al., IEEE Trans. Electron Devices, **65**, 733 (2018).

Kohn-Sham Equation:

$$\left(\frac{p^2}{2m}+V_{\mathrm{nucl}}(\mathbf{r})+V_{\mathrm{coul}}(\mathbf{r})+V_{\mathrm{xc}}(\mathbf{r})\right)\phi_i(\mathbf{r})=\varepsilon_i\phi_i(\mathbf{r})$$

Exchange-Correlation Functionals:

- Semi-local Functional: Perdew–Burke–Ernzerhof (PBE)

$$E_{xc}=\int n(\vec{r})f(n_\uparrow,n_\downarrow,\nabla n_\uparrow,\nabla n_\downarrow)d\vec{r}$$

Fig.1: The Perdew-Burke-Ernzerhof exchange-correlation function is used in Kohn-Sham equation in this study. The calculated WS_2 band structure is closed to experiment results with and reasonable time cost.

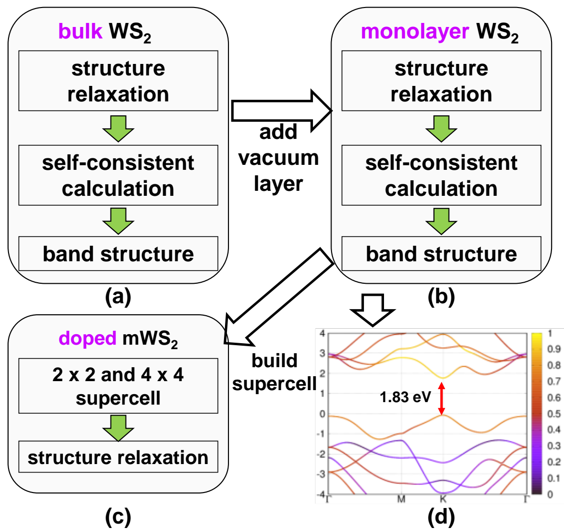

Fig.2: The simulation flow from (a) bulk WS_2 to (c) doped monolayer WS_2. (d) The obtained monolayer WS_2 band structure. The color bars indicate the weighting of band dominated by tungsten atoms. The direct bandgap is 1.83 eV for monolayer WS_2.

Formation energy:

$$E_{form}=E_{doped-mWS2}-E_{mWS2}+\sum n_i\mu_i$$

Fig.3: Specifically, $E_{Doped-mWS2}$ and E_{mWS2} are the total energies of the doped mWS_2 system and the pristine mWS_2, where n_i, and μ_i are the number of atom i added (-1) or removed (+1) and the corresponding chemical potential, respectively.

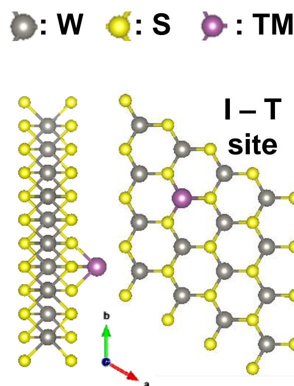

Fig.4: The most stable doped structure of mWS_2 of four possible doping sites is I-T site, the gray, yellow, and brown atoms are W, S, and doping transition metal, respectively. Two interstitial (I-) and two substitutional (S-) sites are simulated to determine the most stable site with lowest formation energy.

Table I: The formation energies (eV) of four doping sites for 4×4 mWS_2 supercell.

E_{form} (eV)	I – H	I – T	S – S	S – W
Sc	-1.735	**-1.855**	1.708	4.806
Ti	-1.656	**-2.245**	1.149	2.620
V	-3.664	**-4.138**	0.302	0.879
Cr	-0.685	**-0.851**	3.673	4.902
Mn	-0.487	**-0.728**	2.986	6.236
Fe	-1.158	**-2.139**	2.336	6.124
Co	-2.170	**-2.713**	2.115	6.667
Ni	-2.670	**-3.202**	1.713	7.722
Cu	-1.051	**-1.092**	3.381	10.177
Zn	-0.033	**-0.036**	5.949	12.437

Table II: The total magnetic moments (Mag. Mom.) of doped monolayer WS_2 supercell (SC.) with different doping concentrations.

Mag. Mom.	*Sc*	*Ti*	*V*	*Cr*	*Mn*
4 x 4 SC.	*3*	*4*	*5*	*6*	*5*
2 x 2 SC.	*1.15*	*4*	*5*	*5.62*	*4.62*
Mag. Mom.	***Fe***	***Co***	***Ni***	***Cu***	***Zn***
4 x 4 SC.	*2*	*1*	*0*	*1*	*0*
2 x 2 SC.	*2*	*1*	*0*	*0.11*	*0*

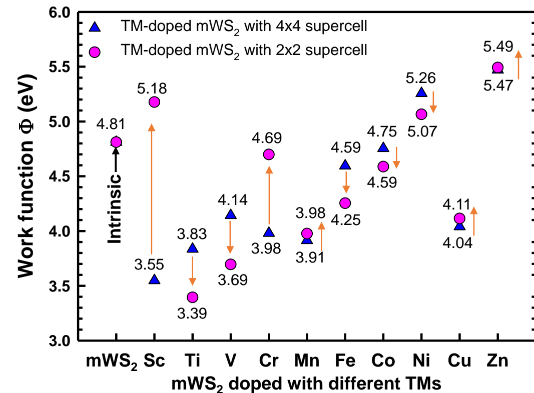

Fig.5: The work function of TM-doped mWS_2 with respect to different TM materials. The triangle and circle symbols are results of 4×4 and 2×2 supercells, respectively. The most stable structure, I-T, is simulated with two different doping concentrations. The arrows indicate how the work function changes as the doping concentration increases.

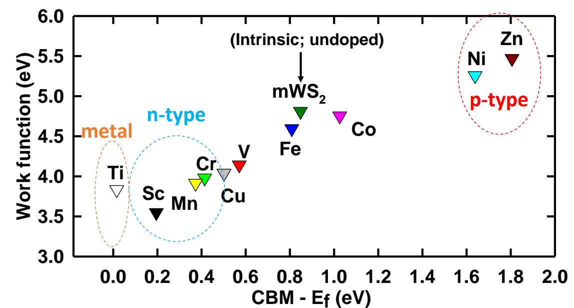

Fig.6: The work function versus the energy difference between the conduction band minimum (CBM) and the fermi level (E_f) of the TM-doped mWS_2

Effect of Stacking Order on Band-to-Band Tunneling in van der Waals TMDC Heterojunctions

F. Hashimoto, N. Mori

Graduate School of Engineering, Osaka University,
2-1 Yamada-oka, Suita, Osaka 565-0871, Japan
{hashimoto, mori}@si.eei.eng.osaka-u.ac.jp

Transition metal dichalcogenides (TMDCs) such as MoS_2 and WS_2 have been attracting much attention and van der Waals (vdW) heterostructures of them show the new possibilities and application fields of nanodevices [1]. Recently, tunnel field-effect transistors utilizing band-to-band (BTB) tunneling in vdW heterojunctions were fabricated, showing excellent device characteristics [2]. Here we study effect of stacking order on the BTB tunneling in TMDC heterojunctions by using the non-equilibrium Green function (NEGF) method combined with a tight-bind (TB) approximation.

We consider a MoS_2/WS_2 vdW heterojunction whose schematic diagram is given in Fig. 1. The channel of length L consists of a vdW heterojunction of MoS_2 and WS_2 with inter-layer distance d. We set L = 0.55 nm and d = 4 Å in the present study. The channel width is considered to be infinite with a periodic boundary condition. Semi-infinite electrodes are attached to the both ends of the channel. We assume that electron transfer between MoS_2 and WS_2 occurs only in the channel region. To investigate effect of stacking order, we consider two types of stacking: AA-stacking [Fig. 1(b)] and AB-stacking [Fig. 1(c)], and calculate integrated transmission functions $\tau(E)$ by using the NEGF method.

We use the 11-band TB model [3] to describe TMCD band-structures. Since the conduction and valence band edges are predominantly contributed by the d-orbitals of metal atoms, we consider the nearest neighbor Mo-W hopping with three parameters $v_{dd\sigma}$, $v_{dd\pi}$, and $v_{dd\delta}$ as the inter-layer interaction. In order to determine TB parameters, we fit the TB band-structures to those obtained by the density functional theory (DFT). Figure 2 shows the fitting results for monolayer MoS_2 (green line) and WS_2 (pink line). Figures 3 and 4 show the fitting results for AA-stacked and AB-stacked vdW heterojunction, respectively. The inter-layer TB parameters are extracted as $v_{dd\sigma} = -0.145$ eV, $v_{dd\pi} = 0.120$ eV, and $v_{dd\delta} = 0.877$ eV for AA-stacking, $v_{dd\sigma} = 0.0847$ eV, $v_{dd\pi} = 0.00630$ eV, and $v_{dd\delta} = -0.108$ eV for AB-stacking. Figure 5 shows $\tau(E)$ for AA-stacking and AB-stacking for the energy window ΔE = 0.1 eV, where the WS_2 valence band and the MoS_2 conduction band overlap. We find that BTB tunneling in AA-stacking becomes larger than that of AB-stacking.

[1] A. K. Geim and I. V. Grigorieva, Nature **499**, 419 (2013). [2] T. Roy *et al.*, Appl. Phys. Lett. **108**, 083111 (2016). [3] E. Ridolfi *et al.*, J. Phys.: Condens. Matter **27**, 365501 (2015).

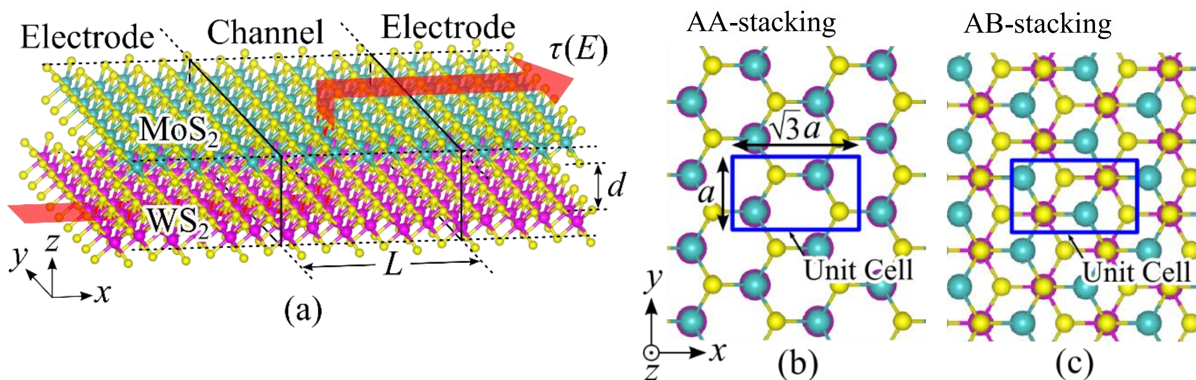

Fig. 1: (a) Device model of MoS_2/WS_2 vdW heterojunction. We set $L = 0.55$ nm and $d = 4$ Å in the present study. Top view of AA-staked (b) and AB-stacked (c) vdW heterojunction.

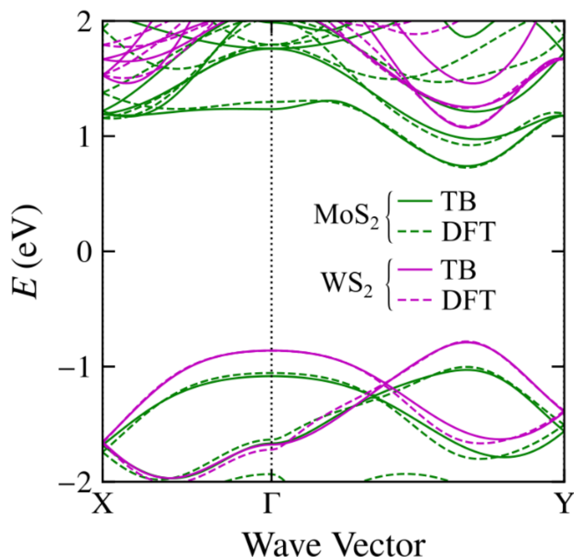

Fig. 2: Band-structure of MoS_2 (green line) and WS_2 (pink line) calculated by DFT (dashed line) compared with the TB band-structure (solid line).

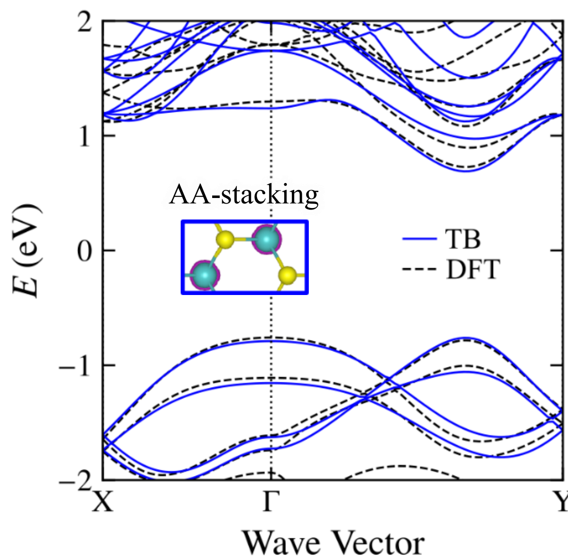

Fig. 3: Band-structure of AA-stacked vdW heterojunction calculated by DFT (dashed line) compared with the TB band-structure (solid line).

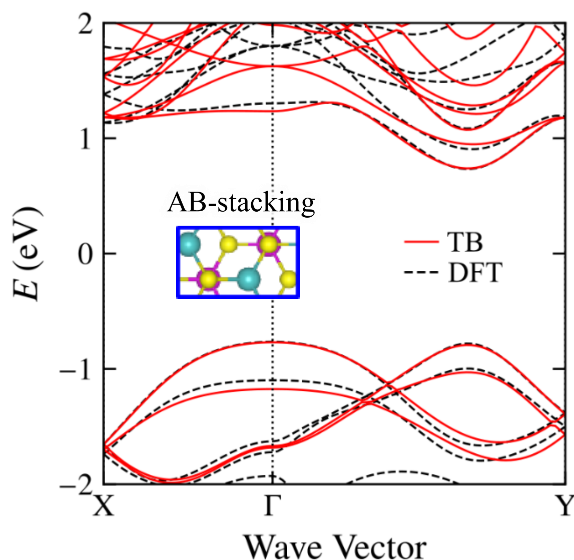

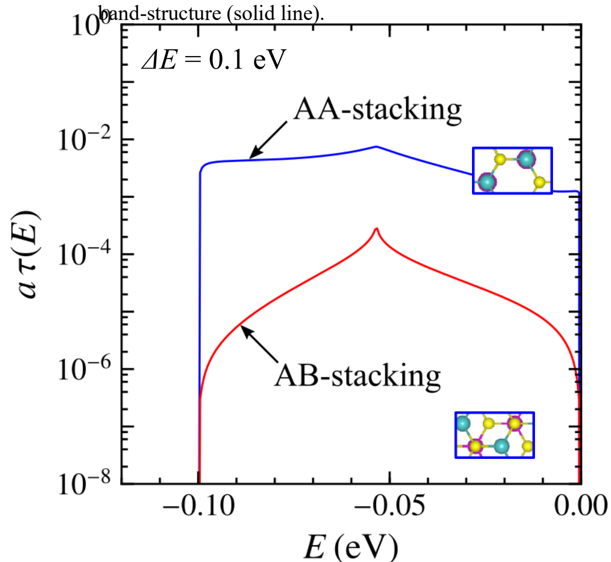

Fig. 5: Integrated transmission function $\tau(E)$ for AA-stacked (blue line) and AB-stacked (red line) vdW heterojunction.

Gate Bias Dependence of Flicker Noise in Graphene as a Result of Carrier Statistics

M. Macucci, P. Marconcini
Dipartimento di Ingegneria dell'Informazione, Università di Pisa
Via Girolamo Caruso 12, 56122 Pisa, Italy
m.macucci@mercurio.iet.unipi.it

Flicker noise in graphene has been investigated by several authors and a variety of behaviors of its power spectral density have been observed as a function of the backgate bias. In particular, in bilayer graphene, but also in a few samples of monolayer graphene, a minimum of flicker noise has been observed at the Dirac point, and several explanations have been proposed. An interesting theory [1] exploited screening of a trapped carrier and the peculiar properties of the graphene bandstructure to explain the observed features of flicker noise. We have developed a different approach [2] that leads to analogous results starting from the mass-action law and from the observation that the prevalent components of flicker noise are slow compared to the generation-recombination times of carriers. Here we further develop such a model and apply it to a wider range of situations.

We rely on the preservation of the electric neutrality of the conductor and, as a result of the mass-action law, of the product of electron and hole concentrations. A direct consequence of these two constraints is that near the Dirac point a trapping event leads to screening by both types of carriers (electrons and holes) and to no net variation of the total available number of carriers. As a result of the symmetry between the transport properties of electrons and holes in graphene, the preservation of the total number of carries leads to the disappearance of generation-recombination noise (which is at the basis of flicker noise, that can be interpreted as a superposition of Lorentzian generation-recombination spectra) in this circumstance. On the other hand, far away from the Dirac point a trapping event leads to a variation of the number of carriers by one unit, as in ordinary doped semiconductors, thereby without any suppression of flicker noise. If we perform a numerical calculation of the flicker noise power spectral density as a function of the carrier concentration, we obtain a good match with the experimental data for bilayer graphene. The observed behavior for monolayer graphene, which does not usually exhibit a minimum at the Dirac point, can be retrieved taking into consideration a disorder model resulting from the presence of randomly located impurities.

[1] B. Pellegrini, Eur. Phys. J. B 86, 373 (2013).
[2] B. Pellegrini et al., J. Stat. Mech. 2016, 054017 (2016).

Fig. 4: Same as Fig. 3 but for AB-stacked vdW heterojunction.

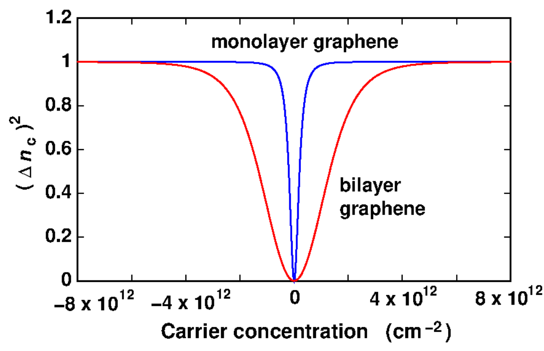

Fig.1: Behavior of the square of the carrier number fluctuation as a function of carrier concentration for monolayer and bilayer graphene.

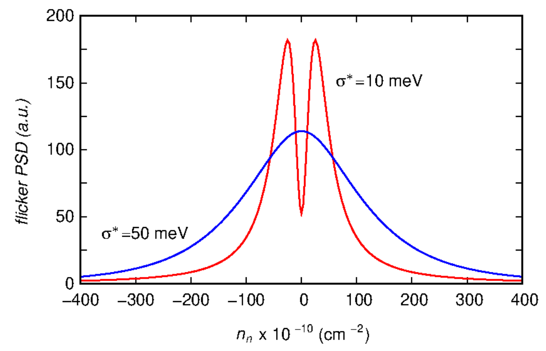

Fig.3: Power spectral density of flicker noise in the presence of disorder, for monolayer graphene.

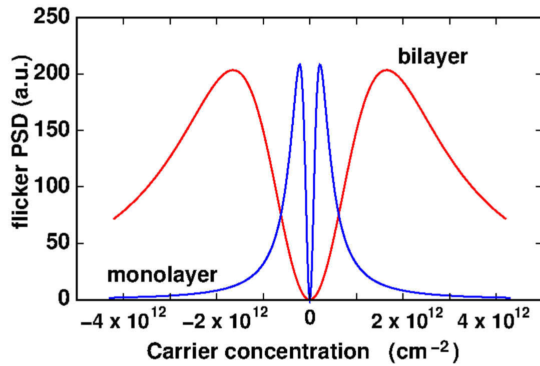

Fig.2: Power spectral density of flicker noise fluctuations as a function of the carrier concentration for monolayer and bilayer graphene.

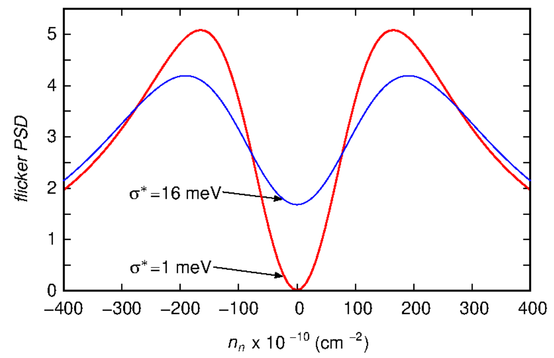

Fig.4: Power spectral density of flicker noise in the presence of disorder, for bilayer graphene.

Band Structure of Zigzag Phosphorene Nanoribbons: A Tight-Binding Hubbard Model

S. Soleimanikahnoj, I. Knezevic
Department of Electrical and Computer Engineering, University of Wisconsin-Madison, Madison, Wisconsin 53706, USA
soleimanikah@wisc.edu

The phosphorene nanoribbon (PNR), a one-dimensional analogue of phosphorene, has received considerable attention owing to its remarkable electronic properties. In particular, PNRs with zigzag edge termination [Fig. 1(a)] have been used as the underlying material for introducing novel nanodevices such as quantum switches, pseudospin valves, and spin filters [1-3]. The functioning of these devices is mainly based on electric- or magnetic-field tuning of the so-called midgap energy bands of zigzag phosphorene nanoribbons (ZPNR)s. The midgap bands are a pair of energy bands in electronic band structure of ZPNRs that cross the Fermi level and are far from the other energy bands. Near-equilibrium electronic transport in ZPNRs is governed by the midgap bands with little to no contribution from the other energy bands. This shows that a careful assessment of the ZPNR electronic properties and the performance of ZPNR-based electronic devices requires employing a model that accurately captures the electronic dispersion of midgap bands. The fifteen-nearest-neighbor tight-binding (TB) Hamiltonian proposed by Rudenko *et al*. [4] provides an accurate band dispersion for bulk phosphorene with respect to density functional theory (DFT) calculations. However, if used for ZPNRs, the TB model fails to capture the band structure and, in particular, the midgap-band energy dispersions accurately. In this work, we show that a Hamiltonian that includes the fifteen-nearest-neighbor TB Hamiltonian for bulk phosphorene along with a Hubbard mean-field-approximation term correctly captures the band dispersion of midgap bands in ZPNRs. In particular, the added Hubbard term dramatically modifies the midgap bands dispersion and upon choosing a proper Hubbard potential replicates the midgap bands dispersion obtained from our DFT calculations. The model presented here is a much-needed tool for careful investigation of electronic properties of ZPNRs and provides the platform for credible assessment of ZPNRs as a material for future developments in nanoelectronics.

[1] S. Soleimanikahnoj and I. Knezevic, Phys. Rev. Applied, **8**, 064021 (2017).
[2] S. Soleimanikahnoj and I. Knezevic, JCEL, **16**, 064021 (2017).
[3] W. Zhou et al., Physica E, **94**, 53–58 (2017).
[4] A. Rudenko et al., Phys. Rev. B, **92**, 085419 (2015).

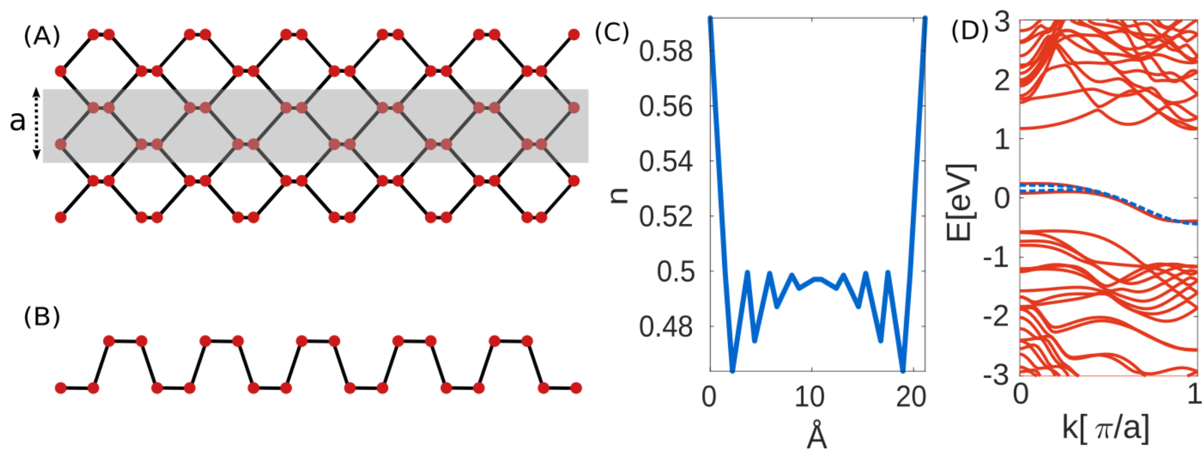

Fig.1: (a) Top view of a single-layer ZPNR. The left and the right edges are zigzag. The gray rectangle denotes a unit cell for this ZPNR. a = 3.31 Å is the length of the unit cell. (b) Side view of a ZPNR. (c) Identical Up-spin and down-spin electron occupation per lattice site across the ribbon. The ribbon is in paramagnetic state. (d) Electronic band structures calculated for the ZPNR in panels (a),(b). Fermi level is at zero energy. Solid-line curves are the band structure from our DFT calculations. Dashed curves are the dispersion of midgap bands obtained from the proposed TB Hubbard model.

Current Estimation in Backward Monte Carlo Simulations

H. Kosina, M. Kampl
Institute for Microelectronics, TU Wien, Austria
kosina@iue.tuwien.ac.at

The theoretical foundations of the backward Monte Carlo (BMC) method for the solution of the semiconductor Boltzmann equation have been laid out three decades ago [1][2]. A modified version of the BMC algorithm that guarantees numerical stability has been developed recently and implemented in a full-band MC device simulator [3].

We have studied the electrical characteristics of a 65nm n-channel MOSFET. The BMC method allows one to calculate the drain current in the entire sub-threshold region including the leakage current in the off-state. Compuation times are on the order of 10 seconds for frozen-field simulations (Fig 1).

The current through a plane is calculated by means of MC integration of the current density. For this integration a distribution of the sampling points has to be assumed which, in the present case, represent the initial states of the backward trajectories. In this work we discuss the properties of the current estimators obtained from different choices of that distribution. Typical choices are Maxwellian and velocity-weighted Maxwellian distributions. Fig. 2 shows the output characteristics and the relative standard deviation of the current for different estimators. A symmetric current estimator produces less statistical error than the non-symmetric ones [3]. This improvement is achieved for all operating conditions, and is particularly large when thermal equilibrium is approached.

By assuming a Maxwellian distribution at elevated temperature the method generates more sampling points at higher energies. This method of statistical enhancement reduces the statistical error of quantities that depend on the high-energy tail of the distribution function. Fig. 3 shows that the estimated current is independent from the injection temperature, whereas the statistical error shows a clear minimum where the injection distribution most closely resembles the actual distribution (Fig. 4).

[1] C. Jacoboni, P. Poli, L. Rota, A new Monte Carlo technique for the solution of the Boltzmann transport equation, Solid-State Electronics 31 (3/4), 523 (1988)
[2] M. Nedjalkov, P. Vitanov, Iteration approach for solving the Boltzmann equation with the Monte Carlo method, Solid-State Electronics 32 (10), 893 (1988)
[3] M. Kampl, H. Kosina, The Backward Monte Carlo Method for Semiconductor Device Simulation, Journal of Computational Electronics 17, 1492 (2018)

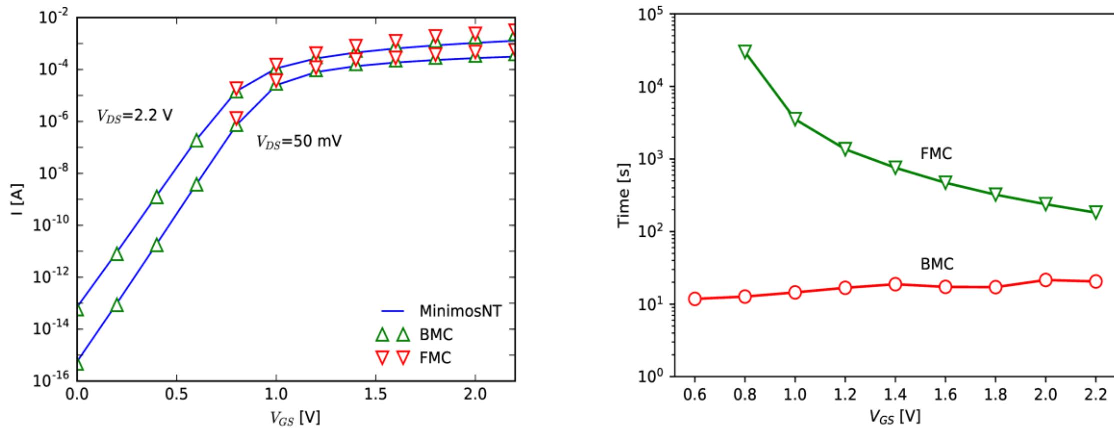

Fig.1: Left: Transfer characteristics of a 65nm n-channel MOSFET simulated using Minimos-NT, the backward and the forward MC methods. Right: Computation times on a single core of an Intel i7 processor for a relative standard deviation of 0.01. VDS=2.2V.

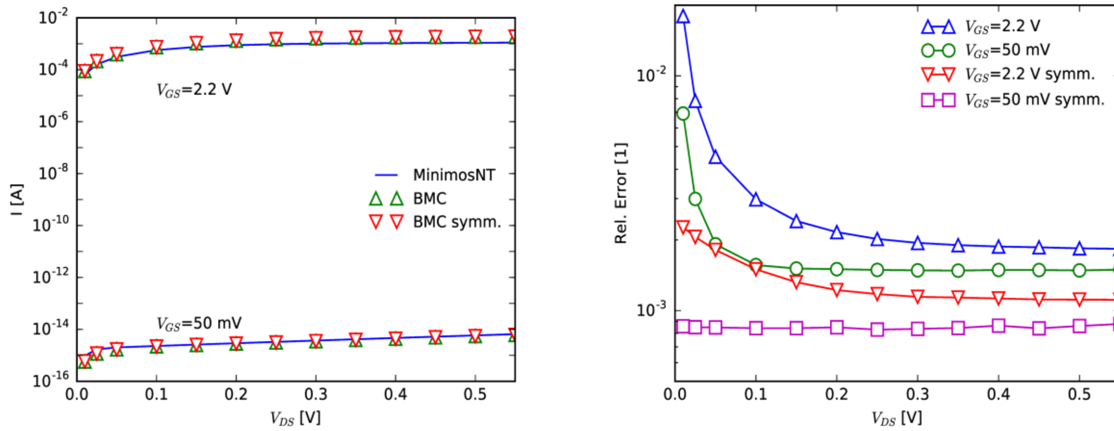

Fig.2: Left: Output characteristics of the MOSFET for two gate voltages, simulated using MinimosNT, the forward and the backward MC methods. Right: Relative standard deviation of the drain current. The non-symmetric and the symmetric estimator based on the velocity-weighted Maxwellian are compared. For each bias point 1e6 backward trajectories are calculated.

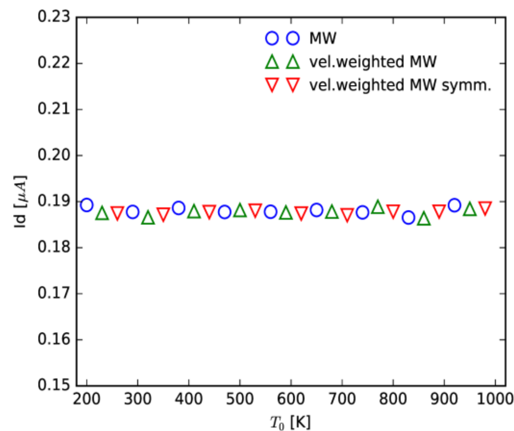

Fig.3: The drain current is independent from the injection temperature and the estimator used. VGS=0.6V, VDS=2.2V.

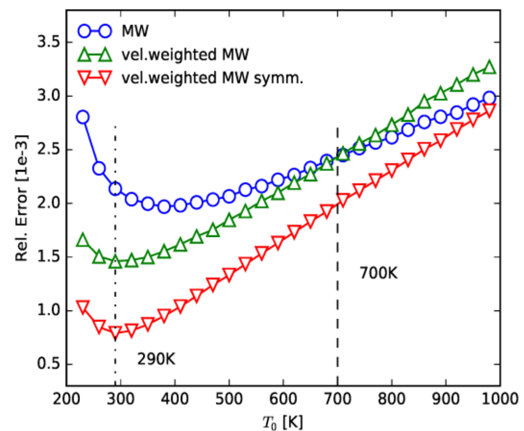

Fig.4: Relative standard deviation of the current for different estimators versus injection temperature. VGS=0.6V, VDS=2.2V.

An Improved Unified Solver for Modeling Defect Dynamics in Materials

A. Shaik[1], D. Brinkman[2], C. Ringhofer[1], D. Vasileska[1]
[1]*Arizona State University, USA*
[2]*San Jose State University, USA*
arshaik@asu.edu

In our previous works, a unified solver was developed and used to explain the copper (Cu) migration in CdTe solar cells [1-3]. In this work we present an improved version of the solver based on an operator splitting scheme, splitting the model equations into the reaction term and drift diffusion term. We employ a finite volume meshing instead of finite difference [1] and finite element meshing [3-4] from our previous solver. The performance improvement is due to our novel method of solving the reactions by a Jacobian method and implicit differencing in time, thus improving stability and accuracy. Although the reaction solver improved the speed and accuracy, we still faced challenges in conservation of charge and mass. We proposed non-linear heuristic correction scheme to avoid the conservation issues. The simulation time scales vary from nano seconds to decades for studying process simulation at elevated temperature to long term stress condition in solar cells. For long term simulation diffusion solver failed to conserve mass and we used method of pseudo inverses to correct them. Finally, we can avoid both issues by not using the operator splitting scheme. This full operator method results in slower simulation speed.

We follow object-oriented programming paradigm of MATLAB to code our numerical engine into classes implementing the different solvers and algorithms. This gives us flexibility to easily incorporate new solver classes and algorithms into our numerical engine. Currently, we support 3 diffusion solvers, 2 reaction solvers and 5 Poisson solvers. In terms of algorithm we support full operator algorithm and operator splitting algorithm.

We validate our solver by comparing the light IV curves simulated through our drift diffusion reaction formalism and Silvaco's atlas commercial solver which implements drift diffusion formalism at thermal equilibrium. The results show that code implementation and our formalism assumptions are correct.

[1] Da Guo et al., J. Phys. D: Appl. Phys., **51**, 153002 (2018).
[2] Da GUO et al., https://nanohub.org/resources/predicts1d. (DOI: 10.21981/D34T6F43J) (2015).
[3] Abdul Shaik et al., https://nanohub.org/resources/predicts2d. (DOI: 10.21981/D32N4ZJ9X) (2016).
[4] Daniel Brinkman et al., J. Appl. Phys. **118**, 035704 (2015).
[5] Silvaco Software Tool., https://www.silvaco.com (2018).

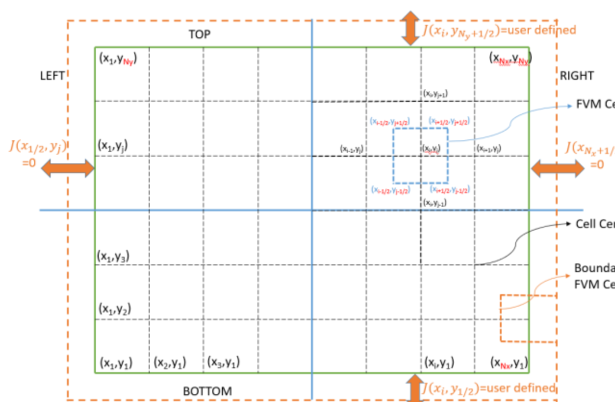

Fig.1: Finite Volume Mesh (FVM) used for discretizing differential equations

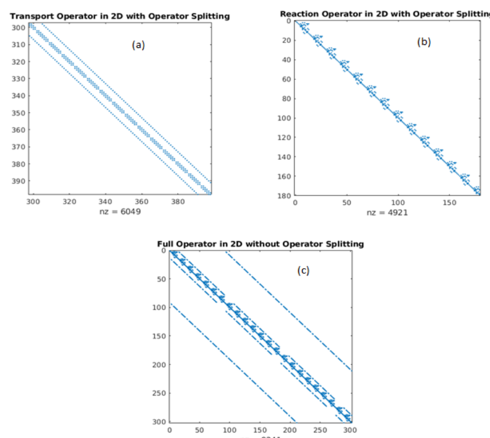

Fig.4: Shape of LU decomposition matrix in operator splitting scheme (a) Transport Operator (b) Reaction Operator and (c) full operator scheme.

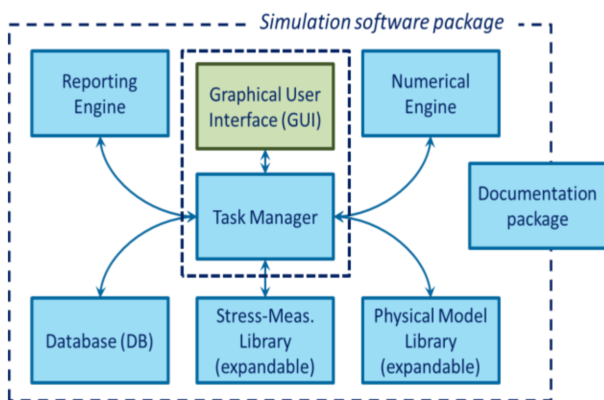

Fig.2: Software modules used in the improved solver..

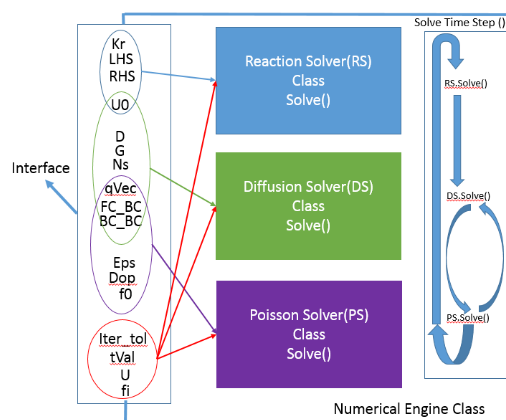

Fig.5 OOP Object organization for implementing numerical engine with reaction solvers, diffusion solver and poisson solvers and algorithms.

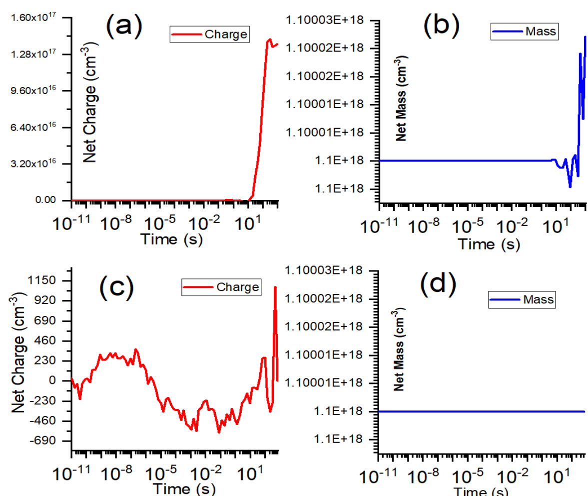

Fig.3: (a) Net charge (b) Net mass without corrections, (c) net charge and (d) net mass with corrections.

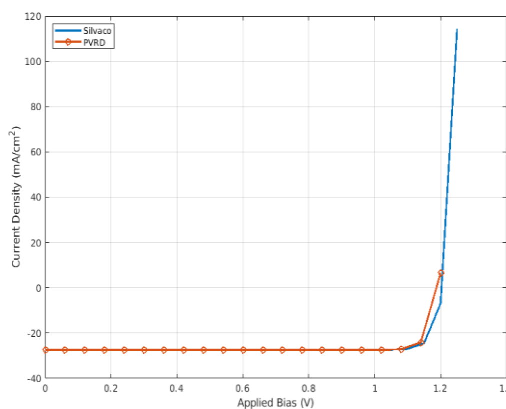

Fig.6: Comparison of light IV curves from our solver to Silvaco atlas solver.

Design of Ultraviolet Light Emitting Diodes Based on Hexagonal Boron Nitride

J. Wang, K.C. Wang, T. Kubis
Network for Computational Nanotechnology, Purdue University,
West Lafayette, IN 47907, USA
wang4205@purdue.edu

Ultraviolet light emitting diodes (UV-LEDs) have numerous applications [1] as light sources for disinfection and sterilization, chemical excitation, replacement of UV lamps, etc. Intrinsic large bandgap of hexagonal boron nitride (*h*-BN)[2-3] and the great development in experimental fabrication facilitates the possibility of flexible UV-LEDs. In this work, we perform a series of atomistic simulations to study the core components of *h*-BN-based LED. The multiple quantum wells (MQWs) are created by selectively putting *h*-BN with different stacking orders and thickness together. Quantum confinement for both valence and conduction bands is found. By analyzing the Schottky barrier of contacts between *h*-BN and various metals, promising metal candidates are identified for p- and n-doped h-BN[4-5]. We also calculate the doping effect of *h*-BN under varied doping levels. A concrete LED structure based on *h*-BN is proposed, which gives clear guidance to experimentalists.

[1] Y. Muramoto et al., Semicond. Sci. Technol., **29**, 084004 (2014)
[2] K. Watanabe et al., Nat. Mater., **3**, 404 (2004)
[3] W. Aggoune et al., Phys. Rev. B, **97**, 241114 (2018)
[4] B. He et al., Appl. Phys. Lett., **95**, 252106 (2009)
[5] S. Majety et al., AIP Adv., **3**, 122116 (2013)

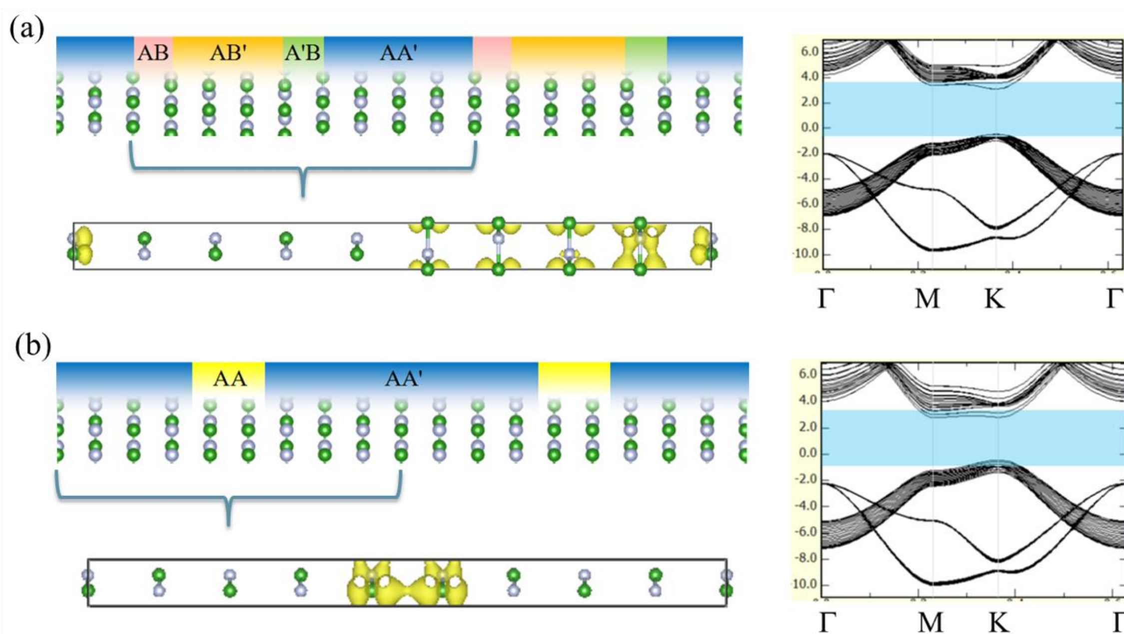

Fig.1: Atomic structures, partial charge densities, and band structures of the two typical multiple quantum wells: (a) MQW-T1 and (b) MQW-T2.

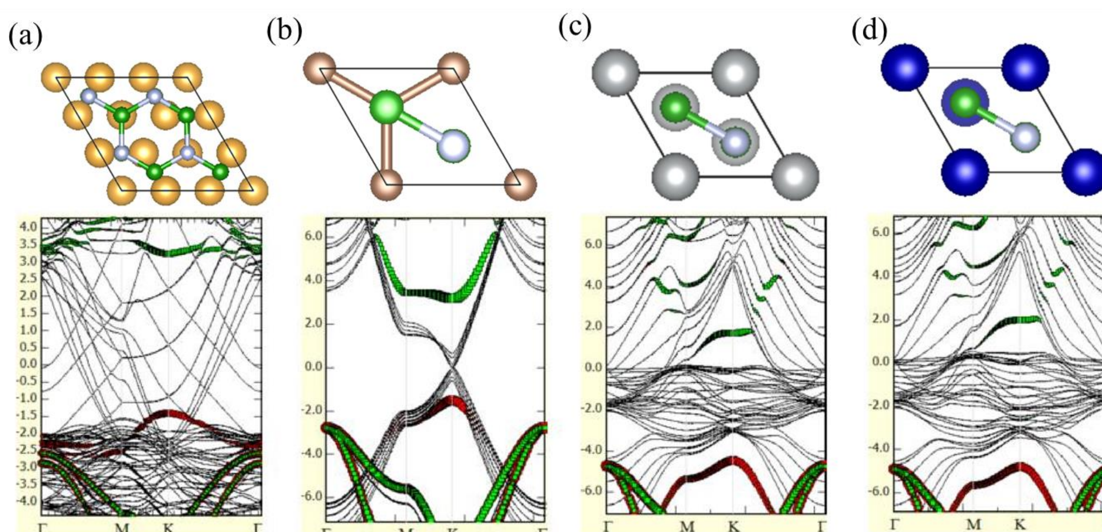

Fig.2: Band structures of monolayer h-BN on (a) Au(111), (b) graphite (0001), (c) Ni(111), and (d) Co(0001).

Coherent Heat Transport in Nanostructures by Numerical Solution of Quantum Kinetic Equation of Phonons

Y. Guo[1], S. Volz[1, 2], M. Nomura[1]
[1]*Institute of Industrial Science, The University of Tokyo, Tokyo 153-8505, Japan*
[2]*LIMMS/CNRS-IIS, The University of Tokyo, Tokyo 153-8505, Japan*
yyguo@iis.u-tokyo.ac.jp, sebastian.volz@centralesupelec.fr

The phonon Boltzmann equation has been widely used in explaining heat transport through nanostructures. However, it becomes no longer valid when the characteristic size of system becomes comparable to or even smaller than the dominant wavelength of phonons, which often happens at very low temperature or in very small nanostructures. In this work, we will propose a methodology to describe the coherent heat transport in nanostructures based on the more fundamental quantum kinetic equation for single-phonon density matrix (Eq. (3) in Page 2) [1]. We also develop a finite difference method for numerical solution of the quantum kinetic equation. The macroscopic field variables including the energy density and heat flux are related to the diagonal components of the density matrix (Eq. (4) and Eq. (5) in Page 2) [2]. The new methodology is demonstrated through modeling heat transport in silicon thin film with a thickness less than 10nm at different temperatures. The results indicate correlation behaviors between different phonon modes at very low temperature, and are reduced to the solution of classical phonon Boltzmann equation around room temperature. With the help of Wigner function (Eq. (6) in Page 2), it is also shown that the phonon Boltzmann equation is recovered from the quantum kinetic equation in the absence of correlations. The present work will promote the understanding and modeling of coherent phonon heat transport in crystals.

[1] F.T. Vasko and O.E. Raichev, Quantum kinetic theory and applications: electrons, photons, phonons. Springer, New York, 2005.
[2] R.J. Hardy, Energy-flux operator for a lattice. Physical Review, 132(1): 168(1963).

The equation of density matrix is the fundamental equation in quantum statistical mechanics [1]:

$$i\hbar\frac{\partial\hat{\eta}_t}{\partial t}=\left[\hat{H},\hat{\eta}_t\right], \tag{1}$$

where $\hat{\eta}_t$ is the many-body density matrix and $\hat{H}$ is the Hamiltonian operator of the system. The solution of Eq. (1) is not easy even for very simple cases. Therefore the one-phonon density matrix is introduced as [1]:

$$N_t\left(\mathbf{k}'j',\mathbf{k}j\right)=\mathrm{Tr}\left(\hat{a}^+_{\mathbf{k}j}\hat{a}_{\mathbf{k}'j'}\hat{\eta}_t\right), \tag{2}$$

where '**k***j*' denotes a phonon mode, $\hat{a}^+_{\mathbf{k}j}$ and $\hat{a}_{\mathbf{k}j}$ being the phonon creation operator and destruction operator respectively. As a first step, we consider the harmonic approximation such that $\hat{H}=\sum_{\mathbf{k}j}\hbar\omega_j\left(\mathbf{k}\right)\left(\hat{a}^+_{\mathbf{k}j}\hat{a}_{\mathbf{k}j}+\frac{1}{2}\right)$. Combining Eq. (1) and Eq. (2), we obtain the quantum kinetic equation of phonons [1]:

$$\left[i\hbar\frac{\partial}{\partial t}-\hbar\left(\omega_{j'}\left(\mathbf{k}'\right)-\omega_j\left(\mathbf{k}\right)\right)\right]N_t\left(\mathbf{k}'j',\mathbf{k}j\right)=0. \tag{3}$$

A finite difference scheme is then devised for numerical solution of Eq. (3). In the harmonic approximation, the calculation of energy density and heat flux is mainly contributed by the diagonal component of the one-phonon density matrix [2]:

$$e=\frac{1}{V}\sum_{\mathbf{k}j}\sum_{\mathbf{k}'j'}\hbar\omega_j\left(\mathbf{k}\right)\delta_{jj'}\delta_{\mathbf{k}\mathbf{k}'}N_t\left(\mathbf{k}'j',\mathbf{k}j\right), \tag{4}$$

$$\mathbf{q}=\frac{1}{V}\sum_{\mathbf{k}j}\sum_{\mathbf{k}'j'}\hbar\omega_j\left(\mathbf{k}\right)\mathbf{v}_{\mathrm{g}}\left(\mathbf{k}j\right)\delta_{jj'}\delta_{\mathbf{k}\mathbf{k}'}N_t\left(\mathbf{k}'j',\mathbf{k}j\right). \tag{5}$$

To obtain the local energy density and heat flux in Eq. (4) and Eq. (5), we have to use the wave packet representation of phonons through a superposition of normal modes with a small spread of wave vectors.

The phonon Wigner function can be defined as [1]:

$$N\left(\mathbf{r},t,\mathbf{k}j\right)=\sum_{\mathbf{g}}\exp\left(i\mathbf{g}\cdot\mathbf{r}\right)N_t^j\left(\mathbf{k}+\frac{\mathbf{g}}{2},\mathbf{k}-\frac{\mathbf{g}}{2}\right), \tag{6}$$

where $N_t\left(\mathbf{k}j,\mathbf{k}'j'\right)=N_t^j\left(\mathbf{k}',\mathbf{k}\right)\delta_{jj'}$ in the absence of correlation between different phonon polarizations. With the help of Eq. (6), one can derive from Eq. (3) the phonon Boltzmann equation without collision term:

$$\frac{\partial N\left(\mathbf{r},t,\mathbf{k}j\right)}{\partial t}+\mathbf{v}_{\mathrm{g}}\left(\mathbf{k}j\right)\cdot\frac{\partial N\left(\mathbf{r},t,\mathbf{k}j\right)}{\partial\mathbf{r}}=0, \tag{7}$$

where the phonon group velocity is: $\mathbf{v}_{\mathrm{g}}\left(\mathbf{k}j\right)=\partial\omega_j\left(\mathbf{k}\right)/\partial\mathbf{k}$. The phonon collision term will be recovered when the anharmonic terms are considered in the Hamiltonian operator.

Modeling Transport in Phosphorus δ-Doped Silicon Tunnel Junctions

L. Maurer, M. Marshall, D.A. Campbell, L. Tracy,
T.-M. Lu, D. Ward, S. Misra
Sandia National Laboratories, Albuquerque, New Mexico 87185, USA
lmaurer@sandia.gov

There is growing interest in electrical devices based on phosphorus-doped Silicon (Si:P) δ layers, which can be fabricated with atomic precision using scanning tunneling microscope (STM) lithography. A STM is used to make lithographic patterns by selectively removing hydrogen from a hydrogen-passivated Si surface. Phosphene gas is then introduced and adsorbs where the hydrogen has been removed. The result is precise, planar structures made from a high density ($\approx 1.7 \times 10^{14} cm^{-2}$) of P donors. While great strides have been made in fabricating nanoelectronics from Si:P δ layers, the electronic structure (Figs. 1, 2) of the Si:P δ layers deviates significantly from that of silicon at normal levels of doping, and theoretical studies have produced inconsistent predictions (Table 1). This makes it difficult to accurately model devices made from Si:P δ layers.

In this work, we flip the problem around and use experimental transport measurements from nanoscale tunnel junctions to study the electronic structure of Si:P δ layers. We model tunnel junctions both with (Fig. 2) and without (Fig. 4) a gate to modulate the potential in the junction. We show that the transport properties of tunnel junctions depend strongly enough on the electronic structure that measurements could provide insight into the electronic structure (Fig. 3). We also model the effect of in-plane (patterned phosphorus, Figs. 4, 5) and surface (metal-dielectric) gates, since such gates will be necessary for more advanced devices. We compare our model to experimental results and find good agreement.

ACKNOWLEDGEMENT: This work was supported by the Laboratory Directed Research and Development Program at Sandia National Labs and was performed, in part, at the Center for Integrated Nanotechnologies, a U.S. Dept. of Energy, Office of Basic Energy Sciences user facility. Sandia National Labs is managed and operated by National Technology and Engineering Solutions of Sandia, LLC, a subsidiary of Honeywell International, Inc., for the U.S. Dept. of Energy's National Nuclear Security Administration under contract DE-NA0003525. The views expressed in the article do not necessarily represent the views of the DOE or the U.S. Government.

[1] D. J. Carter et al., Nanotechnology, **22,** 065701 (2011).
[2] D. W. Drumm et al., Nanoscale Res. Lett., **8**, 111 (2013).
[3] H. Ryu et al., Nanoscale, **5**, 8666 (2013). S. Lee et al., Phys. Rev. B, **84**, 205309 (2011).
[4] G. Qian et al, Phys. Rev. B, **71**, 045309 (2005).
[5] J. S. Smith et al., Phys. Rev. B, **89**, 035306 (2014).

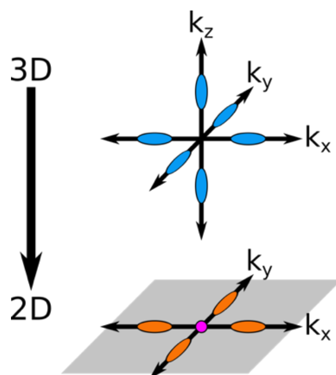

Fig.1: Basic band structure in a δ-layer. The charged δ-layer confines the electrons to a 2D plane. The six valleys in bulk Si (top) are effectively projected into 2D (bottom) — forming two types of bands: The two bulk Si bands along $\pm k_z$ are transformed into two Γ bands centered at $\vec{k} = 0$ (magenta), and the remaining four bands become known as Δ bands (orange).

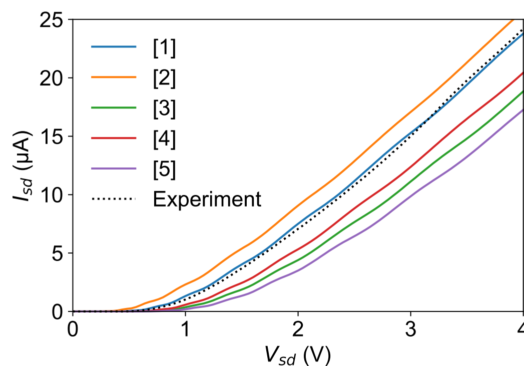

Fig. 3: Predicted total current through a tunnel junction formed from a 35-nm-wide wire with a 15-nm-wide gap for all parameters in Table 1 (references for parameters in legend) as well as experimental data (dotted). For this calculation, a 78 kΩ resistance is placed in series with the tunnel junction to better replicate experimental conditions.

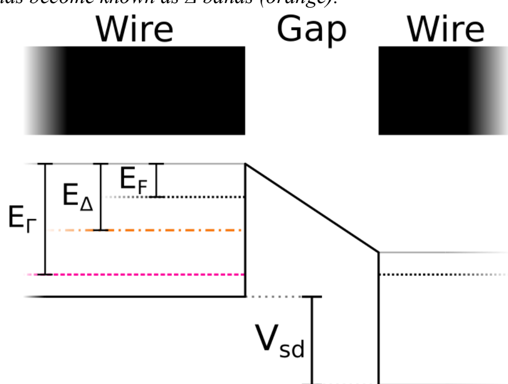

Fig.2: Top: top view of a δ-layer tunnel junction. Bottom: cross section of potential barrier along the wire axis. The barrier is trapezoidal due to a source-drain bias V_{sd} across the junction. The Γ and Δ bands and quasi-Fermi level E_F are shown as dashed curves. The grey curve is the bulk Si conduction-band minimum.

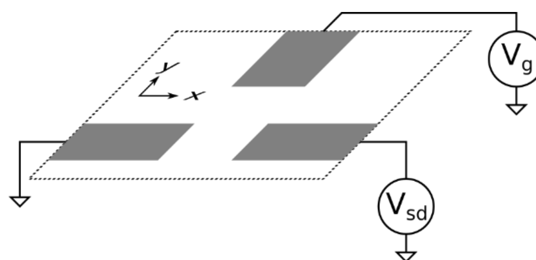

Fig. 4: A more complicated geometry includes an in-plane gate in addition to the tunnel junction. This requires an electrostatics simulation and a 2D treatment of tunneling through the barrier.

Model	E_{Γ_1}	E_{Γ_2}	E_Δ	E_F
DFT (1D) [1]	296	288	165	72
DFT (3D) [2]	369	269	68	23
TB (3D) [3]	401	375	249	115
DFT (1D) [4]	419	394	250	99
TB (3D) [5]	427	421	287	142

Table 1: Predicted band energy minima (see Fig. 1) and Fermi level E_F for quarter-layer doped δ-layer sheets — computed with density functional theory (DFT) and tight binding (TB). Values are measured in meV below the conduction-band minimum.

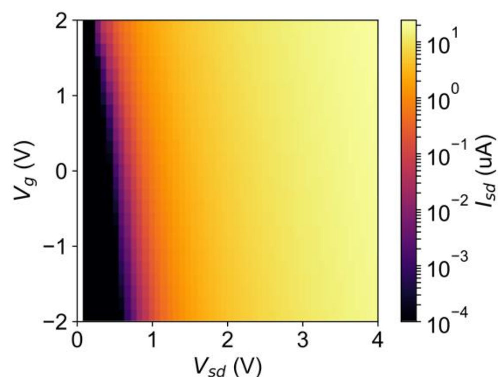

Fig.5: Current through a 35-nm-wide wire with a 15-nm-wide gap with the addition of an in-plane gate (Fig. 4).

Electronic Mobility in a Periodic Superlattice of InSb Quantum Dots

E. S. Skibinsky-Gitlin[1], F. M. Gómez-Campos [1,2], S. Rodríguez-Bolívar [1,2],
J. E. Carceller [1,2], M. Califano [3]

[1]Departamento de Electrónica y Tecnología de los Computadores, UGR, 18071, Spain
[2] CITIC, UGR, Granada, 18071, Spain
[3]Pollard Institute, School of Electronic and Electrical Engineering, University of Leeds, United Kingdom
erikski@ugr.es

Quantum dots (QDs) are gaining attention for their potential use in various technological areas such as in health [1], computing [2], or electronic devices [3]. In this last field, the highly configurable features of QDs, such as energy levels and absorption spectrum via QD size and passivation have interesting potential applications. With colloidal QDs there is also a high monodispersion in fabrication and closed packing, which leads to the possibility of high interaction between these building blocks. This could lead to the formation of a periodic superlattice which would lead to the existence of energy minibands as it happens with atomic lattices in semiconductors.

We present an application of our technique [4] for calculating the band structure and electron mobility arising from the conduction minibands for periodic InSb QD superlattices. The calculations consist of three steps. First we calculated the QD potential and eigenfunctions using the empirical pseudopotential method. The next step is to solve within the tight binding approach a periodic potential built upon this QD. Finally, we use the Fermi Golden Rule to calculate the electron scattering rates due to the presence of different sized, non-periodic QDs. These scattering rates are combined with the carrier velocity and Fermi energy level to obtain a temperature dependent mobility tensor, which is then diagonalized.

[1] S. Pathak, Journal of Neuroscience, **26**(7), 1893–1895, (2006)

[2] J. M. Nichol, L. A. Orona, S. P. Harvey, S. Fallahi, G. C. Gardner, M. J. Manfra, A. Yacoby, Npj Quantum Information, **3**(1), 1–4 (2017)

[3] D. Bera, L. Qian, T. K. Tseng, P. H. Holloway, Materials, **3**(4), 2260–2345 (10)

[4] F. M. Gómez-Campos, S. Rodríguez-Bolívar, E. S. Skibinsky-Gitlin, M. Califano, Nanoscale, **10**(20), 9679–9690 (2018)

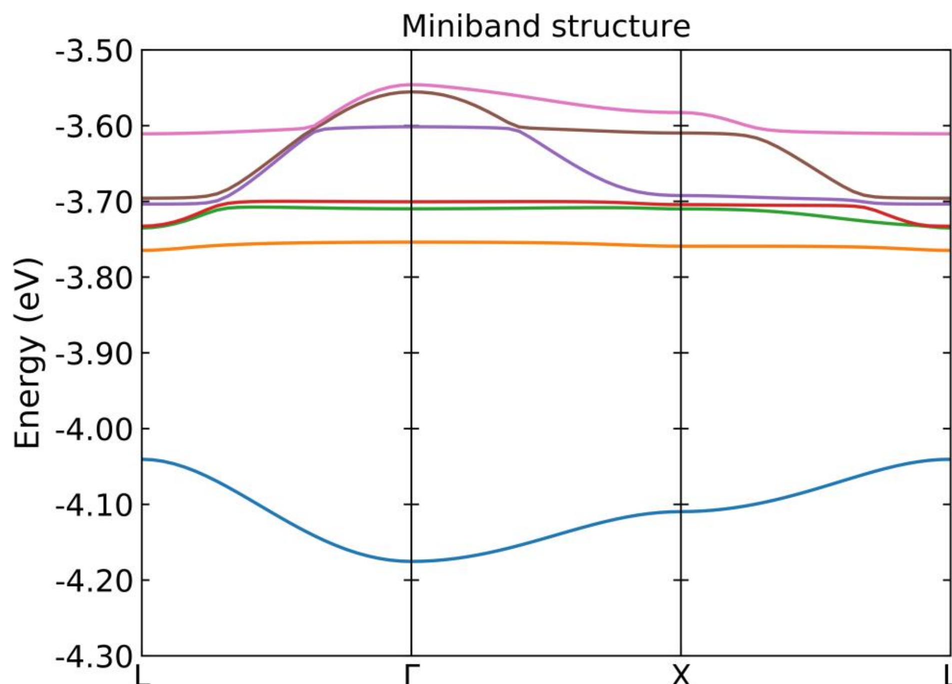

Fig.1: Band structure for the InSb QD superlattice with a lattice constant of 2.6 nm. QDs are one bond-length apart from each other. The energy reference is the vacuum

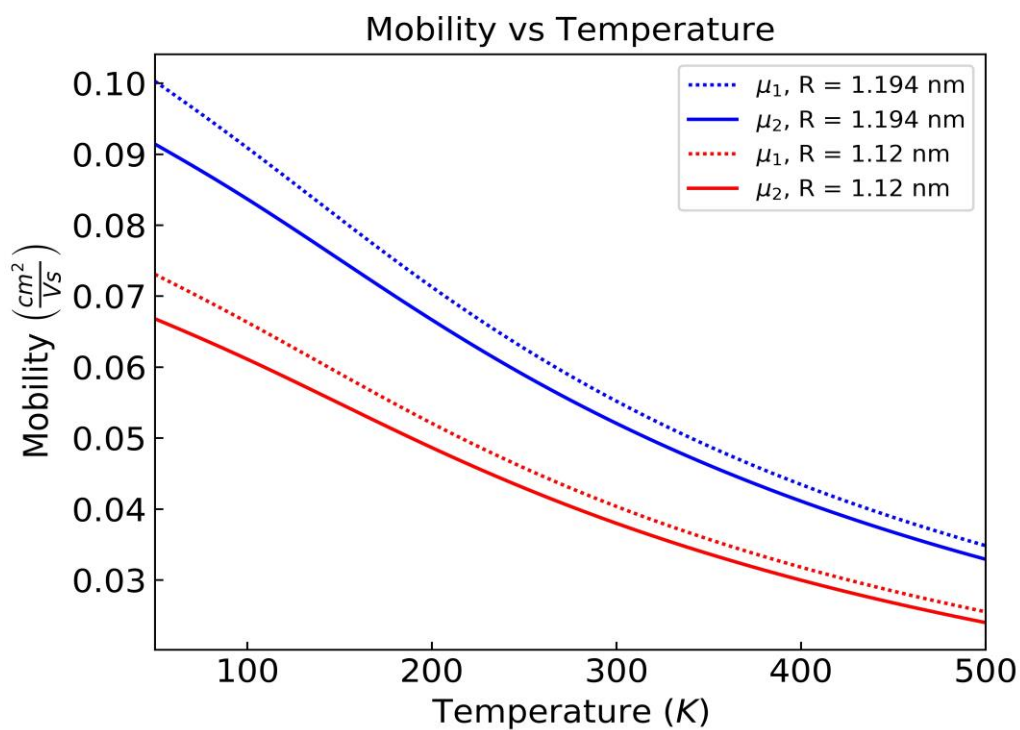

Fig.2 : Mobility eigenvalues for two different non periodic QD radius, 1.194 nm and 1.12 nm, at 1% concentration.

The Multi-Particle Drift-Diffusion Approach for Optoelectronic Devices

D. Rossi, A. Di Carlo, M. Auf der Maur
Department of Electronic Engineering, University of Rome "Tor Vergata",
Via del Politecnico 1, 00133 Rome, Italy
Daniele.Rossi@uniroma2.it

The traditional approach for semiconductor transport modeling in electronic devices is typically based on the drift-diffusion model [1], that describes uniquely the electron and hole flux driven by the gradients of the respective thermodynamic potentials, where each particle is assumed in local thermal equilibrium with the host material. Despite it has been the most used approach for electronic device simulation during the last fifty years, the classical drift-diffusion model exhibits several limitations when considering some mechanisms that occur in new nanoscale optoelectronics devices. We developed a novel generalized multi-particle drift-diffusion (mp-DD) model capable to overcome the limitations imposed by the classic drift-diffusion model. It was designed as flexible and reusable tool that takes into account explicitly multiple carrier populations, whether charged and neutral, allowing to consider also e.g. exciton transport or ionic motion, crucial for a relevant number of device structures. The modeling approach provides first of all the generalization to more than two carrier populations, each one individually assumed in a local thermodynamic equilibrium and characterized by its individual electrochemical potential; secondly, the particles are coupled to each other by recombination-generation terms, formulated to be strictly thermodynamically consistent. Figure 1 shows schematically the basic assumption behind the intra-band and inter-band recombination modeling. [2]

We applied the multi-DD in different application contexts. We calculated the impact of intermediated band charge transport on intermediate band solar cell (IBSC) performance, as show in Figure 2. We also model the optical and electrical operation of a thermally activated delayed fluorescence (TADF) in OLED. This represents a good demonstration of how the explicit inclusion of excitons, within the system of equations, allow us to draw important conclusions about the device emission profile (see Figure 3), accounting for typical exciton quenching processes such as triplet-triplet annihilation (TTA) [3] and triple polaron quenching (TPQ) [4].

[1] W. van Roosbroeck et al., Bell Syst. Tech. J., **4(29)**, 560-607 (1950).
[2] D. Rossi et al., IEEE Trans. Electr. Dev., submitted (2019).
[3] H. Uyoma et al., Nature, **7428(492)**, 234 (2012).
[4] M. A. Baldo et al., Phys. Rev. B, **62**, 10967-10977 (2000).

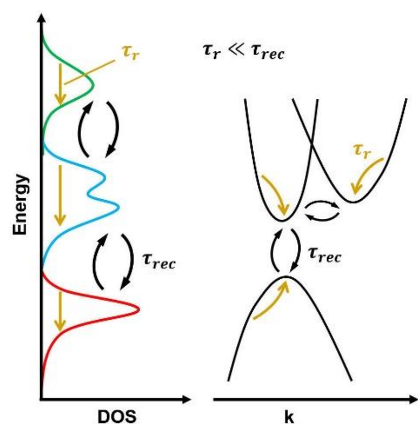

Fig.1: Sketch of the basic assumption in mp-DD model: several particle populations exist (e.g. in different bands, as shown on the right), which are in individual local thermal equilibrium and weakly coupled with each other. τ_r and τ_{rec} represent the characteristic intra-band (relaxation) and inter-band (recombination) scattering times.

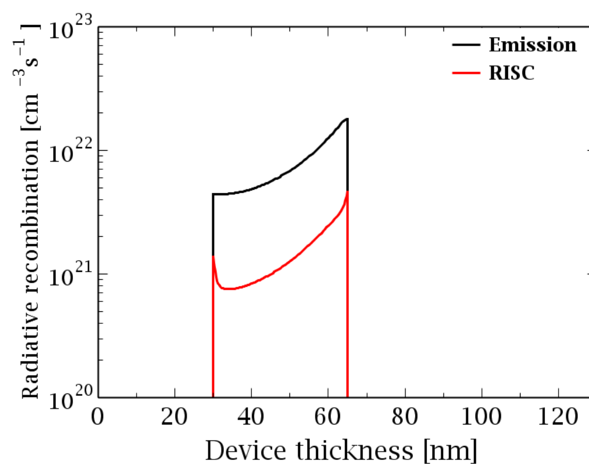

Fig.3: Radiative emission profile (black) and reverse inter-system crossing rate (red) calculated with mp-DD simulation at 6V bias operation within the emitter of a TADF OLED consisting of a TCTA/CBP:4CzIPN/TBPi stack.

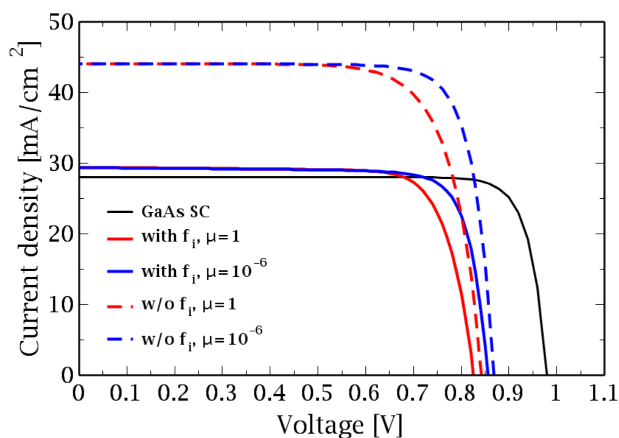

Fig.2: J-V characteristics comparison between experimental results on GaAs based solar cell and on GaAs based IBSC simulations for different electron mobility within the intermediate band (IB). Furthermore, we calculated the carrier generation by absorption accounting (full-lines) and neglecting (dashed lines) the actual occupation of VB,CB and IB.

9 783950 473803